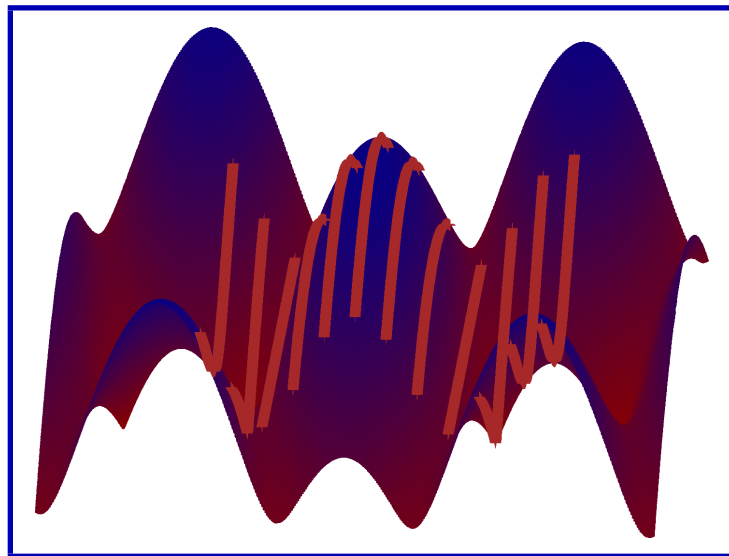


Many-particle theory of optical properties in low-dimensional nanostructures

Dynamics in single-walled carbon nanotubes
and semiconductor quantum dots

by Ermin Malić



Technische Universität Berlin
Institut für Theoretische Physik



Berlin, August 2008

Many-particle theory of optical properties in low-dimensional nanostructures

Dynamics in single-walled carbon nanotubes and
semiconductor quantum dots

Vorgelegt von Diplom-Physiker
Ermin Malić
aus Livno

von der Fakultät II: Mathematik und Naturwissenschaften
der Technische Universität Berlin

zur Erlangung des akademischen Grades

Doktor der Naturwissenschaften
— **Dr. rer. nat.** —

Genehmigte Dissertation

Promotionsausschuss

Vorsitzende : Prof. Dr. rer. nat. Ulrike Woggon, TU Berlin
1. Gutachter : Prof. Dr. rer. nat. Andreas Knorr, TU Berlin
2. Gutachterin : Prof. Dr. rer. nat. Stephanie Reich, FU Berlin

Tag der wissenschaftlichen Aussprache: 2. September 2008

Berlin, 2008
D 83

One ought to arrange one's life so that every moment of it becomes significant.

I. Turgenev in "Fathers and Sons"

Abstract

This work focuses on the theoretical investigation of optical properties of low-dimensional nanostructures, specifically single-walled carbon nanotubes (CNTs) and self-assembled InAs/GaAs quantum dots (QDs). The density-matrix formalism, an established technique for a quantum-mechanical description of many-particle systems, is applied to explain recent experimental results and to give insight into the underlying physics.

CNTs are ideal model systems to study the physics of one-dimensional structures. Due to their unique electronic and optical properties, they also attract great technological interest. However, the problems of the characterization of specific CNTs and their low luminescence efficiency are still substantial challenges in current research. A microscopic calculation of the absorption coefficient and the Rayleigh scattering cross section is performed by a novel approach combining the density-matrix formalism with the tight-binding wave functions. The derived excitonic Bloch equations allow the study of CNTs of arbitrary chiral index. In agreement with experiment, the calculated spectra of metallic nanotubes show a double-peaked structure resulting from the trigonal warping effect. The intensity ratios of the four lowest-lying transitions in both absorption and Rayleigh spectra can be explained by the different behavior of the optical matrix elements along the high-symmetry lines $K-\Gamma$ and $K-M$. Also in agreement with experiment, the Rayleigh line shape is predicted to be asymmetric, with an enhanced cross section for lower photon energies arising from non-resonant contributions of the optical susceptibility.

Furthermore, the Coulomb interaction is shown to be maximal when the momentum transfer is low. For intersubband processes with a perpendicular momentum transfer, the coupling strength is reduced to less than 5%. Due to their reduced dimensionality, CNTs have a strong Coulomb interaction that considerably changes their optical spectra. While the electron-electron interaction renormalizes the band gap, the electron-hole coupling leads in both semiconducting and metallic CNTs to the formation of excitons with binding energies of up to 1 eV. The chirality and diameter dependence of the excitonic binding energy and the transition frequency are presented in Kataura plots. Furthermore, the influence of the surrounding environment on the optical properties of CNTs is investigated.

Extending the confinement to all three spatial dimensions, semiconductor Bloch equation are derived to describe the dynamics in QD semiconductor lasers and amplifiers. A detailed microscopic analysis of the nonlinear turn-on dynamics of electrically pumped InAs/GaAs QD lasers is performed, showing the generation of relaxation oscillations on a nanosecond time scale in both the photon and charge carrier density. The complex interplay between strongly nonlinear Coulomb scattering rates and radiative processes gives rise to these oscillations, which are generated after a characteristic delay time of approximately 1 ns. In agreement with experiments, the theory predicts a strong damping of relaxation oscillations indicating the crucial importance of the Coulomb interaction between the bound QD and continuous wetting-layer states for a fast dynamical response of the laser.

Moreover, the ultrafast gain dynamics in QD semiconductor optical amplifiers has been investigated. It is found to be affected by the strength of the Coulomb scattering rates as well as by temperature, dephasing time, and pump power. Furthermore, the so called coherent artifact is shown to be a result of interference effects between the pump and the probe pulse rather than a consequence of two-photon absorption processes as often claimed in literature. The obtained results contribute to a better understanding of the limiting mechanisms for the ultrafast gain recovery in QD amplifiers.

Publications

- E. Malić, M. Hirtschulz, F. Milde, M. Richter, J. Maultzsch, S. Reich, and A. Knorr
„Coulomb effects in carbon nanotubes“
Physica Status Solidi (b) 245, 2155 (2008)
 - M. Hirtschulz, F. Milde, E. Malić, C. Thomsen, S. Reich, and A. Knorr
„Theory of ultrafast intraband relaxations in carbon nanotubes“
Physica Status Solidi (b) 245, 2164 (2008)
 - K. Lüdge, M. Bormann, E. Malić, P. Hövel, M. Kuntz, D. Bimberg, A. Knorr, and E. Schöll
„Turn-on dynamics and modulation response in semiconductor quantum dot lasers“
Physical Review B 78, 035316 (2008)
 - E. Malić, M. Hirtschulz, F. Milde, Y. Wu, J. Maultzsch, T. F. Heinz, A. Knorr, and S. Reich
„Theory of Rayleigh scattering from metallic carbon nanotubes“
Physical Review B 77, 045432 (2008)
 - M. Hirtschulz, F. Milde, E. Malić, S. Butscher, C. Thomsen, S. Reich, and A. Knorr
„CNT Bloch equations: a many-body approach to nonlinear and ultrafast optical properties“
Physical Review B 77, 035403 (2008)
 - S. Butscher, F. Milde, M. Hirtschulz, E. Malić, and A. Knorr
„Hot Electron Relaxation and Phonon Dynamics in Graphene“
Applied Physics Letters 91, 203103 (2007)
 - E. Malić, M. J. P. Bormann, P. Hövel, A. Knorr, E. Schöll, M. Kuntz, and D. Bimberg
„Coulomb damped relaxation oscillations in quantum dot semiconductor lasers“
IEEE Journal of Selected Topics in Quantum Electronics, Vol. 13, 1242 (2007)
 - E. Malić, M. Hirtschulz, F. Milde, Y. Wu, J. Maultzsch, T.F. Heinz, A. Knorr, and S. Reich
„Theoretical approach to Rayleigh and absorption spectra of semiconducting CNTs“
Physica Status Solidi (b) 244, 4236 (2007)
 - E. Malić, M. Hirtschulz, F. Milde, A. Knorr, and S. Reich
„Analytical approach to optical absorption in carbon nanotubes“
Physical Review B 74, 195431 (2006)
 - E. Malić, K. Ahn, M. Bormann, P. Hövel, E. Schöll, A. Knorr, M. Kuntz, and D. Bimberg
„Theory of relaxation oscillations in quantum dot semiconductor lasers“
Applied Physics Letters 89, 101107 (2006)
-
- J. Gomis-Bresco, S. Dommers, V. Temnov, U. Woggon, M. Lämmling, D. Bimberg, E. Malić, M. Richter, E. Schöll, and A. Knorr
„Amplification of ultrafast pulse trains in InGaAs QDs: mechanisms and limitations“
submitted for publication in Physical Review Letters (2008)

Conference Contributions

2008

- K. Lüdge, E. Malić, M. Kuntz, D. Bimberg, and E. Schöll
„Decoupled electron and hole dynamics in the turn-on behavior of quantum dot lasers“
talk at the International Semiconductor Laser Conference (ISLC08), Sorrento, Italy, September 2008
- J. E. Kim, E. Malić, M. Richter, and A. Knorr
„Quantum-dot vertical-cavity surface-emitting lasers (VCSELs): Combining finite-difference time-domain (FDTD) and calculation with microscopic material models“
International Nano-Optoelectronic Workshop (iNOW), Lake Saiko, Japan, August 2008
- K. Lüdge, E. Malić, and E. Schöll
„The role of decoupled electron and hole dynamics in the turn-on behavior of semiconductor quantum dot lasers“
International Conference on the Physics of Semiconductors (ICPS08), Rio de Janeiro, Brazil, July 2008
- S. Dommers, J. Gomis-Bresco, V. Temnov, U. Woggon, M. Lämmling, D. Bimberg, E. Malić, M. Richter, E. Schöll, and A. Knorr
„InGaAs quantum dot population and polarisation dynamics for ultrafast pulse train amplification“
talk at the International Conference on Semiconductor Quantum Dots (QD2008), Gyeongju, South Korea, May 2008
- K. Lüdge, E. Malić, A. Knorr, and E. Schöll
„Dynamic response of quantum dot lasers - Influence of nonlinear electron-electron scattering“,
talk at the International Conference on Lasers and Electro-Optics (CLEO/QELS), San Jose, USA, May 2008
- J. Gomis-Bresco, S. Dommers, V. Temnov, U. Woggon, M. Lämmling, D. Bimberg, E. Malić, M. Richter, E. Schöll, and A. Knorr
„InGaAs quantum dot population and polarisation dynamics for ultrafast pulse train amplification“
talk at the International Conference on Lasers and Electro-Optics (CLEO/QELS), San Jose, USA, May 2008
- F. Milde, S. Butscher, M. Hirtschulz, E. Malić, and A. Knorr
„Theory of nonthermal phonon and electron relaxation dynamics in graphene“
NOEKS08, Klink/Müritz, Germany, May 2008
- S. Dommers, J. Gomis-Bresco, V. Temnov, U. Woggon, M. Lämmling, D. Bimberg, E. Malić, M. Richter, E. Schöll, and A. Knorr
„Amplification of ultrafast pulse trains in InGaAs QD based semiconductor optical amplifiers“
NOEKS08, Klink/Müritz, Germany, May 2008
- E. Malić, M. Hirtschulz, F. Milde, Marten Richter, Janina Maultzsch, S. Reich, and A. Knorr
„Coulomb effects in carbon nanotubes“
International Winterschool (IWEPNM08), Kirchberg, Austria, March 2008

- M. Hirtschulz, F. Milde, E. Malić, S. Butscher, C. Thomsen, S. Reich, and A. Knorr
„Carrier-carrier interaction in SWCNTs: Theory of non-equilibrium and ultrafast nonlinear optical properties“
 International Winterschool (IWEPNM08), Kirchberg, Austria, March 2008
- E. Malić, K. Lüdge, M. J. P. Bormann, P. Hövel, M. Kuntz, D. Bimberg, A. Knorr, and E. Schoell
„Relaxation oscillations in quantum dot lasers“
invited talk, DPG, Berlin, Germany, February 2008
- Kathy Lüdge, E. Malić, A. Knorr, and E. Schoell
„Dynamic response of quantum dot lasers: Influence of nonlinear electron-electron scattering“
 talk at the DPG, Berlin, Germany, February 2008
- M. Hirtschulz, F. Milde, E. Malić, S. Butscher, C. Thomsen, S. Reich, and A. Knorr
„Influence of the Coulomb interaction on linear and nonlinear optical properties of SWCNTs“
 DPG, Berlin, Germany, February 2008
- F. Milde, S. Butscher, M. Hirtschulz, E. Malić, and A. Knorr
„Phonon induced carrier relaxation and hot phonon dephasing dynamics in graphene“
 DPG, Berlin, Germany, February 2008

2007

- E. Malić
„Rayleigh scattering from individual carbon nanotubes“
 seminar talk at the University of Modena and Reggio Emilia, Modena, Italy, September 2007
- E. Malić, M. Hirtschulz, F. Milde, J. Maultzsch, S. Reich, and A. Knorr
„Rayleigh scattering from single-walled carbon nanotubes“
 International Conference on Carbon Nanotubes (NT07), Ouro Preto City, Brazil, June 2007
- M. Hirtschulz, F. Milde, E. Malić, S. Butscher, C. Thomsen, S. Reich, and A. Knorr
„Carbon nanotube Bloch equations: A many-body approach to excitonic spectra, optical gain and the dynamical Stark effect“
 International Conference on Carbon Nanotubes (NT07), Ouro Preto City, Brazil, June 2007
- F. Milde, S. Butscher, M. Hirtschulz, E. Malić, and A. Knorr
„Phonon induced electron relaxation and dephasing dynamics in graphene and single-walled carbon nanotubes“
 International Conference on Carbon Nanotubes (NT07), Ouro Preto City, Brazil, June 2007
- E. Malić, M. J. P. Bormann, P. Hövel, M. Kuntz, D. Bimberg, A. Knorr, and E. Schoell
T₁ turn-on dynamics in semiconductor quantum dot lasers“
 International Conference on Lasers and Electro-Optics, (CLEO/QELS), Baltimore, USA, May 2007
- E. Malić, M. Hirtschulz, F. Milde, A. Knorr, and S. Reich
„Chirality dependence in the absorption and Rayleigh spectra of carbon nanotubes“
 International Conference on Lasers and Electro-Optics, (CLEO/QELS), Baltimore, USA, May 2007

- E. Malić, M. J. P. Bormann, P. Hövel, M. Kuntz, D. Bimberg, A. Knorr, and E. Schöll
„Turn-On dynamics and modulation response in in semiconductor quantum dot lasers“
 DPG, Regensburg, Germany, March 2007
- E. Malić, M. Hirtschulz, F. Milde, A. Knorr, and S. Reich
„Chirality dependence in the absorption spectra of carbon nanotubes“
 International Winterschool (IWEPNM07), Kirchberg, Austria, March 2007

2006

- E. Malić, K. Ahn, M. Bormann, P. Hövel, M. Kuntz, D. Bimberg, E. Schöll, and A. Knorr
„Coulomb damped relaxation oscillations in semiconductor quantum dot lasers“
 International Semiconductor Laser Conference (ISLC06), Hawaii, USA, September 2006
- E. Malić, M. Hirtschulz, F. Milde, A. Knorr, and S. Reich
„Analytical Approach to Optical Properties of Carbon Nanotubes“
 seminar talk at the Columbia University, New York, USA, August, 2006
- E. Malić, M. Hirtschulz, F. Milde, A. Knorr, and S. Reich
„Optical absorption in carbon nanotubes“
 International Conference on Carbon Nanotubes (NT06), Nagano, Japan, June 2006
- E. Malić, M. Bormann, P. Hövel, M. Kuntz, D. Bimberg, E. Schöll, and A. Knorr
„Theory of relaxation oscillations in semiconductor quantum dot lasers“
 DPG, Dresden, Germany, March 2006

Contents

1	Introduction	15
1.1	Motivation	15
1.2	Structure of the work	17
2	Theoretical Framework	19
2.1	Density matrix theory	19
2.1.1	Second quantization	21
2.2	Hamilton operator	21
2.2.1	Length vs. velocity gauge	23
2.3	Band structure	24
2.3.1	Effective-mass approach	24
2.3.2	Tight-binding approach	25
2.4	Bloch equations	27
2.4.1	Approximations	30
2.5	Absorption coefficient	32
2.6	Optical susceptibility	33
2.7	Rayleigh scattering	34
3	Single-Walled Carbon Nanotubes	37
3.1	Introduction	37
3.2	Structure and symmetry	39
3.3	Wave functions	41
3.3.1	Zone-folding approach	41
3.3.2	Trigonal warping effect	42

3.3.3	Nanotube band structure	44
3.3.4	Linear and helical quantum numbers	48
3.4	Matrix elements	49
3.4.1	Optical matrix element	49
3.4.2	Coulomb matrix element	55
3.4.3	Electron-phonon matrix element	59
3.5	Free-particle spectra	62
3.5.1	Absorption	62
3.5.2	Rayleigh scattering	69
3.5.3	Summary	74
3.6	Excitonic effects	75
3.6.1	Coulomb interaction	75
3.6.2	Band gap renormalization	78
3.6.3	Excitons	79
3.6.4	Dark excitons	81
3.6.5	Kataura plots	83
3.6.6	Background screening	86
3.6.7	Excitonic oscillator strength	90
3.6.8	Metallic nanotubes	91
3.6.9	Excitonic Rayleigh scattering spectra	93
3.6.10	Summary	95
3.7	Exciton-phonon coupling - an outlook	95
4	Quantum Dots	97
4.1	Introduction	97
4.2	Structure and symmetry	99
4.3	Wave functions	100
4.4	Matrix elements	102
4.4.1	Optical matrix elements	102
4.4.2	Coulomb matrix elements	103
4.5	Coulomb scattering rates	104

4.5.1	T_1 and T_2 times	108
4.6	Quantum dot amplifiers	110
4.6.1	Experiment	110
4.6.2	Gain dynamics	111
4.6.3	Summary	118
4.7	Quantum dot laser	119
4.7.1	Experiment	119
4.7.2	Turn-on-dynamics	120
4.7.3	Summary	127
5	Conclusions	129
	Appendix	131
A	Bloch Equations	131
A.1	Hartree-Fock	131
A.2	Coulomb scattering	133
B	Spontaneous Emission	137
C	Coulomb Matrix Elements	141
C.1	CNT Coulomb matrix elements	141
C.2	QD Coulomb matrix elements	144
D	Rayleigh Scattering Cross Section	149
E	Material Parameters	153
	Bibliography	157
	Index	169
	Acknowledgements	169

Chapter 1

Introduction

1.1 Motivation

Recent advances in the area of growth techniques have created numerous possibilities to design structures on a nanometer scale with unique optical, electronic, and transport characteristics.¹ A better understanding of these properties is a precondition for future device applications based on nanostructures.

This work focuses on the theoretical investigation of optical properties of low-dimensional nanostructures, i.e. systems of intermediate size lying between the macroscopic molecular and microscopic atomic length scale. Exemplary for these structures, single-walled carbon nanotubes (SW-CNTs) and self-assembled InAs/GaAs quantum dots (QDs) are investigated. The density-matrix formalism,^{2,3} an established technique for the quantum-mechanical treatment of the dynamics of many-particle systems, is applied to explain recent experimental results and to give insight into the underlying physics.

A main characteristic of low-dimensional structures is their density of states (DOS), see Fig.1.1. For a bulk semiconductor, the DOS is proportional to $\propto \sqrt{E}$; for low-dimensional structures, it is reduced to a step function in two-dimensional quantum wells, to Van Hove singularities $\propto \frac{1}{\sqrt{E}}$ in one-dimensional quantum wires (and SWCNTs), and to δ -functions in zero-dimensional QDs.

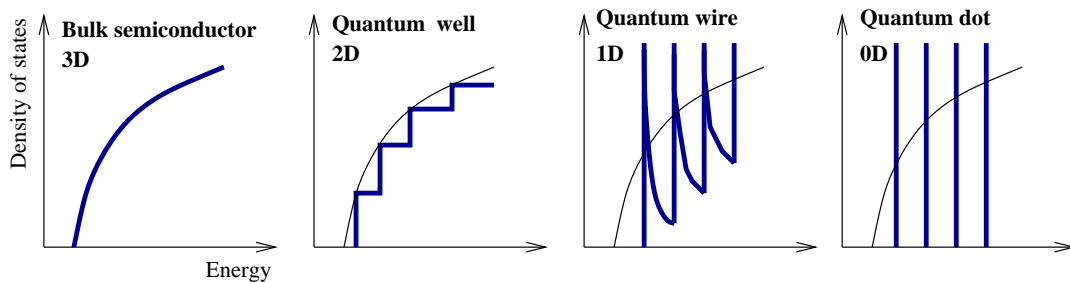


Figure 1.1: Density of states for three-, two-, one-, and zero-dimensional structures. For comparison, the three-dimensional density of states $\propto \sqrt{E}$ is shown in the background.

This leads to well-defined characteristic optical spectra making them excellent candidates for various opto-electronic applications.

Carbon nanotubes

Single-walled carbon nanotubes are tiny hollow cylinders constructed by rolling up graphene (a single layer of graphite) into a cylinder, see Fig. 1.2. They are prototypical one-dimensional structures, since their diameter is in the range of one nanometer, whereas their length can reach several micrometers. Depending on the rolling angle, a variety of nanotubes with different chiralities can be created. The characterization of specific SWCNTs is still a substantial challenge in current research. The well-pronounced optical transitions can be exploited for structural assignment. Optical spectroscopy methods, such as absorption, photoluminescence, Raman, and Rayleigh scattering are among the most important characterization techniques for SWCNTs.⁵⁻⁹

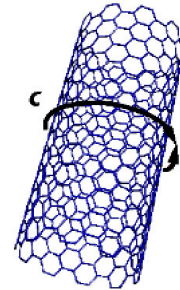


Figure 1.2: A carbon nanotube (taken from Reich et al.).⁴

For a long time, the optical excitations in SWCNTs were believed to be completely understood within the one-particle picture. Recent experiments on two-photon absorption have revealed the excitonic character of optical excitations in nanotubes.^{10,11} A number of theoretical investigations on excitonic properties have been performed by incorporating the Coulomb interaction within the Bethe-Salpeter equation combined with the GW method.¹²⁻¹⁷ This approach reaches good agreement with experimental data. However, due to its numerical complexity, it is limited to several specific nanotubes with small radii and small unit cells. In this work, microscopic calculations of the absorption coefficient $\alpha(\omega)$ and the Rayleigh scattering cross section $\sigma(\omega)$ are performed by a novel approach combining the density-matrix formalism with zone-folded tight-binding wave functions. The derived Bloch equations allow the study of arbitrary SWCNTs.

Quantum dots

When a material is grown on a substrate to which it is not lattice-matched, the resulting strain produces pyramid-shaped quantum dots in the interface between the materials,¹⁹ see Fig. 1.3. They form spontaneously on a surrounding wetting-layer (WL). They are considered to be zero-dimensional, since their size in all three spatial dimensions is comparable to the de Broglie wavelength of the charge carriers at room temperature.

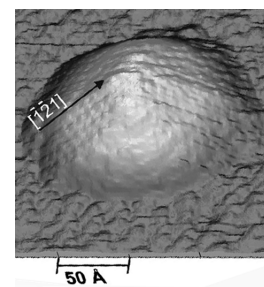


Figure 1.3: A pyramidal quantum dot (taken from Marquez et al.).¹⁸

Currently, there is an increasing interest in developing infrared QD lasers for high-speed data transmission. These lasers show a high potential for fast dynamical response, which is characterized by the frequency and the damping rate of the occurring relaxation oscillations (ROs).²⁰ The latter are oscillations of the photon density around its steady state evolving during turn-on processes of a gain switched laser. QD lasers have been found to show a strong damping of ROs compared to quantum well lasers.^{21,22} The underlying dynamic mechanisms are still being discussed in literature.^{23,24}

Furthermore, QDs are considered excellent candidates for applications as optical amplifiers in ultrafast ethernet networks. The acceleration of the gain recovery requires efficient scattering

channels to refill the QD ground state. Recent experiments show that there is a limiting delay time, below which the QDs cannot be completely refilled any more.²⁵ These limiting mechanisms for the ultrafast gain recovery are still not understood and present a substantial challenge in current research.

In this work, both the generation of strongly damped relaxation oscillations in QD lasers as well as the ultrafast gain recovery in QD optical amplifiers are addressed by a microscopic approach containing the semiconductor Bloch equations for the polarisation and population dynamics. The incorporated microscopically calculated Coulomb scattering rates describe the Auger transitions between localized QD and continuous WL states.

1.2 Structure of the work

In chapter 2, a brief overview of the applied theoretical methods is given. Chapters 3 and 4 contain the investigations on single-walled carbon nanotubes and the InAs/GaAs quantum dots, respectively. Both chapters start with an introductory section, followed by the description of the symmetry, the wave functions, and the matrix elements of the investigated structure. Chapter 3 then continues with the optical properties of carbon nanotubes within the free-particle picture and concludes with the investigation of excitonic effects. In chapter 4, the turn-on dynamics of electrically pumped QD lasers and the gain dynamics of QD based optical amplifier are subsequently investigated. Finally, chapter 5 contains a brief summary of the achieved results and gives an outlook for future research. The appendix shows detailed derivations of equations used in this work, giving the interested reader the opportunity to follow the calculations.

Life has no meaning a priori. Before you live, life itself is nothing. It is up to you to give it a meaning. Its value is nothing else than this meaning that you choose.

Jean-Paul Sartre

Chapter 2

Theoretical Framework

In this chapter, the basic theoretical methods applied in this work are presented. All investigations are based on the formalism of the density matrix theory. It is a powerful method allowing the microscopic calculation of expectation values of any observable. As a first step, the Hamilton operator of the system is determined. Then, applying the Heisenberg equation, the dynamics of the density matrix elements is obtained, resulting in the semiconductor Bloch equations. Finally, interesting observables, such as the absorption coefficient and the Rayleigh scattering cross section are calculated.

2.1 Density matrix theory

This work focuses on the theoretical description of low-dimensional nanostructures with carrier confinement in one, two or all three spatial directions below the size of carrier's de Broglie wavelength. As a result, these structures exhibit a variety of phenomena, which cannot be understood within the classical physics. In the past, two different quantum-mechanical approaches for the theoretical description of the dynamics of many-particle systems were developed: the Green's function theory and the density matrix theory.¹ Both approaches are quantum kinetic theories starting from a generalization of the classical concept of a distribution function. In this work, the density matrix formalism is applied. It can be used to calculate expectation values of any observable. It allows a straight-forward inclusion of many-body interactions, such as electron-electron or electron-phonon coupling, as well as the description of nonlinear effects.¹

The exact description of a quantum confined solid state structure requires the complete knowledge of the state, which can be obtained by performing a measurement of the complete set of commuting observables. With the exception of some model systems, this requirement cannot be fulfilled in practice, since, in general, the state vector of the system is not known, but rather the classical probabilities for various possible state vectors. Such statistical mixtures of states are described by the density operator ρ

$$\rho = \sum_i p_i |\Psi_i\rangle\langle\Psi_i| \quad \text{with} \quad \sum_i p_i = 1, \quad (2.1)$$

which is a sum of projectors onto the possible state vectors $|\Psi_i\rangle$, each weighted by a classical probability p_i with $0 \leq p_i \leq 1$. A system determined by a single state vector is called a pure

state, while a mixed state is described by a density operator consisting of an incoherent sum of pure-state contributions.^{26,27} This statistical uncertainty is only due to the insufficient knowledge of the system and can theoretically be removed by exactly determining the state vector of the system. In contrast, the quantum mechanical uncertainty is inherent and cannot be reduced. The state vector $|\Psi(t)\rangle$ of a system is given in the Schrödinger picture by $|\Psi(t)\rangle = \sum_i c_i(t)|u_i\rangle$, where the vectors $|u_n\rangle$ form an orthonormal basis of the state space. The evolution of the state vector is described by the Schrödinger equation

$$i\hbar \frac{d}{dt} |\Psi(t)\rangle = H |\Psi(t)\rangle \quad (2.2)$$

with the Hamilton operator H . The expectation value of an observable A is defined as $\langle A \rangle(t) = \langle \Psi(t) | A | \Psi(t) \rangle = \sum_{i,j} c_i^*(t) c_j(t) \langle u_i | A | u_j \rangle$. It is determined by the coefficients $c_i(t)$. In a pure state, a system can be described both by a density operator as well as by a state vector. The density operator has the advantage that the existence of an arbitrary global phase factor $e^{i\chi}$ is eliminated ($|\Psi(t)\rangle$ and $e^{i\chi}|\Psi(t)\rangle$ describe the same physical state). Furthermore, the expectation value is linear in $\rho(t)$, whereas it is quadratic with respect to $|\Psi(t)\rangle$. The density operator is represented in the $|u_n\rangle$ basis by a matrix called the density matrix with the elements $\rho_{ij}(t) = \langle u_i | \rho(t) | u_j \rangle = \sum_k \langle u_i | \phi_k(t) \rangle \langle \phi_k(t) | u_j \rangle = c_i^*(t) c_j(t)$ (for the pure state with $p_k = 1$). The expectation value of the observable can now be expressed as the trace over the density operator

$$\langle A \rangle(t) = \text{Tr}[\rho(t)A], \quad (2.3)$$

since $\langle A \rangle(t) = \langle \Psi(t) | A | \Psi(t) \rangle = \sum_{i,j} \langle u_i | \rho(t) | u_j \rangle \langle u_i | A | u_j \rangle = \sum_i \langle u_i | \rho(t) A | u_i \rangle$. The density operator is hermitian, i.e. $\rho^\dagger(t) = \rho(t)$, and in the case of a pure state it fulfils the relations $\rho^2(t) = \rho(t)$ and $\text{Tr}[\rho^2(t)] = 1$. The time evolution of the density operator is given by the Von Neumann equation

$$i\hbar \frac{d}{dt} \rho(t) = [H, \rho(t)]. \quad (2.4)$$

This equation directly follows from the Schrödinger equation: $\frac{d}{dt} \rho(t) = |\dot{\Psi}(t)\rangle \langle \Psi(t)| + |\Psi(t)\rangle \langle \dot{\Psi}(t)| = \frac{1}{i\hbar} H |\Psi(t)\rangle \langle \Psi(t)| - \frac{1}{i\hbar} |\Psi(t)\rangle \langle \Psi(t)| H = \frac{1}{i\hbar} [H, \rho(t)]$.

For many structures, a two-band system already gives good insight into the optical properties. Here, the state vector is given by $|\Psi(t)\rangle = c_1(t)|u_1\rangle + c_2(t)|u_2\rangle$ and the density operator can be written as a 2×2 matrix

$$\rho = \begin{pmatrix} c_1^*(t)c_1(t) & c_1^*(t)c_2(t) \\ c_2^*(t)c_1(t) & c_2^*(t)c_2(t) \end{pmatrix} = \begin{pmatrix} \rho_{11}(t) & \rho_{12}(t) \\ \rho_{21}(t) & \rho_{22}(t) \end{pmatrix}.$$

The positive real number $\rho_{ii}(t) = |c_i(t)|^2$ expresses the probability to find the system in the state $|u_i\rangle$. It describes the population dynamics of the states i . The non-diagonal elements $\rho_{12}(t) = \rho_{21}^*(t) = c_1^*(t)c_2(t)$ express the interference effects between the states $|u_1\rangle$ and $|u_2\rangle$ which can only appear when $|\Psi\rangle$ is a coherent linear superposition of these states. They correspond to the probability amplitude for an optical transition, and are often called coherence or microscopic polarization, see Fig. 2.1.

In the case of a mixture of states, the probabilities p_k for finding the system in the state $|\Psi_k(t)\rangle$ need to be considered. Taking into account that the state is undetermined before the measurement, the real positive number $\rho_{ii}(t) = \sum_k p_k |c_i^{(k)}(t)|^2$ describes the average probability of finding the system in the state $|u_i\rangle$. The complex quantity $\rho_{12}(t) = \sum_k p_k c_{1,k}^*(t) c_{2,k}(t)$ expresses the average of interference effects taken over all possible states of the statistical mixture.

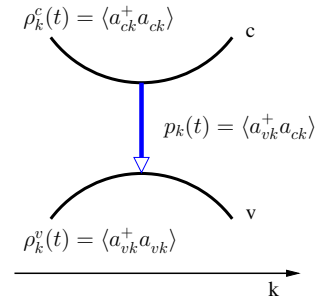


Figure 2.1: Illustration of the density matrix elements.

2.1.1 Second quantization

For reasons of clarity, the notation of the density matrix elements is simplified labelling the population probability with $\rho_k^\lambda(t) = \langle a_{\lambda,k}^+ a_{\lambda,k} \rangle$ and the microscopic polarisation with $p_k(t) = \langle a_{\lambda,k}^+ a_{\lambda',k} \rangle$ with the band indices λ, λ' and the index k denoting all quantum numbers of the system. These quantities allow the calculation of expectation values of any observable, such as the macroscopic polarisation $P(t)$ or the macroscopic current density $j(t)$ which are necessary to determine the absorption coefficient $\alpha(\omega)$ and the scattering cross section $\sigma(\omega)$. The description of many-particle systems requires much effort due to the necessary symmetrisation. The simplification of the second quantization formalism is based on the introduction of creation a_l^+ and annihilation a_l operators with the compound index $l = (\lambda, k)$. Then, the symmetry conditions are expressed in fundamental commutation relations between these operators

$$[a_l, a_{l'}^+]_{\mp} = a_l a_{l'}^+ \mp a_{l'}^+ a_l = \delta_{l,l'} , \quad (2.5)$$

$$[a_l, a_{l'}]_{\mp} = [a_l^+, a_{l'}^+]_{\mp} = 0 . \quad (2.6)$$

The fermion's operators anti-commute ($[\dots]_+$), while the boson's operators commute ($[\dots]_-$). All many-particle (anti-)symmetric states can now be traced back to a vacuum state $|0\rangle$. For example, an N-particle state can be expressed by creation operators as follows²⁸

$$|\phi_{l_1} \cdots \phi_{l_N}\rangle^{\pm} = \frac{1}{\sqrt{N!}} a_{l_1}^+ a_{l_2}^+ \cdots a_{l_N}^+ |0\rangle .$$

To complete the formalism the observables expressed by operators need to be transformed into the second quantization notation, as well. All physically relevant N-particle observables A_N can be described by a sum of one-particle A_1^i and two-particle operators $A_2^{(i,j)}$ yielding²⁸

$$A_N = \sum_{i=1}^N A_1^i + \frac{1}{2} \sum_{i,j}^{i \neq j} A_2^{(i,j)} = \sum_{l,l'} \langle \phi_l | A_1 | \phi_{l'} \rangle a_l^+ a_{l'} + \frac{1}{2} \sum_{l_i, l'_i} \langle \phi_{l_1} \phi_{l_2} | A_2^{(1,2)} | \phi_{l'_1} \phi_{l'_2} \rangle a_{l_1}^+ a_{l_2}^+ a_{l'_2} a_{l'_1} .$$

The symmetry is completely contained in the creation and annihilation operators. The complicated process of (anti-)symmetrisation is redundant in second quantisation, since it is induced in the fundamental commutation relations.

2.2 Hamilton operator

The Hamilton operator introduced in Eq. (2.2) determines the dynamics of a physical system, in particular the dynamics of the density matrix elements $\rho_k^\lambda(t)$ and $p_k(t)$. Considering a gas of charge carriers in a crystal under an applied electromagnetic field, the carriers interact with each other as well as with the phonon modes of the crystal leading to different contributions in the Hamilton operator

$$H = H_c + H_{c-c} + H_{0,ph} + H_{c-ph} . \quad (2.7)$$

The first term H_c describes the non-interacting carrier system in the presence of the external electromagnetic field. In this work, a semiclassical approach is applied, i.e. the charge carriers are treated quantum-mechanically, while the field is considered to be classical. The light-matter interaction is described by (minimal coupling Hamiltonian)

$$H_c = \frac{1}{2m_0} [\mathbf{p} - e\mathbf{A}(\mathbf{r}, t)]^2 + e\psi(\mathbf{r}, t) + V(r) \quad (2.8)$$

with the canonical momentum \mathbf{p} , the scalar and vector potentials $\psi(\mathbf{r}, t)$ and $\mathbf{A}(\mathbf{r}, t)$ of the electromagnetic field, the electrostatic potential $V(r)$, the carrier's mass m_0 and charge e (for electrons $e = -e_0$). In contrast to the vector and scalar potential, the electric and magnetic fields are gauge-independent and satisfy the relations

$$\mathbf{E}(\mathbf{r}, t) = -\dot{\mathbf{A}}(\mathbf{r}, t) - \nabla\psi(\mathbf{r}, t), \quad (2.9)$$

$$\mathbf{B}(\mathbf{r}, t) = \nabla \times \mathbf{A}(\mathbf{r}, t). \quad (2.10)$$

Within the radiation gauge, i.e. $\nabla \cdot \mathbf{A}(\mathbf{r}, t) = 0$ and $\psi(\mathbf{r}, t) = 0$, and the dipole approximation with $\mathbf{k} \cdot \mathbf{r} \ll 1$, the carrier Hamiltonian H_c can be reduced to

$$H_c^{(p \cdot A)} = H_{0,c} + H_{c-f}^{(p \cdot A)} = \left[\frac{p^2}{2m_0} + V(r) \right] + \left[-\frac{e}{m_0} \mathbf{p} \cdot \mathbf{A}(\mathbf{r}_0, t) + \frac{e^2}{2m_0} A^2(\mathbf{r}_0, t) \right]. \quad (2.11)$$

The dipole approximation assumes a space independence of the vector potential, i.e. $\mathbf{A}(\mathbf{r} + \mathbf{r}_0, t) = \mathbf{A}(t) \exp[i\mathbf{k} \cdot (\mathbf{r} + \mathbf{r}_0)] \simeq \mathbf{A}(t) \exp[i\mathbf{k} \cdot \mathbf{r}_0]$. It consists of the unperturbed free-carrier part $H_{0,c}$ and the carrier-field interaction part H_{c-f} . The contribution with the quadratic vector potential is usually small and can be neglected.²⁹ The Hamilton operator from Eq. (2.11) is often called the $\mathbf{p} \cdot \mathbf{A}$ Hamiltonian. Another form of the carrier Hamiltonian can be derived starting from the Schrödinger equation and using the local gauge invariance. A solution $\Psi(\mathbf{r}, t)$ of the Schrödinger equation, can be determined except for an arbitrary phase $\exp[-i\chi(\mathbf{r}, t)]$. Using the gauge transformation

$$\Psi(\mathbf{r}, t) = \exp\left[\frac{ie}{\hbar} \mathbf{r} \cdot \mathbf{A}(\mathbf{r}_0, t)\right] \Phi(\mathbf{r}, t) \quad (2.12)$$

with $\chi = -\frac{e}{\hbar} \mathbf{r} \cdot \mathbf{A}(\mathbf{r}_0, t)$ yields the electric-dipole interaction Hamilton operator, which is also known as the $\mathbf{r} \cdot \mathbf{E}$ Hamiltonian

$$H_c^{(r \cdot E)} = H_{0,c} + H_{c-f}^{(r \cdot E)} = \left[\frac{p^2}{2m_0} + V(r) \right] + \left[-e\mathbf{r} \cdot \mathbf{E}(\mathbf{r}_0, t) \right]. \quad (2.13)$$

The two different forms of the carrier-field contributions need to be used with care, since they can lead to different results in certain situations (non-linear effects, non-resonant regions). This aspect will be discussed in more detail in the next section.

Applying the formalism of the second quantization with the carrier creation and annihilation operators a_l^\dagger and a_l , the free carrier part $H_{0,c}$ can be expressed as $H_{0,c} = \sum_l \varepsilon_l a_l^\dagger a_l$. The $\mathbf{p} \cdot \mathbf{A}$ carrier-field operator transforms to

$$H_{c-f}^{(p \cdot A)} = i \frac{e_0 \hbar}{m_0} \sum_{l,l'} \mathbf{M}_{l,l'} \cdot \mathbf{A}(t) a_l^\dagger a_{l'} \quad (2.14)$$

with the optical matrix elements $\mathbf{M}_{l,l'} = \int d\mathbf{r} \Phi_l^*(\mathbf{r}) \nabla \Phi_{l'}(\mathbf{r})$. Here, the relation $\mathbf{p} = \frac{\hbar}{i} \nabla$ has been used. Within the $\mathbf{r} \cdot \mathbf{E}$ approach the carrier-field coupling is described by

$$H_{c-f}^{(r \cdot E)} = \sum_{l,l'} \mathbf{d}_{l,l'} \cdot \mathbf{E}(t) a_l^\dagger a_{l'} \quad (2.15)$$

with the dipole matrix elements $\mathbf{d}_{l,l'} = \frac{e_0}{V} \int d\mathbf{r} \Phi_l^*(\mathbf{r}) \mathbf{r} \Phi_{l'}(\mathbf{r})$.

The second contribution of the Hamilton operator from Eq. (2.7) is given by the carrier-carrier interaction

$$H_{c-c} = \frac{1}{2} \sum_{l_1, l_2, l_3, l_4} V_{l_3, l_4}^{l_1, l_2} a_{l_1}^\dagger a_{l_2}^\dagger a_{l_4} a_{l_3} \quad (2.16)$$

with the Coulomb matrix elements $V_{l_3, l_4}^{l_1, l_2} = \int d\mathbf{r} \int d\mathbf{r}' \Phi_{l_1}^*(\mathbf{r}) \Phi_{l_2}^*(\mathbf{r}') V_{Coul}(\mathbf{r} - \mathbf{r}') \Phi_{l_3}(\mathbf{r}') \Phi_{l_4}(\mathbf{r})$. where $V_{Coul}(\mathbf{r} - \mathbf{r}')$ is the screened Coulomb potential.

Finally, the last two parts of Eq. (2.7) describe the coupling between charge carriers and phonons. The free-phonon Hamiltonian $H_{0,ph}$ describes a system of non-interacting phonons. In analogy to the free-carrier part, it is given by $H_{0,ph} = \sum_i \hbar\omega_i (b_i^\dagger b_i + \frac{1}{2})$ with the phonon creation and annihilation operators b_i^\dagger and b_i . The compound index i contains the phonon mode γ and the phonon wave vector \mathbf{q} . The interaction of carriers with the phonon modes of the crystal is given by³⁰

$$H_{c-ph} = \sum_{l, l'} \sum_i [g_{l, l'}^i a_l^\dagger b_i a_{l'} + g_{l, l'}^{i*} a_{l'}^\dagger b_i^\dagger a_l] . \quad (2.17)$$

The carrier-phonon matrix elements $g_{l, l'}^i = \int d\mathbf{r} \Phi_l^*(\mathbf{r}) \delta V_i \Phi_{l'}(\mathbf{r})$ are determined via the phonon-induced disturbed deformation potential δV_i . The first contribution from Eq. (2.17) describes the processes of phonon absorption, while the second term describes the processes of the phonon emission.

2.2.1 Length vs. velocity gauge

In the last section, it was shown that the carrier-field interaction can be treated within the $\mathbf{p} \cdot \mathbf{A}$ or within the $\mathbf{r} \cdot \mathbf{E}$ approach. The corresponding Hamilton operators are given in Eq. (2.11) and Eq. (2.13), respectively. They are also called minimal coupling and direct coupling Hamiltonians, which are related via the gauge transformation from Eq. (2.12). In literature, the expressions length and velocity gauge are common. Since quantum mechanics is gauge invariant, i.e. a physical quantity can be described in any gauge with the same result, the two approaches are expected to lead to same results. Unfortunately, this turns out not to be the case in certain situations.³¹⁻³⁴ In numerical solutions of the time-dependent Schrödinger equation, gauge invariance has been confirmed. However, when describing realistic systems, often approximations, such as dipole, rotating wave or two-level approximation, have to be applied. When physical quantities are calculated using approximations, different results might be obtained in length and velocity gauge.

To show the difference between these two approaches, the ratio between the corresponding matrix elements is estimated.³⁵ Assuming an linearly polarized electric field with $\mathbf{E}(0, t) = \mathbf{E}_0 \cos \omega t$ interacting with an atom at the position $\mathbf{r} = 0$. The corresponding vector potential can be determined via Eq. (2.9) yielding $\mathbf{A}(0, t) = -\frac{1}{\omega} \mathbf{E}_0 \sin \omega t$. The matrix elements calculated between an initial eigenstate $|s\rangle$ and final eigenstate $|f\rangle$ of the unperturbed Hamiltonian $H_0 = \frac{p^2}{2m} + V(r)$, i.e. $H_0|s\rangle = \hbar\omega_s|s\rangle$ and $H_0|f\rangle = \hbar\omega_f|f\rangle$ are given by

$$\mathbf{M}_{rE} = \langle s | -e\mathbf{r} \cdot \mathbf{E}_0 | f \rangle, \quad \mathbf{M}_{pA} = \langle s | \frac{e}{m\omega} \mathbf{p} \cdot \mathbf{E}_0 | f \rangle . \quad (2.18)$$

Using the fundamental commutation relation $[r_i, p_j] = i\hbar\delta_{ij}$, it follows $\mathbf{p} = m\mathbf{v} = -\frac{im}{\hbar}[\mathbf{r}, H_0]$. Exploiting the fact that $|s\rangle, |f\rangle$ are the eigenstates of H_0 , the matrix element can be expressed in the velocity gauge as

$$M_{pA} = -\frac{e}{\hbar\omega} \langle s | -H_0\mathbf{r} + H_0\mathbf{r} | f \rangle \cdot \mathbf{E}_0 = -i \frac{\omega_f - \omega_s}{\omega} \langle s | \mathbf{r} | f \rangle \cdot \mathbf{E}_0 . \quad (2.19)$$

Now, the ratio between the two matrix elements can be calculated easily yielding

$$\left| \frac{M_{pA}}{M_{rE}} \right| = \frac{\omega_{gap}}{\omega} . \quad (2.20)$$

The matrix elements differ by the ratio of the transition frequency $\omega_{gap} = \omega_f - \omega_s$ and the field frequency ω . This leads to differences in measurable quantities, such as transition rates. As a result, the transformation between the length and velocity gauge has to be performed with care, in particular when non-resonant effects are investigated. It is crucial to perform the gauge transformation of both wave functions and potentials to obtain gauge-invariant results.^{33,35} In the example above, only the potentials have been transformed. This incomplete transformation often leads to correct results, since for $\mathbf{A}(t_s) = \mathbf{A}(t_f) = 0$ the gauge transformation corresponds to the identity operator.

2.3 Band structure

The description of the dynamics of a physical system requires the calculation of a set of eigenfunctions $\Phi_n(\mathbf{r})$ and the corresponding eigenenergies E_n of the non-interacting-carrier Hamiltonian. The label n denotes a set of discrete or continuous quantum numbers which determine the physical state. In this one-particle basis, the carrier-field, carrier-carrier and carrier-phonon matrix elements introduced in the previous section can be calculated. In the absence of static fields the wave functions $\Phi_n(\mathbf{r})$ correspond to the Bloch states of the crystal with the compound index $n = (\lambda, \mathbf{k})$ containing the wave vector \mathbf{k} and the band index λ .

Different approaches have been developed to calculate the electronic band structure. In the nearly free electron model, the crystal potential is assumed to be small. As a result the band structure is harmonic and the wave functions are plane waves. In contrast, the tight-binding model starts from the opposite assumption, i.e. the electrons are assumed to be tightly bound to their nuclei.

In this work, the effective mass approximation as well as the tight-binding approach will be used.

2.3.1 Effective-mass approach

The effective-mass method is convenient for the discussion of optical spectra since it allows the determination of the band structure over the entire Brillouin zone. The eigenfunction of the non-interacting Hamiltonian comply with the Bloch theorem and can be separated into a phase factor and a function $u_\lambda(\mathbf{k}, \mathbf{r})$ fulfilling the periodicity of the lattice

$$\Phi_\lambda(\mathbf{k}, \mathbf{r}) = \exp(i\mathbf{k} \cdot \mathbf{r})u_\lambda(\mathbf{k}, \mathbf{r}). \quad (2.21)$$

These orthogonal wave functions are often called Bloch functions. It is sufficient to calculate the periodic functions $u_{\mathbf{k},\lambda}(\mathbf{r})$ to solve the one-particle Schrödinger equation

$$\left[-\frac{\hbar^2}{2m}\Delta + \hbar\frac{\mathbf{k} \cdot \mathbf{p}}{m} + \frac{\hbar^2\mathbf{k}^2}{2m} + U(\mathbf{r}) \right] u_\lambda(\mathbf{k}, \mathbf{r}) = E_\lambda(\mathbf{k})u_\lambda(\mathbf{k}, \mathbf{r}) \quad (2.22)$$

with the periodic potential $U(\mathbf{r})$. Here, the wave functions $\Phi_\lambda(\mathbf{k}, \mathbf{r})$ from Eq. (2.21) have been inserted into the Schrödinger equation [Eq. (2.2)] and the nabla operator coming from the relation $\mathbf{p} = \frac{\hbar}{i}\nabla$ has been applied, paying attention to the product rule. The eigenvalue equation [Eq. (2.22)] for the energies $E_\lambda(\mathbf{k})$ can be solved in an easier way than the Schrödinger equation from Eq. (2.2), since now the periodicity of the functions $u_\lambda(\mathbf{k}, \mathbf{r})$ can be exploited. Within the effective-mass method, the electronic bandstructure is calculated considering the terms with $\mathbf{k} \cdot \mathbf{p}$ and \mathbf{k}^2 as perturbations. Assuming the energies $E_\lambda(\mathbf{k}_0)$ and the functions $u_\lambda(\mathbf{k}_0, \mathbf{r})$ are known, the method

can be used to calculate the band structure near any point \mathbf{k}_0 by expanding Eq. (2.22). Starting from a small number of experimentally determined energy gaps and optical matrix elements, the electronic band structure over the entire Brillouin zone can be determined. Assuming that the band structure has a minimum at $E_\lambda(\mathbf{k}_0)$ the energy (and the corresponding eigenfunctions $u_\lambda(\mathbf{k}_0)$) can be expanded into a Taylor-series³⁶

$$E_\lambda(\mathbf{k}) = E_\lambda(\mathbf{k}_0) + \left(\frac{\partial E_\lambda(\mathbf{k})}{\partial \mathbf{k}} \right)_{\mathbf{k}_0} (\mathbf{k} - \mathbf{k}_0) + \left(\frac{1}{2} \frac{\partial^2 E_\lambda(\mathbf{k})}{\partial \mathbf{k}^2} \right)_{\mathbf{k}_0} (\mathbf{k} - \mathbf{k}_0)^2. \quad (2.23)$$

The linear term in \mathbf{k} vanishes because of the assumed minima at \mathbf{k}_0 yielding (for $\mathbf{k}_0 = 0$)

$$E_\lambda(\mathbf{k}) = E_\lambda(\mathbf{k}_0) + \frac{\hbar^2 \mathbf{k}^2}{2m_\lambda^*} \quad (2.24)$$

with the effective mass of the band λ

$$\frac{1}{m_\lambda^*} = \frac{1}{\hbar^2} \left(\frac{\partial^2 E_\lambda(\mathbf{k})}{\partial \mathbf{k}^2} \right). \quad (2.25)$$

As a result, the mass of an electron in a solid differs from the mass of a free electron. This difference arises from the coupling of electronic states from different bands, and it is expressed by the $\mathbf{k} \cdot \mathbf{p}$ term in Eq. (2.22). The higher the curvature of the band, the smaller is the corresponding effective mass.

This approach will be used in Sec. 4.3 to calculate the bands structure in the two-dimensional WL.

2.3.2 Tight-binding approach

The tight-binding (TB) method is based on the assumption that electrons are tightly bound to their nuclei. The idea of this approach is to start from isolated atoms. Their eigenfunctions and eigenvalues are assumed to be known. Then the modifications are investigated, when the atoms are brought together. When they are close enough, their wave functions overlap and lead to chemical bonds and to the formation of crystals. Due to this interaction, the electronic energies broaden and build continuous bands,³⁷ see Fig. 2.2.

The electronic wave functions $\Phi_\lambda(\mathbf{k}, \mathbf{r})$ can be approximated as a linear combination of the atomic wave functions $\psi_\lambda(\mathbf{k}, \mathbf{r})$

$$\Phi_\lambda(\mathbf{k}, \mathbf{r}) = \frac{1}{\sqrt{N_0}} \sum_{\mathbf{R}_j}^{N_0} e^{i\mathbf{k} \cdot \mathbf{R}_j} \psi_\lambda(\mathbf{r} - \mathbf{R}_j) \quad (2.26)$$

where N_0 is the number of unit cells in the crystal and \mathbf{R}_j are lattice vectors. The wave functions $\Phi_\lambda(\mathbf{k}, \mathbf{r})$ are the eigenfunctions of the unperturbed Hamiltonian H_0 , and they fulfil the Bloch

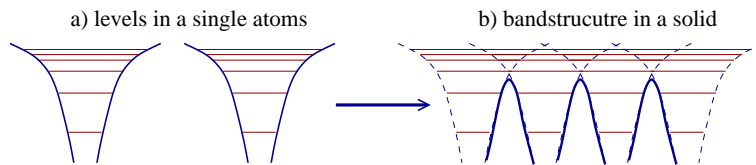


Figure 2.2: Illustration of formation of bands in solid starting from isolated atoms.

theorem $\Phi_\lambda(\mathbf{k}, \mathbf{r} + \mathbf{R}) = e^{i\mathbf{k}\cdot\mathbf{R}}\Phi_\lambda(\mathbf{k}, \mathbf{r})$. The eigenfunctions of the complete Hamiltonian $H = H_0 + H_{int}$ including the interacting part H_{int} can be expressed as a linear combination of $\Phi_\lambda(\mathbf{k}, \mathbf{r})$

$$\Psi(\mathbf{k}, \mathbf{r}) = \sum_{\lambda} C_{\lambda}(\mathbf{k})\Phi_{\lambda}(\mathbf{k}, \mathbf{r}). \quad (2.27)$$

The eigenvalue problem $H\Psi_{\lambda}(\mathbf{k}, \mathbf{r}) = E_{\lambda}(\mathbf{k})\Psi_{\lambda}(\mathbf{k}, \mathbf{r})$ has a solution only if the secular equation is fulfilled

$$\det[\hat{\mathbf{H}} - E_{\lambda}(\mathbf{k})\hat{\mathbf{S}}] = 0 \quad (2.28)$$

with the interacting matrix elements $\hat{H}_{\lambda,\lambda'} = \langle \Phi_{\lambda}|H|\Phi_{\lambda'} \rangle$ and the overlap between the Bloch functions $\hat{S}_{\lambda,\lambda'} = \langle \Phi_{\lambda}|\Phi_{\lambda'} \rangle$.

Restricting the problem to graphene, a one-atom layer of graphite, that contains the atoms A and B in the unit cell, a system of two linear equations is obtained. The equivalence of the two atoms further simplifies the equations due to the relations $\hat{H}_{AA} = \hat{H}_{BB}$, $\hat{H}_{AB} = \hat{H}_{BA}^*$ and $\hat{S}_{AA} = \hat{S}_{BB}$, $\hat{S}_{AB} = \hat{S}_{BA}^*$. Then, the eigenvalue problem can be easily solved using the quadratic formula yielding

$$E_{v,c} = \frac{1}{2} \frac{2\hat{H}_{AA}\hat{S}_{AA} - 2Re[\hat{H}_{AB}\hat{S}_{AB}^*]}{|\hat{S}_{AA}|^2 - |\hat{S}_{AB}|^2} + c_{\lambda} \sqrt{\left(\frac{-2\hat{H}_{AA}\hat{S}_{AA} + 2Re[\hat{H}_{AB}\hat{S}_{AB}^*]}{|\hat{S}_{AA}|^2 - |\hat{S}_{AB}|^2} \right)^2 - \hat{H}_{AA}^2 + |\hat{H}_{AB}|^2}.$$

The two eigenvalues E_v with $c_{\lambda} = +1$ and E_c with $c_{\lambda} = -1$ describe the valence and the conduction band in the band structure of graphene. This energy dispersion relation can be further simplified by assuming that only the first nearest-neighbors interact with each other

$$\hat{H}_{AB} = \langle \Phi_A|H|\Phi_B \rangle \approx \frac{1}{N} \sum_{\mathbf{R}_A} \sum_{\mathbf{R}_i=1,2,3} e^{i\mathbf{k}\cdot(\mathbf{R}_A-\mathbf{R}_i)} \langle \phi(\mathbf{r}-\mathbf{R}_A)|H|\phi(\mathbf{r}-\mathbf{R}_i) \rangle = \gamma_0 e(\mathbf{k})$$

with the carbon-carbon interaction energy $\gamma_0 \equiv \langle \phi(\mathbf{r}-\mathbf{R}_A)|H|\phi(\mathbf{r}-\mathbf{R}_B) \rangle$ and $e(\mathbf{k}) = \sum_{i=1}^3 \exp(i\mathbf{k}\cdot\mathbf{b}_i)$.

The vectors \mathbf{b}_i connect the atom located at \mathbf{r}_0 with its three nearest-neighbors at \mathbf{r}_i ($i = 1, 2, 3$), see Fig. 2.3. Analogous calculations yield $\hat{S}_{AB} = s_0 e(\mathbf{k})$ with the overlap integral $s_0 \equiv \langle \phi(\mathbf{r}-\mathbf{R}_A)|\phi(\mathbf{r}-\mathbf{R}_B) \rangle$. Finally, assuming the atomic wave functions $\phi(\mathbf{r})$ to be normalized yields $\hat{S}_{AA} = 1$ and $\hat{H}_{AA} = \epsilon_0$ with a constant parameter ϵ_0 . Inserting these matrix element into Eq. (2.3.2) leads to the energy dispersion relation for graphene

$$E_{v,c} = \frac{\epsilon_0 + c_{\lambda}\gamma_0|e(\mathbf{k})|}{1 - c_{\lambda}s_0|e(\mathbf{k})|}. \quad (2.29)$$

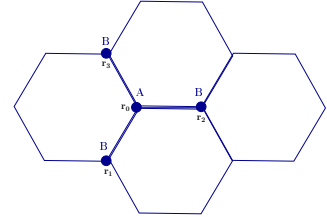


Figure 2.3: Illustration of the nearest-neighbor approximation.

The three parameters ϵ_0 , γ_0 , and s_0 are determined by fitting to experimental data or to first-principle results. Adjusting them for an accurate description of the band structure around the optically important K point (graphene is metallic at this point, i.e. $E_c = E_v$) leads to $\epsilon_0 = 0 \text{ eV}$, $-3 \text{ eV} \leq \gamma_0 \leq -2.5 \text{ eV}$ and $s_0 < 0.1$. The overlap parameter s_0 accounts for the asymmetry of conduction and valence bands, but since its influence on the absorption spectra in the optically relevant region $E < 4 \text{ eV}$ is vanishingly small, it is neglected in this work. A better agreement between the first-principle and the tight-binding calculations of the electronic band structure of graphene over the entire Brillouin zone can be achieved by extending the number of considered neighbors. However, being particularly interested in linear

optics which takes place around the K point, the presented nearest-neighbor tight-binding model is a good approximation.

The corresponding eigenfunctions to the eigenvalues of Eq. (2.29) are given by Eq. (2.27) with the coefficient functions $C_\lambda(\mathbf{k})$. The latter can be determined starting from the secular equation [Eq.(2.28)] yielding

$$C_A^{v,c}(\mathbf{k}) = C_B^{v,c}(\mathbf{k}) \frac{E_{v,c} S_{AB} - H_{AB}}{H_{AA} - E_{v,c} S_{AA}} = c_\lambda \frac{e(\mathbf{k})}{|e(\mathbf{k})|} C_B^{v,c}(\mathbf{k}). \quad (2.30)$$

Exploiting the normalization of the wave function $|\Psi(\mathbf{k}, \mathbf{r})|^2 = 1$ yields the relation for $C_B^{v,c}(\mathbf{k})$

$$C_B^{v,c}(\mathbf{k}) = \frac{1}{\sqrt{2}} \sqrt{\frac{1}{1 - c_\lambda s_0 e(\mathbf{k})}}. \quad (2.31)$$

Here, the eigenvalue problem has been solved for graphene. In Sec. 3.3, the presented solutions in Eqs. (2.29)-(2.31) will be taken as the starting point for a description of the band structure of carbon nanotubes.

2.4 Bloch equations

The calculation of the absorption coefficient $\alpha(\omega)$ and the Rayleigh scattering cross section $\sigma(\omega)$, furthermore the description of non-linear pump-probe experiments are in the focus of this work. These quantities can be expressed using the single-particle density matrix elements, i.e. the microscopic polarization $p_{\mathbf{k}}(t) = \langle a_{v,\mathbf{k}}^+ a_{c,\mathbf{k}} \rangle$ and the population probabilities in the conduction $\rho_{\mathbf{k}}^c(t) = \langle a_{c,\mathbf{k}}^+ a_{c,\mathbf{k}} \rangle$ and the valence band $\rho_{\mathbf{k}}^v(t) = \langle a_{v,\mathbf{k}}^+ a_{v,\mathbf{k}} \rangle$. In this section, the temporal evolution of these quantities is derived. The starting point is the Hamilton operator for a many-particle system within the formalism of the second quantization

$$\begin{aligned} H &= H_{0,c} + H_{c-f} + H_{c-c} + H_{0,ph} + H_{c-ph} \\ &= \sum_l \varepsilon_l a_l^+ a_l + \sum_{l,l'} \mathbf{d}_{l,l'} \cdot \mathbf{E}(t) a_l^+ a_{l'} + \frac{1}{2} \sum_{l_1, l_2, l_3, l_4} V_{l_3, l_4}^{l_1, l_2} a_{l_1}^+ a_{l_2}^+ a_{l_4} a_{l_3} \\ &\quad + \sum_i \hbar \omega_i \left(b_i^+ b_i + \frac{1}{2} \right) + \sum_{l,l'} \sum_j (g_{l,l'}^i a_l^+ b_i a_{l'} + g_{l,l'}^{i*} a_{l'}^+ b_i^+ a_l). \end{aligned} \quad (2.32)$$

The single contributions of the Hamiltonian have been discussed in Sec. 2.2. The time evolution of an observable \hat{O} can be obtained from the Heisenberg equation of motion

$$i\hbar \frac{d}{dt} \hat{O}(t) = [\hat{O}(t), H]_- + \frac{\partial}{\partial t} \hat{O}(t). \quad (2.33)$$

If $\hat{O}(t)$ has no explicit time dependence, the second contribution vanishes. In contrast to the Schrödinger equation, the observables are considered to contain the entire time dependence (Heisenberg picture). The equation of motion for the corresponding expectation value is called the Ehrenfest-theorem

$$i\hbar \frac{d}{dt} \langle \hat{O}(t) \rangle = \langle [\hat{O}(t), H]_- \rangle. \quad (2.34)$$

It is independent of the quantum-mechanical picture and can be easily derived using Eq. (2.3) $\frac{d}{dt} \langle \hat{O} \rangle = \frac{d}{dt} \text{Tr}[\rho \hat{O}(t)] = \text{Tr}[\frac{d}{dt}(\rho) \hat{O}(t)] + \text{Tr}[\rho \frac{d}{dt} \hat{O}(t)] = \text{Tr}[\frac{1}{i\hbar} \rho [\hat{O}(t), H]_-]$. Note that the density

operator ρ has no time dependence within the Heisenberg picture. Applying the Hamilton operator from Eq. (2.32), exploiting Eq. (2.34), and the commutation relations from Eqs. (2.5)-(2.6), the equations of motion for the microscopic polarisation $p_{\mathbf{k}}(t)$ and the population probabilities $\rho_{\mathbf{k}}^j(t)$ ($j = c, v$) can be derived

$$\dot{p}_{\mathbf{k}}(t) = -i\omega_{\mathbf{k}}p_{\mathbf{k}}(t) - i\Omega(t)[\rho_{\mathbf{k}}^c(t) - \rho_{\mathbf{k}}^v(t)] \quad (2.35)$$

$$\begin{aligned} & -\frac{i}{\hbar} \sum_{\mathbf{k}'} [V_{ren}(\mathbf{k}, \mathbf{k}')p_{\mathbf{k}}(t) + V_{exc}(\mathbf{k}, \mathbf{k}')p_{\mathbf{k}'}(t) + V_{dep}(\mathbf{k}, \mathbf{k}')p_{\mathbf{k}'}(t)] - \frac{1}{T_2}p_{\mathbf{k}}(t) \\ & + \frac{i}{\hbar} \sum_{q, \gamma, \lambda} \left[g_{\mathbf{k}, q, \mathbf{k}+q}^{c\lambda, \gamma*} S_{\mathbf{k}, q, \mathbf{k}+q}^{v\lambda, \gamma} - g_{\mathbf{k}+q, q, \mathbf{k}}^{\lambda v, \gamma*} S_{\mathbf{k}+q, q, \mathbf{k}}^{\lambda c, \gamma} + g_{\mathbf{k}+q, q, \mathbf{k}}^{\lambda c, \gamma} S_{\mathbf{k}+q, q, \mathbf{k}}^{\lambda v, \gamma*} - g_{\mathbf{k}, q, \mathbf{k}+q}^{v\lambda, \gamma} S_{\mathbf{k}, q, \mathbf{k}+q}^{c\lambda, \gamma*} \right], \end{aligned}$$

$$\dot{\rho}_{\mathbf{k}}^j(t) = 2Im[\Omega^*(t)p_{\mathbf{k}}(t)] + \frac{2}{\hbar} Im \left[p_{\mathbf{k}}(t) \sum_{\mathbf{k}'} V^j(\mathbf{k}, \mathbf{k}')p_{\mathbf{k}'}(t) \right] - \frac{1}{T_{1,j}}\rho_{\mathbf{k}}^j(t) + S_j^{in} \quad (2.36)$$

$$+ \frac{i}{\hbar} \sum_{q, \gamma, \lambda} \left[g_{\mathbf{k}, q, \mathbf{k}+q}^{j\lambda, \gamma*} S_{\mathbf{k}, q, \mathbf{k}+q}^{j\lambda, \gamma} - g_{\mathbf{k}+q, q, \mathbf{k}}^{\lambda j, \gamma*} S_{\mathbf{k}+q, q, \mathbf{k}}^{\lambda j, \gamma} + g_{\mathbf{k}+q, q, \mathbf{k}}^{\lambda j, \gamma} S_{\mathbf{k}+q, q, \mathbf{k}}^{\lambda j, \gamma*} - g_{\mathbf{k}, q, \mathbf{k}+q}^{j\lambda, \gamma} S_{\mathbf{k}, q, \mathbf{k}+q}^{j\lambda, \gamma*} \right].$$

These three differential equations are called semiconductor Bloch equations.² Their derivation is straight-forward, but lengthy. It is presented in detail in App. A. The color illustrates, which part of the Hamilton operator leads to which contribution in the Bloch equations. The free-particle contributions are colored blue. The first term in Eq. (2.35) describes the free dynamics of the carriers due to the free-carrier part of the Hamiltonian $H_{0,c}$. It leads to an oscillation of the microscopic polarization with the frequency $\omega_{\mathbf{k}} = \omega_{c\mathbf{k}} - \omega_{v\mathbf{k}}$ corresponding to the band gap. The second part describes the carrier-field coupling which depends on the difference in population probabilities for the two involved states. Its strength is given by the Rabi frequency $\Omega(t) = \frac{1}{\hbar} \mathbf{d}_{vc} \cdot \mathbf{E}(t)$ within the $\mathbf{r} \cdot \mathbf{E}$ picture (Eq. (2.13)) or $\Omega(t) = -i \frac{e_0}{m_0} \mathbf{M}_{vc} \cdot \mathbf{A}(t)$ if the $\mathbf{p} \cdot \mathbf{A}$ carrier-field Hamiltonian from Eq. (2.11) is used. Free-particle contributions will be further discussed in Sec. 3.5, where absorption and Rayleigh spectra of carbon nanotubes are investigated. In the following, the Hartree-Fock and higher correlations contributions are discussed separately.

Hartree-Fock contributions

The many-particle interactions are colored red (carrier-carrier) and green (carrier-phonon). They account for the fact that the set of equations obtained from the Heisenberg equation is not closed. The carrier-carrier and the carrier-phonon interaction couple the dynamics of single-particle elements of the density matrix to higher-order correlation terms. The dynamics of two-operator quantities couples to four-operator terms $\frac{d}{dt} \langle a_1^\dagger a_2 \rangle \propto \langle a_A^\dagger a_B^\dagger a_C a_D \rangle$ which describe correlations between carriers. Applying the Heisenberg equation to obtain an equation of motion for the four-operator quantities again leads to a set of equations that is not closed, since the many-particle interactions couple them to six-operator terms $\frac{d}{dt} \langle a_1^\dagger a_2^\dagger a_3 a_4 \rangle \propto \langle a_A^\dagger a_B^\dagger a_C^\dagger a_D a_E a_F \rangle$, six-operator terms couple to eight-operator terms and so on. The infinite hierarchy has to be truncated at some level. This hierarchy problem is common in many-particle physics. In this work, the correlation expansion³⁸ is used to obtain the presented Bloch equations. The idea of this approximation is that higher-order terms involving an increasing number of carriers become less important.^{1,39} The four-operator term is factorized into products of two-operator terms with:

$$\langle a_1^\dagger a_2^\dagger a_3 a_4 \rangle = \langle a_1^\dagger a_4 \rangle \langle a_2^\dagger a_3 \rangle - \langle a_1^\dagger a_3 \rangle \langle a_2^\dagger a_4 \rangle + \langle a_1^\dagger a_2^\dagger a_3 a_4 \rangle^c, \quad (2.37)$$

where $\langle \dots \rangle^c$ denotes the correlation term. This factorisation leads to a closed set of equations of motion for the single-particle elements of the density matrix. If the correlation term is neglected, the truncation is called Hartree-Fock factorisation or mean-field approximation. Then,

the carrier-carrier interaction leads to: i) $V_{ren}(\mathbf{k}, \mathbf{k}')$ - renormalization of the single-particle energy, ii) $V_{exc}(\mathbf{k}, \mathbf{k}')$ - formation of excitons and iii) $V_{dep}(\mathbf{k}, \mathbf{k}')$ - depolarization part describing processes with no momentum transfer. These effects are discussed in more detail in Sec. 3.6.

Correlation contributions (second order)

For some investigations in this work, the correlation of carriers plays an important role. Therefore, the Bloch equations (Eqs. (2.35)-(2.37)) have been derived beyond the Hartree-Fock approximation going up to the second order in the carrier-carrier and carrier-phonon interaction. The evaluation of the correlation terms, i.e. the consideration of two-particle correlations (also known as the second Born approximation), describes the scattering contributions leading to the coherence decay time T_2 and the population scattering time T_1 . Applying the Markov approximation, which neglects all memory effects (see next section), yields the Boltzmann equation for the occupation probability of an arbitrary state α

$$\frac{d}{dt}\rho_\alpha = S_\alpha^{in}(1 - \rho_\alpha) - S_\alpha^{out}\rho_\alpha = -\frac{1}{T_{1,\alpha}}\rho_\alpha + S_\alpha^{in}. \quad (2.38)$$

The Coulomb in- and out-scattering rates S_α^{in} and S_α^{out} describe the Coulomb induced capture and escape of charge carriers into the state α . In Fig. 2.4a, the process of the Coulomb interaction is sketched in a Feynman diagram. The Coulomb scattering rates will turn out to play a crucial role for understanding of the turn-on dynamics of QD lasers and of the gain dynamics of QD amplifiers, discussed in chapter 4. A detailed derivation of the Boltzmann equation and the Coulomb scattering rates is given in App. A.

Finally, the Bloch equations also contain the coupling of carriers to the phonon modes of the crystal. The carrier-phonon interaction has been calculated beyond the Markov approximation since the formation of phonon sidebands is in the focus of interest. This leads to phonon-assisted quantities $S_{\mathbf{k}_1, \mathbf{q}, \mathbf{k}_2}^{\lambda_1 \lambda_2, \gamma} = \langle a_{\lambda_1 \mathbf{k}_1}^+ b_{\gamma \mathbf{q}} a_{\lambda_2 \mathbf{k}_2} \rangle$ and $S_{\mathbf{k}_1, \mathbf{q}, \mathbf{k}_2}^{\lambda_1 \lambda_2, \gamma*} = \langle a_{\lambda_2 \mathbf{k}_2}^+ b_{\gamma \mathbf{q}}^+ a_{\lambda_1 \mathbf{k}_1} \rangle$ which describe the transition of an carrier accompanied by phonon emission or absorption, see Fig. 2.4b-c. Their time evolution is calculated using the Heisenberg equation

$$\begin{aligned} \dot{S}_{\mathbf{k}_1, \mathbf{q}, \mathbf{k}_2}^{vc, \gamma} &= -i(\omega_{c\mathbf{k}_2} - \omega_{v\mathbf{k}_1} + \omega_{\gamma\mathbf{q}})S_{\mathbf{k}_1, \mathbf{q}, \mathbf{k}_2}^{vc, \gamma} \\ &+ \sum_{\mathbf{k}'} \left[\left(V_{v\mathbf{k}_1, c\mathbf{k}'+\mathbf{q}}^{c\mathbf{k}_2, v\mathbf{k}'} - V_{c\mathbf{k}'+\mathbf{q}, v\mathbf{k}_1}^{c\mathbf{k}_2, v\mathbf{k}'} \right) S_{\mathbf{k}', \mathbf{q}, \mathbf{k}'+\mathbf{q}}^{vc, \gamma} + \left(V_{c\mathbf{k}_2, v\mathbf{k}'}^{c\mathbf{k}_2, v\mathbf{k}'} - V_{v\mathbf{k}', v\mathbf{k}_2}^{c\mathbf{k}_2, v\mathbf{k}'} \right) S_{\mathbf{k}_1, \mathbf{q}, \mathbf{k}_2}^{vc, \gamma} \right] \\ &+ (n_{\gamma\mathbf{q}} + 1)g_{\mathbf{k}_1, \mathbf{q}, \mathbf{k}_2}^{cc, \gamma*} (p_{\mathbf{k}_1} - p_{\mathbf{k}_2}). \end{aligned} \quad (2.39)$$

For reasons of clarity, the equation of motion is given only for the important case of $\lambda_1 = v$ and $\lambda_2 = c$ is shown. Different contributions arising from different parts of the Hamilton operator in Eq. (2.32) are again marked with different colors. The first term coming from the free-carrier part already reveals the expected position of the phonon sidebands corresponding to the phonon

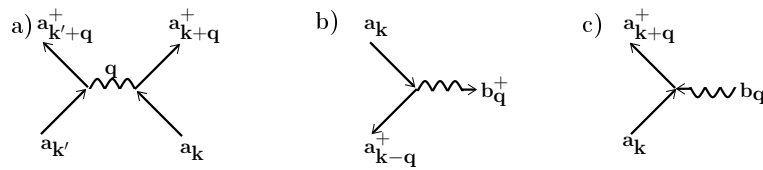


Figure 2.4: Feynman diagrams illustrating the many-particle interactions: a) Coulomb interaction, b) phonon absorption, and c) phonon emission.

energy $\hbar\omega_{\gamma q}$. The last contributions stem from the carrier-phonon Hamiltonian. It shows that the phonon assisted quantity $S_{\mathbf{k}_1, \mathbf{q}, \mathbf{k}_2}^{vc, \gamma}$ is driven by the difference of the microscopic polarization for the two wave vectors \mathbf{k}_1 and \mathbf{k}_2 . Finally, the second term describes the exciton-phonon coupling. In analogy to the excitonic contribution in the Bloch equation for $p_{\mathbf{k}}$, there is one part ($\propto S_{\mathbf{k}', \mathbf{q}, \mathbf{k}' + \mathbf{q}}^{vc, \gamma}$) that leads to a renormalization of the energy and one part ($\propto S_{\mathbf{k}', \mathbf{q}, \mathbf{k}' + \mathbf{q}}^{vc, \gamma}$) that is responsible for a transfer of the oscillator strength to the phonon sidebands. Further discussion of the exciton-phonon coupling can be found in Sec. 3.7.

2.4.1 Approximations

Except for some simple model system, the semiconductor Bloch equations [Eqs. (2.35)-(2.36)] cannot be solved analytically. Numerical solutions are obtained within the Runge-Kutta algorithm which is an established numerical method for solving initial value problems of ordinary differential equations. To keep the numerical complexity low, some approximations need to be applied. Depending on the focus of the investigation, the following approximations can be exploited.

Rotating Wave Approximation (RWA)

Both the microscopic polarisation $p_{\mathbf{k}}(t)$ and the Rabi frequency $\Omega(t)$ can be expressed as a product of a fast oscillating part and a slowly varying envelope function $\Omega(t) = (e^{i\omega_l t} + e^{i\omega_l t})e^{i\phi}\Omega_0(t)$ and $p_{\mathbf{k}}(t) = e^{-i\omega_{\mathbf{k}} t}\hat{p}_{\mathbf{k}}(t)$ with the frequency of light ω_l , the band gap frequency $\omega_{\mathbf{k}}$, and an arbitrary phase ϕ . Inserting these expressions into the Bloch equation (2.35) and neglecting carrier-carrier contributions for reasons of simplicity (since they do not change the argument) yields

$$\dot{\hat{p}}_{\mathbf{k}}(t) = -i(\omega_{\mathbf{k}} - \omega)\hat{p}_{\mathbf{k}}(t) - i\left(e^{i(\omega + \omega_l)t} + e^{i(\omega - \omega_l)t}\right)e^{i\phi}\Omega_0(t)(\rho_{\mathbf{k}}^c(t) - \rho_{\mathbf{k}}^v(t)).$$

For interactions near resonance, the exponential function with the relatively small argument ($\omega_l - \omega$) contributes considerably more than the one with ($\omega_l + \omega$). The latter oscillates fast, and as a result, its contribution vanishes when integrated over a time interval which is long compared to the time of a single oscillation,^{36,37} see Fig. 2.5.

Within the rotating wave approximation (RWA), the rapidly oscillating term $e^{i(\omega_l + \omega)t}$ is neglected and a modified Rabi frequency is introduced $\tilde{\Omega}(t) = e^{i(-\omega_l + \omega)t}e^{i\phi}\Omega_0(t)$. The semiconductor Bloch equation reads now

$$\dot{\hat{p}}_{\mathbf{k}}(t) = -i(\omega_{\mathbf{k}} - \omega)\hat{p}_{\mathbf{k}}(t) - i\tilde{\Omega}(t)(\rho_{\mathbf{k}}^c(t) - \rho_{\mathbf{k}}^v(t)).$$

This simplified equation is numerically less demanding, since the time resolution does not have to be very fine when the Runge-Kutta loop is evaluated. However, the RWA has this advantage only as long as $\omega_{\mathbf{k}} - \omega$ is a small quantity. Therefore, this approximation will be used for the description of quantum dots in chapter 4. The dynamics of carbon nanotubes will be investigated beyond the RWA, since the relevant energies can be in the range $0 \text{ eV} \leq \hbar(\omega_{\mathbf{k}} - \omega) \leq 10 \text{ eV}$.

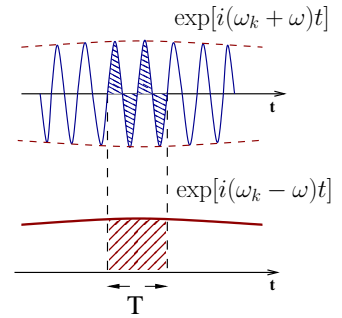


Figure 2.5: Comparison of fast and slowly oscillating contributions.

Markov Approximation

Due to the hierarchy problem discussed in the previous section, equations of motions for the four-particle correlation quantities $\sigma_{1234}^c = \langle a_1^+ a_2^+ a_3 a_4 \rangle$ need to be solved. The Markov approximation offers a fast way to give a formal time local solution of these quantities in terms of single particle functions. Using the Heisenberg equation leads to an equation of motion for $\sigma_{1234}^c(t)$ (see App. A)

$$\frac{d}{dt}\sigma_{1234}^c(t) = \frac{i}{\hbar}(\varepsilon_1 + \varepsilon_2 - \varepsilon_3 - \varepsilon_4)\sigma_{1234}^c(t) + \frac{i}{\hbar}Q(t) - \gamma\sigma_{1234}^c(t).$$

The solution of this linear differential equation is given by

$$\begin{aligned}\sigma_{1234}^c(t) &= \frac{i}{\hbar} \int_{-\infty}^t dt' e^{(\frac{i}{\hbar}\Delta\varepsilon + \gamma)(t-t')} Q(t') = \frac{i}{\hbar} \int_0^{\infty} ds e^{(\frac{i}{\hbar}\Delta\varepsilon + \gamma)\cdot s} Q(t-s) \\ &\approx \frac{i}{\hbar} Q(t) \int_0^{\infty} ds e^{(\frac{i}{\hbar}\Delta\varepsilon + \gamma)\cdot s} = -iQ(t)\pi\delta(\Delta\varepsilon).\end{aligned}$$

with $\Delta\varepsilon = (\varepsilon_1 + \varepsilon_2 - \varepsilon_3 - \varepsilon_4)$ and $s = t - t'$. The last relation is obtained using the representation of the δ -distribution (also called Heitler-Zeta function) $\lim_{\gamma \rightarrow 0} \frac{i}{\omega + i\gamma} = \pi\delta(\omega) + iPV(\frac{1}{\omega})$. The Cauchy integral principal value PV is neglected, since its contribution is assumed to be taken into account with the renormalization of the single-particle energies. The core of the Markov approximation is the negligence of the memory kernel of the integral, i.e. $Q(t-s) \approx Q(t)$. As a result of quantum mechanical smearing of wave functions, carriers retain some memory of the past collisions with other carriers in the system. This memory is greatly influenced by damping processes. The stronger the damping, the less important are the memory effects. By applying the Markov approximation all memory effects are neglected. This corresponds to taking only processes into account which fulfil the energy conservation. This is a good approximation for large many-particle systems where screening effects are crucial, furthermore for systems with short scattering time scales. The Markov approximation considerably reduces the numerical complexity. However, it cannot be applied for investigations where memory effects play a crucial role. In Sec. 3.7, the exciton-phonon interaction in carbon nanotubes is studied. Here, the experimentally observed formation of phonon sidebands can only be explained beyond the Markov approximation.

Random Phase Approximation (RPA)

The presented Bloch equations consist of equations of motion for the microscopic polarisation $p_{\mathbf{k}}(t) = \langle a_{v,\mathbf{k}}^+ a_{c,\mathbf{k}} \rangle$ and the occupation probabilities $\rho_{\mathbf{k}}^i(t) = \langle a_{i,\mathbf{k}}^+ a_{i,\mathbf{k}} \rangle$ with $i = c, v$. Within the random-phase approximation, these in \mathbf{k} diagonal quantities are considered to be dominant for the description of the investigated system. The non-diagonal quantities $\langle a_{v,\mathbf{k}}^+ a_{c,\mathbf{k}'} \rangle$ and $\langle a_{i,\mathbf{k}}^+ a_{i,\mathbf{k}'} \rangle$ are assumed to vanish. Generally, these quantities are complex numbers containing phase factors. Assuming that these phase factors are not correlated, these quantities cancel each other under the sum

$$\sum_{\mathbf{k}'} \langle a_{\lambda,\mathbf{k}}^+ a_{\lambda',\mathbf{k}'} \rangle \approx \langle a_{\lambda,\mathbf{k}}^+ a_{\lambda',\mathbf{k}} \rangle. \quad (2.40)$$

Only the diagonal contribution survives. This approximation is of great importance since it considerably reduces the number of relevant quantities.

The assumption of a homogeneous space, leads to the same result. This can be shown using the Wigner function⁴⁰ $f_{\mathbf{k}}(\mathbf{r}, t) = \sum_{\mathbf{k}'} e^{i\mathbf{k}'\cdot\mathbf{r}} \langle a_{i,\mathbf{k}}^+ a_{\mathbf{k}+\mathbf{k}'} \rangle$. Summed over \mathbf{k} it gives the entire occupation

density of a system at the position \mathbf{r} and at the time t . Using the assumption that the space is homogeneous, i.e. $f_{\mathbf{k}}(\mathbf{r}, t) = f_{\mathbf{k}}(\mathbf{r}', t)$ yields directly Eq. (2.40).

Linear optics

Most investigations in this work focus on the case of linear optics. Here, the driving field is considered to be small. As a result, the occupation in valence and conduction band is assumed to remain in thermodynamic equilibrium, i.e. the change in occupations is vanishingly small justifying the approximation of a full valence band ($\rho_v = 1$), and an empty conduction band ($\rho_c = 0$). Therefore, in the limiting case of linear optics, the dynamics of a system is fully determined by the microscopic polarisation.

2.5 Absorption coefficient

Under the influence of an electromagnetic field, a system is disturbed from its equilibrium state. The starting point for a study on how a material responds to such a perturbation are the Maxwell equations

$$\begin{aligned} \operatorname{div} \mathbf{E}(\mathbf{r}, t) &= \frac{\rho_0(\mathbf{r}, t)}{\varepsilon_0}, & \operatorname{div} \mathbf{B}(\mathbf{r}, t) &= 0, \\ \operatorname{rot} \mathbf{E}(\mathbf{r}, t) &= -\dot{\mathbf{B}}(\mathbf{r}, t), & \operatorname{rot} \mathbf{B}(\mathbf{r}, t) &= \mu_r \mu_0 \mathbf{j}(\mathbf{r}, t) + \frac{1}{c_m^2} \dot{\mathbf{E}}(\mathbf{r}, t) \end{aligned} \quad (2.41)$$

with the charge carrier density ρ_0 , the current density $\mathbf{j} = \sigma \mathbf{E}$ (σ is the electrical conductivity) furthermore with ε_0 (ε) as the permittivity and μ_0 (μ_r) as the permeability in the free space (in material). The speed of light in a medium is given by $c_m = \frac{1}{\sqrt{\mu_r \mu_0 \varepsilon \varepsilon_0}} = \frac{c}{n}$ with the refractive index $n = \sqrt{\mu_r \varepsilon}$ and the speed of light in vacuum $c = \frac{1}{\sqrt{\mu_0 \varepsilon_0}}$. In the presence of an electric field, a material responds by forming a microscopic dipole. While the positive nuclei move in the direction of the field, the electrons are displaced in the opposite direction resulting in a polarization $\mathbf{P}(\mathbf{r}, t)$ of the material. A magnetic field can lead to a magnetization $\mathbf{M}(\mathbf{r}, t)$ of certain materials. The relation between the field, the polarisation and the magnetisation are called material equations^{41,42}

$$\mathbf{D}(\mathbf{r}, t) = \varepsilon_0 \mathbf{E}(\mathbf{r}, t) + \mathbf{P}(\mathbf{r}, t), \quad \mathbf{H}(\mathbf{r}, t) = \frac{1}{\mu_0} \left(\mathbf{B}(\mathbf{r}, t) - \mathbf{M}(\mathbf{r}, t) \right). \quad (2.42)$$

In linear, isotrope, and homogeneous materials, the electric displacement $\mathbf{D}(\mathbf{r}, t)$ can be written in the frequency room as $\mathbf{D}(\omega) = \varepsilon(\omega) \varepsilon_0 \mathbf{E}(\omega)$. As a result, the polarisation and the electrical field are parallel

$$\mathbf{P}(\omega) = \varepsilon_0 (\varepsilon(\omega) - 1) \mathbf{E}(\omega) = \varepsilon_0 \chi(\omega) \mathbf{E}(\omega) \quad (2.43)$$

with the optical susceptibility describing the linear response of the system to a perturbation (often called response function)

$$\chi(\omega) = \varepsilon(\omega) - 1. \quad (2.44)$$

The propagation of electromagnetic waves through a medium with $\rho_0 = 0$ and $\mathbf{j} = 0$ is described by the homogeneous wave equation

$$\square \mathbf{E}(\mathbf{r}, t) = 0 \quad (2.45)$$

with the d'Alembert operator $\square \equiv \nabla^2 - \frac{1}{c_m^2} \frac{\partial^2}{\partial t^2}$. Generalizing the wave equation for homogeneous, uncharged electrical conductors, i.e. $\rho_0(\mathbf{r}, t) = 0$ and $\mathbf{j}(\mathbf{r}, t) \neq 0$, leads to the telegraph equation

$$\square \mathbf{E}(\mathbf{r}, t) = \mu_r \mu_0 \sigma \frac{\partial}{\partial t} \mathbf{E}(\mathbf{r}, t). \quad (2.46)$$

It can be easily derived from Maxwell equations. On one hand, for considered materials with $\rho_0(\mathbf{r}, t) = 0$, the divergence of the electrical field vanishes resulting in the relation $\text{rot rot } \mathbf{E}(\mathbf{r}, t) = \text{grad}(\text{div } \mathbf{E}(\mathbf{r}, t)) - \Delta \mathbf{E}(\mathbf{r}, t) = -\Delta \mathbf{E}(\mathbf{r}, t)$. On the other hand the relation $\text{rot rot } \mathbf{E}(\mathbf{r}, t) = -\text{rot } \dot{\mathbf{B}}(\mathbf{r}, t) = -\mu_r \mu_0 \sigma \dot{\mathbf{E}}(\mathbf{r}, t) + \frac{1}{c_m^2} \ddot{\mathbf{E}}(\mathbf{r}, t)$ is obtained from Maxwell equations. Combining the two relations yields Eq. (2.46).

For electromagnetic waves propagating in z -direction, a solution of the telegraph equation is given by $\mathbf{E}(z, t) = \mathbf{E}_0 e^{i(kz - \omega t)}$. Inserting this ansatz into Eq. (2.46) yields

$$k^2 = \frac{\omega^2}{c^2} (\varepsilon + i \frac{\sigma}{\varepsilon_0 \omega}) \mu_r \Rightarrow k' + ik'' = \frac{\omega^2}{c^2} (\varepsilon' + i\varepsilon'') \quad (2.47)$$

with the real parts k' , ε' and the imaginary parts k'' , ε'' of the wave vector $k(\omega)$ and the dielectric function $\varepsilon(\omega)$, respectively. Consequently, in a medium, the waves propagate with a complex wave vector $k(\omega)$. Its real and imaginary part can be separated using the relations⁴² $\varepsilon'(\omega) = \frac{c^2}{\omega^2} [k'(\omega)^2 - k''(\omega)^2]$ and $\varepsilon''(\omega) = 2 \frac{c^2}{\omega^2} k'(\omega) k''(\omega)$

$$k''(\omega) = \frac{\omega}{2n(\omega)c} \varepsilon''(\omega), \quad (2.48)$$

$$k'(\omega) = \frac{\omega}{c} \sqrt{\frac{1}{2} \left(\varepsilon'(\omega) + \sqrt{(\varepsilon'(\omega))^2 + (\varepsilon''(\omega))^2} \right)}. \quad (2.49)$$

Then, the solution of the telegraph equation has the form of a damped plane wave

$$\mathbf{E}(z, t) = \mathbf{E}_0 e^{ik(\omega)z} e^{-i\omega t} = \mathbf{E}_0 e^{-k''(\omega)z} e^{i(k'(\omega)z - \omega t)}. \quad (2.50)$$

The Beer-Lambert law for the intensity $I(z)$ of an electromagnetic wave follows directly

$$I(\omega) = |E(z)|^2 = e^{-2k''(\omega)z} = e^{-\alpha(\omega)z} \quad (2.51)$$

with the absorption coefficient $\alpha(\omega) = 2k''(\omega)$. It determines the distance of the light through the material. The real part of the wave vector gives the refractive index $n(\omega)$ with $n(\omega) = \frac{c}{\omega} k'(\omega)$. It determines the change of the speed of light in a medium $c_m(\omega) = \frac{c}{n(\omega)}$. For most structures the real part of the dielectric function $\varepsilon(\omega)$ is larger than the imaginary part resulting in the widely used approximation $n(\omega) \approx \sqrt{\varepsilon(\omega)}$. Often, the refractive index has only a weak dependence on frequency. Therefore, the absorption coefficient can be simplified to

$$\alpha(\omega) \propto \omega \text{Im } \varepsilon(\omega) = \omega \text{Im } \chi(\omega) \quad (2.52)$$

with the dielectric function $\varepsilon(\omega) = \chi(\omega) + 1$ introduced in Eq. (2.44).

2.6 Optical susceptibility

The determination of the absorption coefficient $\alpha(\omega)$ requires the calculation of the optical susceptibility $\chi(\omega)$. The latter can be calculated either with the Fourier transform of the macroscopic polarisation $P(\omega)$ or the current density $j(\omega)$. Equations (2.43) and (2.44) are valid for each component of the electrical field and the polarisation. As a result, the optical susceptibility can be written as⁴³

$$\chi(\omega) = \frac{P(\omega)}{\varepsilon_0 E(\omega)}. \quad (2.53)$$

The classical macroscopic polarisation $P(\mathbf{r}, t) = e \sum_i \mathbf{r} \delta(\mathbf{r} - \mathbf{r}')$ is defined as dipole density. In second quantization it can be written as a sum over the microscopic polarisation $p_{\mathbf{k}}(t) = \langle a_{v\mathbf{k}}^+ a_{c\mathbf{k}} \rangle$ and the dipole matrix element $d_{vc}(\mathbf{k})$ [Eq. (2.15)]

$$P(t) = \sum_{\mathbf{k}} d_{vc}(\mathbf{k}) p_{\mathbf{k}}(t) + \text{c.c.} . \quad (2.54)$$

The dynamics of the microscopic polarisation can be calculated with the Bloch equations [Eqs. (2.35)-(2.37)]. The optical matrix element $d_{vc}(\mathbf{k})$ is often adjusted to experimental data.

Within the $\mathbf{p} \cdot \mathbf{A}$ approach, the optical susceptibility can be expressed as a function of the current density $j(\omega)$ and the vector potential $A(\omega)$

$$\chi(\omega) = \frac{j(\omega)}{\varepsilon_0 \omega^2 A(\omega)} . \quad (2.55)$$

This equation can be easily transformed into Eq. (2.53) by using the relations $\mathbf{j} = \frac{\partial \mathbf{P}}{\partial t}$ and $\mathbf{E} = -\dot{\mathbf{A}} - \nabla \phi$ (the scalar potential ϕ vanishes within the Coulomb gauge) stemming from Maxwell equations. The macroscopic current density $\mathbf{j}(t)$ is defined as

$$\mathbf{j}(t) = \frac{e_0}{2m_0} \sum_{\lambda, \lambda', \mathbf{k}, \mathbf{k}'} \left(\langle \lambda \mathbf{k} | \mathbf{p} - e \mathbf{A}(t) | \lambda' \mathbf{k}' \rangle \langle a_{\lambda, \mathbf{k}}^+ a_{\lambda', \mathbf{k}'} \rangle + \text{c.c.} \right) .$$

After applying the dipole approximation (photon momentum is negligible in comparison to a typical electron momentum) and considering only a two-band system, i.e. $\lambda, \lambda' \in \{v, c\}$, the equation reads

$$\begin{aligned} \mathbf{j}(t) &= \frac{e_0}{2m_0 V} \sum_{\mathbf{k}} \left[\langle c \mathbf{k} | \mathbf{p} | v \mathbf{k} \rangle \langle a_{c, \mathbf{k}}^+ a_{v, \mathbf{k}} \rangle + \langle v \mathbf{k} | \mathbf{p} | c \mathbf{k} \rangle \langle a_{v, \mathbf{k}}^+ a_{c, \mathbf{k}} \rangle - e_0 \mathbf{A}(t) (\langle a_{c, \mathbf{k}}^+ a_{c, \mathbf{k}} \rangle + \langle a_{v, \mathbf{k}}^+ a_{v, \mathbf{k}} \rangle) + \text{c.c.} \right] \\ &= \frac{1}{V} \frac{2e_0}{m_0} \frac{\hbar}{i} \sum_{\mathbf{k}} \text{Re} \left[\mathbf{M}^{vc}(\mathbf{k}) p_{\mathbf{k}}(t) \right] - \frac{e_0^2}{m_0} \mathbf{A}(t) n_{tot} \end{aligned} \quad (2.56)$$

with the optical matrix element $\mathbf{M}^{vc}(\mathbf{k}) = \langle c, \mathbf{k} | \nabla | v, \mathbf{k} \rangle$, the microscopic polarization $p_{\mathbf{k}}$ and the total electronic density $n_{tot} = \frac{1}{V} \sum_{\lambda} \sum_{\mathbf{k}} \langle a_{\lambda, \mathbf{k}}^+ a_{\lambda, \mathbf{k}} \rangle$. Here, the symmetry-imposed selection rule for the optical matrix elements $\sum_{\mathbf{k}} \langle \lambda \mathbf{k} | \nabla | \lambda \mathbf{k} \rangle = 0$ has been exploited. The second term in Eq.(2.56) is known to be largely suppressed when Coulomb interaction is included.^{43,44} Hence, inserting the first contribution from Eq. (2.56) into Eq. (2.55), the optical susceptibility $\chi(\omega)$ can be expressed as

$$\chi(\omega) \propto -i \sum_{\mathbf{k}} \frac{\text{Re} [\mathbf{M}^{vc}(\mathbf{k}) p_{\mathbf{k}}(\omega)]}{\varepsilon_0 \omega^2 A(\omega)} . \quad (2.57)$$

Depending on whether the dipole matrix element $d_{vc}(\mathbf{k})$ or the optical matrix element $M_{vc}(\mathbf{k})$ can be derived more easily, Eq. (2.53) or Eq. (2.57) can be used to calculate the susceptibility $\chi(\omega)$ and the absorption coefficient $\alpha(\omega)$.

2.7 Rayleigh scattering

Rayleigh scattering is defined as scattering of light by particles which are much smaller than the wavelength of light. The Rayleigh scattering spectroscopy provides information about the investigated structure through resonant enhancement of the elastically scattered light when the

photon energy matches that of an electronic transition. Treating Rayleigh scattering from nanotubes as electromagnetic scattering from a long cylinder with a diameter small compared to the wavelength of light, the scattering cross section per unit length reads as^{9,45}

$$\sigma(\omega) = \frac{\pi^2}{4c^3} r^4 \omega^3 |\chi(\omega)|^2, \quad (2.58)$$

where ω is the angular frequency of the light, r the radius of the nanotube, and c the speed of light. Starting from Maxwell equations [Eq. (2.41)], the expression for $\sigma(\omega)$ can be derived by solving the wave equation in cylindrical coordinates, and exploiting the limit of small nanotube radii.

A sketch of the derivation of Eq. (2.58) is presented here. For more details, see App. D. The scattering cross section is given by the ratio of the rate $W_s = rL \int_0^{2\pi} (\mathbf{S}_s)_r d\phi$ at which energy passes through the scattering surface A and the incident irradiance I_i .⁴⁵ The rate W_s is determined by the radial component of the Poynting vector of the scattered field $\mathbf{S}_s = \frac{1}{2} \text{Re}[\mathbf{E}_s \times \mathbf{H}_s^*]$. The electric and magnetic field satisfy the vector wave equation from Eq. (2.45). Note that their components do not separately fulfil the scalar wave equation $\square\psi = 0$. By introducing $\mathbf{M} = \nabla \times (\mathbf{c}\psi)$ and $\mathbf{N} = \frac{\nabla \times \mathbf{M}}{k}$ with a scalar function ψ and a constant vector \mathbf{c} the problem can be simplified, since these functions satisfy both the vector and scalar wave equation. Once they are calculated, the electric and magnetic field can be expanded in \mathbf{M} and \mathbf{N} with $\mathbf{E} = \sum_{n=-\infty}^{\infty} [A_n \mathbf{M}_n + B_n \mathbf{N}_n]$. The scalar function ψ is called a generating function for the vector harmonics \mathbf{M} and \mathbf{N} . Its choice depends on the investigated system, its symmetries and boundary conditions. For Rayleigh scattering from a cylinder, the scalar function should satisfy the wave equation in cylindrical polar coordinates (ρ, ϕ, z)

$$\frac{1}{\rho} \frac{\partial}{\partial \rho} \left(\rho \frac{\partial \psi}{\partial \rho} \right) + \frac{1}{\rho^2} \frac{\partial^2 \psi}{\partial \phi^2} + \frac{\partial^2 \psi}{\partial z^2} + k^2 \psi = 0. \quad (2.59)$$

An ansatz for the solution is

$$\psi(\rho, \phi, z) = Z_n(r) e^{in\phi} e^{ihz} \quad (2.60)$$

with $Z_n(r)$ as Bessel functions of first and second kind of integral order n and with $r = \sqrt{k^2 - h^2}$. The quantum number h satisfies the boundary conditions between the cylinder and the surrounding medium. For an infinite cylinder of radius r being illuminated by a plane homogeneous wave $\mathbf{E}_i = \mathbf{E}_0 e^{ik\mathbf{e}_i \cdot \mathbf{r}}$ with the propagation direction \mathbf{e}_i and the polarization parallel to the axis of the cylinder, the expansion of the incident electromagnetic field is given by

$$\mathbf{E}_i = \sum_{n=-\infty}^{\infty} E_n \mathbf{N}_n, \quad \mathbf{H}_i = \frac{-ik}{\omega\mu_0} \sum_{n=-\infty}^{\infty} E_n \mathbf{M}_n \quad (2.61)$$

with $E_n = \frac{E_0 (-i)^n}{k \sin \zeta}$ and ζ as the angle between the incident wave and the cylinder axis, see Fig. 2.6. The boundary constant reads $h = -k \cos \zeta$. In a similar way, the scattering fields \mathbf{E}_s and \mathbf{H}_s

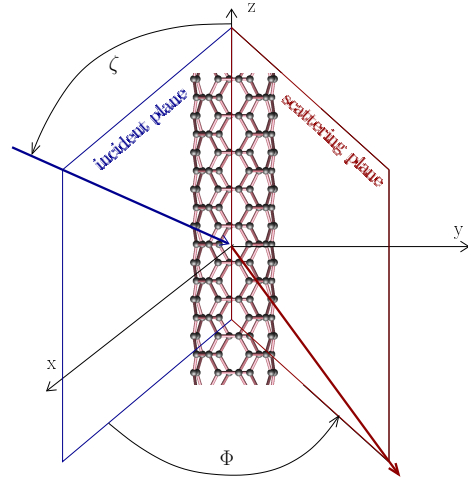


Figure 2.6: Illustration of the Rayleigh scattering from a carbon nanotube.

can be expanded in the vector harmonics M and N . Now, the scattering cross section can be written as

$$\sigma = \frac{W_s}{I_s} = \frac{4rL}{\mathbf{k} \cdot \mathbf{r}} \left[|b_0|^2 + 2 \sum_{n=1}^{\infty} (|a_n|^2 + |b_n|^2) \right] \quad (2.62)$$

with the coefficients a_n , b_n which are complicated expressions determined by Bessel and Henkel functions of different kinds,⁴⁵ see App. D. However, in the limit of small particles, i.e. for cylinders with a diameter much smaller than the wavelength of light ($\mathbf{k} \cdot \mathbf{r} \ll 1$), this equation simplifies to the scattering cross section $\sigma(\omega)$ from Eq. (2.58).

Both Rayleigh scattering cross section $\sigma(\omega)$ and the absorption coefficient α are determined by the linear optical susceptibility $\chi(\omega)$. Unlike absorption, however, Rayleigh scattering has a contribution from the real part of $\chi(\omega)$ and, hence, includes effects from off-resonant optical transitions. This leads to important differences in the characteristics of Rayleigh and absorption spectra. These features are discussed in detail in Sec. 3.5.2.

Chapter 3

Single-Walled Carbon Nanotubes

In this chapter, the theoretical methods presented in the previous chapter are applied to describe optical properties of quasi-one-dimensional single-walled carbon nanotubes. Especially the problem of the characterization of tubes of an arbitrary chiral angle is addressed. The chapter starts with an introduction into the symmetry of carbon nanotubes. After calculating the band structure and the optical, Coulomb and electron-phonon matrix elements, absorption and Rayleigh scattering spectra are determined. First, the free-particle properties are investigated. Then, the model is extended to excitonic effects, which are shown to considerably change the optical properties of carbon nanotubes.

3.1 Introduction

Carbon nanotubes (CNTs) are tiny hollow cylinders constructed by rolling up a single or multiple layers of graphite into a cylinder, see Fig. 3.1. In the case of graphene (one sheet of graphite), they are called single-walled carbon nanotubes (SWCNTs). They have diameters in the range of one nanometer, while their length can reach several micrometers. As a result, CNTs are prototypical one-dimensional systems, i.e. the carriers can move freely only along the axis of the cylinder (denoted as the z -axis throughout this work).

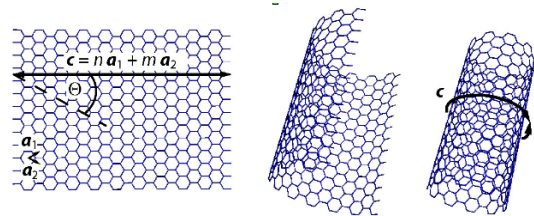


Figure 3.1: Rolling up of graphene to a nanotube along the chiral vector c (taken from Reich et al.).⁴⁶ The chiral indices n, m correspond to n_1, n_2 .

Since their discovery in 1991 by Iijima^{47,48} they have attracted both scientific and technological interest. SWCNTs are ideal model systems to study fundamental physics of one dimensional structures. Their reduced dimensionality leads to unique optical, electronic, and mechanic properties, making them excellent candidates for various opto-electronic applications. They have an extreme toughness-to-weight ratio due to their chemical sp^2 bonds, which are stronger than the sp^3 bonds of diamond. Arising from the quantum-confinement, CNTs can be either semiconducting or metallic. Furthermore, they are effective thermal conductors showing ballistic electron transport. Their optical properties are characterized by well-defined spectra. The latter are in the focus of this chapter.

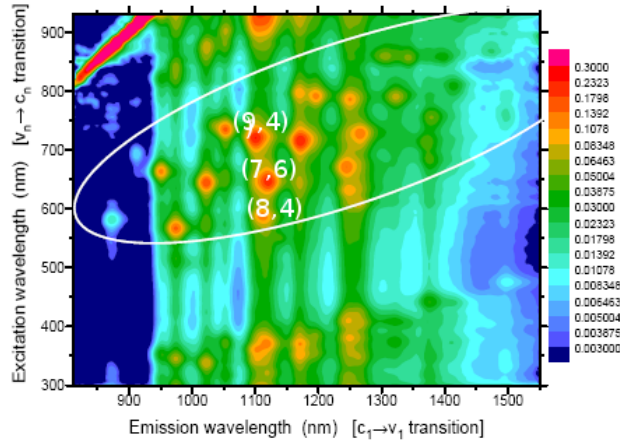


Figure 3.2: Three dimensional plot of the luminescence intensity (coded by different colors) of individual SWCNTs in solution as a function of the emission and excitation energy (taken from Bachilo et al.).⁵ Bright points correspond to high intensity indicating a specific nanotube. The structural assignment is labeled by chiral indices (n_1, n_2) .

Until recently, the optical excitations in SWCNTs were believed to be completely understood within the one-particle picture. Here, the optical excitations are determined by band-to-band transitions. The corresponding absorption spectra are characterized by Van Hove singularities reflecting the typical density of states of one-dimensional structures ($\propto \frac{1}{\sqrt{E}}$). However, in 2005, experiments on two-photon absorption revealed the excitonic character of optical excitations in nanotubes.^{10,11} The excitonic binding energy is in the range of 0.2 – 0.4 eV, which is much larger than in conventional structures without confinement (few meV). Its value also exceeds by far the thermal energy at room temperature (≈ 25 meV). Hence, excitonic effects are visible at 300 K. They considerably change the optical spectra of SWCNTs by reshaping the characteristic Van Hove singularities to red-shifted Lorentzians.

A number of theoretical investigations on excitonic properties have been performed by incorporating the Coulomb interaction within the Bethe-Salpeter equation combined with the GW method (based on Green's functions).¹²⁻¹⁷ This approach reaches good agreement with experimental data. However, due to its numerical complexity it is limited to several specific nanotubes with small radii and small unit cells. The carbon nanotube Bloch equation (CNBE) approach, presented in this work, is based on the many-body density matrix theory,^{2,3} see chapter 2. The combination with tight-binding wave functions allows the study of arbitrary nanotubes. The inclusion of further many-particle interactions, such as exciton-phonon coupling, and the consideration of nonlinear effects is straight-forward.

The characterization of specific SWCNTs is a substantial challenge in current research. While successful techniques for the separation of metallic and semiconducting nanotubes have been developed,⁴⁹ it is still not possible to control the growth of single CNTs. Their well-pronounced optical transitions can be exploited for structural assignment. Optical spectroscopy methods, such as absorption, photoluminescence, and Raman scattering, are among the most important characterization techniques for SWCNTs.⁵⁻⁹ Rayleigh scattering was successfully added to these established methods. It provides information about the nanotube structure through resonant enhancement of the elastically scattered light. An advantage of Rayleigh scattering lies in its ability to uncover the optical properties of *individual* nanotubes.⁹ By combining the data of different methods, a good structural assignment of SWCNTs can be achieved. In this work, optical absorption and Rayleigh scattering from SWCNTs are investigated theoretically.

3.2 Structure and symmetry

The microscopic structure of carbon nanotubes is uniquely determined by their diameter d and their chiral angle ϕ . The information on both parameters is contained in the chiral vector $\mathbf{c} = n_1\mathbf{a}_1 + n_2\mathbf{a}_2$ with the graphene basis vectors \mathbf{a}_1 and \mathbf{a}_2 , see Fig. 3.1. As a result, a nanotube is entirely characterized by the chiral indices (n_1, n_2) . Its diameter is given by the length of the chiral vector c (Fig. 3.1)

$$d = \frac{|\mathbf{c}|}{\pi} = \frac{a_0}{\pi}\sqrt{N} \quad (3.1)$$

with $N = n_1^2 + n_1n_2 + n_2^2$ and the graphene lattice constant $|\mathbf{a}_1| = |\mathbf{a}_2| = a_0 = 0.246$ nm. The chiral angle ϕ specifies in which direction the graphene sheet is wrapped into a cylinder. It is defined as the angle between \mathbf{a}_1 and \mathbf{c} and can be expressed as

$$\phi = \arccos \frac{\mathbf{a}_1 \cdot \mathbf{c}}{|\mathbf{a}_1||\mathbf{c}|} = \arccos \left[\frac{n_1 + \frac{n_2}{2}}{\sqrt{N}} \right]. \quad (3.2)$$

Due to the hexagonal symmetry of graphene, the chiral angle can take the values $0^\circ \leq \phi \leq 30^\circ$. Two different types of nanotubes of high symmetry can be created: zigzag tubes $(n, 0)$ with $\phi = 0^\circ$ and armchair tubes (n, n) with $\phi = 30^\circ$. Their names refer to the edge of their unit cell, which resembles zigzag or armchair chains, see Fig. 3.3. Both armchair and zigzag tubes have mirror planes, see Sec. 3.4.1, and are therefore considered as achiral. In contrast, tubes of all other chiral angles are called chiral nanotubes.

The unit cell of graphene is spanned by the lattice vectors \mathbf{a}_1 and \mathbf{a}_2 . It contains two non-equivalent atoms, denoted by A and B . The unit cell of a nanotube corresponds to the translational period a along the tube axis. It is determined by the smallest graphene lattice vector \mathbf{a} perpendicular to the chiral vector \mathbf{c}

$$\mathbf{a} = -\frac{2n_2 + n_1}{nR}\mathbf{a}_1 + \frac{2n_1 + n_2}{nR}\mathbf{a}_2 \quad \text{with } |\mathbf{a}| = \frac{a_0}{\pi}\sqrt{N}. \quad (3.3)$$

Here, n is the greatest common divisor of n_1 and n_2 , and R is an integer with $R = 3$ if $(n_1 - n_2)$ is a multiple of $3n$ and $R = 1$ otherwise. The number of graphene hexagons in a nanotube unit cell is given by $q = \frac{2N}{nR}$. This relation follows from the ratio of the area of a CNT unit cell $|\mathbf{a}||\mathbf{c}| = \frac{\sqrt{3}a_0^2N}{nR}$ and the area of a graphene unit cell $|\mathbf{a}_1 \times \mathbf{a}_2| = \frac{\sqrt{3}a_0^2}{2}$. The high-symmetric achiral nanotubes possess small unit cells, containing $2q = 4n$ carbon atoms (the number 2 accounts for the two atoms A and B). In contrast, the unit cell of chiral nanotubes can be very long and contain hundreds of atoms, see Fig. 3.3.

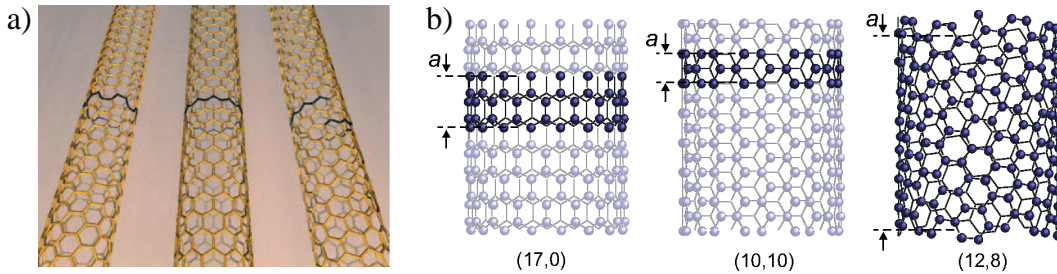


Figure 3.3: a) The classification of nanotubes in armchair tubes (n, n) with $\phi = 30^\circ$, zigzag tubes $(n, 0)$ with $\phi = 0^\circ$ and chiral tubes (n_1, n_2) with $n_2 \neq 0, n_1 \neq n_2$, and $0^\circ < \phi < 30^\circ$ is illustrated (taken from Hönlein et al.).⁵⁰ b) The structure of different types of nanotubes with the corresponding unit cells (taken from Reich et al.).⁴⁶

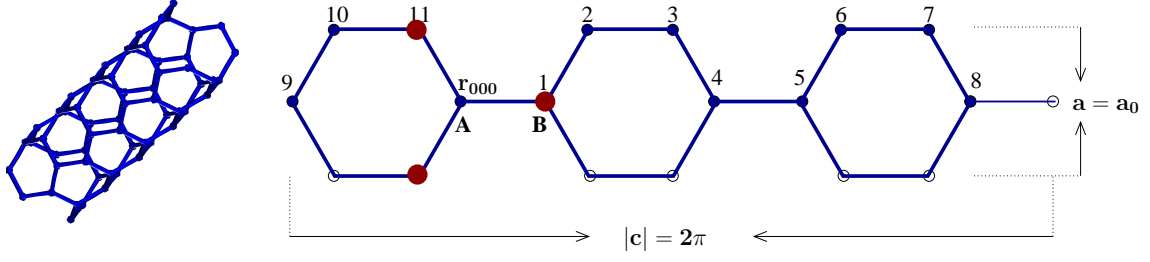


Figure 3.4: The construction of the (3,3) armchair nanotube by applying the line group symmetries is illustrated. The nearest neighbors of the reference atom at \mathbf{r}_{000} are colored red.

The symmetry of carbon nanotubes can be described by line groups.⁵¹ In analogy to crystal space groups, this approach describes the symmetry of systems which are periodic in one direction. Every nanotube belongs to a different line group (except for armchair and zigzag tubes with the same n). The corresponding symmetry operations allow a construction of an entire nanotube starting from one single atom at the position $\mathbf{r}_{000} = (\rho_0, \phi_0, z_0)$

$$\mathbf{r}_{tsu} = (C_q^{rt} C_n^s U^u | \frac{tna}{q}) \mathbf{r}_{000} = \left(\rho_0, (-1)^u \phi_0 + 2\pi \left(\frac{r}{q} t + \frac{1}{n} s \right), (-1)^u z_0 + \frac{na}{q} t \right). \quad (3.4)$$

This equation contains the following symmetry operations:⁵¹

- the U-operation maps atoms of type A to atoms of type B ($u = 0, 1$),
- the pure rotation around the tube axis C_n^s ($s = 0, 1, \dots, n - 1$) generates all other hexagons with the atom A on the circumference,
- the screw axis rotation ($C_q^{rt} | \frac{tna}{q}$) (combination of rotations and translations with $t = 1 - \frac{q}{2n}, \dots, \frac{q}{2n}$) maps these atoms to all other remaining atoms of the unit cell,
- and the translation by the unit cell length a .

The parameter r in Eq. (3.4) characterizes the screw axis operations. It is defined by⁵¹

$$r = \frac{q}{n} Fr \left[\frac{n}{qR} \left(3 - 2 \frac{n_1 - n_2}{n_1} \right) + \frac{n}{n_1} \left(\frac{n_1 - n_2}{n} \right)^{\phi(n_1/n) - 1} \right] \quad (3.5)$$

with $Fr[x]$ as the fractional part of x . Furthermore, $\phi(n)$ is the Euler function giving the number of positive integers less than n , that are coprime to n , i.e. they have no common factor other than 1 (e.g. $\phi(5) = 4$). To illustrate the power of Eq. (3.4), a simple highly symmetric (3,3) armchair nanotube is constructed starting from one single atom at the position \mathbf{r}_{000} . The unit cell of armchair tubes corresponds to the unit cell of graphene, i.e. $a = a_0$. The (3,3) tube consists of $2q = 4n = 12$ atoms. The screw axis parameter r equals 1. The positions of all 12 atoms \mathbf{r}_{tsu} can be determined by applying the appropriate line group symmetry labeled by the indices t, s, u

(Fig. 3.4):

$$\begin{aligned}
0: \quad \mathbf{r}_{000} &= \left(\frac{d}{2}, \phi_0, z_0 \right), & 1: \quad \mathbf{r}_{011} &= \left(\frac{d}{2}, -\phi_0 + \frac{2\pi}{3}, -z_0 \right), \\
2: \quad \mathbf{r}_{100} &= \left(\frac{d}{2}, \phi_0 + \frac{2\pi}{6}, z_0 + \frac{a_0}{2} \right), & 3: \quad \mathbf{r}_{111} &= \left(\frac{d}{2}, -\phi_0 + \pi, -z_0 + \frac{a_0}{2} \right), \\
4: \quad \mathbf{r}_{010} &= \left(\frac{d}{2}, \phi_0 + \frac{2\pi}{3}, z_0 \right), & 5: \quad \mathbf{r}_{021} &= \left(\frac{d}{2}, -\phi_0 + \frac{4\pi}{3}, -z_0 \right), \\
6: \quad \mathbf{r}_{110} &= \left(\frac{d}{2}, \phi_0 + \pi, z_0 + \frac{a_0}{2} \right), & 7: \quad \mathbf{r}_{121} &= \left(\frac{d}{2}, -\phi_0 + \frac{5\pi}{3}, -z_0 + \frac{a_0}{2} \right), \\
8: \quad \mathbf{r}_{020} &= \left(\frac{d}{2}, \phi_0 + \frac{4\pi}{3}, z_0 \right), & 9: \quad \mathbf{r}_{001} &= \left(\frac{d}{2}, -\phi_0, -z_0 \right), \\
10: \quad \mathbf{r}_{120} &= \left(\frac{d}{2}, \phi_0 + \frac{5\pi}{3}, z_0 + \frac{a_0}{2} \right), & 11: \quad \mathbf{r}_{101} &= \left(\frac{d}{2}, -\phi_0 + \frac{2\pi}{6}, -z_0 + \frac{a_0}{2} \right).
\end{aligned}$$

The nearest neighbors of the reference atom \mathbf{r}_{000} (which will be needed in the next sections) are colored red. Since the unit cell of an armchair nanotube is small, the third neighbor already belongs to the next unit cell. Its coordinates are given by $\mathbf{r}_{-111} = \left(\frac{d}{2}, -\phi_0 + \frac{\pi}{3}, -z_0 - \frac{a_0}{2} \right)$.

This procedure of constructing an entire nanotube will be applied for the calculation of the optical and Coulomb matrix elements in Sec. 3.4.1 and Sec. 3.4.2.

3.3 Wave functions

3.3.1 Zone-folding approach

The starting point for the calculation of the band structure of carbon nanotubes are the tight-binding wave functions of graphene discussed in Sec. 2.3.2

$$\Psi(\mathbf{k}, \mathbf{r}) = \sum_{j=A,B} C_j(\mathbf{k}) \frac{1}{\sqrt{N_0}} \sum_{\mathbf{R}_j}^{N_0} e^{i\mathbf{k} \cdot \mathbf{R}_j} \phi_j(\mathbf{r} - \mathbf{R}_j) \quad (3.6)$$

with the coefficient functions $C_j(\mathbf{k})$ defined in Eqs. (2.30)-(2.31), the lattice vectors \mathbf{R}_j , and the atomic wave functions $\phi_j(\mathbf{r} - \mathbf{R}_j)$.

Assuming that the tube is infinitely long, the component of the reciprocal vector along the nanotube axis k_z is continuous. Along the circumference \mathbf{c} , periodic boundary conditions are imposed on the wave function $\Psi(\mathbf{k}, \mathbf{r} + \mathbf{c}) = \Psi(\mathbf{k}, \mathbf{r})$. Applying the Bloch theorem $\Psi(\mathbf{k}, \mathbf{r} + \mathbf{c}) = e^{i\mathbf{k} \cdot \mathbf{c}} \Psi(\mathbf{k}, \mathbf{r})$, the boundary condition reads

$$\mathbf{k} \cdot \mathbf{c} = \mathbf{k}_\perp \cdot \mathbf{c} = m2\pi \Rightarrow |\mathbf{k}_\perp| = m \frac{2\pi}{|\mathbf{c}|} = m \frac{2}{d} \quad (3.7)$$

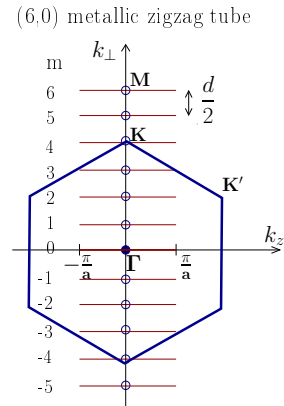


Figure 3.5: Illustration of the zone-folding approximation. The circles at $k_z = 0$ denote the Γ points in a nanotube.

with the integer $m \in \left(-\frac{q}{2}, +\frac{q}{2}\right]$ labelling the nanotube subbands arising from the boundary condition. As a result, the Brillouin zone (BZ) of graphene is divided into q allowed lines, each corresponding to a subband. The number of lines is determined by the length of the BZ. The lines are parallel to the nanotube axis and equally separated by $\frac{2}{d}$, see Fig. 3.5. Their orientation is determined by the chiral angle ϕ , defined in Eq. (3.2). The basic assumption of the zone-folding approach is that curvature effects do not play an important role for optical and electronic properties of CNTs. Then, the band structure of a nanotube can be approximated by the graphene energies along the allowed lines, as shown in Fig. 3.5. In numerous investigations, this approach has been shown to be a good approximation for tubes with a diameter around 1 nm and larger, since for these tubes the curvature effects are negligible.^{46,52} For smaller CNTs, this approach is not applicable.

3.3.2 Trigonal warping effect

The graphene high-symmetry point $K = \frac{1}{3}(\mathbf{k}_1 - \mathbf{k}_2)$ (Fig. 3.5) plays a crucial role for the optical properties, since at this point the conduction and valence bands cross, i.e. graphene is a semi-metal, see Fig. 3.6a. If this point is allowed for nanotubes, the corresponding tube is metallic, otherwise it is semiconducting. The condition whether a tube is metallic or not, can be derived directly from the boundary condition [Eq. (3.7)] applied at the K point

$$\mathbf{K} \cdot \mathbf{c} = m2\pi = \frac{1}{3}(\mathbf{k}_1 - \mathbf{k}_2) \cdot (n_1\mathbf{a}_1 + n_2\mathbf{a}_2) = \frac{2\pi}{3}(n_1 - n_2) \Rightarrow m = \frac{n_1 - n_2}{3}. \quad (3.8)$$

As a result, a nanotube is metallic only if the difference between the chiral indices n_1 and n_2 is a multiple of three, i.e. one third of all CNTs is metallic. A consequence of Eq. (3.8) is that armchair nanotubes with $n_1 = n_2$ are always metallic. If the condition from Eq. (3.8) is not fulfilled, the tube is semiconducting. Then, it exhibits a band gap that varies with its diameter. The semiconducting tubes are further divided into two families. Depending whether the allowed line next to the K point is located on the KM - or on the $K\Gamma$ -side, the corresponding tube belongs to the $+1$ or -1 family, see Fig. 3.6c-d. The dispersion on the $K\Gamma$ side is stronger than on the KM side, as can be seen in Fig. 3.6a. As a result, the -1 tubes have larger band gaps. Altogether, there are three nanotube families:

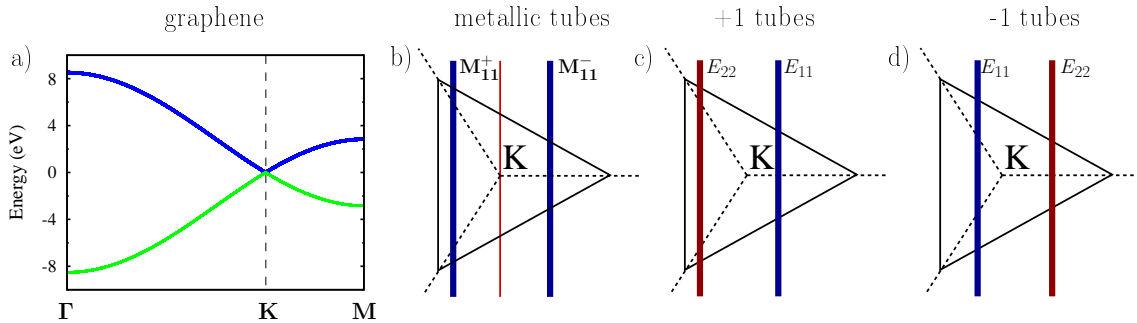


Figure 3.6: a) Band structure of graphene along the high-symmetry line ΓKM . b)-d) Simplified energy contour of graphene around the K point. The deviation from a circle is exaggerated to illustrate trigonal warping. The vertical lines correspond to the lowest subbands of b) metallic zigzag nanotubes with $\nu = 0$ and semiconducting zigzag tubes with c) $\nu = +1$ and d) $\nu = -1$. Dashed lines indicate the three KM directions.

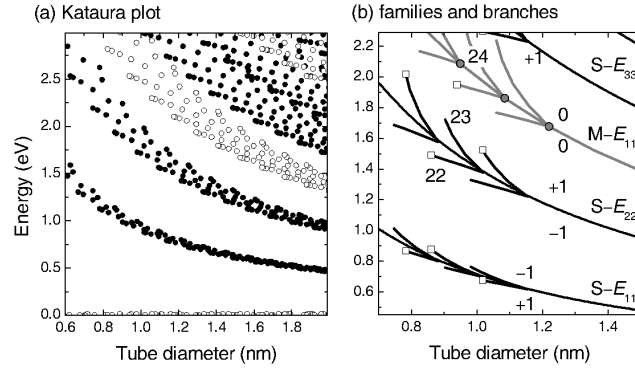


Figure 3.7: a) Kataura plot showing the transition energy as a function of the nanotube diameter. Semiconducting tubes are denoted by filled circles, while metallic tubes are marked by open circles. b) The typical V-shaped branches of the Kataura plot are sketched revealing the different family behavior (taken from Thomsen et al.).⁴

- metallic tubes if $(n_1 - n_2) \bmod 3 = 0$,
- +1 semiconducting tubes if $(n_1 - n_2) \bmod 3 = 1$, and
- -1 semiconducting tubes if $(n_1 - n_2) \bmod 3 = 2$.

The different behavior of the three families can be seen in the Kataura plot in Fig. 3.7, where the transition energy is plotted as a function of the diameter. It shows a general $1/d$ dependence of the transition energy. However, the tubes also exhibit a specific V-shaped distribution, which is typical for different families. For the energetically lowest transition E_{11} , +1 tubes are located below, while -1 tubes can be found above the main $1/d$ line. For the second transition E_{22} , this behavior is inverse.

Metallic nanotubes surprisingly show a similar behavior. All metallic tubes belong to one family, since the distance between the two allowed lines closest to the K point is the same, see Fig. 3.6b. Therefore, one would not expect a V-shaped Kataura plot. In optical spectra, there should be only one degenerate transition. However, the experiments clearly show two peaks M_{11}^+ and M_{11}^- (for metallic tubes, the transitions are labeled by M_{ii}^+ and M_{ii}^- indicating that the two transitions + and - correspond to one E_{ii} in analogy to semiconducting tubes). Their splitting strongly depends on the chiral angle. It is maximal for zigzag tubes and vanishes for the armchair constellation, see Fig. 3.32. This behavior arises from the so-called trigonal warping effect. It describes the deviation of the equi-energy contours from circles in the Brillouin zone of graphene around the K point, as shown in Fig. 3.8. The positions of Van Hove singularities in the spectra correspond to the k_z values at which the allowed lines touch the energy contour. Here, the band structure has an extremum. Due to the trigonal shape, the lines can touch different energy contours to the left and to the right of the K point, even though they

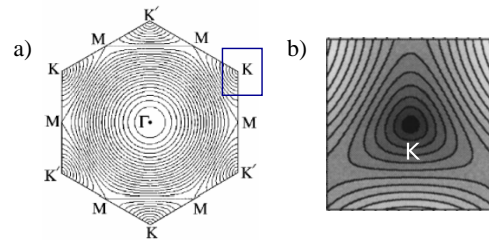


Figure 3.8: a) Energy contour plot of graphene (taken from Saito et al.).⁵³ b) The blow-up illustrates the triangular shape of the energy contours around the K point (taken from Reich et al.).⁵⁴

have the same distance to the K point. The energy splitting depends on the orientation of the triangle. For armchair nanotubes, the allowed lines run perpendicularly to the base of the triangle (the triangle in Fig. 3.6b is rotated by 90°), i.e. the energy to the left and right of the K point is the same. Therefore, trigonal warping has no effect on armchair tubes. Consequently, they can be found in the center of the V -shaped branches in the Kataura plot. In contrast, in zigzag tubes, the allowed lines left and right from the K point can touch the tip and the base of the triangle, as shown in Fig. 3.6b. Here, the energy splitting is maximal. This explains why zigzag tubes are located at the ends of the V -shaped branches.

Trigonal warping also effects semiconducting nanotubes. It does not lead to a splitting of peaks, since they are not degenerate. However, it accounts for an energy shift which is different for the two semiconducting families. This arises from the fact that their lowest transitions are located on opposite sides of the K -point, see Fig. 3.6c-d. The trigonal warping effect will turn out to be of crucial importance for many investigations presented in this work.

3.3.3 Nanotube band structure

An analytic expression for the band structure of graphene can be derived by restricting the interaction between the carbon atoms to nearest neighbors (see Sec. 2.3.2)

$$E_{v,c} = \frac{\epsilon_0 + c_\lambda \gamma_0 |e(\mathbf{k})|}{1 - c_\lambda s_0 |e(\mathbf{k})|} \quad (3.9)$$

with $e(\mathbf{k}) = \sum_{i=1}^3 \exp(i\mathbf{k} \cdot \mathbf{b}_i)$ and $c_\lambda = +1$ for the valence band v and $c_\lambda = -1$ for the conduction band c . The evaluation of this expression requires the knowledge of the positions of the interacting atoms, in particular of the vectors \mathbf{b}_i connecting the reference atom to its first three neighbors.

In Fig. 3.9, the structure of graphene and of carbon nanotubes is illustrated. It shows the unit cell of graphene with the basis vectors \mathbf{a}_1 and \mathbf{a}_2 and the corresponding hexagonal Brillouin zone including the high-symmetry points Γ , K and M and the reciprocal lattice vectors \mathbf{k}_1 and \mathbf{k}_2 . Furthermore, the three nearest neighbors of the atom 0 are highlighted.

Starting from the atom positions in graphene, the symmetry of nanotubes can be exploited to obtain the corresponding coordinates of an atom in a nanotube, as shown in Eq. (3.4). Here, the atom A at $\mathbf{r}_0 = \frac{1}{3}(\mathbf{a}_1 + \mathbf{a}_2)$ is chosen to be the reference atom. The positions of its first nearest neighbors can be read off from Fig. 3.9

$$\mathbf{r}_1 = \frac{1}{3}(2\mathbf{a}_1 - \mathbf{a}_2), \quad \mathbf{r}_2 = \frac{1}{3}(-\mathbf{a}_1 + 2\mathbf{a}_2), \quad \text{and} \quad \mathbf{r}_3 = \frac{1}{3}(2\mathbf{a}_1 + 2\mathbf{a}_2).$$

The corresponding connecting vectors \mathbf{b}_i are given by

$$\mathbf{b}_1 = \mathbf{r}_1 - \mathbf{r}_0 = \frac{1}{3}(\mathbf{a}_1 - 2\mathbf{a}_2), \quad \mathbf{b}_2 = \mathbf{r}_2 - \mathbf{r}_0 = \frac{1}{3}(-2\mathbf{a}_1 + \mathbf{a}_2), \quad \text{and} \quad \mathbf{b}_3 = \mathbf{r}_3 - \mathbf{r}_0 = \frac{1}{3}(\mathbf{a}_1 + \mathbf{a}_2). \quad (3.10)$$

Now, all ingredients are available to evaluate the band structure of graphene from Eq. (3.9). Inserting the next neighbor positions from Eq. (3.10) and expressing the wave vector \mathbf{k} in i) the coordinates of the reciprocal lattice vectors \mathbf{k}_1 , \mathbf{k}_2 , and ii) the Cartesian coordinates \mathbf{k}_x , \mathbf{k}_y (for

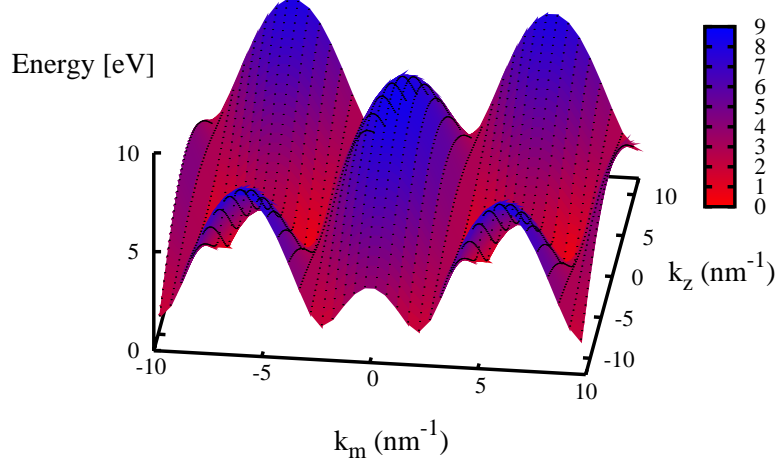


Figure 3.10: Band structure of graphene showing the crossing of the conduction and the valence bands at the six corners of the hexagon corresponding to the K and K' points.

To obtain the band structure of CNTs, the zone-folding approximation is applied. It is assumed that the wave functions of graphene remain unaltered when rolling up the tube. Then, the two-dimensional graphene wave vector \mathbf{k} is decoupled in a continuous component k_z along the nanotube axis and a perpendicular component k_\perp , which is quantized according to the boundary condition $k_\perp = \frac{2}{d}m e_\perp$. Within the zone-folding approach, the band structure of nanotubes can be approximated by the graphene energies along the allowed lines denoted by the subband index m , as illustrated in Fig. 3.12. Throughout this work, the reciprocal lattice is spanned by the orthogonal vectors k_z along and k_\perp perpendicular to the nanotube axis, since their interpretation is advantageous for following investigations. Exploiting the general relations $k_\perp \cdot \mathbf{c} = 2\pi$, $k_\perp \cdot \mathbf{a} = 0$ and $k_z \cdot \mathbf{c} = 0$, $k_z \cdot \mathbf{a} = 2\pi$ yields

$$\mathbf{k}_\perp = \frac{2n_1 + n_2}{2N} \mathbf{k}_1 + \frac{2n_2 + n_1}{2N} \mathbf{k}_2 \quad \text{and} \quad \mathbf{k}_z = -\frac{n_2}{q} \mathbf{k}_1 + \frac{n_1}{q} \mathbf{k}_2. \quad (3.15)$$

Now, the band structure of CNTs can be derived by inserting Eq. (3.15) into Eq. (3.14)

$$E_{v,c}(k_z, m) = \pm \gamma_0 \left[3 + 2 \cos \left(2\pi m \frac{2n_1 + n_2}{2N} - 2\pi \frac{n_2}{q} k_z \right) + 2 \cos \left(2\pi m \frac{2n_2 + n_1}{2N} + 2\pi \frac{n_1}{q} k_z \right) + 2 \cos \left(2\pi m \frac{n_1 - n_2}{2N} - 2\pi \frac{n_1 + n_2}{q} k_z \right) \right]^{\frac{1}{2}} \quad (3.16)$$

with $k_z = (-\frac{1}{2}, \frac{1}{2}]$ corresponding to the first Brillouin zone. Figure 3.13 shows the band structure of the (6,0) zigzag, the (6,6) armchair, and the (6,1) chiral nanotube. For zigzag and armchair tubes, the subbands with the index m and $-m$ are degenerate. This follows directly from Eq. (3.16). Furthermore, all subbands show extrema at the K point, which is located at $k_z = 0$ for zigzag tubes (and all tubes with $R = 1$) and at $k_z = \frac{2}{3} \frac{\pi}{a}$ for armchair tubes (and all tubes with

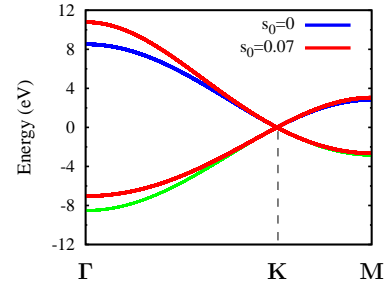


Figure 3.11: Illustration of the importance of the overlap parameter s_0 .

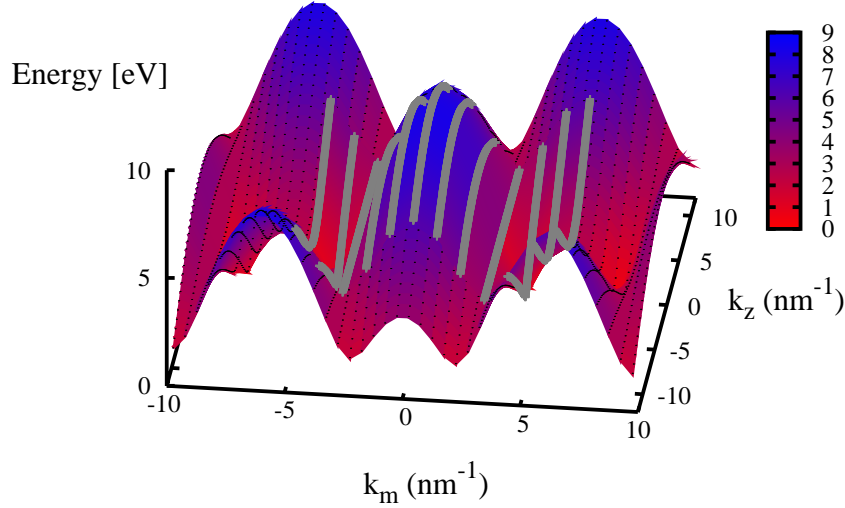


Figure 3.12: Band structure of the (6,0) armchair nanotube is obtained by applying the zone-folding approach to the energies of graphene, see also Fig. 3.5. The allowed k values in nanotubes build lines in the graphene band structure. They are i) equally separated by $\frac{2}{q}$, ii) parallel to the nanotube axis, and iii) oriented according to the chiral angle. Their length is given by $\frac{2\pi}{a}$ with a denoting the length of the nanotube unit cell. For the shown zigzag (6,0) tube with $a = \sqrt{3}a_0$, the lines are shorter than the BZ of graphene which is given by $\frac{2\pi}{a_0}$.

$R = 3$), see Fig. 3.9. These extrema correspond to Van Hove singularities in the absorption and Rayleigh spectra. In Sec. 3.5.1, it will be shown that the subbands showing minima will lead to singularities with a long asymmetric tail towards higher energies, while the subbands showing maxima will account for singularities with an enhanced absorption at lower energies, see Fig. 3.28. This is easy to understand, since an optical transition is maximal at the gap energy. If the involved bands have maxima, transitions can take place before the photon reaches the band gap energy resulting in a tail towards lower energies. If the involved bands have minima, the lowest possible energy is the gap energy. Only transitions at higher energies can take place resulting in the asymmetry towards higher energies.

In most considerations, the energetically lowest transitions are of great interest. These correspond to the minima of the subband with the smallest distance to the K point. For zigzag tubes, the position of the K point can be found in Fig. 3.5: $K = (k_z, m) = (0, \pm\frac{q}{3})$. The closest line to the K point leads to the first Van Hove singularity, usually denoted as E_{11} . For the metallic zigzag (6,0) tube, the conduction and valence band with $m = \frac{q}{3} = 4$ cross at the K point. As a result, the energetically lowest transition E_{11} stems from the minimum of the next subband $m = 5$ ($m = 3$ possesses a maximum). For the semiconducting (6,1) nanotube, the transition E_{11} stems from the subband $m = 29$ and E_{22} from $m = 28$, since $\frac{q}{3} = 28\frac{2}{3}$. Nanotubes with the parameter $R = 3$ show a different behavior. The Fermi level in these tubes is more difficult to determine. Group-theoretical considerations yield $K = (k_z, m) = (\frac{2\pi}{3a}, nr \bmod q)$. In the case of the best known tubes of this type, the armchair nanotubes, this gives $K = (\frac{2\pi}{3a}, n)$, as can be seen in Figs. 3.5 and 3.9. These relations will be of great use in the following investigations, since often only the first transitions will be of interest.

The nanotube band structure calculated within the nearest-neighbor tight-binding method and

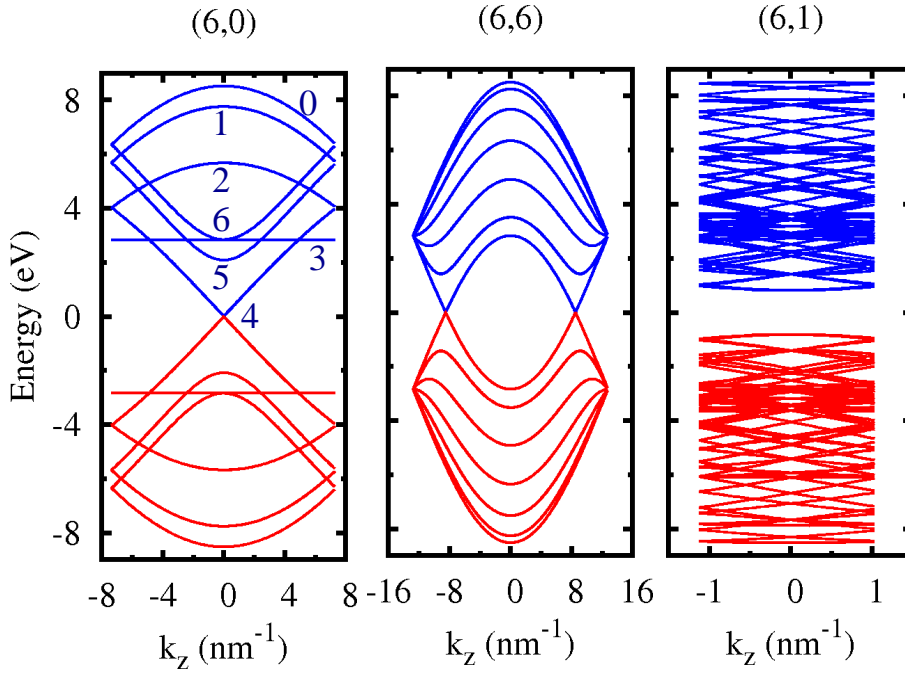


Figure 3.13: The band structure of the (6, 0) zigzag, (6, 6) armchair, and (6, 1) chiral nanotube. The numbers in the band structure of the (6, 0) tube index the subbands (corresponding to the band index m).

the zone-folding approximation shows good agreement with first-principle results and experimental data around the K point. To achieve good results over the entire Brillouin zone, the number of considered neighbors needs to be extended.⁵⁵

3.3.4 Linear and helical quantum numbers

According to the Noether theorem, any symmetry corresponds to a conservation law for a related physical quantity, e.g. conservation of momentum results from the homogeneity of space. Since nanotubes are described by line groups containing a screw axis, two different sets of quantum numbers are possible (corresponding to two ways of decomposing the group): linear (k, m) and helical (\tilde{k}, \tilde{m}) quantum numbers.^{46,56} The linear k corresponds to the pure translational subgroup of the line group. Here, the linear momentum along the tube axis is a conserved quantity. However, the quasi-angular momentum m contains both pure rotations and screw axis operations. As a result, it is not fully conserved and Umklapp rules need to be taken into account, when the Brillouin zone or the Γ point is crossed. In contrast, the helical angular momentum \tilde{m} is a conserved quantity, since it corresponds to pure rotations of the nanotube. Consequently, Umklapp processes do not appear.

The transformation between the linear (k_z, m) and helical indices (\tilde{k}_z, \tilde{m}) is given by

$$(\tilde{k}_z, \tilde{m}) = \left(k_z + m \frac{r}{n} \frac{2\pi}{a} + \tilde{K} \frac{q}{n} \frac{2\pi}{a}, m + \tilde{M}n \right), \quad (3.17)$$

$$(k_z, m) = \left(\tilde{k}_z - \tilde{m} \frac{r}{n} \frac{2\pi}{a} + K \frac{q}{n} \frac{2\pi}{a}, \tilde{m} - Kp + Mq \right) \quad (3.18)$$

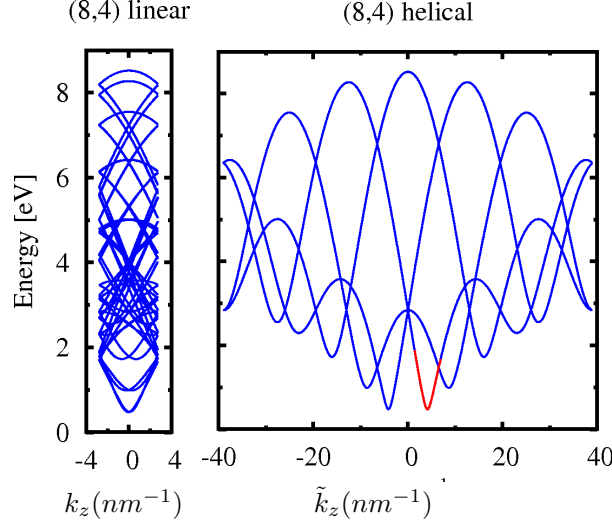


Figure 3.14: Band structure of the (8, 4) nanotube calculated with a) linear quantum numbers (k_z, m) and b) helical quantum numbers (\tilde{k}_z, \tilde{m}) . The linear band corresponding to the energetically lowest transition E_{11} is also shown in the helical picture (colored red).

with $p = qFr \left[\frac{nR}{2n_1+n_2} \left(\frac{2n_2+n_2}{nR} \right)^{\phi((2n_1+n_2)/(nR)-1)} - \frac{n_2nR}{q(2n_1+n_2)} \right]$ and K, M, \tilde{K} , and \tilde{M} as integers used to assure that the momenta are from the intervals

$$\tilde{k}_z \in \left(-\frac{q}{n} \frac{\pi}{a}, \frac{q}{n} \frac{\pi}{a} \right], \quad \tilde{m} \in \left(-\frac{n}{2}, \frac{n}{2} \right], \quad \text{and} \quad k_z \in \left(-\frac{\pi}{a}, \frac{\pi}{a} \right], \quad m \in \left(-\frac{q}{2}, \frac{q}{2} \right]. \quad (3.19)$$

Figure 3.14 illustrates the differences in the nanotube band structure obtained within the linear and helical set of quantum numbers. The latter ones have the advantage of being more clear, since the number of bands is considerably reduced. In this work, linear quantum numbers are used for investigation of free-particle properties. Here, neglecting the momentum of the photon (dipole approximation), the wave vector \mathbf{k} does not exceed the first Brillouin zone. In the case of excitonic properties, however, this can happen, since the Coulomb interaction involves wave vectors $\mathbf{k}' = \mathbf{k} + \mathbf{q}$ (with a momentum transfer \mathbf{q}). Here, the linear angular momentum m is not conserved any more, and Umklapp rules become necessary. To avoid this tedious procedure, a transformation to helical quantum numbers \tilde{k}, \tilde{m} is performed according to Eq. (3.18).

3.4 Matrix elements

3.4.1 Optical matrix element

Derivation

The optical matrix element $M(\mathbf{k})$ and the joint density of states determine the optical strength of a transition as a function of the wave vector \mathbf{k} . Furthermore, it contains all symmetry-imposed selection rules. The interband optical matrix element for transitions from a state in the valence band $\Psi^v(\mathbf{k})$ to a state in the conduction band $\Psi^c(\mathbf{k}, \mathbf{r})$ is given by

$$\hat{M}_{opt}^{vc}(\mathbf{k}) = -\frac{\hbar e_0}{im} \mathbf{A}(\mathbf{k}_{ph}) \cdot \langle \Psi^v(\mathbf{k}, \mathbf{r}) | \nabla_{\mathbf{k}} | \Psi^c(\mathbf{k}, \mathbf{r}) \rangle, \quad (3.20)$$

when using the $\mathbf{p} \cdot \mathbf{A}$ carrier-field interaction Hamiltonian, see Eq. (2.14). The vector potential can be separated from the expectation value within the dipole approximation, i.e. when the photon wave vector \mathbf{k}_{ph} is negligible compared to the electronic wave vector \mathbf{k} . In the following, the expression *optical matrix element* will refer to

$$M(\mathbf{k}) = \langle \Psi^v(\mathbf{k}, \mathbf{r}) | \nabla_{\mathbf{k}} | \Psi^c(\mathbf{k}, \mathbf{r}) \rangle. \quad (3.21)$$

In this work, the focus lies on light polarized parallel to the nanotube axis. Hence, only the z -component of the optical matrix element $M_z(\mathbf{k})$ is of interest. This accounts for the depolarization effect that strongly suppresses light polarized perpendicular to the nanotube axis.⁵⁷

To calculate $M_z(\mathbf{k})$, the tight-binding approach is combined with the zone-folding approximation. Inserting the wave functions $\Psi^c(\mathbf{k}, \mathbf{r})$ and $\Psi^v(\mathbf{k}, \mathbf{r})$ from Eq. (3.6) into Eq. (3.21) and using the nearest-neighbor approximation gives

$$\begin{aligned} M_z(\mathbf{k}) &= \frac{1}{N_0} \sum_{A,B} \sum_{\mathbf{R}_j} \sum_{\mathbf{R}_{j'}}^{N_0} e^{i\mathbf{k} \cdot (\mathbf{R}_{j'} - \mathbf{R}_j)} C_{j'}^{v,*}(\mathbf{k}) C_j^c(\mathbf{k}) \langle \phi(\mathbf{r} - \mathbf{R}_j) | \nabla_{\mathbf{k}} | \phi(\mathbf{r} - \mathbf{R}_{j'}) \rangle \\ &= \frac{\sqrt{3}M_c}{a_0|e(\mathbf{k})|} \text{Re} \left[e^*(\mathbf{k}) \sum_{i=1}^3 e^{i\mathbf{k} \cdot \mathbf{b}_i} b_{i,z} \right]. \end{aligned} \quad (3.22)$$

M_c denotes the constant optical matrix element for the two nearest-neighbor atoms⁵⁸ $M_c = \langle \phi(\mathbf{r} + \mathbf{R}_i) | \frac{\partial}{\partial z} | \phi(\mathbf{r}) \rangle$. With the overlap parameter $s_0 = 0$, the coefficients $C_j^{\pm}(\mathbf{k})$ read [Eq. (2.31)]

$$C_A^{v,c}(\mathbf{k}) = \pm C_B^{v,c}(\mathbf{k}) \frac{e(\mathbf{k})}{|e(\mathbf{k})|} \quad (3.23)$$

with $C_B^{v,c}(\mathbf{k}) = \frac{1}{\sqrt{2}}$ and $+(-)$ standing for the valence (conduction) band. The vectors \mathbf{b}_i connect the atom located at \mathbf{r}_0 with its three nearest neighbors at \mathbf{r}_i ($i = 1, 2, 3$). To evaluate Eq. (3.22), an expression for \mathbf{b}_i for arbitrary (n_1, n_2) nanotubes is required. According to Eq. (3.4), the atomic positions in a tube are obtained in cylindrical coordinates.^{46,51,59} Then, the distance between neighboring atoms can be calculated. The reference atom has the position $\mathbf{r}_0 = \mathbf{r}_{000} = (\rho_0, \phi_0, z_0) = \left(\frac{d}{2}, 2\pi \frac{n_1 + n_2}{2N}, a_0 \frac{n_1 - n_2}{2\sqrt{3}N} \right)$ corresponding to $r_0 = \frac{1}{3}(\mathbf{a}_1 + \mathbf{a}_2)$, see Fig. 3.9. Then, the connecting vectors \mathbf{b}_i are given by

$$\mathbf{b}_i = \mathbf{r}_i - \mathbf{r}_0 = \left(0, -2\phi_0 + 2\pi \left(\frac{r}{q} t_i + \frac{1}{n} s_i \right), -2z_0 + \frac{na}{q} t_i \right) \quad (3.24)$$

with the operation indices $u_i = 1$ and^{51,59}

$$\begin{aligned} t_1 &= -\frac{n_2}{n}, \quad t_2 = \frac{n_1}{n}, \quad t_3 = t_1 + t_2, \\ s_1 &= \frac{2n_1 + (1 + rR)n_2}{qR}, \quad s_2 = \frac{2n_2 + (1 - rR)n_1}{qR}, \quad s_3 = s_1 + s_2. \end{aligned}$$

These indices follow from the geometry shown in Fig. 3.9. For the special case of an armchair tube, they are derived and illustrated in Sec. 3.2. Inserting Eq. (3.24) into Eq. (3.22) yields

$$\begin{aligned} M_z(\mathbf{k}) &= \frac{M_c}{2\sqrt{N_0}|e(\mathbf{k})|} \left[(n_1 - n_2) \cos[\mathbf{k} \cdot (\mathbf{a}_1 - \mathbf{a}_2)] \right. \\ &\quad \left. - (2n_1 + n_2) \cos(\mathbf{k} \cdot \mathbf{a}_1) + (n_1 + 2n_2) \cos(\mathbf{k} \cdot \mathbf{a}_2) \right]. \end{aligned} \quad (3.25)$$

This expression for the optical matrix element resembles the dispersion relation from Eq. (3.11). As mentioned above, the allowed wave vectors \mathbf{k} of a nanotube are quantized due to the periodic boundary conditions around the tube. They are expressed by a quantized wave vector $m\mathbf{k}_\perp$, where m labels the bands, and \mathbf{k}_\perp is given in Eq. (3.15). Using \mathbf{k} , the optical matrix element can be expressed as a function of the chiral index (n_1, n_2) , the band index m , and the wave vector along the axis k_z

$$M_z(m, k_z) = \frac{M_c}{2\sqrt{N_0}|e(\mathbf{k})|} \left[(n_1 - n_2) \cos \Psi_3 - (2n_1 + n_2) \cos \Psi_1 + (n_1 + 2n_2) \cos \Psi_2 \right] \quad (3.26)$$

with

$$\Psi_1 = \pi m \frac{2n_1 + n_2}{N} - 2\pi \frac{n_2}{q} k_z, \quad \Psi_2 = \pi m \frac{n_1 + 2n_2}{N} + 2\pi \frac{n_1}{q} k_z, \quad \Psi_3 = \pi m \frac{n_1 - n_2}{N} - 2\pi \frac{n_1 + n_2}{q} k_z,$$

and

$$|e(\mathbf{k})| = \sqrt{3 + 2 \cos(\Psi_1) + 2 \cos(\Psi_2) + 2 \cos(\Psi_3)}.$$

In the following, this analytical expression for the optical matrix element is discussed in detail. First, the symmetry-imposed selection rules that are fully covered by the above expression, are considered. Then, the dependence of the matrix element on the nanotube family, the band index m , the chiral angle ϕ , and the wave vector k_z is discussed.

Selection rules

The symmetry of CNTs imposes selection rules for optical band-to-band transitions.^{46,59} Generally, for light polarized along the nanotube axis, transitions are allowed between electronic states with $\Delta m = 0$, since this light has no angular momentum. Furthermore, assuming the wave vector of photons to be small, only vertical transitions, i.e. $\Delta k = 0$ are allowed. Achiral nanotubes have a vertical (σ_v) and horizontal (σ_h) mirror plane, see Fig. 3.15. Reflections in the σ_h plane in armchair tubes and in the σ_v plane in zigzag tubes leave the carbon atom invariant.⁴⁶ These additional symmetries account for further selection rules for zigzag and armchair tubes. In the following, $+/-$ denotes the electron parity under σ_h and A, B the parity under σ_v reflections.^{46,60} Because of its A_0^- symmetry, z -polarized light preserves the vertical mirror parity σ_v , whereas the parity for the horizontal mirror plane σ_h is reversed.⁶⁰

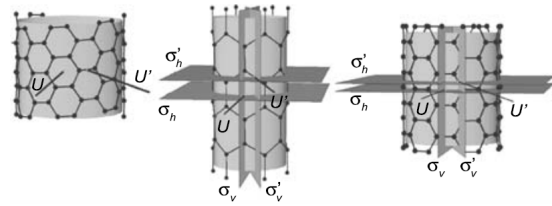


Figure 3.15: Illustration of rotational axes and mirror planes in nanotubes (taken from Reich et al.).⁴⁶

The symmetry-imposed selection rules are governed by the analytic expression for $M_z(m, k_z)$ in Eq. (3.26), which is an important test for the matrix element. M_z vanishes in (n, n) armchair nanotubes for i) $k_z = 0$, ii) $m = 0$, and iii) $m = n$. In armchair tubes, the conduction and the valence bands with $m = 0$ and $m = n$ have the opposite σ_v parity, see Fig. 3.16a. The corresponding two transitions are forbidden, since the parity with respect to σ_v cannot be preserved optically. The matrix element is zero for $k_z = 0$ reflecting the σ_h selection rule. As can be seen in Fig. 3.16a the valence and conduction bands with the same m have the same σ_h parity at the Γ point in armchair nanotubes.⁵⁹ The z -polarized light cannot reverse the σ_h parity. As a result, the matrix element vanishes for $k_z = 0$ for all subbands m . In zigzag tubes, the conduction and valence

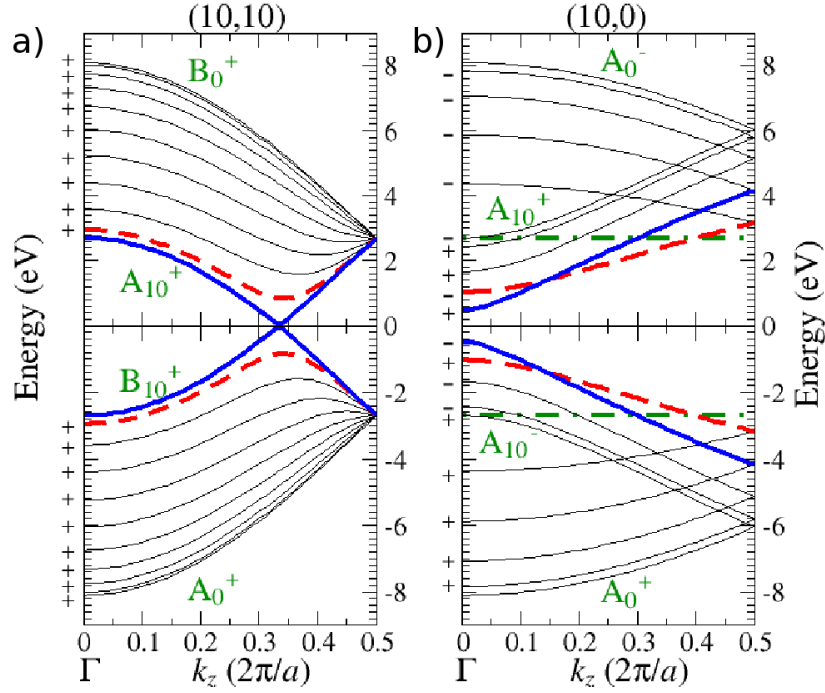


Figure 3.16: Band structure of an a) (10,10) armchair and b) (10,0) zigzag nanotube. $+/-$ denotes the electron parity under σ_h and A/B the parity under σ_v reflections,^{46,60} see Fig. 3.15. In a) the bold (dashed) band emphasizes the crossing bands ($m = 10$) and the bands with the smallest bandgap ($m = 9$) leading to the energetically lowest transition E_{11} . In b) the $m = 7$ bands (leading to E_{11}) are indicated by full bold, the $m = 6$ bands (leading to E_{22}) by dashed, and the remarkable dispersionless $m = 5$ bands by dashed-dotted lines.

bands have the opposite parity with respect to σ_h . Consequently, the optical transitions between valence and conduction bands with the same m fulfil the symmetry-imposed selection rules, as can be seen in Fig. 3.16b. This is in excellent agreement with Eq. (3.26), where M_z remains non-zero for $(n, 0)$ tubes at $k_z = 0$, in contrast to the (n, n) armchair case.

High-symmetry lines

Now, the dependence of the optical matrix element $M_z(\mathbf{k})$ on the subband index m is discussed. This corresponds to the behavior of $M_z(\mathbf{k})$ along certain high-symmetry lines in graphene. Figure 3.17a shows the optical matrix element at the Γ point of zigzag nanotubes ($k_z = 0$). This is equivalent to the ΓKM high-symmetry line of graphene, see inset of Fig. 3.17a. The matrix element is zero for $m = 0$, which corresponds to the Γ point of graphene. At this high-symmetry point optical absorption is forbidden in graphene for the π bands, which carries over to nanotubes. The magnitude of $M_z(m, 0)$ decreases when going from K to Γ , but increases from K to M . This leads to a chirality and family dependence of the matrix element as will be discussed below.

Figure 3.17b shows the dependence of the matrix element on m in armchair nanotubes for the k_z with a high electronic density of states (maxima and minima in the band structure, see Fig. 3.16a). Varying m corresponds to going along the high-symmetry line MK as shown in the inset of Fig. 3.17b. The magnitude of the matrix element is maximal at the M point, it decreases towards

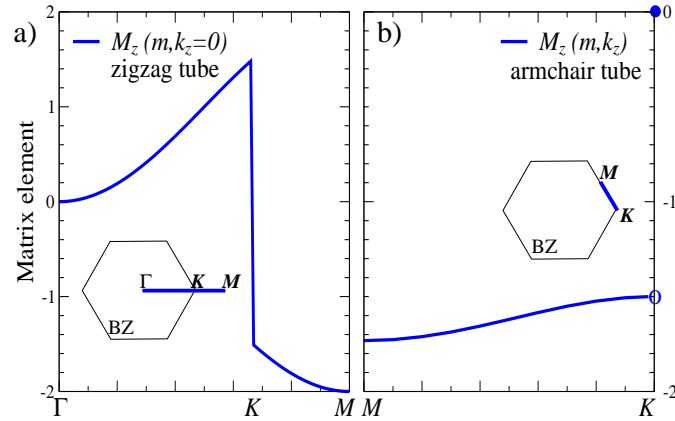


Figure 3.17: Optical matrix element $M_z(\mathbf{k})$ as a function of the subband index m . a) In zigzag nanotubes $M_z(m, 0)$ corresponds to the high-symmetry line ΓKM , see inset. In b), the optical matrix element in armchair nanotubes is shown for the k_z vectors that give rise to the Van Hove singularities. This corresponds to the the MK line of graphene, see the inset.

the K point, where it vanishes because of the σ_v selection rule. Note that the matrix elements along the two KM segments in Fig. 3.17a-b differ, because the polarization of the absorbed light is fixed to be parallel to the tube.

Chirality dependence

Figure 3.18 illustrates the dependence of the matrix element on the chiral angle ϕ for the two semiconducting nanotube families $+1$ and -1 . A similar dependence of M_z on ϕ was obtained numerically by Grüneis *et al.*⁵⁸ M_z is evaluated at the k_z that correspond to the first two Van Hove singularities (transitions E_{11} , E_{22}). The result reflects the behavior of the matrix element shown in Fig. 3.17. For zigzag nanotubes ($\phi = 0^\circ$) the magnitude of the matrix element is larger for the \mathbf{k} on the KM than on the ΓK line in Fig. 3.17a. Consequently, $|M_z(\mathbf{k})|$ is higher for E_{11} than for E_{22} in $+1$ tubes, since these transitions originate from opposite sides of the graphene K

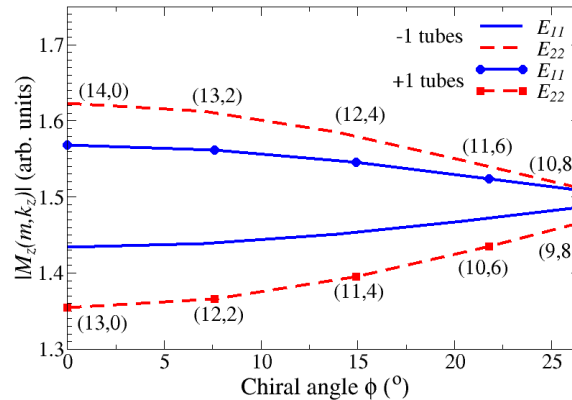


Figure 3.18: The magnitude of the optical matrix element $M_z(\mathbf{k})$ as a function of the chiral angle ϕ for the first two Van Hove singularities. The two semiconducting tube families $\nu = +1, -1$ with $\beta = 2n_1 + n_2 = 26, 28$ are evaluated. The tubes have a fairly constant diameter $d \approx 1.1$ nm.

point as indicated in Fig. 3.6. The difference becomes smaller with increasing chiral angle ϕ . It almost vanishes for armchair tubes, where the dependence of M_z on m is weak, see Fig. 3.17b. The energy minima for +1 and -1 tubes for a given transition E_{ii} are located on different sides of the graphene K point. The matrix elements, therefore, exhibit a family dependence. For -1 nanotubes, $|M_z(\mathbf{k})|$ is larger at the second transition E_{22} than at E_{11} (in contrast to +1 tubes), since the E_{22} Van Hove singularity originates from the KM line (Fig. 3.6). The two families differ even for the same transition E_{ii} . For E_{11} the +1 family has larger M_z than the -1 family. This can be again explained with the absolute values of M_z in zigzag tubes, Fig. 3.17a, and the zone-folding approximation. Interestingly, the difference in the magnitude of M_z to the right and left of K in Fig. 3.17a is mainly due to the explicit dependence of the matrix elements on $e(\mathbf{k})$. The contributions stemming from cosine terms in Eq. (3.26) lead to a linear dependence of M_z on \mathbf{k} close to the K point.

Similarity to the dispersion relation

Figure 3.19 shows the matrix element for a) the (10,0) zigzag and b) the (10,10) armchair nanotube as a function of k_z for the two lowest bands. For the (10,0) zigzag tube, the bands with $m = 3$ and 4 are also shown to illustrate the relation to the band structure in Fig. 3.16b. The matrix element $M(7, k_z)$ is negative in the (10,0) tube at the first Van Hove singularity in agreement with Fig. 3.17a. It exhibits a minimum at the Γ point followed by a rapid increase. In contrast, $M(6, k_z)$ (the second singularity) is positive and the maximal absolute value is smaller than for the $m = 7$ band, because the Van Hove singularity originates from the ΓK line of graphene. The k_z dependence of the matrix elements for bands with $m < \frac{n}{2}$ such as $m = 3$ and 4 in Fig. 3.19a differ from bands with $m > \frac{n}{2}$ mirroring the band structure of a $(n, 0)$ zigzag nanotube. Figure 3.16b shows that the bands of zigzag tubes have minima at Γ for $m > \frac{n}{2}$, but maxima $m < \frac{n}{2}$. The two types of bands intersect at $k_z = \frac{\pi}{a}$. The band with $m = \frac{n}{2}$ shows no dispersion within the nearest-neighbor tight-binding approximation. This has an interesting influence on the absorption spectra and will be discussed in Sec. 3.5.1.

In the (10,10) armchair nanotube in Fig. 3.19b the matrix element is zero for $M_z(m, 0)$ as explained above. It decreases when going away from Γ with minima for $M_z(9, 0.68\frac{\pi}{a})$ and $M_z(8, 0.74\frac{\pi}{a})$. The extrema correspond to the positions of the energy minima in the band structure in Fig. 3.16a.

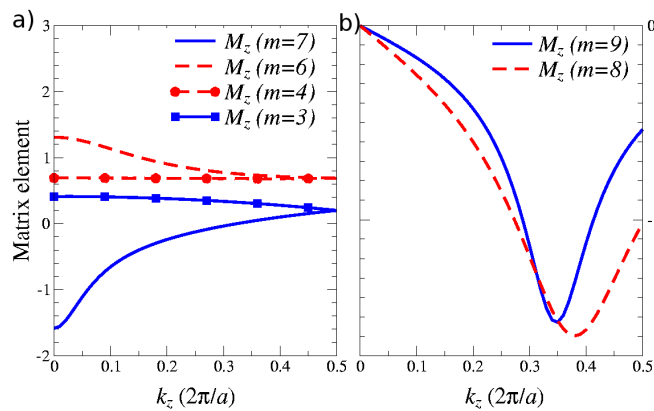


Figure 3.19: Optical matrix element as a function of k_z ; a) bands with $m = 7, 6, 4,$ and 3 in the (10,0) zigzag nanotube and b) bands with $m = 9$ and 8 in the (10,10) armchair nanotube.

3.4.2 Coulomb matrix element

Derivation

The Coulomb interaction in one-dimensional structures needs to be treated with care since the ground state is known to have an infinite energy.⁶¹ This problem can be avoided by introducing a regularized Coulomb potential that takes into account that CNTs are not strictly one-dimensional. In this chapter, the unscreened Coulomb interaction is parametrized by the Ohno potential, which stems from polymer chemistry and has already been shown to be a good approximation for CNTs.^{13,14,17}

The Coulomb matrix elements are given by

$$V_{l_3, l_4}^{l_1, l_2} = \int d\mathbf{r} \int d\mathbf{r}' \Psi_{l_1}^*(\mathbf{r}) \Psi_{l_2}^*(\mathbf{r}') V_{Coul}(|\mathbf{r} - \mathbf{r}'|) \Psi_{l_3}(\mathbf{r}') \Psi_{l_4}(\mathbf{r}) \quad (3.27)$$

with the compound index l containing the band index $\alpha = c, v$ and the wave vector \mathbf{k} . Applying the TB single-particle wave functions $\Psi^\alpha(\mathbf{k}, \mathbf{r})$ from Eq. (3.6) yields

$$V_{\alpha_3 \mathbf{k}_3, \alpha_4 \mathbf{k}_4}^{\alpha_1 \mathbf{k}_1, \alpha_2 \mathbf{k}_2} = \sum_{i, i', j, j'}^{A, B} C_i^{\alpha_1*}(\mathbf{k}_1) C_j^{\alpha_2*}(\mathbf{k}_2) C_{i'}^{\alpha_3}(\mathbf{k}_3) C_{j'}^{\alpha_4}(\mathbf{k}_4) \frac{1}{N_0^2} \sum_{l, l', n, n'}^N e^{-i\mathbf{k}_1 \cdot \mathbf{R}_l^i} e^{-i\mathbf{k}_2 \cdot \mathbf{R}_n^j} e^{i\mathbf{k}_3 \cdot \mathbf{R}_{l'}^{i'}} e^{i\mathbf{k}_4 \cdot \mathbf{R}_{n'}^{j'}} \times \\ \times \int \int d^3r d^3r' \phi^*(\mathbf{r} - \mathbf{R}_l^i) \phi^*(\mathbf{r}' - \mathbf{R}_n^j) V_{Coul}(|\mathbf{r} - \mathbf{r}'|) \phi(\mathbf{r} - \mathbf{R}_{l'}^{i'}) \phi(\mathbf{r}' - \mathbf{R}_{n'}^{j'}).$$

with the lattice vectors \mathbf{R}_l^i , the normalization factor N_0 , and with the TB coefficient functions $C_i^\alpha(\mathbf{k})$ with the wave vector $\mathbf{k} = (k_z, m)$. Taking into account only the strongest contribution where the interacting particles are on the same site, i.e. $(i, l) = (i', l')$ simplifies this expression to

$$V_{\alpha_3 \mathbf{k}_3, \alpha_4 \mathbf{k}_4}^{\alpha_1 \mathbf{k}_1, \alpha_2 \mathbf{k}_2} = \sum_{i, j}^{A, B} \gamma_{ij}(\alpha \mathbf{k}) \frac{1}{N_0^2} \sum_{l, n}^{N_0} e^{-i(\mathbf{k}_1 - \mathbf{k}_3) \cdot \mathbf{R}_l^i} e^{-i(\mathbf{k}_2 - \mathbf{k}_4) \cdot \mathbf{R}_n^j} V_{Coul}(|\mathbf{R}_l^i - \mathbf{R}_n^j|).$$

Here, the abbreviation $\gamma_{ij}(\alpha \mathbf{k}) \equiv C_i^{\alpha_1*}(\mathbf{k}_1) C_j^{\alpha_2*}(\mathbf{k}_2) C_{i'}^{\alpha_3}(\mathbf{k}_3) C_{j'}^{\alpha_4}(\mathbf{k}_4)$ has been introduced. Furthermore, since the atoms are located at the positions \mathbf{R}_l^i , it is $|\phi(\mathbf{r} - \mathbf{R}_l^i)|^2 = \delta(\mathbf{r} - \mathbf{R}_l^i)$. After introducing the center-of-mass coordinate $\hat{\mathbf{R}}^{ij} = \frac{\mathbf{R}_l^i + \mathbf{R}_n^j}{2}$ and the relative coordinate $\hat{\mathbf{r}}^{ij} = \mathbf{R}_l^i - \mathbf{R}_n^j$, the equation reads (for more details, see App. C.1)

$$V_{\alpha_3 \mathbf{k}_3, \alpha_4 \mathbf{k}_4}^{\alpha_1 \mathbf{k}_1, \alpha_2 \mathbf{k}_2} = \sum_{i, j}^{A, B} \gamma_{ij}(\alpha \mathbf{k}) \delta_{\mathbf{k}_1 - \mathbf{k}_3, \mathbf{k}_4 - \mathbf{k}_2} V^{ij}(\mathbf{q}). \quad (3.28)$$

Here, the Fourier transform $V^{ij}(\mathbf{q})$ of the Coulomb potential has been introduced by

$$V^{ij}(\mathbf{q}) = \frac{1}{N_0} \sum_{\hat{\mathbf{r}}} e^{i\mathbf{q} \cdot \hat{\mathbf{r}}^{ij}} V^{ij}(|\hat{\mathbf{r}}^{ij}|) \quad (3.29)$$

with the momentum transfer $\mathbf{q} = \mathbf{k}_3 - \mathbf{k}_1 = \mathbf{k}_2 - \mathbf{k}_4 = (q_z, \Delta m)$. The conservation of the momentum follows from the Kronecker delta $\delta_{\mathbf{k}_1 - \mathbf{k}_3, \mathbf{k}_4 - \mathbf{k}_2}$.

The unscreened Coulomb interaction $V^{ij}(|\hat{\mathbf{r}}^{ij}|)$ is parametrized by the Ohno potential⁶²

$$V^{ij}(|\hat{\mathbf{r}}^{ij}|) = \frac{U}{\sqrt{\left(\frac{4\pi\epsilon_0}{e^2} U |\hat{\mathbf{r}}^{ij}\right)^2 + 1}} \quad (3.30)$$

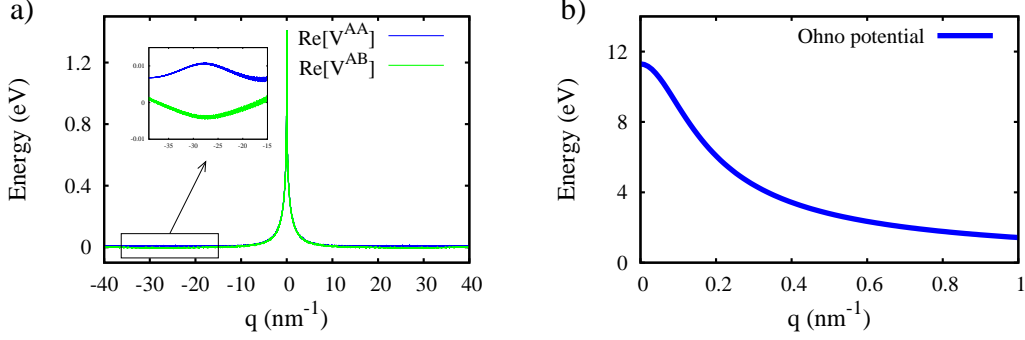


Figure 3.20: a) The real part of the Fourier transform of the Coulomb potentials $V^{AA}(q_z, \Delta m = 0)$ and $V^{AB}(q_z, \Delta m = 0)$ for the (8,4) nanotube. $V^{AB}(\mathbf{q})$ also has a non-zero imaginary part, but it is much smaller than the real part. The largest difference between $V^{AA}(\mathbf{q})$ and $V^{AB}(\mathbf{q})$ is far away from the $q_z = 0$ point, as illustrated in the inset. b) Illustration of the Ohno potential from Eq. (3.30).

with $U = 11.3$ eV representing the necessary energy to place two electrons on a single site.

The Fourier transform of the Coulomb potential is performed atom-wise using the line group symmetry operations described in Sec. 3.2, i.e. the sum in Eq. (3.29) is expressed by

$$\sum_{\hat{r}} \rightarrow \sum_c \sum_t \sum_s \sum_u \quad (3.31)$$

with i) u expressing the U-operation responsible for mapping atom A to atom B , ii) s denoting the pure rotation around the tube axis C_n^s , iii) t describing the pure translations and screw axis rotations $(C_q^{rt} | \frac{tna}{q})$, and finally iv) c expressing the number of unit cells considered in the calculation. This atom-wise procedure distinguishes between the atoms of type A and B. As a result, there are four different Fourier transforms $V^{AA}(\mathbf{q})$, $V^{BB}(\mathbf{q})$, $V^{AB}(\mathbf{q})$, and $V^{BA}(\mathbf{q})$. However, they are related to each other by $V^{AA}(\mathbf{q}) = V^{BB}(\mathbf{q})$ and $V^{AB}(\mathbf{q}) = V^{BA*}(\mathbf{q})$. For the calculation of these quantities, it is important to calculate the scalar product $\mathbf{q} \cdot \hat{\mathbf{r}}^{AA}$ and $\mathbf{q} \cdot \hat{\mathbf{r}}^{BA}$, see Eq. (3.29). Using Eq. (3.4) and considering the cylinder as unrolled (i.e. neglecting curvature effects) leads to the expressions

$$\mathbf{q} \cdot \hat{\mathbf{r}}^{AA} = q_z \hat{\mathbf{r}}_z^{AA} + q_\perp \hat{\mathbf{r}}_\perp^{AA} = q_z \left(t \frac{na}{q} + c_i a \right) + m \left[2\pi \left(t \frac{r}{q} + \frac{s}{n} \right) \right], \quad (3.32)$$

$$\mathbf{q} \cdot \hat{\mathbf{r}}^{AB} = q_z \hat{\mathbf{r}}_z^{BA} + q_\perp \hat{\mathbf{r}}_\perp^{BA} = q_z \left(t \frac{na}{q} + c_i a - 2z_0 \right) + m \left[2\pi \left(t \frac{r}{q} + \frac{s}{n} \right) - 2\phi_0 \right]. \quad (3.33)$$

Figure 3.20 illustrates the difference between V^{AA} and V^{AB} . They are shown as a function of the momentum transfer q_z along the nanotube axis and for transitions with $\Delta m = 0$, i.e. no angular momentum is transferred. The difference is vanishingly small for the maximal peak at $q_z = 0$. At higher wave vectors, both Fourier transforms show a small extremum, V^{AA} a maximum and V^{AB} a minimum. These small oscillations stem from the Bessel-function-like behavior of the Coulomb matrix elements. Integrating Eq. (3.29) continuously, i.e. not considering the geometry of the nanotube, would lead to a modified Bessel function of the second kind $V(q_z) \propto K(0, |q_z|/c)$ with $c = \frac{4U\pi\epsilon_0}{e^2}$. The difference between V^{AA} and V^{AB} is completely expressed by the application of the U symmetry on the reference atom $r_{000} = (d/2, \phi_0, z_0)$, see Eqs. (3.32)-(3.33). According to Eq. (3.33), $V^{AB}(\mathbf{q})$ depends on z_0 , i.e. it has the phase factor $e^{2iq_z z_0}$. The latter is responsible for the fact, that $V^{AB}(\mathbf{q})$ is not periodic with the Brillouin zone, since the periodic length of the cosine

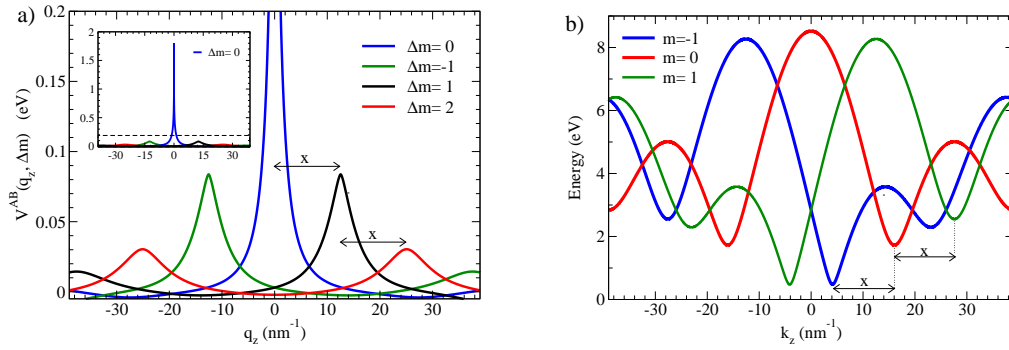


Figure 3.21: a) The figure shows the Fourier transform of the Coulomb potential $V^{AB}(q_z, \Delta m)$ for the (8,4) tube as a function of the momentum transfer q_z along the nanotube axis ($V^{AA}(q_z, \Delta m)$ has a similar behavior). The region marked with a dashed line in the inset is plotted as a blow-up in the main figure showing the Coulomb contribution which arises from processes with a momentum transfer perpendicular to the nanotube axis, i.e. $\Delta m \neq 0$. b) The band structure of the (8,4) tube shows that the distance $x = \frac{r}{n} \frac{2\pi}{a}$ between the band minima exactly corresponds to the relative maxima of the Coulomb interaction in Fig. 3.21a.

does not correspond to the BZ length. It repeats periodically after $\frac{3n}{n_1 - n_2}$ -fold of the BZ (for the (8,4) tube this factor corresponds exactly to a factor of 3).

Momentum transfer

Figure 3.21a shows the Fourier transform of the Coulomb potential as a function of the momentum transfer q_z along the nanotube axis for processes with $\Delta m = 0$ and $\Delta m \neq 0$. The Coulomb interaction reaches the maximal value when the involved electrons have the same momentum, i.e. for processes with $\Delta m = 0$ and $q_z = 0$. The second maximum is found for $\Delta m = 1$ at $q_z = \frac{r}{n} \frac{2\pi}{a}$, i.e. for transitions between two energetically neighbored subbands. For this process, the Coulomb interaction is strongly enhanced when a momentum of $q_z = \frac{r}{n} \frac{2\pi}{a}$ is carried over along the nanotube axis. This corresponds to a transition between the subband minima, see Fig. 3.21b. However, the coupling strength decreases strongly with increasing momentum transfer perpendicular to the nanotube axis, e.g. the Coulomb interaction for the process with $\Delta m = 1$ ($\Delta m = 2$) is less than 5% (2%) of the absolute maxima for $\Delta m = 0$. Consequently, intersubband processes with a transfer of angular momentum should be suppressed. Nevertheless, it will turn out to be of importance to take these interactions into account, since they have an influence on the position of the excitonic peak in the absorption spectra.

Screening

One important effect of many-body interactions in an electron plasma is screening.⁴² Due to the presence of other electrons and the surrounding material, the Coulomb interaction affecting a single electron is screened. The effects arising from the electrons in the core states and the surrounding medium are taken into account by introducing a dielectric background constant ε_{bg} . The screening stemming from other valence electrons within the allowed subbands are calculated within an effective single-particle Hamiltonian approach leading to the renowned Lindhard approximation

$$\varepsilon(\mathbf{q}, \omega) = 1 - V(\mathbf{q})P(\mathbf{q}, \omega) \quad (3.34)$$

where $\varepsilon(q, \omega)$ is the dielectric function. Then, the screened Coulomb potential $W(\mathbf{q}, \omega)$ is given by

$$W(\mathbf{q}, \omega) = \frac{V(\mathbf{q})}{\varepsilon_{bg}\varepsilon(\mathbf{q}, \omega)}. \quad (3.35)$$

The quantum mechanical derivation of the Lindhard formula is shown in many textbooks of solid state physics.^{36,42} Hence, here, the focus lies on its evaluation for the case of one-dimensional structures, such as carbon nanotubes. The polarisation $P(\mathbf{q}, \omega)$ is a function of the electron charge density $\hat{\rho}_{\mathbf{q}} = \frac{1}{V} \sum_{\mathbf{k}} \langle a_{\mathbf{k}-\mathbf{q}}^{\dagger} a_{\mathbf{k}} \rangle$. Applying the Heisenberg equation, an equation of motion for the electron charge carrier density can be derived^{17,36} resulting in

$$P(\mathbf{q}, \omega) = \sum_{\mathbf{k}} \langle a_{\mathbf{k}-\mathbf{q}}^{\dagger} a_{\mathbf{k}} \rangle = 2 \sum_{\lambda, \lambda'} \sum_{\mathbf{k}}^{c, v} \frac{\rho_{\mathbf{k}-\mathbf{q}}^{\lambda'} - \rho_{\mathbf{k}}^{\lambda}}{\hbar(\omega + i\gamma) + \varepsilon_{\mathbf{k}-\mathbf{q}}^{\lambda'} - \varepsilon_{\mathbf{k}}^{\lambda}} \left| \int \psi_{\mathbf{k}, \lambda}^*(\mathbf{r}) e^{-i\mathbf{q} \cdot \mathbf{r}} \psi_{\mathbf{k}-\mathbf{q}, \lambda'} \right|^2. \quad (3.36)$$

To reduce the numerical complexity, the static limit of the Lindhard approximation, i.e. $(\omega + i\gamma) \rightarrow 0$, is taken into account. Inserting the TB wave functions, considering only the strongest contribution with atoms at the same site (in analogy to the derivation of the Coulomb matrix element), and assuming the conduction band to be empty, i.e. $\rho_{\mathbf{k}}^c = 0$, and the valence band to be full, i.e. $\rho_{\mathbf{k}}^v = 1$ (linear optics limit), gives

$$P(\mathbf{q}) = \sum_{\mathbf{k}} \frac{4}{\varepsilon_{\mathbf{k}-\mathbf{q}}^v - \varepsilon_{\mathbf{k}}^c} \left| C_A^{c*}(\mathbf{k}) C_A^v(\mathbf{k}-\mathbf{q}) + C_B^{c*}(\mathbf{k}) C_B^v(\mathbf{k}-\mathbf{q}) \right|^2. \quad (3.37)$$

Inserting the expressions for the coefficient functions $C_i^{\lambda}(\mathbf{k})$ from Eq. (3.23) yields the dielectric function $\varepsilon(\mathbf{q})$

$$\varepsilon(\mathbf{q}) = 1 - V(\mathbf{q}) \sum_{\mathbf{k}} \frac{2}{\gamma_0 |e(\mathbf{k}-\mathbf{q})| + \gamma_0 |e(\mathbf{q})|} \left[1 - \text{Re} \left(\frac{e^*(\mathbf{k}) e(\mathbf{k}-\mathbf{q})}{|e(\mathbf{k}) e(\mathbf{k}-\mathbf{q})|} \right) \right]. \quad (3.38)$$

The equations illustrate that the screening effects are of crucial importance for metallic nanotubes, where the denominator can become very small, see Fig. 3.22. The characteristic dependence of the screening on the wave vector \mathbf{q} stems from the contribution $1 - \text{Re} \left(\frac{e^*(\mathbf{k}) e(\mathbf{k}-\mathbf{q})}{|e(\mathbf{k}) e(\mathbf{k}-\mathbf{q})|} \right)$, which vanishes at $\mathbf{q} = 0$. As a result, at this point $\varepsilon(0) = 1$ resulting in no screening of the Coulomb interaction.

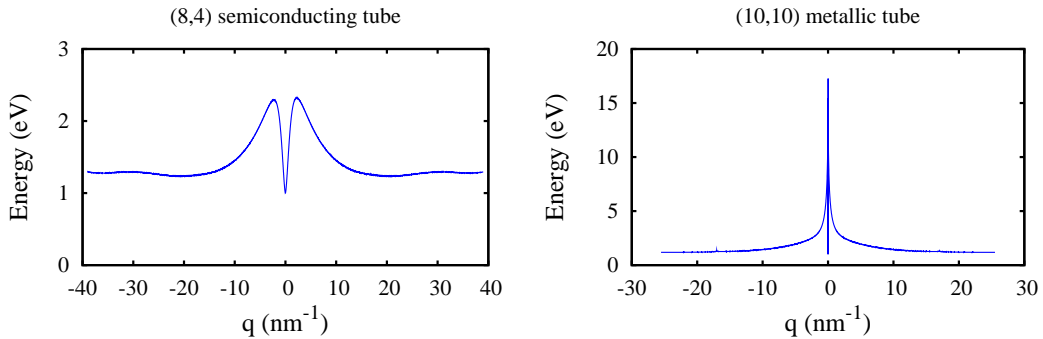


Figure 3.22: The screening of the Coulomb interaction is illustrated for the (8,4) semiconducting and the (10,10) metallic nanotube. The dielectric background constant ε_{bg} is set to 1 to show the influence of the internal screening according to Eq. (3.38).

3.4.3 Electron-phonon matrix element

A periodic displacement of atoms around the equilibrium sited gives rise to the electron-phonon interaction. Similar to the optical matrix element, first the electron-phonon coupling of graphene is calculated. Then, the corresponding matrix elements for CNTs are determined by applying the zone-folding approximation, see Sec. 3.3.1.

The electron-phonon matrix elements $g_{\mathbf{q},\nu}^{k,ii'}$ for graphene have already been calculated and successfully evaluated by M. Lazzeri et al.:^{63–66}

$$g_{\mathbf{q},\nu}^{k,ii'} = \frac{\hbar}{2m\omega_{\mathbf{q}\nu}} \langle \Psi^i(\mathbf{k} + \mathbf{q}) | \frac{\partial V}{\partial u(\mathbf{q}, \nu)} | \Psi^{i'}(\mathbf{k}) \rangle \quad (3.39)$$

with the TB wave functions $\Psi^i(\mathbf{k})$ from Eq. (3.6) where i and \mathbf{k} denote the electron band index wave vector, respectively. Furthermore, Eq. (3.39) contains the phonon frequency $\omega_{\mathbf{q},\nu}$, which can be calculated by solving the secular equation including the dynamical matrix^{66,67} determined by Eq. (3.39). The corresponding phonon energies for the six possible modes of graphite are shown in Fig. 3.23. Graphite has two atoms per unit cell. As a consequence, six phonon modes exist. They are divided into three optical and three acoustic modes in dependence of the relative displacements of atoms in the unit cell. If they oscillate in opposite (the same) directions, the corresponding modes are called optical (acoustic). Moreover, in graphite, there is a difference between in-plane modes and out-plane modes (ZA, ZO). The in-plane modes can be further separated into transverse (TO, TA) and longitudinal (LO, LA) according to the direction of their displacements with respect to the wave vector (propagation direction),* see Fig. 3.23.

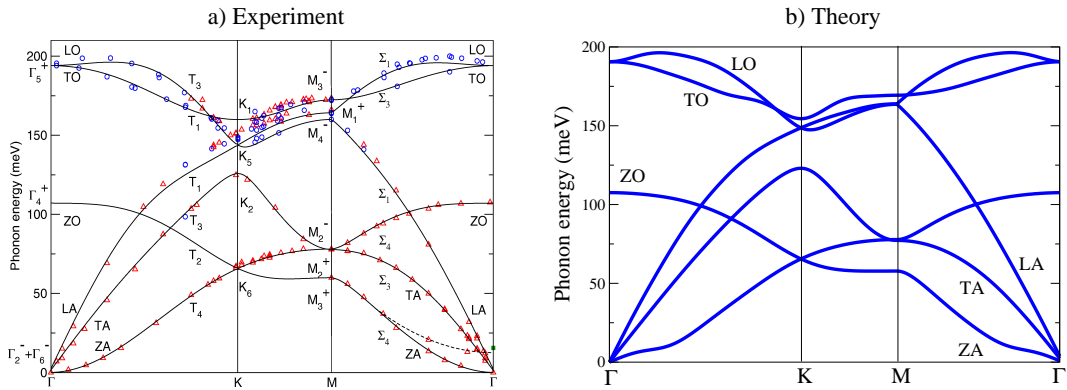


Figure 3.23: a) The experimental phonon dispersion of graphite is shown (taken from Mohr et al.).⁶⁸ The three optical (LO, TO, ZO) and acoustic (LA, TA, ZA) modes are shown, respectively. Experimental data is obtained from inelastic x-ray scattering. Circles and triangles denote different data sets.^{68,69} Solid lines show results from force-constant calculations from the fifth-nearest neighbor fit. The corresponding symmetry representations are given in space group notation. b) The corresponding theoretical simulation is illustrated. The results are obtained from calculations performed by M. Lazzeri et al.⁶⁴

*In literature, phonons are labeled using different criteria,⁶⁶ such as their symmetry, the direction of the atomic displacements with respect to the nanotube axis, the longitudinal or transversal character of the graphene phonon branch from which they originate, etc. Here, phonon modes are denoted as longitudinal if $\epsilon \parallel \mathbf{q}$ and transverse if $\epsilon \perp \mathbf{q}$ where \mathbf{q} is the wave vector giving the direction of the phonon propagation and ϵ is the phonon polarization giving the direction of the atomic displacement.

For a DFT calculation of the electron-phonon matrix elements from Eq. (3.39), the derivative of the deformation potential V with respect to the displacement needs to be calculated. The displacement function is given by

$$u(\mathbf{q}, \nu) = \sum_{li\hat{n}} e^{-\mathbf{q} \cdot (\mathbf{R}_l + \boldsymbol{\tau}_i)} \tau_{li\hat{n}} \epsilon_{i\hat{n}}^*(\mathbf{q}, \nu) \quad (3.40)$$

with the nearest-neighbor positions $\mathbf{R}_l + \boldsymbol{\tau}_i$ and with ν and \mathbf{q} denoting the phonon mode and the wave vector, respectively. The displacement function $u(\mathbf{q}, \nu)$ is determined by the polarization vector $\epsilon_{i\hat{n}}(\mathbf{q}, \nu)$ with \hat{n} standing the direction of displacement. To avoid the numerically demanding DFT solution, the derivative of the potential with respect to the atomic distance in equilibrium is adjusted to the results of first-principle calculations yielding

$$\langle \phi_l | \frac{\partial V}{\partial \tau_{li, \hat{n}}} | \phi_l \rangle \approx \beta \quad \longrightarrow \quad \langle \phi_l | \frac{\partial V}{\partial \tau_{li, \hat{n}}} | \phi_{l'} \rangle \approx \beta \hat{n} \cdot \mathbf{C}_{l'i', li} \quad (3.41)$$

with the atomic wave functions ϕ_l and the vector $\mathbf{C}_{l'i', li}$ denoting the distance between the atom (l', i') and (l, i) . Now, the electron-phonon matrix can be calculated by inserting Eq. (3.41) and the TB wave functions into Eq. (3.39). The obtained results for the inter- and intraband electron-phonon coupling of ΓLO , ΓTO and $K LO$ phonons* are shown in Fig. 3.24. Considering the interband electron-phonon interaction, also called $\pi^*\pi$ coupling, the ΓTO is found to be zero, see Fig. 3.24a. This can be traced back to the symmetry of transversal phonon modes. The ΓTO phonon in armchair nanotubes belongs to the symmetry ${}_0B_0^-$.⁴⁶ As discussed in Sec. 3.4.1, this means that these phonons do not preserve the parity with respect to the horizontal mirror plane σ_h . Since the valence and conduction bands belonging to the same m have equal parities under σ_h reflection (Fig. 3.16) the interband electron-phonon coupling vanishes for ΓTO phonons. This behavior carries over for graphene. As a direct consequence, also the intra-band electron-phonon matrix elements for longitudinal phonons ΓLO and KL must vanish, as nicely confirmed by the presented calculations, see Fig. 3.24b.

Up to now, the electron-phonon coupling for graphene has been considered. Applying the zone-folding approximation, the corresponding matrix elements for SWCNTs can be obtained. This approach has already been discussed for electrons in Sec. 3.3.1.

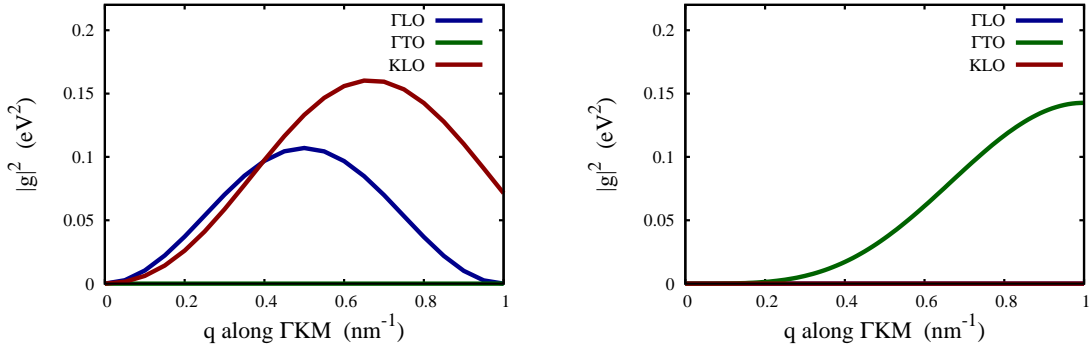


Figure 3.24: Illustration of electron-phonon matrix elements $g(\mathbf{q}, \mathbf{k})^2$ for the ΓLO , ΓTO , and $K LO$ phonon modes along the high-symmetry line ΓKM in graphite calculated for a) inter-band interaction ($\pi^*\pi$ coupling) and b) intra-band interaction ($\pi\pi$ coupling).

*A ΓLO ($K LO$) phonon is characterized by an electron wave vector $\mathbf{k} = 0$ ($\mathbf{k} = \mathbf{K}$). Transversal and longitudinal vectors are defined by the displacement function from Eq. (3.40).

The same procedure can be applied for phonons under certain restrictions, e. g. Kohn anomalies appearing in metallic nanotubes⁶³ cannot be described within this approximation. Furthermore, zone-folding is not applicable for the description of the radial-breathing mode (RBM). Nevertheless, the high energy optical modes (LO and TO), which are in the focus of considerations are well described within the zone-folding approximation.⁴ The latter is applied by transforming the Cartesian coordinate system (k_x, k_y) into the physically more intuitive k_z, k_\perp system, see Fig. 3.25. The rotation angle

$$\phi_{yz} = \arccos\left(\frac{1}{2\sqrt{N}(2n_1 + n_2)}\right) \quad (3.42)$$

is calculated by expressing k_z and k_\perp from Eq. (3.15) as a function of $\mathbf{k}_1 = \frac{2\pi}{a_0}\mathbf{e}_x - \frac{2\pi}{\sqrt{3}a_0}\mathbf{e}_y$ and $\mathbf{k}_2 = \frac{4\pi}{\sqrt{3}a_0}\mathbf{e}_y$ (Fig. 3.9) and calculating the scalar product $\mathbf{k}_z \cdot \mathbf{e}_y = \frac{2\pi}{a} \cos \phi_{zy}$. Then, the k_\perp coordinate is quantized according to the boundary condition, as discussed in Sec. 3.3.1.

After performing the zone-folding approximations, a number of subbands in the phonon dispersion is obtained. Figure 3.26 shows the ΓLO and ΓTO phonon energies as a function of wave vector q_z along the nanotube axis for two exemplary tubes: the (10, 0) zigzag tube and the chiral (8, 4) tube. The phonon subband is $m = 0$ is illustrated describing intrasubband electron-phonon processes. The two phonon modes touch at the Γ point. Moreover, the energy of the ΓLO mode is higher, reflecting the dispersion of graphite from Fig. 3.23. However, the variation in energy as a function of q_z is very small justifying the widely used assumption of constant optical phonon modes.

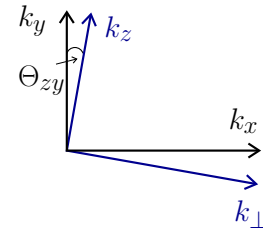


Figure 3.25: Rotation into the (k_z, k_\perp) coordinate system.

The corresponding intraband electron-phonon matrix elements for the ΓLO and ΓTO phonon modes are shown in Fig. 3.27. In both tubes, the electron-phonon matrix elements $g(q_z)$ are much stronger for the ΓLO phonons around the Γ point, i.e. at $q_z = 0$. The coupling with the ΓTO phonons even vanishes at the Γ point. In the case of zigzag tubes, this can again be explained by symmetry allowing only interband coupling, since ΓTO phonons do not preserve the parity with respect to the horizontal mirror plane σ_h .⁴⁶

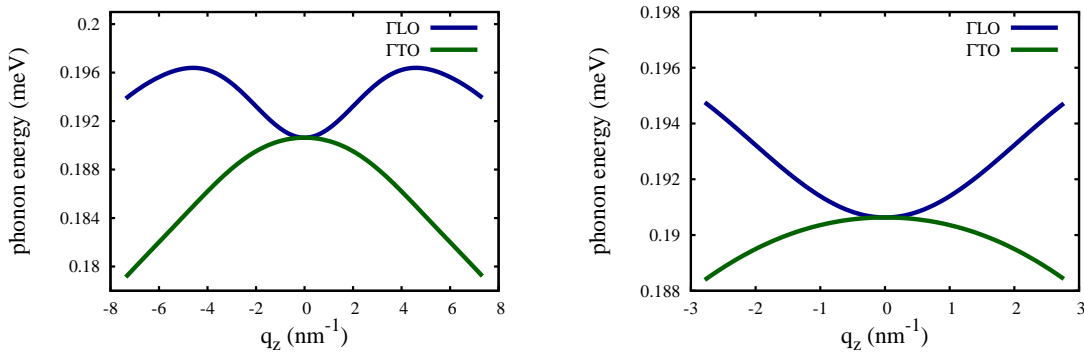


Figure 3.26: Comparison of the ΓLO and ΓTO phonon modes as a function of q_z (wave vector along the nanotubes axis) for the a) (10, 0) zigzag tube and the (8, 4) chiral tube. The band index m is fixed to 0, since the focus lies on intra-band phonon processes.

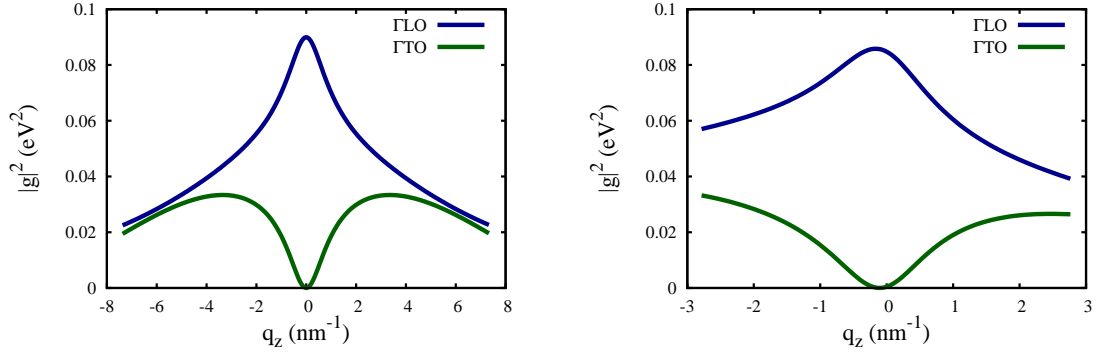


Figure 3.27: Illustration of electron phonon matrix elements $|g^{\pi\pi}(\mathbf{q}, \mathbf{k})|^2$ for the ΓLO and ΓTO phonon modes calculated for the a) (10, 0) zigzag tube and b) the (8, 4) chiral tube.

3.5 Free-particle spectra

Nanotubes, as prototypical one-dimensional systems, show well-defined optical transitions that can be exploited for structural assignment. Optical spectroscopies are among the most important characterization techniques for single-walled carbon nanotubes.⁵⁻⁹ They allow the identification of the microscopic structure of isolated tubes as well as for samples of many tubes. It has also been attempted to measure the abundance of nanotube chiralities from the intensities of the optical spectra.⁵ For this, a better understanding of the optical cross section and its dependence on nanotube chirality is needed. In this section, the absorption and Rayleigh scattering from carbon nanotubes are investigated theoretically. As a first approximation, the focus lies on the free-particle properties. For semiconducting nanotubes, excitonic transitions have been shown to dominate observed spectra^{10,11} and even for metallic nanotubes bound excitons have been predicted.¹² Nevertheless, the band-to-band transition model, i.e. the excitation of an electron from the valence into the conduction band can also give good insight into the optical properties as a function of chirality.^{58,70,71} The underlying assumption, that the excitonic absorption follows the oscillator strength found for uncorrelated electron-hole pairs is discussed in Sec. 3.6.9.

In this section, the absorption coefficient $\alpha(\omega)$ and the Rayleigh scattering cross section $\sigma(\omega)$ are calculated microscopically. Their dependence on the diameter, the chiral angle, and the family index is discussed.

3.5.1 Absorption

Assuming the driving field to be weak, the change in occupation probabilities is negligibly small justifying the linear optics approximation $\rho_{\mathbf{k}}^v = 1$ and $\rho_{\mathbf{k}}^c = 0$. This allows the calculation of linear spectra, which are independent of the excitation pulse. The dynamics is only determined by the microscopic polarisation $p_{\mathbf{k}}$.

The absorption coefficient has been derived in Sec. 2.5. Within the $\mathbf{p} \cdot \mathbf{A}$ approach, it can be expressed as a function of the macroscopic current $j(\omega)$ and the vector potential $A(\omega)$

$$\alpha \propto \text{Im} \chi(\omega) = \text{Im} \frac{j(\omega)}{\varepsilon_0 \omega^2 A(\omega)}. \quad (3.43)$$

The current density $j(\omega)$ is determined by the microscopic polarisation $p_{\mathbf{k}}$ according to Eq. (2.56). The Hamilton operator of the free-particle CNT system (for light polarized along the nanotube axis) consists of only two parts according to Eq. (2.32)

$$H = H_{0,c} + H_{c-f} = \sum_l \varepsilon_l a_l^\dagger a_l + i \frac{e_0 \hbar}{m_0} \sum_{l,l'} M_z^{vc} A_z(t) a_l^\dagger a_{l'} \quad (3.44)$$

with i) the free electron contribution $H_{0,c}$ containing the single-particle energy ε_l , which is calculated within the tight-binding approach, and ii) the electron-light interaction H_{c-f} , which is determined by the z -component of the vector potential $A_z(t)$ and the optical matrix element^{58,72-75} M_z^{vc} . Including this Hamiltonian into the Heisenberg equation of motion leads to the free-particle Bloch equation for the microscopic polarisation $p_{\mathbf{k}}(t)$

$$\dot{p}_{\mathbf{k}}(t) = -i\Delta\omega_{\mathbf{k}} p_{\mathbf{k}}(t) + g_{\mathbf{k}}(t) - \gamma p_{\mathbf{k}}(t) \quad (3.45)$$

with the subband transition frequency $\Delta\omega_{\mathbf{k}} = (\omega_c(\mathbf{k}) - \omega_v(\mathbf{k}))$, which determines the transition energy, and the Rabi frequency $g_{\mathbf{k}}(t) = \frac{e_0}{m_0} M_z(\mathbf{k}) A(t)$ describing the optical oscillator strength. The phenomenological parameter γ is introduced to describe dephasing, resulting from electron-phonon interaction. It corresponds to the inverse of the T_2 time in Eq. (2.35). Its value determines the linewidth in the calculated spectra and is set to $\gamma = (0.0125/\hbar)$ eV (corresponding to $\gamma \approx 20$ ps⁻¹).

Equation 3.45 can be solved analytically in the Fourier space yielding⁷²

$$p_{\mathbf{k}}(\omega) = -\frac{e_0}{m_0} \frac{\mathbf{M}^{vc}(\mathbf{k}) \cdot \mathbf{A}_0(\omega_L - \omega)}{i(\Delta\omega_{\mathbf{k}} - \omega) + \gamma}, \quad (3.46)$$

with the vector potential $\mathbf{A}(t) = \mathbf{A}_0(\omega) \cos(\omega_L t)$ with ω_L denoting the light frequency. Inserting this solution into the equation for the macroscopic current [Eq. (2.56)] leads to the expression

$$\mathbf{j}(\omega) = \frac{1}{V} \frac{2e_0}{m_0} \frac{\hbar}{i} \sum_{\mathbf{k}} \text{Re} \left[\mathbf{M}^{vc}(\mathbf{k}) p_{\mathbf{k}}(\omega) \right]. \quad (3.47)$$

Considering the case of z -polarized light yields

$$j_z(\omega) = -\frac{1}{V} \frac{2\hbar e_0^2}{im_0^2} \sum_{\mathbf{k}} \text{Re} \left[\frac{|M_z^{vc}(\mathbf{k})|^2 A_0^z(\omega_L - \omega)}{i(\Delta\omega_{\mathbf{k}} - \omega) + \gamma} \right].$$

Finally, applying the representation of the δ -function⁴²

$$\lim_{\gamma \rightarrow 0} \frac{\gamma}{(\Delta\omega_{\mathbf{k}} - \omega)^2 + \gamma^2} = \pi \delta(\Delta\omega_{\mathbf{k}} - \omega) \quad (3.48)$$

the absorption coefficient $\alpha(\omega)$ reads

$$\alpha(\omega) \propto \frac{\hbar\pi e_0^2}{m_0^2 \omega} \sum_{\mathbf{k}} |M_z^{vc}(\mathbf{k})|^2 \delta(\Delta\omega_{\mathbf{k}} - \omega). \quad (3.49)$$

The strength of the optical absorption is given by the square of the optical matrix element $M_z^{vc}(\mathbf{k})$ and the joint density of states (JDOS) expressed by the δ -function. To find $\alpha(\omega)$, the analytical expression for the optical matrix element from Eq. (3.26) is inserted into Eq. (3.49) and numerically summed over the wave vector $\mathbf{k} = (k_z, m)$.

In the special case of zigzag nanotubes, even an analytical expression for the absorption coefficient $\alpha(\omega)$ can be obtained. According to Eq. (3.16), the electronic dispersion relation for a $(n, 0)$ zigzag nanotube is given by

$$E_{zz}^{c,v} = \pm \gamma_0 \sqrt{3 + 2 \cos(2\pi \frac{m}{n}) + 4 \cos(\pi \frac{m}{n}) \cos(\pi k_z)}. \quad (3.50)$$

With this relation and the matrix element from Eq. (3.26), the absorption coefficient $\alpha_{zz}(\omega)$ for arbitrary zigzag nanotubes is determined by

$$\alpha(\omega)_{zz} \propto \sum_{m=-\frac{q}{2}+1}^{\frac{q}{2}} \frac{\left(\cos(\pi \frac{m}{n}) \cos(\pi k_z(\omega)) - \cos(2\pi \frac{m}{n}) \right)^2}{(\hbar\omega)^2 \cos(\pi \frac{m}{n}) \sin(\pi k_z(\omega))}. \quad (3.51)$$

The two-dimensional sum over \mathbf{k} is separated into sums over the band index m and the wave vector k_z along the nanotube axis. The latter is evaluated as an integral over energy with $\frac{dE_{zz}^{\pm}}{dk_z} = -\frac{2\pi\gamma_0^2}{E_{zz}^{\pm}} \cos(\pi \frac{m}{n}) \sin(\pi k_z)$. Then, the nanotube wave vector corresponding to a given photon energy $k_z(\omega)$ is obtained from Eq. (3.50)

$$k_z(\omega) = \frac{1}{\pi} \arccos \left[\frac{(\frac{1}{2}\hbar\omega)^2 - E_m^2}{c_m^2} \right],$$

where $c_m^2 = 4\gamma_0^2 \cos(\pi \frac{m}{n})$ and $E_m^2 = \gamma_0^2 [3 + 2 \cos(2\pi \frac{m}{n})]$. The analytical expression for the absorption coefficient is valid for $\gamma \rightarrow 0$, where Eq. (3.48) is applicable. Furthermore, the expression under the square root in Eq. (3.50) has to be positive.

The dependence of the optical matrix element on nanotube chirality and transition energy E_{ii} is often assumed to indicate the variation in absorption strength.⁵⁸ However, the absorption coefficient also contains the contributions from joint density of electronic states. Here, the different contributions to $\alpha(\omega)$ in Eq. (3.49) are discussed. Furthermore, the dependence of the absorption intensities of band-to-band transitions on nanotube chirality is investigated.

Absorption spectra

Figure 3.28 shows absorption spectra of the $(8, 8)$ metallic armchair, $(13, 0)$ semiconducting zigzag, $(10, 5)$ semiconducting, and $(9, 6)$ metallic chiral nanotube. The pronounced peaks in the spectra, denoted as Van Hove singularities, correspond to band-to-band transitions from valence to conduction band with the same m , according to the selection rule for parallel polarized light. The peaks in the spectra of the $(8, 8)$ nanotube in Fig. 3.28 (full lines) stem from transitions between bands with $m = 7, 6, 5$ and 4 when going from lower to higher energies. The selection rules in armchair nanotubes ($k_z = 0$, $m = 0$ and $m = n$) reduce the number of peaks compared to the calculation with constant matrix elements (dashed lines). Transitions with $m = 3, 2$ and 1 do not appear since for $m < \frac{n}{2}$ the band extrema are at the Γ -point (Fig. 3.16a), where the optical matrix element is zero. Similarly, optical transitions between the valence and conduction band crossing at the Fermi level are forbidden, which is known as the optical band gap of armchair tubes.

In the spectrum of the $(13, 0)$ zigzag nanotube eight peaks ($m = 9, 8, 10, 7, 11, 12, 13$ and 6 with increasing energy) can be seen. Transitions that are higher in energy are not forbidden, but very weak due to the E^{-2} dependence of the absorption coefficient, see Eq. (3.51). As discussed in Sec. 3.3.3, the band structure of a zigzag nanotube exhibits minima for $m > \frac{n}{2}$ and maxima $m < \frac{n}{2}$

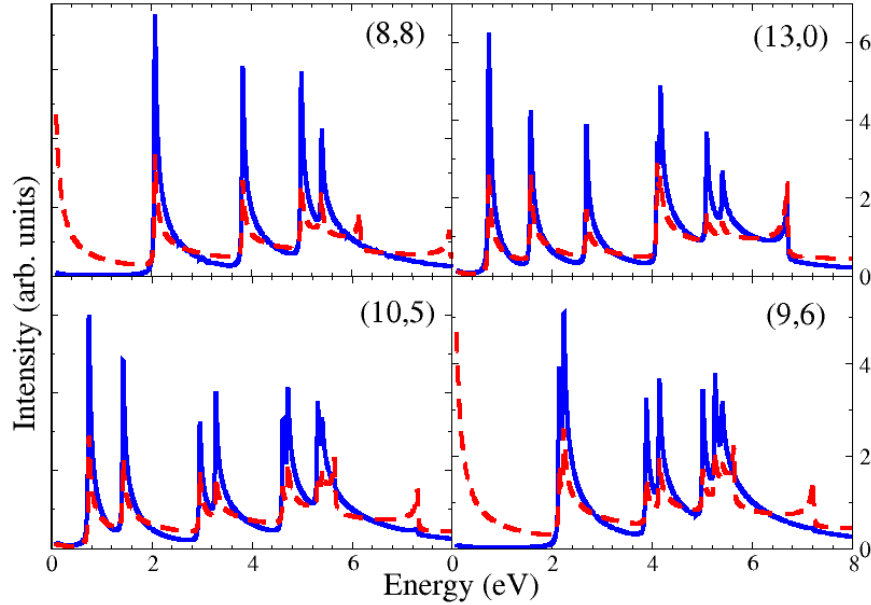


Figure 3.28: Optical absorption of the (8,8) armchair, (13,0) zigzag, (10,5) semiconducting, and (9,6) metallic chiral nanotubes. The solid lines are calculated using the optical matrix element from Eq. (3.26). The dashed lines show the absorption given only by the JDOS. Here, the matrix element is set to $M_z(\mathbf{k}) = 1$. The four nanotubes have a similar diameter $d \approx 1$ nm. The parameters needed for the evaluation of Eq. (3.49) are used in agreement with experimental results and previous theoretical investigations $\gamma_0 = -2.7$ eV, $\gamma = 20$ ps $^{-1}$, and $M_c = 1$.^{46,58}

at the nanotube Γ point, see Fig. 3.16b. As a direct consequence, the transition energy increases strongly from $E_{\frac{n}{2}}$ to $E_{\frac{n}{2}-1}$ resulting in weak intensities of transitions with $m < \frac{n}{2}$.

Chiral nanotubes have no additional symmetry-imposed selection rules besides $\Delta m = 0$. It is controversial whether results obtained for the higher-symmetry armchair and zigzag tubes such as the existence of an optical gap, see the (8,8) tube in Fig. 3.28, can be extended to chiral tubes. Figure 3.28 demonstrates that including the optical matrix elements of chiral tubes leads to similar conclusions about the absorption spectra as for achiral tubes. In particular, the absorption diminishes for the bands crossing at the Fermi level in metallic nanotubes (optical gap) as can be seen for the (9,6) tube in Fig. 3.28. Also, the transitions originating from maxima rather than minima in the electronic band structure are strongly suppressed (for comparison, see the full and dashed lines for the (10,5) and the (9,6) tube in Fig. 3.28). These transitions are very high in energy (> 6 eV) and are strictly zero in armchair tubes. The optical gap in zigzag nanotubes can also be obtained from the analytic expression for the absorption spectra in Eq. (3.51). The bands crossing at the Fermi level have $m = 2n/3$. Inserting this m into Eq. (3.51) and assuming a linear electronic dispersion close to the Fermi level yields $\alpha(\omega) \propto k_z$. The absorption is weak at the Γ point; then it slowly increases (the factor between α and k_z is small). The $1/\sin$ -type singularities that dominate the transitions with $m \neq 2n/3$ are suppressed.

Comparing the band-to-band absorption peaks for constant matrix elements in Fig. 3.28 (dashed lines) with the full calculation according to Eq.(3.49) (solid lines), it turns out that the peaks are more pronounced when including the optical matrix elements. This can be understood by looking at the k_z dependence of M_z in Fig. 3.19. The magnitude of M_z is maximal at k_z values that correspond to Van Hove singularities. This enhances the absorption probability at the band extrema

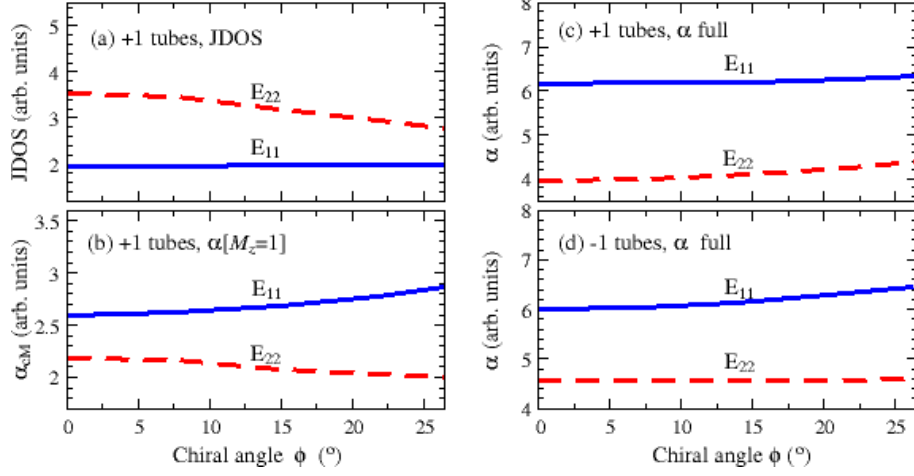


Figure 3.29: Chirality and family dependence of the absorption intensity. a)-c) are shown for +1 nanotubes with $2n_1 + n_2 = 26$ ($d \approx 1.02 - 1.15$ nm). a) Joint density of states for E_{11} (full lines) and E_{22} (dashed); b) absorption intensity α_{cM} when assuming constant matrix elements $M_z(\mathbf{k}) = 1$; c) absorption intensity α including the matrix element M_z in Eq. (3.26). d) Same as c) for -1 nanotubes ($2n_1 + n_2 = 28$ and $d = 1.10 - 1.22$ nm).

and reduces the absorption intensity away from the minima and maxima in the electronic band structure. For zigzag nanotubes, an analytic expression for the energy E_{eq} is found at which the absorption intensity with a constant matrix element equals the full calculation using Eq. (3.26). It reads

$$E_{eq} = -M_c \gamma_0 \sqrt{\sum_m \left[\cos\left(\pi \frac{m}{n}\right) \cos(\pi k_z) - \cos\left(2\pi \frac{m}{n}\right) \right]^2}. \quad (3.52)$$

For a given m the absorption is stronger for $E < E_{eq}$ when including the matrix element and weaker for $E > E_{eq}$.

Chirality and family dependence of the absorption intensity

From the dependence of the optical matrix elements on nanotube family and chiral angle, shown in Fig. 3.18, one might expect a decrease in absorption intensity with chiral angle for the first transition E_{11} of +1 nanotubes, but an increase for -1 tubes. However, this turns out to be incorrect: $\alpha(\omega)$ always increases with the chiral angle for the first two optical transitions.

Figure 3.29a-c illustrates how the different contributions to $\alpha(\omega)$ in Eq. (3.49) combine to the overall chirality dependence of the optical absorption for +1 semiconducting tubes. The joint density of states in +1 tubes is nearly constant for the E_{11} transition, but decreases with chiral angle for E_{22} , see Fig. 3.29a. This is related to trigonal warping and whether the transitions originate from the left or right of the K point of graphene in the zone-folding approximation, see Sec. 3.3.2. The absorption coefficient α_{cM} corresponding to α with a constant matrix element $M_z(\mathbf{k}) = 1$ is plotted in Fig. 3.29b. In this case, the absorption, is determined by the JDOS divided by the transition frequency ω , see Eq. (3.49). The latter decreases with increasing chiral angle ϕ , since the diameter decreases slightly along a Kataura branch denoted by $2n_1 + n_2 = \text{const.}$ As a result the absorption intensity related to α_{cM} becomes larger with ϕ . The decreasing JDOS of the second Van Hove singularity E_{22} leads to a resulting slight decrease of $\alpha_{cM}(E_{22})$ with chiral angle.

Taking the full expression of the optical matrix element into account for the calculation of the absorption coefficient α , the intensities shown in Fig. 3.29c are obtained. For both transitions, the

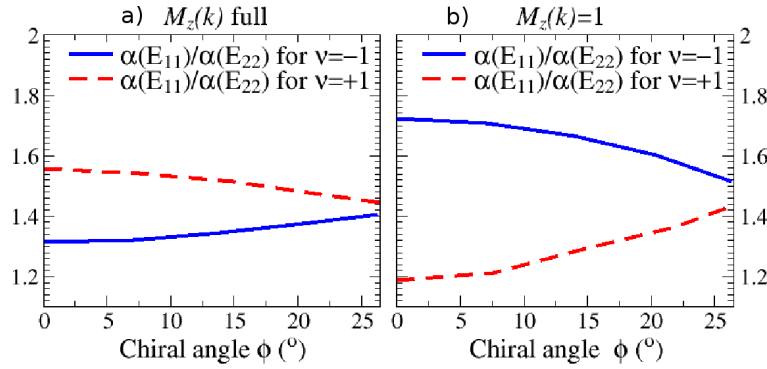


Figure 3.30: Intensity ratios $\alpha(E_{11})/\alpha(E_{22})$ of the first two peaks in the absorption spectra for -1 (full lines) and $+1$ nanotubes (dashed). The ratios in a) are calculated with and in b) without the matrix element, respectively.

intensity increases from the zigzag to the armchair direction, i.e. with increasing chiral angle. The increase of $\alpha(E_{22})$ is larger than of $\alpha(E_{11})$.

Trigonal warping also leads to a family dependence of the absorption coefficient. The comparison to Fig. 3.29d showing the absorption intensities for the -1 tubes, illustrates that the intensity of the first transition $\alpha(E_{11})$ increases strongly whereas $\alpha(E_{22})$ remains approximately constant - in contrast to the behavior of the $+1$ tubes. This can be explained by zone folding. According to Fig. 3.6, the position of the first two transitions for the two semiconducting families originate from opposite sides of the graphene K point.

The family dependence of the absorption coefficient and the importance of the matrix element for understanding the absorption spectra are further illustrated in Fig. 3.30, where the ratio $\alpha(E_{11})/\alpha(E_{22})$ is shown for both semiconducting nanotube families. The intensity ratios obtained for a constant matrix element $M_z(\mathbf{k}) = 1$ (Fig. 3.30b) considerably differ from the ratios obtained by using the \mathbf{k} -dependence of $M_z(\mathbf{k})$, see Fig. 3.30a. The reason is the chirality dependence of the optical matrix element itself. It decreases with ϕ for transitions with Van Hove singularities on the KM high-symmetry line and increases for transitions stemming from the $K\Gamma$ line, see Fig. 3.18. Since the absorption coefficient depends on the squared matrix element, the intensity of transitions between bands originating from the KM line of graphene is reduced with increasing chiral angle, which changes the intensity ratios for the two semiconducting nanotube families in Fig. 3.30.

The intensity in photoluminescence excitation (PLE) experiments I_{PLE} on single-walled carbon nanotubes is given by⁶⁷

$$I_{\text{PLE}} = \alpha \alpha_{\text{rel}} \alpha_{\text{em}} \quad (3.53)$$

with the α , α_{rel} and α_{em} denoting the probability of the incident light to be absorbed by the sample (into E_{22}), the probability that the photoexcited electron relaxes to the emitting state E_{11} , and the probability of its emission. The latter can be assumed to be a constant,⁶⁷ if there are no other efficient relaxation channels from the emitting state. The determination of the relaxation rate is difficult. It is predominately given by electron-phonon coupling, but it also depends on defects in the sample. As a first study, the decay rate is assumed to be approximately constant. Under this assumption, the PLE intensity is already reflected by the absorption intensity α for the second transition E_{22} . As a result, the observed increase of the intensity of the E_{22} for both semiconducting families with increasing chiral angle (Fig. 3.29c-d) is also expected for the PLE intensity. This trend is also observed experimentally, although the increase is much larger than the predicted

11% for +1 and 1% for -1 tubes.^{5,6} The discrepancy comes most likely from the non-constant decay rates from the second to the first subband, a topic that is studied intensively.⁷⁶⁻⁷⁸ Furthermore, excitonic effects can also contribute to a stronger chirality dependence. This open question will be investigated in Sec. 3.6.7. Note also that the absolute intensity for $\alpha(E_{22})$ is by 15% larger for -1 tubes than for the +1 tubes (for $\phi = 0^\circ$). This agrees quite well with the higher experimental PLE intensity of -1 semiconducting tubes.⁶ The explanation for this trend is still a widely open question in current research.⁷⁶

Dispersionless band in zigzag tubes

A pronounced absorption band at high energies which is characteristic for $(n, 0)$ zigzag nanotubes with n even is discussed in the following. Figure 3.31 compares the absorption spectra of the $(10, 0)$ nanotube with two chiral tubes and the $(11, 0)$ zigzag nanotube (with n odd). The spectra of the $(10, 0)$ nanotube contains a characteristic peak at $E = 5.4$ eV that dominates in intensity over all other transitions. It does not have the typical $1/\sqrt{E}$ -form. Within the tight-binding model, $(n, 0)$ zigzag nanotubes with n even have a band $m = \frac{n}{2}$ that is free of dispersion (Fig. 3.16) which gives rise to this intense peak. According to Eq. (3.50), the energy of the $m = 5$ band of the $(10, 0)$ nanotube is $E_{zz}^\pm = \pm 2\gamma_0$. The energy is independent of k_z and leads to an infinite density of states. None of the other nanotubes exhibit such an intense peak. Observing this UV transition would allow to easily identify zigzag nanotubes with n even, discriminating against all other tube chiralities. However, including more neighbors in the tight-binding model or using *ab-initio* techniques to calculate the band structure leads to a small dispersion of the $n/2$ band in $(n, 0)$ tubes. Also, excitonic effects are expected to change the dispersion relation. This will result in a drastic change of these spectra, as will be shown in Sec. 3.6.

In the discussion of the nanotube optical properties, excitons and the curvature of the nanotube wall have been neglected so far. The effect of curvature on the nanotube optical properties is two-fold: First, curvature induces a σ -contribution in the electronic wave functions.^{55,79} The σ -like part of the wave function, however, yields little or no optical absorption intensity. This is best

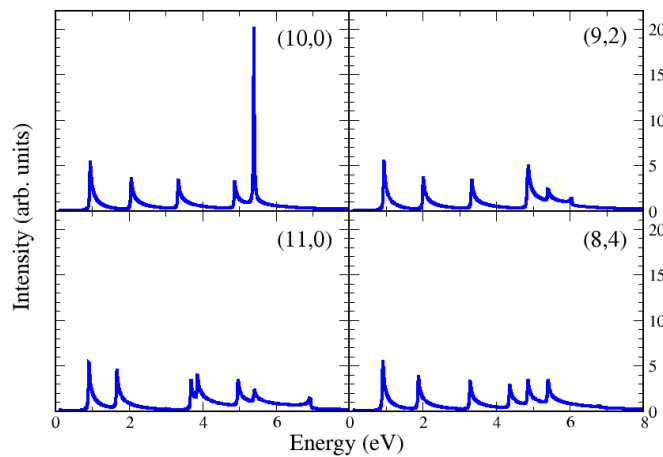


Figure 3.31: Illustration of the pronounced peak at 5.4 eV for $(n, 0)$ zigzag nanotubes with n even. Beside the $(10, 0)$ nanotube, another zigzag tube with n odd and two chiral nanotubes with similar diameter are shown. Only the $(10, 0)$ zigzag nanotube exhibits the pronounced peak at 5.4 eV, the others show a regular peak with the $1/\sqrt{E}$ -form at this energy.

understood for zigzag tubes, because of their high symmetry. The bonding and anti-bonding σ states both transform even under σ_h . Optical absorption is, therefore, forbidden for parallel polarization (see Sec. 3.4.1), which reduces the overall magnitude of $M_z(\mathbf{k})$ if curvature is included. The second effect of curvature is to shift the E_{11} optical transition energies of +1 tubes and the E_{22} transition energies of -1 tubes to smaller energies for small chiral angles^{5,7,55,71,79} (these are the bands with the strongest $\sigma - \pi$ mixing).⁵⁵ Since α depends on E_{ii}^{-2} [Eqs. (3.49) and (3.26)] this shift will increase α for tubes with small chiral angles when curvature is included. The two effects are expected to cancel each other for tubes with a diameter ≈ 1 nm and not to affect the dependence of α on chiral angle.

3.5.2 Rayleigh scattering

In addition to the established methods of optical spectroscopy, such as absorption, photoluminescence and Raman spectroscopy,⁵⁻⁸ Rayleigh scattering has recently emerged as a characterization technique for individual single-walled carbon nanotubes.^{9,80,81} Similarly to other optical methods Rayleigh scattering spectroscopy provides information about the nanotube structure through resonant enhancement of the elastically scattered light when the photon energy matches that of an electronic transition. An advantage of Rayleigh scattering lies in its ability to uncover the optical properties of *individual* nanotubes.⁹ Optical absorption, in contrast, is challenging for individual nanosystems, because the sample (e.g. single tubes, nanoparticles) changes the intensity of the incoming light by approximately 10^{-5} to 10^{-4} . Scattering techniques measure an absolute signal instead of a fractional change. In this respect Rayleigh scattering (elastic light scattering) is similar to Raman scattering (inelastic scattering). However, to obtain the optical properties from a Raman experiment, many spectra with varying laser energy need to be recorded.^{7,8} The most widely used optical technique for studying single-walled carbon nanotubes is photoluminescence.^{5,6} However, it is limited to semiconducting tubes with small diameters. Rayleigh scattering offers rapid data collection, an assignment of (n_1, n_2) chirality, and it is applicable to both semiconducting and metallic tubes. It has been used to confirm the electronic structure of nanotubes (trigonal warping effect in metallic tubes), to study tube-tube interactions, and to characterize individual tubes in combination with transport and electron-diffraction experiments.^{9,80,81} This wealth of experimental studies has not yet been complemented by theoretical work.

In this work, an expression for the Rayleigh scattering cross section per unit length is derived using analytical results for the optical matrix elements of arbitrary (n_1, n_2) nanotubes and transition energies within the tight-binding approximation. The theory is applied to the features of the Rayleigh scattering spectra for metallic and semiconducting nanotubes with diameters of approximately 2 nm, since these nanotubes have been investigated experimentally.⁸⁰ The comparison of tight-binding and DFT calculations has shown that the tight-binding method is suitable for the description of such large nanotubes.⁵⁵ Working within the free-particle model is assumed to already give good insight into the intensity ratio of the double-peaked structure as a consequence of the trigonal warping effect. The inclusion of excitonic effects is expected to modify the Rayleigh line shape, but not to change the characteristic features, such as the enhanced strength of the lower-energy component of the split metallic peaks. This assumption is investigated in Sec. 3.6.9, where excitonic Rayleigh spectra are calculated.

Treating Rayleigh scattering from SWCNTs as electromagnetic scattering from a long cylinder with a diameter small compared to the wavelength of light, the scattering cross section per unit length can be written as^{9,45} [Eq. (2.58)]

$$\sigma(\omega) \approx \frac{\pi^2}{4c^3} r^4 \omega^3 |\chi(\omega)|^2. \quad (3.54)$$

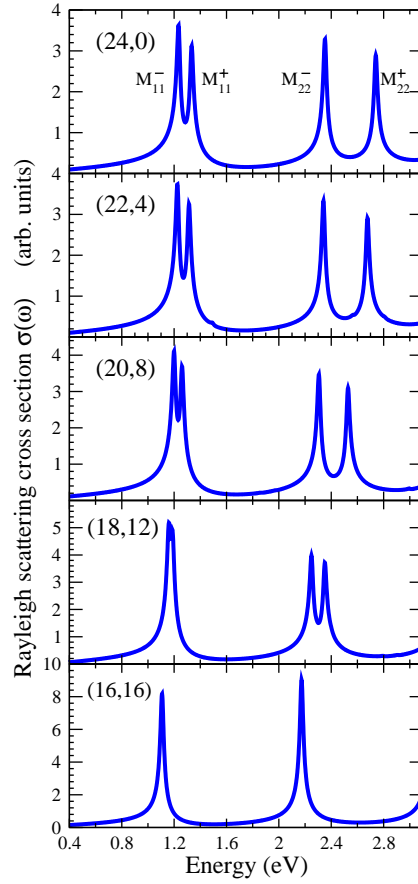


Figure 3.32: Rayleigh spectra of metallic nanotubes with a diameter of approx. 2 nm corresponding to the Kataura branch with $2n_1 + n_2 = 48$. The chiral angle increases from top to bottom. The figure illustrates the peak splitting caused by the trigonal warping effect that diminishes with increasing chiral angle (towards the armchair configuration) and increasing transition energy.^{53,54}

In analogy to the calculations of the absorption coefficient, the Rayleigh scattering cross section is only considered for incident light polarized along the nanotube axis, since this gives the dominant scattering response.⁹ Information about electronic properties of the nanotube enters into the Rayleigh scattering cross section through the frequency-dependent optical susceptibility⁴² $\chi(\omega) = \varepsilon(\omega) - 1$, where $\varepsilon(\omega)$ denotes the dielectric function of the nanotube. It is determined by the square of the linear optical susceptibility $\chi(\omega)$. In this sense, it is similar to the optical absorption, which is also given by $\chi(\omega)$. Unlike absorption, however, Rayleigh scattering has a contribution from the real part of $\chi(\omega)$ and, hence, includes effects from off-resonant optical transitions. This leads to important differences in the characteristics of Rayleigh and absorption spectra, which is discussed below.

Rayleigh scattering from metallic nanotubes

Figure 3.32 shows the four lowest-lying transitions, denoted by M_{11}^- , M_{11}^+ , M_{22}^- , and M_{22}^+ , in metallic carbon nanotubes with a diameter of approximately 2 nm. It illustrates three important features:

- The Rayleigh scattering spectra of metallic nanotubes show a double-peaked structure that arises from the trigonal warping, which describes the deviation of the equi-energy contours

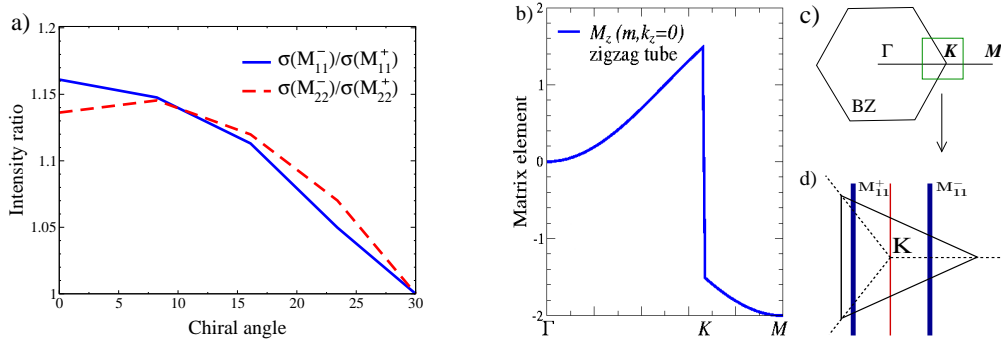


Figure 3.33: a) Intensity ratios of transitions M_{11}^- and M_{11}^+ , and of M_{22}^- and M_{22}^+ as a function of the chiral angle. b) Optical matrix element $M_z(\mathbf{k})$ along the high-symmetry line $\Gamma K M$ of graphene corresponding to confined states of zigzag nanotubes. c) Brillouin zone of graphene with the high-symmetry line $\Gamma K M$. d) Simplified triangular energy contour of graphene around the K point of the Brillouin zone. The deviation from the circle is exaggerated to illustrate the trigonal warping. The vertical lines are the allowed wave vector lines corresponding to the lowest Van Hove singularities of a metallic zigzag nanotube. The dashed lines indicate the three $K M$ -directions. Note that the matrix element $M_z(m, 0)$ has a smaller absolute value on the ΓK - than on the $K M$ -side. This will influence the oscillator strength of transitions. Depending on the side on which the corresponding Van Hove singularity is located with respect to the K point, the transition is expected to be stronger or weaker in intensity.

from circles in the Brillouin zone of graphene around the K point [Fig. 3.33c)]. The triangular shape of these equi-energy contours makes it important on which side of the K point the Van Hove singularities are located, see Sec. 3.3.2. As a result, there is peak splitting in the spectra of metallic nanotubes, as already known from absorption measurements.⁴⁶ The width of the splitting depends strongly on the chiral angle: It is maximal for zigzag tubes and decreases with increasing chiral angle, with no splitting present for the arm-chair configuration.^{53,54} Figure 3.28 also confirms that the trigonal warping effect is larger at higher transition energies, as can be seen in the wider separation of the third and fourth peak.

- The relative intensities of the Rayleigh peaks have a distinctive behavior. For all nanotubes within a given Kataura branch, the lower-lying transition in the double-peaked structure is stronger in intensity, i.e. M_{11}^- is stronger than M_{11}^+ , and M_{22}^- is stronger than M_{22}^+ .
- The Rayleigh spectra exhibit a slight enhancement of the scattering cross section at lower photon energies, see also Fig. 3.34.

The characteristic behavior of relative intensities in the double-peak structure of metallic tubes in Fig. 3.28 has also been observed experimentally. The lower-energy peak of the split transition is always greater in intensity than the upper one.⁸¹ Figure 3.33 demonstrates that this intensity difference decreases with the increasing chiral angle, connected to the decrease of the trigonal warping effect. At first sight, this seems to contradict the dependence of the density of states on chiral angle that has been shown to be enhanced for higher-lying transitions.⁵³ However, an explanation for the peak ratio is found in the interplay of the density of states with the optical matrix element $M_z(\mathbf{k})$. The oscillator strength of optical transitions is determined by both the density of states and the optical matrix element.^{72,73} Especially for studies of the chirality dependence, it is important to consider the influence of the matrix element $M_z(\mathbf{k})$. As can be seen in Fig 3.33, its absolute value is higher on the $K M$ - than on the ΓK -side. The Van Hove singularities located at the ΓK -side lead to transitions at a higher energy,⁵³ see Fig. 3.33c. Since the absolute

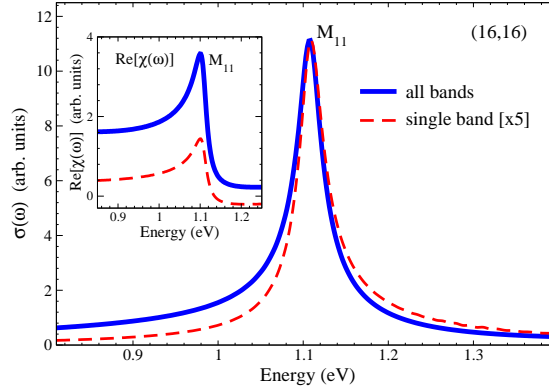


Figure 3.34: Asymmetry towards lower energies in the Rayleigh spectra. The cross section is plotted for the M_{11} transition of the (16,16) armchair nanotube. Single-band and all-band results are compared (the maxima are normalized to the value of the M_{11} peak in the all-band calculation) to illustrate that the enhancement of the Rayleigh scattering cross section at lower energies occurs only when the non-resonant response is included. The inset shows the corresponding real part of the susceptibility $\chi(\omega)$. Constructive interference of the non-resonant contribution in the low-energy wing of the resonant response accounts for the observed asymmetry.

value of the matrix element is smaller on the ΓK branch, and since the cross section depends on the square of the matrix element, the corresponding transition intensities are weaker, despite the enhanced density of states.

In agreement with experimental results,^{9,80,81} the Rayleigh peaks in Fig. 3.28 have an asymmetry towards lower energies, i.e. the scattering cross section is enhanced at lower energies. To see this more clearly, in Fig. 3.34 the cross section $\sigma(\omega)$ for the first (M_{11}) transition of the (16,16) armchair nanotube is plotted on an expanded frequency scale. The dotted-dashed line shows results from a single-band calculation. The characteristic asymmetry is observed only when all subband transitions are taken into consideration (solid line).

An explanation for the enhanced Rayleigh scattering cross section at lower energies lies in the influence of the real part of the optical susceptibility $\chi(\omega)$. It has a long tail on the low energy side of each transition, since the wing of the resonant response adds in phase with the non-resonant background below the resonance, but interferes destructively above the resonance. The inset in Fig. 3.34 illustrates the behavior around the M_{11} transition of the (16,16) nanotube. The off-resonant contributions of higher subband transitions yield a background (see inset in Fig. 3.34) that produces the observed asymmetry of Rayleigh peaks, as shown in Fig. 3.34.

This interference effect stemming from the non-resonant background also leads to a slight red-shift in the center of the Rayleigh peaks compared with the center of the absorption line, the latter being determined solely by the imaginary part of the optical susceptibility, see Fig. 3.35. The shift is typically about 10 meV in magnitude and is largely independent of the chiral angle. Note that a similar importance of the overlap between the real and imaginary part of the optical susceptibility has also been shown for Raman spectra.⁴

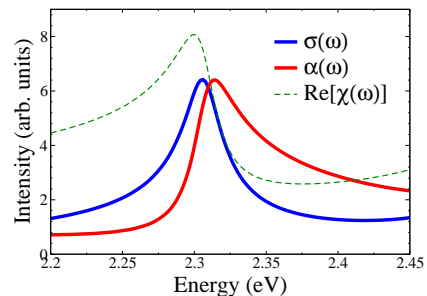


Figure 3.35: Red-shift of Rayleigh peaks.

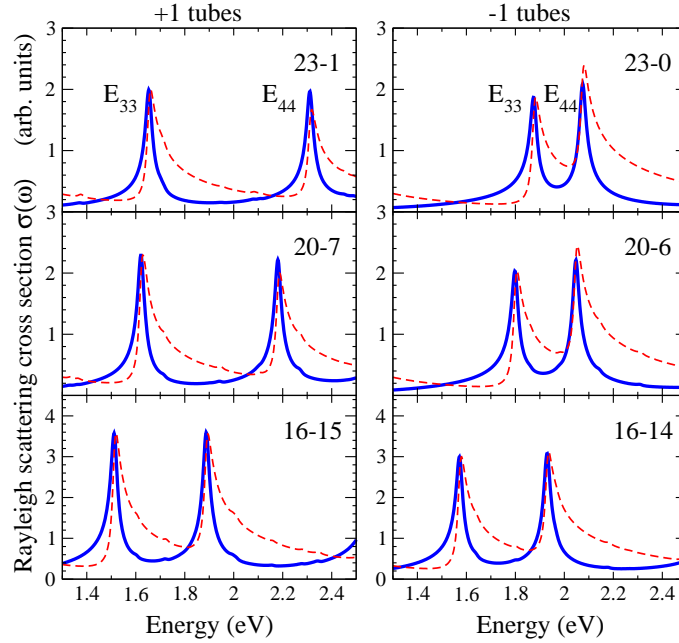


Figure 3.36: Rayleigh spectra of semiconducting +1 and -1 nanotubes with a diameter of approx. 2 nm corresponding to the Kataura branch⁴ with $2n_1 + n_2 = 48$. The chiral angle increases from top to bottom. The third E_{33} and fourth E_{44} transitions are shown. Note that for -1 tubes the energetically lower transition E_{33} is weaker in intensity, whereas +1 tubes show an inverse behavior. The figure also illustrates the corresponding absorption spectra (dashed line) with the characteristic Van Hove singularities. The absorption coefficient is normalized to the value of the E_{33} peak in the corresponding Rayleigh spectra.

Rayleigh scattering from semiconducting nanotubes

Figure 3.36 compares absorption and Rayleigh spectra showing the third and fourth transition E_{33} and E_{44} in semiconducting carbon nanotubes with an approximately constant diameter of about 2 nm. Figure 3.36 shows that for -1 semiconducting tubes, the third transition E_{33} is weaker in intensity than E_{44} . In contrast, the +1 semiconducting tubes have the opposite behavior: E_{33} is slightly stronger in intensity. This different family behavior cannot be explained by considering only the joint density of states (JDOS), which has been shown to be generally enhanced for energetically higher transitions.^{53,72} As a result, the transitions E_{33} is expected to be smaller in intensity than E_{44} independently of the tube family - in contrast to the observation for metallic tubes in Fig. 3.32.

An explanation can be found by taking the optical matrix element $M_z(\mathbf{k})$ into account. Depending on the side, on which the Van Hove singularity is located with respect to the K point, the transition intensity is enhanced or reduced, see Fig. 3.37. The observed different family behavior of relative intensities arises from the fact that the energy minima for +1 and -1 tubes for a given transition E_{ii} are located on opposite sides of the graphene K point.^{4,72} For +1 tubes the E_{33} Van Hove singularity originates from the KM -line, whereas E_{44} stems from the ΓK -line, see Fig. 3.6.

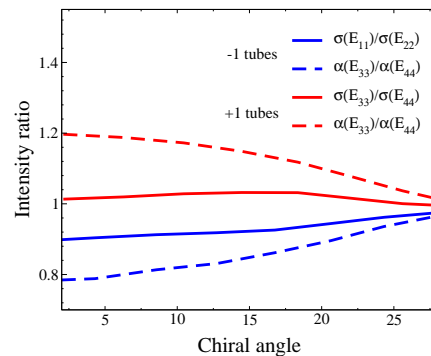


Figure 3.37: Chirality dependence of intensity ratios.

The resulting enhancement of E_{33} with respect to E_{44} , since the matrix element $M_z(\mathbf{k})$ is larger on the KM -side, see Fig. 3.33b. The difference in intensity for +1 tubes, however, is much smaller than for -1 tubes. This can be traced back to the geometry factor $\omega^3 r^4$ in Eq. (3.54) that enhances the energetically higher transition E_{44} leading to a reduction of the intensity differences for +1 tubes.

3.5.3 Summary

The optical absorption coefficient $\alpha(\omega)$ and the Rayleigh scattering cross $\sigma(\omega)$ have been calculated for arbitrary metallic and semiconducting single-walled carbon nanotubes within the free-particle picture. The optical oscillator strength is shown to decrease with the chiral angle. In general, absorption is weaker for +1 than for -1 nanotube families. This chiral angle and nanotube family dependence originates from combined effects of the joint density of electronic states and the optical matrix element. Furthermore, the intensity ratios of the four lowest-lying peaks in the absorption and Rayleigh spectra have been explained by the different behavior of the optical matrix element along the two high-symmetry lines $K\Gamma$ and KM . The consideration of all allowed subband transitions has turned out to be crucial for understanding the characteristic features of a Rayleigh spectrum. The lineshape of Rayleigh peaks exhibits stronger response at lower energies as a consequence of the non-resonant contributions to the optical susceptibility of higher subband transitions. The latter also leads to a slight red-shift in the Rayleigh spectra compared to the Van Hove singularities in the absorption spectra.

The presented results are in good agreement with experimental data. As will be shown in Sec. 3.6.9, excitonic effects enhance the investigated features in the Rayleigh scattering and absorption spectra leading to a better agreement with the experiment.⁸²

3.6 Excitonic effects

The calculations of the absorption coefficient and the Rayleigh scattering cross section, presented in the last section, are extended by including the Coulomb interaction. The electron-electron and electron-hole coupling leads to a renormalization of the free-particle energies and to a formation of excitons - bound electron-hole states. A large part of the spectral weight is transformed from the free-particle Van Hove singularities to excitonic Lorentzians. As a result, the inclusion of Coulomb interaction is crucial to correctly describe the optical absorption. In this section, the excitonic effects are investigated as a function of the chiral angle, the diameter, and the family index in both absorption and Rayleigh scattering spectra. Furthermore, the splitting of excitonic states in dark and bright excitons as a consequence of the Coulomb intervalley mixing is discussed.

3.6.1 Coulomb interaction

Over the last years, different approaches were developed to model the Coulomb interaction in carbon nanotubes. In 1996, Ando⁸³ calculated the excitonic excitations within the screened Hartree-Fock approximation. In 1997, Egger⁸⁴ developed an effective low-energetic theory for CNTs taking into account that Coulomb interaction can lead to a Luttinger liquid behavior in one-dimensional structures. The studies by Petersen, Kane, and Mele^{85,86} started from a variational approach, which is based on the minimization of the energy applying a test wave function with free parameters. This approach led to a resolution of the discrepancy between experiment and theory with respect to the transition energy ratios, also known as the ratio problem.⁸⁶ Spataru and Louie¹², furthermore Chang, Ruini, and Molinari¹⁵ performed first-principle calculations to describe excitonic properties in carbon nanotubes. They incorporated the Coulomb interaction within the Bethe-Salpeter equation combined with the GW method. The latter is based on the density functional theory and allows the incorporation of the renormalized free-particle energies due to the electron-electron interaction. It is a powerful method, but numerically very demanding. Hence, the calculation of excitonic properties is only possible for certain selected nanotubes with small radii and small unit cells, i.e. mainly achiral tubes. Perebeinos, Avouris,¹³ and Saito¹⁷ used an intermediate level of theory by combining the Bethe-Salpeter equation with the TB approach. They found scaling laws for excitonic binding energies, their size, and oscillator strength in dependence of diameter. Finally, Capaz¹⁶ used a symmetry-based variational method within the effective mass and envelope function approximation using TB wave functions to investigate the chirality dependence of excitonic properties.

In this work, microscopic calculations of the excitonic susceptibility $\chi(\omega)$ are performed by a novel approach combining the density-matrix formalism with the zone-folded tight-binding wave functions. The derived Bloch equations allow the study of CNTs of arbitrary chiral index. A further advantage of this approach is the straightforward inclusion of many-body interactions, such as exciton-phonon coupling and non-linear effects.

Excitonic Bloch equation

The Hamilton operator of the excitonic CNT system consists of three parts according to Eq. (2.32)

$$H = H_{0,c} + H_{c-f} + H_{c-c} = \sum_l \varepsilon_l a_l^\dagger a_l + i \frac{e_0 \hbar}{m_0} \sum_{l,l'} M_z^{vc} A_z(t) a_l^\dagger a_{l'} + \frac{1}{2} \sum_{l_1, l_2, l_3, l_4} V_{l_3, l_4}^{l_1, l_2} a_{l_1}^\dagger a_{l_2}^\dagger a_{l_4} a_{l_3}. \quad (3.55)$$

In this section, excitonic properties are in the focus of investigation. Therefore, the electron-phonon interaction is neglected. However, it is taken into account in Sec. 3.7. The free electron contribution $H_{0,c}$ contains the single-particle energy ε_l calculated within the tight-binding approach.^{46,53,55,71} The second part of Eq. (3.55) H_{c-f} describes the electron-light interaction which is determined by the z -component of the vector potential $A_z(t)$ and the optical matrix element^{58,72} M_z^{vc} , calculated in Sec. 3.4.1. The third contribution is the Coulomb interaction H_{c-c} . The characteristics of the Coulomb matrix elements $V_{l_3,l_4}^{l_1,l_2}$ have already been discussed in Sec. 3.4.2. They are derived in detail in App. C.1.

Here, the free-particle Bloch equation for the microscopic polarisation $p_{\mathbf{k}}(t)$ from Eq. (3.45) is extended to Coulomb interaction. Using the Heisenberg equation of motion from Eq. (2.33), and the Hamilton operator from Eq. (3.55) leads to

$$i\hbar\dot{p}_{\mathbf{k}} = [p_{\mathbf{k}}, H] = (\varepsilon_{c\mathbf{k}} - \varepsilon_{v\mathbf{k}})p_{\mathbf{k}} + \sum_{ABC} (V_{BC}^{c\mathbf{k}A} \langle a_{v\mathbf{k}}^+ a_A^+ a_C a_B \rangle - V_{v\mathbf{k}D}^{AB} \langle a_A^+ a_B^+ a_C a_{c\mathbf{k}} \rangle) \quad (3.56)$$

with A, B, C as compound indices containing the wave vector \mathbf{k}_i and the band index $\lambda_i = c, v$ ($i = A, B, C$). To obtain a closed set of equations, the two-particle density matrices are factorized into single-particle density matrices

$$\langle a_1^+ a_2^+ a_3 a_4 \rangle = \langle a_1^+ a_4 \rangle \langle a_2^+ a_3 \rangle - \langle a_1^+ a_3 \rangle \langle a_2^+ a_4 \rangle. \quad (3.57)$$

This corresponds to the Hartree-Fock or mean-field approximation, where all correlations between the carriers are neglected, see Sec. 2.4. The excitonic effects, however, can already be described on the Hartree-Fock level. Auger contributions are not considered here. They are essential for the description of relaxation processes and the corresponding life times.⁸⁷

Performing the sums in Eq. (3.56) within the random phase approximation (see Sec. 2.4.1) and exploiting the limit of linear optics, i.e. the valence (conduction) band is assumed to be full (empty), leads to the excitonic carbon nanotube Bloch equation⁸⁸ for the microscopic polarisation

$$\dot{p}_{\mathbf{k}}(t) = -i\Delta\omega_{\mathbf{k}}p_{\mathbf{k}}(t) + g_{\mathbf{k}}(t) - \gamma p_{\mathbf{k}}(t). \quad (3.58)$$

The phenomenological damping parameter γ accounts for the dephasing. It results from neglected many-particle interactions, such as electron-phonon coupling. Its value determines the linewidth in the calculated spectra, but has no influence on the position of the peaks. The structure of the Bloch equation has not changed after including the Coulomb interaction. The latter only leads to a renormalization of the free-particle contributions. However, these contributions are responsible for a considerable change in the optical properties of carbon nanotubes.

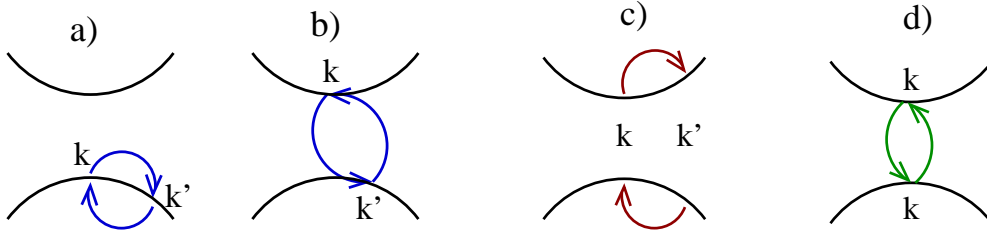


Figure 3.38: Illustration of Coulomb contributions leading to a) - b) the renormalization of the free-particle energy due to the repulsive electron-electron interaction, c) the formation of excitons due to the attractive electron-hole interaction, and d) the depolarization contribution, characterized by zero momentum transfer, i.e. $\mathbf{k} = \mathbf{k}'$

The microscopic polarization $p_{\mathbf{k}}(t)$ is determined by the renormalized energy transition frequency

$$\Delta\omega_{\mathbf{k}} = (\omega_{c\mathbf{k}} - \omega_{v\mathbf{k}}) + \frac{1}{\hbar} \sum_{\mathbf{k}'} V_{ren}(\mathbf{k}, \mathbf{k}') \quad (3.59)$$

and the excitonic Rabi frequency

$$g_{\mathbf{k}}(t) = \frac{e_0}{m_0} M_z^{cv}(\mathbf{k}) A_z(t) - \frac{i}{\hbar} \sum_{\mathbf{k}'} \left[V_{exc}(\mathbf{k}, \mathbf{k}') p_{\mathbf{k}'} + \tilde{V}_{exc}(\mathbf{k}, \mathbf{k}') p_{\mathbf{k}'}^* \right]. \quad (3.60)$$

For details, see the derivation of the Bloch equations presented in App. A. The second term $\propto p_{\mathbf{k}'}^*$ vanishes within the rotating wave approximation (RWA). However, in Sec. 2.4.1, it was shown that the RWA is only advantageous if the energy dispersion is small or if only the area around the band gap is of importance. Since the entire Brillouin zone are considered and the energy dispersion in nanotubes can reach values up to several eV, the theory is evaluated beyond the RWA and the terms $\propto p_{\mathbf{k}'}^*$ are taken into account.

The Coulomb contributions leading to a \mathbf{k} -dependent renormalization of the free-particle energy $\varepsilon_{\mathbf{k}}$ are given by

$$V_{ren}(\mathbf{k}, \mathbf{k}') = V_{v\mathbf{k}, v\mathbf{k}'}^{v\mathbf{k}', v\mathbf{k}} - V_{v\mathbf{k}', c\mathbf{k}}^{c\mathbf{k}, v\mathbf{k}'} \quad (3.61)$$

The involved matrix elements are illustrated in Fig. 3.38a-b with c, v denoting the conduction and the valence band, respectively. Both intra- and interband processes contribute to the energy renormalization, which is discussed below. The Coulomb matrix elements are given by

$$V_{\mathbf{k}_3, \mathbf{k}_4}^{\mathbf{k}_1, \mathbf{k}_2} = \sum_{i, j} \gamma_{\mathbf{k}_1, \mathbf{k}_2, \mathbf{k}_3, \mathbf{k}_4}^{ij} \delta_{\mathbf{k}_1 - \mathbf{k}_3, \mathbf{k}_4 - \mathbf{k}_2} V^{ij}(\mathbf{q}) \quad (3.62)$$

with $\gamma_{\mathbf{k}_1, \mathbf{k}_2, \mathbf{k}_3, \mathbf{k}_4}^{ij}$ as the product of TB coefficient functions (i, j label the graphene unit cell atoms A, B , \mathbf{k}_i is a compound index containing the band index and the wave vector) and the Fourier transform of the Coulomb potential $V^{ij}(\mathbf{q})$. For more details, see Sec. 3.4.2 and App. C.1.

The renormalization of the Rabi-frequency is determined by the following Coulomb contributions

$$V_{exc}(\mathbf{k}, \mathbf{k}') = V_{c\mathbf{k}', v\mathbf{k}}^{c\mathbf{k}, v\mathbf{k}'} - V_{v\mathbf{k}, c\mathbf{k}'}^{c\mathbf{k}, v\mathbf{k}'} \quad (3.63)$$

$$\tilde{V}_{exc}(\mathbf{k}, \mathbf{k}') = V_{v\mathbf{k}', v\mathbf{k}}^{c\mathbf{k}, c\mathbf{k}'} - V_{v\mathbf{k}, v\mathbf{k}'}^{c\mathbf{k}, c\mathbf{k}'} \quad (3.64)$$

The Coulomb matrix elements from Eq. (3.63) are illustrated in Fig. 3.38c-d. The first terms in Eqs. (3.63)-(3.64) describe Coulomb processes with a momentum transfer $\mathbf{q} = \mathbf{k} - \mathbf{k}'$. They lead to the formation of excitons, which change the free-particle spectra considerably, as shown in Fig. 3.39. The essential contribution stems from the process illustrated in Fig. 3.38c. In contrast to all other contributions, the second terms in Eqs. (3.63)-(3.64) stem from the Hartree part of the Hartree-Fock factorization. They are often called depolarization terms. In contrast to the Fock terms, they include no momentum transfer, i.e. $\mathbf{q} = 0$.

Solving the equation of motion for the microscopic polarisation $p_{\mathbf{k}}$ from Eq. (3.58) allows the calculation of the excitonic susceptibility $\chi(\omega)$, see Eq. (2.57). Then, the excitonic absorption coefficient $\alpha(\omega)$ and the Rayleigh scattering cross section $\sigma(\omega)$ can be determined for nanotubes of arbitrary chiral indices (n_1, n_2) . Figure 3.39 shows the absorption spectra of the (8,4) chiral nanotube illustrating the different contributions to the microscopic polarization. The free electron spectra are characterized by Van Hove singularities (red line), as shown in the previous

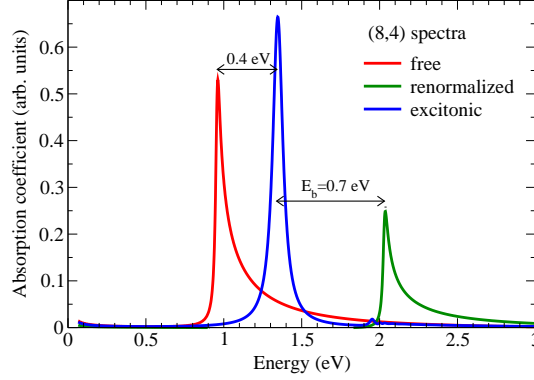


Figure 3.39: Absorption spectra of the (8,4) nanotube (for reasons of clarity only the first transition E_{11} is shown). Coulomb interaction leads to i) band gap renormalization due to the electron-electron coupling (blue shift of the Van Hove singularity) and ii) formation of excitons due to the electron-hole interaction (red-shift of the renormalized Van Hove singularity and reshaping into a Lorentzian), see also Hirtschulz et al.⁸⁸

section. Including the renormalization of the band gap due to the electron-electron interaction according to Eq. (3.59) leads to a relatively large blue shift (green line). The reduction in intensity arises from the ω^{-1} dependence of the absorption coefficient, see Eq. (2.57). After including the electron-hole coupling from Eq. (3.60), the renormalized Van Hove singularity is red-shifted and reshaped to a Lorentzian (blue line) resulting in a net blue-shift and an increased oscillator strength. The excitonic binding energy E_b of 0.7eV can be easily determined as the difference between the peak with and without electron-hole coupling. The spectral weight is almost completely transferred to the excitonic excitation. The renormalized free band-edge can still be seen, but it is largely suppressed. However, in metallic nanotubes it will turn out to still play an important role, see Sec. 3.6.8. The width of the peak is determined by the phenomenological parameter¹² $\gamma = (0.0125/\hbar)$ eV in Eq. (3.58). Excitonic effects do not lead to a visible broadening of the peak. However, it is difficult to resolve the small width, since the current calculation is performed beyond the RWA approximation and the time grid needs to be very precise.

3.6.2 Band gap renormalization

The Coulomb contribution $V_{ren}(\mathbf{k}, \mathbf{k}')$ from Eq. (3.59) can be grouped with the free-carrier contribution $\propto (\omega_{c\mathbf{k}} - \omega_{v\mathbf{k}})$. Both terms are driven by the microscopic polarisation $p_{\mathbf{k}}$ with the same wave vector \mathbf{k} . Hence, $V_{ren}(\mathbf{k}, \mathbf{k}')$ determines the \mathbf{k} -dependent strength of the band gap renormalization. Inserting the involved Coulomb matrix elements from Eqs. (C.12)-(C.13) yields

$$V_{ren}(\mathbf{k}, \mathbf{k}') = \text{Re} \left[\frac{e^*(\mathbf{k}')e(\mathbf{k})}{|e(\mathbf{k}')e(\mathbf{k}')|} V^{AB}(\mathbf{q}) \right] \quad (3.65)$$

with $\mathbf{q} = (q_z, \Delta m)$ and $e(\mathbf{k}) = \sum_{i=1}^3 \exp(i\mathbf{k} \cdot \mathbf{b}_i)$ where \mathbf{b}_i are the nearest-neighbor tight-binding vectors, see Sec.2.3.2. The Kronecker delta from Eq. (3.62) describing the momentum conservation requires $q_z = k'_z - k_z$ and $\Delta m = m' - m$. Furthermore, the Fourier transform of the Coulomb potential

$$V^{ij}(\mathbf{q}) = \frac{1}{N_0} \sum_{\hat{\mathbf{r}}} e^{i\mathbf{q} \cdot \hat{\mathbf{r}}^{ij}} V^{ij}(|\hat{\mathbf{r}}^{ij}|) \quad (3.66)$$

has been introduced. As discussed in Sec. 3.4.2, the Coulomb potential $V^{ij}(|\hat{\mathbf{r}}^{ij}|)$ is parametrized by the Ohno potential,⁶² see Eq. (3.30). Figure 3.39 shows the band gap renormalization arising

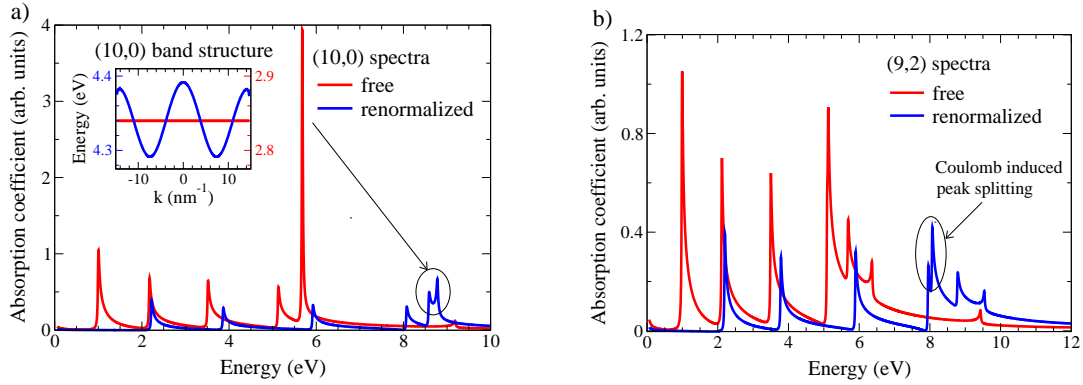


Figure 3.40: Illustration of the importance of the band gap renormalization for a) the highly symmetric (10, 0) zigzag tube and the (9, 2) chiral tube. The dispersionless band with $m=5$ in the (10, 0) tube gains a small oscillating dispersion after the inclusion of the electron-electron coupling, as shown in the inset. As a result, the pronounced peak with the high intensity splits up into two peaks with a similar coupling strength. A similar effect can be seen in the absorption spectra of the (9, 2) nanotube.

from $V_{ren}(\mathbf{k}, \mathbf{k}')$ for the (8, 4) nanotube (green line). The free-particle Van Hove singularity (blue line) is blue-shifted by 1.1 eV, which is about 100% of the free band gap. This is a sign for the strong Coulomb interaction in carbon nanotubes. The energy renormalization always leads to a blue-shift within linear optics, since the intraband matrix elements $V_{v\mathbf{k},v\mathbf{k}'}^{vk',vk}$ are always larger than the corresponding interband matrix elements $V_{vk',ck}^{ck,vk'}$, see Eq. (3.61).

Furthermore, the band gap renormalization has a drastic effect on certain nanotubes. In Sec. 3.5.1, it was shown that $(n, 0)$ zigzag nanotubes with n even have a pronounced peak at higher energies, which dominates the overall intensity in the absorption spectra. This effect was explained by a specific feature in the band structure of these nanotubes. It was shown that the subband with $m = n/2$ is free of dispersion within the tight-binding approximation. This leads to a formally infinite density of states resulting in a very pronounced peak in the absorption spectra of these zigzag tubes. Additionally, a degeneracy with the band $m = n$ further increases the intensity of the peak. However, Coulomb effects essentially change this picture due to a slight change in the dispersion of the subband $m = n/2$, see the renormalized band structure of the (10, 0) tube in the inset of Fig. 3.6.2a. The gain of dispersion in the $n/2$ subband results in a finite density of states and a much smaller intensity of the corresponding peak, which does not distinguish any more from other transitions in the spectra. Moreover, this slight change in dispersion also accounts for the lifting of the mentioned degeneracy with the band $m = n$, leading to a peak splitting, shown in Fig. 3.6.2a. A similar effect can be observed in the spectra of other nanotubes, where the energy renormalization often enlarges the distance between peaks. As a result, energetically close transitions can be resolved in the spectra after the Coulomb interaction is included, as exemplary shown for the (9, 2) nanotube in Fig. 3.6.2b.

3.6.3 Excitons

In the previous section it was shown that the repulsive electron-electron part of the Coulomb interaction leads to a renormalization of the transition energy (band gap renormalization). Here, the attractive part of the Coulomb interaction is discussed. Its inclusion leads to the formation

of bound electron-hole states accompanied by a red-shift due to the exciton binding energy. Furthermore, excitonic spectra are characterized by symmetric Lorentzians, see Fig. 3.39. This considerable change of optical properties is due to the attractive Coulomb contributions $V_{exc}(\mathbf{k}, \mathbf{k}')$ and $\tilde{V}_{exc}(\mathbf{k}, \mathbf{k}')$ from Eqs. (3.63)-(3.64). They can be grouped with the carrier-field interaction $\propto \frac{e_0}{m_0} M_z^{vc}(\mathbf{k}) A_z(t)$ [Eq. (3.60)] contributing to the renormalization of the Rabi frequency. This attractive Coulomb interaction causes an additional internal field, which renormalizes the external field given by the vector potential $A_z(t)$. These contributions are driven by the microscopic polarization $p_{\mathbf{k}'}$ with $\mathbf{k}' = \mathbf{k} + \mathbf{q}$, where \mathbf{q} describes the involved momentum transfer during the process.

Inserting the Coulomb matrix elements from Eq. (C.14) and Eq. (C.16) into Eq. (3.63) yields for the first part of the attractive electron-hole interaction

$$V_{exc}(\mathbf{k}, \mathbf{k}') = \underbrace{\frac{1}{2} \left[V^{AA}(\mathbf{q}) + Re \left(\frac{e^*(\mathbf{k}')e(\mathbf{k})}{|e(\mathbf{k}')e(\mathbf{k}')|} V^{AB}(\mathbf{q}) \right) \right]}_{\text{excitonic part}} - \underbrace{\frac{1}{2} [V^{AA}(0) - Re V^{AB}(0)]}_{\text{depolarization part with } \mathbf{q}=0}. \quad (3.67)$$

The first term is the dominant contribution for the formation of excitons. The corresponding Coulomb matrix elements describe the interaction between an electron in the conduction band and a hole in the valence band, see Fig. 3.38c. They lead to the formation of bound electron-hole states. The formation of excitons is accompanied by a considerable red-shift, which partly cancels the blue-shift arising from the band gap renormalization. This shift corresponds to the excitonic binding energy. In comparison to free-particle spectra, there is still a notable net-blue shift. In the case of the chiral (8, 4) nanotube, shown in Fig. 3.39, the excitonic binding energy is 0.7 eV and the net-blue shift is 0.4 eV. These values strongly depend on the surrounding medium. In Fig. 3.39, the absorption spectra are calculated for the dielectric background constant $\epsilon_{bg} = 1$ corresponding to air or vacuum as surrounding medium. In the next section, the dependence of the excitonic position and binding energy on ϵ_{bg} is discussed in detail.

The above process involves a momentum transfer \mathbf{q} , which can be carried out as linear momentum along the nanotube axis ($q_z = k'_z - k_z$) or as angular momentum connected to intersubband processes ($\Delta m = m' - m$). The combined electron-hole wave vector $\mathbf{Q} = \mathbf{k}_e + \mathbf{k}_h$ corresponds to the wave vector of the involved photon, which is negligibly small, i.e. $\mathbf{Q} \approx 0$. In contrast, the second term in Eq. (3.67), often denoted as depolarization term, describes processes between states with the same wave vector \mathbf{k} , i.e. no momentum is transferred during the Coulomb interaction, see Fig. 3.38d. It contributes to the renormalization of the Rabi frequency. However, it is less important since the two contributions $V^{AA}(0)$ and $Re(V^{AB}(0))$ cancel each other to a large extent.

Finally, inserting the matrix elements from Eq. (C.15) and Eq. (C.17), the last Coulomb contribution from Eq. (3.64) can be expressed as

$$\tilde{V}_{exc}(\mathbf{k}, \mathbf{k}') = \frac{1}{2} \left[V^{AA}(\mathbf{q}) - Re \left(\frac{e^*(\mathbf{k}')e(\mathbf{k})}{|e(\mathbf{k}')e(\mathbf{k}')|} V^{AB}(\mathbf{q}) \right) \right] - \frac{1}{2} [V^{AA}(0) + Re V^{AB}(0)]. \quad (3.68)$$

These terms resemble the ones from Eq. (3.67). They contribute to the renormalization of the Rabi frequency. However, in comparison to the dominant term discussed above they play a minor role. They are driven by the complex conjugate of the microscopic polarisation $p_{\mathbf{k}}^*$. Within the rotating frame, they oscillate with a higher frequency and would vanish within the RWA, see Sec. 2.4.1. Unfortunately, this approximation is not applicable for investigations in carbon nanotubes, since non-resonant contributions can play an essential role, as shown in the discussion of the Rayleigh scattering from nanotubes.

3.6.4 Dark excitons

Up to now, the discussion has been focused on bright excitons, i.e. optically active bound electron-hole states. However, the existence of optically forbidden states, also called dark excitons, has been predicted theoretically.^{89,90} Due to the time reversal symmetry,^{59,91} both electron and hole states are degenerate in energy at the K and the K' point, see Fig. 3.43. The strong Coulomb interaction in carbon nanotubes is expected to considerably mix these states resulting in a partial lifting of the fourfold degeneracy. When considering the spin, the degeneracy is even sixteenfold. However, only one of them, an odd parity singlet state, is predicted to be optically active.^{11,90,92}

The mixing of these degenerate electron and hole states is often referred to as Coulomb induced intervalley mixing. It is determined by the strength of the electron-hole Coulomb interaction, which describes the coupling between different valleys. The interesting feature in SWCNTs is the prediction that the energetically lowest lying excitonic state is dark.^{89,90,92,94} This would have essential influence on the optical properties of nanotubes, since an optically forbidden state below the optical band gap creates a non-radiative channel for the relaxation of electrons. Measurements of the radiative lifetime in nanotubes have revealed that there is a discrepancy of three to four orders of magnitude between the fluorescence decay time and the radiative time.⁹⁵ This implies that there are strong non-radiative channels in nanotubes. The assumption, that the existence of dark excitons could lead to a relaxation bottleneck (Fig. 3.41) being responsible for the experimentally observed low quantum efficiency,⁹⁵⁻⁹⁷ is still controversially discussed in literature.^{89,93,98,99} If the theoretical predictions of a small dark-bright splitting in the order of some meV are correct, a thermal equilibrium between the dark and bright states would arise, contradicting the idea of a relaxation bottleneck. Another possible explanation for the low quantum efficiency might be the exciton-phonon coupling between the lowest excitonic state and the ground state, which is discussed in Sec. 3.7.

The existence of dark excitons can be explained by the high symmetry in carbon nanotubes. From the six-fold rotation (60°) of the hexagon around its midpoint only the two-fold rotation C_2 (180°) remains a symmetry operation in carbon nanotubes.⁴⁶ The corresponding rotational axis, often denoted as U axis, is perpendicular to the tube axis, see Fig. 3.42. It is present in both chiral and achiral nanotubes. Rotations by any other angle are not symmetry operations of the nanotube, since they would tilt the tube axis. Applying the U rotation maps the atom A into the atom B of the graphene unit cell, i.e. $U r_A = r_B$. Due to the U -axis symmetry, the states, denoted by the wave vector k and the angular momentum m , form a double degenerate band, since $U|km\rangle = |-k-m\rangle$. The corresponding two bands have minima at the K and the K' point, respectively. The electron-hole contribution of the Coulomb interaction mixes these states leading to a partial lifting of the degeneracy of electron and hole states.

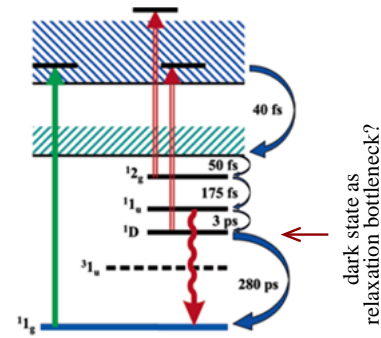


Figure 3.41: Relaxations paths in a SWCNT (taken from Seferyan et al.).⁹³

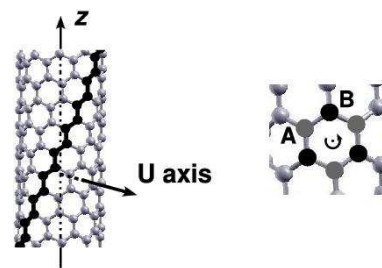


Figure 3.42: Illustration of the C_2 rotation (corresponding to a π rotation) around the U axis, which is perpendicular to the nanotube axis (taken from Chang et al.).⁹⁴

Depending on the symmetry of the resulting exciton states, they are optically active (bright) or inactive (dark). Hence, in the literature this lifting is often referred to as dark-bright splitting. Whether an excitonic state is bright, depends on its parity with respect to the C_2 rotation around the U axis. The states are called *gerade*, when the parity is $+1$, and *ungerade* for -1 parity. The *ungerade* states are bright, whereas the *gerade* states are optically forbidden, since the photon with a polarization along the nanotube axis has a -1 parity with respect to the U axis.⁶⁰

For long time, the dark-bright splitting remained a theoretical prediction. In 2004, Zaric et al.¹⁰⁰ proved experimentally the existence of dark excitons by applying large magnetic fields over 55 T. These strong fields break the symmetry with respect to the U rotation leading to a peak splitting in the magneto-optical spectra corresponding to two bright excitons. However, they could not measure the splitting since the field changes the intrinsic dark-bright splitting. The theoretical determination of the splitting energy is still controversial. The predicted values differ from few meV^{90,101} up to 0.1 eV.^{16,89,94}

Within the presented approach, the dark-bright splitting can be visualized by changing the optical matrix element of one of the involved states. Within the free-particle picture, the transition energy is only determined by the energy gap. The Rabi frequency containing the field and the optical matrix element determines the oscillator strength, but has no influence on the peak position, see Eq. (3.58). Including Coulomb interaction leads to shifts in the spectra, as discussed in the previous section. However, these are only dependent on the Coulomb matrix elements.

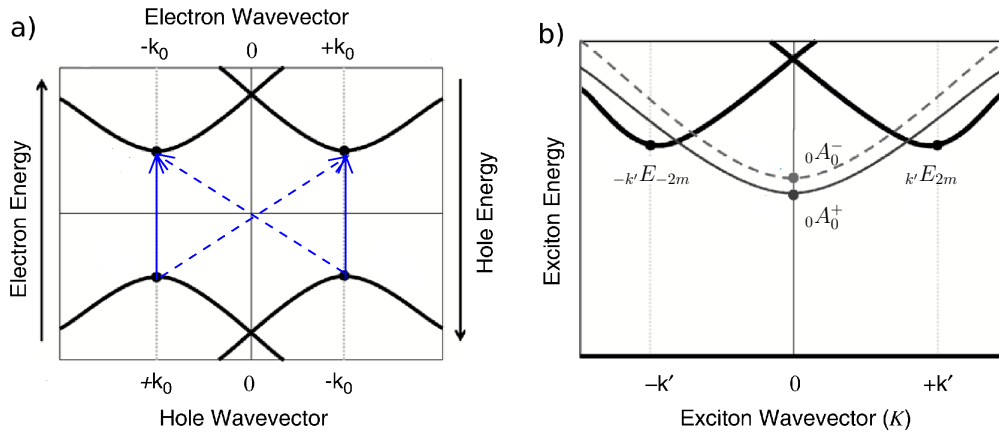


Figure 3.43: Sketch of the a) electronic and b) excitonic band structure of an arbitrary chiral nanotube (n_1, n_2) (taken from Barros et al.,⁹¹ but labels are adjusted to the line group formalism). The band minima are located at k_0 and $-k_0$ derived from the graphene K and K' points. The Coulomb induced intervalley mixing is indicated with blue arrows. The state labelled by ${}_0A_0^+$ is optically forbidden (dark exciton), while the state ${}_0A_0^-$ is optically active (bright exciton). They are both non-degenerate and have no angular momentum. In contrast, the exciton states ${}_kE_{2m}$ and ${}_{-k}E_{-2m}$ are degenerate and have a quasi-angular momentum of $2m$ and $-2m$, respectively (with m denoting the considered electron band). The exciton states are labelled according to their irreducible representations in the line group formalism.⁵⁹ The letter A describes a non-degenerate state, while E stands for a two-fold degeneracy. The superscript $+/-$ describes the parity under the C_2 rotation around the U axis (Fig. 3.42) the right subscript labels the quasi-angular momentum, and the left subscript denotes the wave vector of the considered state. Consequently, the difference between the two non-degenerate states lies in their behavior with respect to the U rotation which maps the atom A into the atom B of the graphene unit cell: $Ur_A = r_B$ in real space or in reciprocal space $U|km\rangle = |-k-m\rangle$. These two atoms are non-equivalent leading to also non-equivalent K and K' points in the graphene BZ.

Consequently, the optical matrix element is a possible switch to make the dark state theoretically visible without changing the position of the involved peaks. This argumentation is only valid in the limit of linear optics with small excitation fields. A mathematical argument for the dark state is that the linear combination of degenerate states $|km\rangle$ and $| -k - m\rangle$ is zero for the dark state. A slight change of the oscillator strength for one of the bands m or $-m$ makes the dark state visible. Using this method, the position of the dark state can be determined. For the (5, 0) zigzag tube a dark-bright splitting in the range of 50 meV is observed. This is in good agreement with Spataru et al.⁸⁹ However, in contrast to the latter, the dark state is found to be above the bright state. This statement deviates from the widely accepted prediction that the energetically lowest state in nanotubes is optically forbidden. Since it is difficult to resolve the small dark-bright splitting, up to now only one calculation on the very small (5, 0) nanotube was performed. For tubes of this diameter, curvature effects are essential. As a result, the zone-folded TB wave functions, used in this work, are not appropriate any more. Hence, further investigations on the dark-bright splitting are needed.

3.6.5 Kataura plots

The excitonic excitation depends on the diameter d and the chiral angle ϕ of the considered nanotube. These dependencies are usually illustrated in the so-called Kataura plot.¹⁰² Here, the transition energy of tubes with chiral indices (n_1, n_2) is shown as a function of their diameter. The Kataura plot reveals a number of essential features. The most important observation is that the transition energies have a general $1/d$ dependence. Tubes fulfilling the relation $n_1 - n_2 = \text{const.}$ build a group, characterized by a similar chiral angle ϕ and varying diameters d . They lie on $1/d$ lines in the Kataura plot. In addition, nanotubes also exhibit a specific V -shaped distribution around the main $1/d$ lines arising from the dependence on the chiral angle, see Fig. 3.44a. The Kataura plot is divided into characteristic branches according to $2n_1 + n_2 = \text{const.}$, which groups tubes with a similar diameter and varying chiral angles. In the center of such a V -shaped branch, one always finds armchair nanotubes (n, n) with a chiral angle $\phi = 30^\circ$. The tubes with the minimal ϕ , i.e. either zigzag tubes with $\phi = 0^\circ$ or tubes with $(n, 1)$ are found at the end of each branch. Consequently, the chiral angle of the tubes along the Kataura branches decreases from the center to the end. This observation reminds of the discussion of the double-peak structure in the Rayleigh spectra in Sec. 3.5.2. The latter was explained by trigonal warping describing the deviation of the equi-energy contours from circles in the Brillouin zone of graphene around the K point, see Fig. 3.8. This effect is also responsible for the observed chiral dependence along the Kataura branches. The smaller the chiral angle ϕ , the stronger is the trigonal warping resulting in the observed maximal distance of tubes with a small ϕ from the main $1/d$ line. Since armchair nanotubes are not influenced by the trigonal warping effect, they only show a diameter dependence, and therefore lie in the center of the $1/d$ line.

The Kataura plot shows, furthermore, specific family patterns characterized by well-separated lines corresponding to the transition E_{ii} , see Fig. 3.44a. Nanotubes are grouped to metallic tubes $[(n_1 - n_2) \bmod 3 = 0]$, +1 semiconducting tubes $[(n_1 - n_2) \bmod 3 = 1]$, and -1 semiconducting tubes $[(n_1 - n_2) \bmod 3 = 2]$. The two semiconducting families build one E_{ii} -line in the Kataura plot. Whether +1 or -1 tubes are forming the upper or lower branches for a given E_{ii} depends on the transition denoted by i . Since -1 tubes have a larger band gap,⁴ they build the upper branches of the lowest transition E_{11} . However, this behavior alternates for the next transitions, i.e. the -1 tubes lie on the lower branches of the E_{22} line, and then again on the upper branches of E_{33} . This characteristic family behavior can also be explained by the trigonal warping effect.

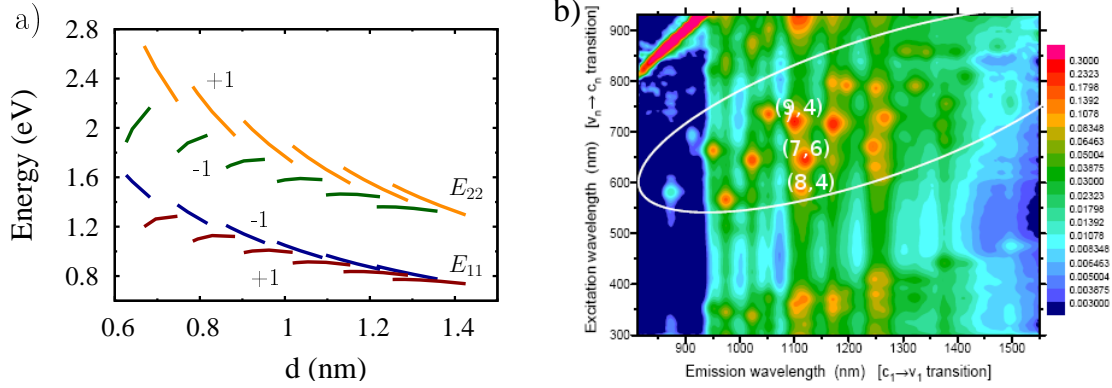


Figure 3.44: a) Experimental Kataura plot for the first two transitions E_{11} and E_{22} for semiconducting tubes with diameters in the range of 0.6 – 1.4 nm. The plot is obtained from the data given in Weisman et al.¹⁰³ b) Experimental determination of the Kataura plot. The structural assignment of specific (n_1, n_2) carbon nanotubes is performed via spectrofluorimetric measurements.⁵ The plot shows the luminescence intensity (coded by different colors) of individual SWCNTs in solution as a function of the emission and excitation energy. Bright points correspond to high intensity indicating a specific nanotube. The combination with resonance Raman data allows an unambiguous mapping of emission energies to specific chiral indices (n_1, n_2) .

As discussed in Sec. 3.5.1 and 3.5.2, the triangular shape of the equi-energy contours makes it important on which side of the K point the allowed k -lines are located. The energy dispersion of graphene is stronger on the $K\Gamma$ side, see Fig. 3.6. Consequently, the trigonal warping is affecting transitions on this side stronger, i.e. -1 tubes will build the upper branches of the Kataura lines for the transitions E_{11} and E_{33} and the lower branches for the transitions E_{22} and E_{44} (red lines). In contrast, $+1$ tubes show the inverse behavior.

The microscopic calculation of the Kataura plot has turned out to be intricate. To obtain the subtle Kataura branches (the variation in energy is in the range of some meV), it is necessary to take the full Brillouin zone $(-\frac{q}{n}\frac{\pi}{a}, \frac{q}{n}\frac{\pi}{a}]$ into account. It is not sufficient to focus on the k -range around one minimum in the band structure, or to restrict the investigation to single subbands. This leads to kinks within single branches. It is crucial to treat all tubes (within one branch) equally. For

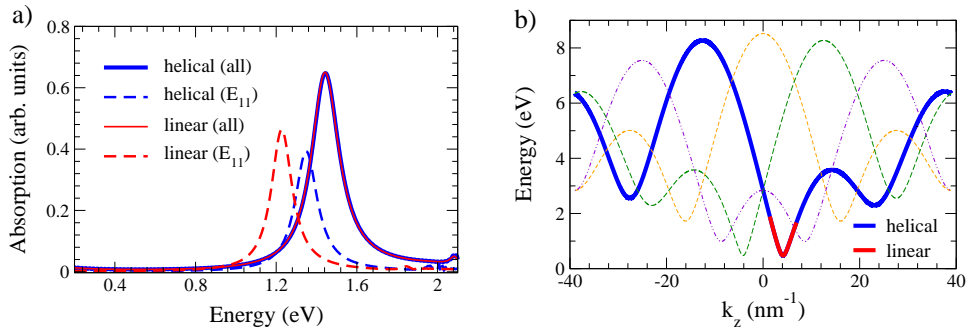


Figure 3.45: a) The absorption spectra of the $(8,4)$ nanotube calculated with linear or helical indices, see Sec. 3.14. Furthermore, the calculation considering only the subband which leads to the first transition E_{11} (dashed lines) with calculations including all subbands (solid lines) are compared. b) The band structure of the $(8,4)$ nanotube. The thick lines correspond to the subbands accounting for E_{11} (the linear subband is shifted). The thin lines are the other helical subbands.

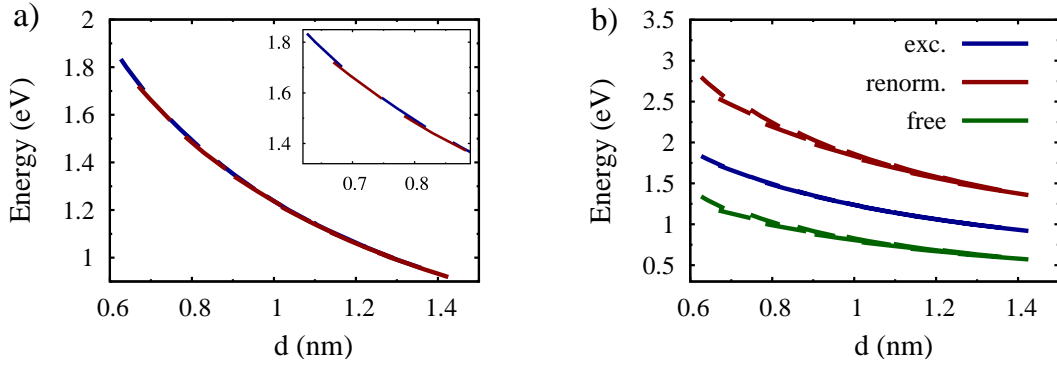


Figure 3.46: Theoretical Kataura plots are shown. a) The energetically lowest excitonic transition energy E_{11} is plotted as a function of the diameter. The considered semiconducting nanotubes have diameters in the range of 0.6 – 1.4 nm corresponding to the experimental Kataura plot in Fig. 3.44a. To see the subtle Kataura branches, induced by the chirality dependence, a zoom into a smaller region is shown in the inset. Blue lines show -1 tubes building the upper branch, while red lines show $+1$ tubes building the lower branch. b) Comparison of Kataura plots of E_{11} obtained calculating the free-particle, renormalized free-particle, and excitonic transition energies.

example, using linear subband indices $m \in [-\frac{q}{2} + 1, \frac{q}{2}]$ with the corresponding wave vectors $k_z \in (\frac{\pi}{a}, \frac{\pi}{a}]$ requires the consideration of all subbands, see Fig. 3.45. Otherwise, symmetric tubes with a small unit cell and a correspondingly large BZ are treated in a different way than less symmetric tubes with a short BZ. The position of excitonic peaks sensitively shift (Fig. 3.45) resulting in an incorrect reflection of the chirality dependence.

The calculation of transition energies and excitonic binding energies for the Kataura plot is performed by solving the excitonic Bloch equation for the microscopic polarisation from p_k , see Eq. (3.58). The calculation considers the full BZ including all subbands and the corresponding inter-subband interactions. The theoretically calculated Kataura plots are shown in Fig. 3.46. The excitonic transition energies are plotted over the diameter for a number of semiconducting nanotubes with diameters in the range of 0.6 – 1.4 nm. The approach also allows the calculation of metallic tubes. However, it is difficult to resolve the fine double-peaked structure in metallic tubes, when all subbands and the corresponding intersubband interactions are taken into account. The expected general $1/d$ dependence of transition energies is reproduced in the theoretically calculated Kataura plot. The latter also contains the characteristic Kataura branches, see the inset of Fig. 3.46a. However, the dependence on the chiral angle turns out to be weak. The plot contains the characteristic Kataura branches, see the inset of Fig. 3.46a. However, they are not as pronounced as in the experiment. In Fig. 3.46b, the corresponding Kataura plots for the free-particle and the renormalized transitions are shown illustrating more diversified Kataura branches. Obviously, the general pattern of the characteristic Kataura branches arises from the free-particle transition. Including the electron-electron interaction, only leads to a blue-shift in the Kataura plot. The branches reflecting the chirality dependence remain unchanged comparing to the free-particle case. It is the attractive electron-hole interaction that reduces the chirality induced spread within the Kataura branches. The simple nearest-neighbor tight-binding model, applied for these calculations, is not accurate enough to reflect the subtle chirality dependence. It is already known¹⁷ that an extended tight-binding model (ETB), also called non-orthogonal tight-binding model,⁷¹ which takes into account the curvature effects, is required to describe the pronounced V -shaped Kataura branches.

Figure 3.47a shows the Kataura plot for the lowest three transitions E_{11} , E_{22} and E_{33} . The stronger

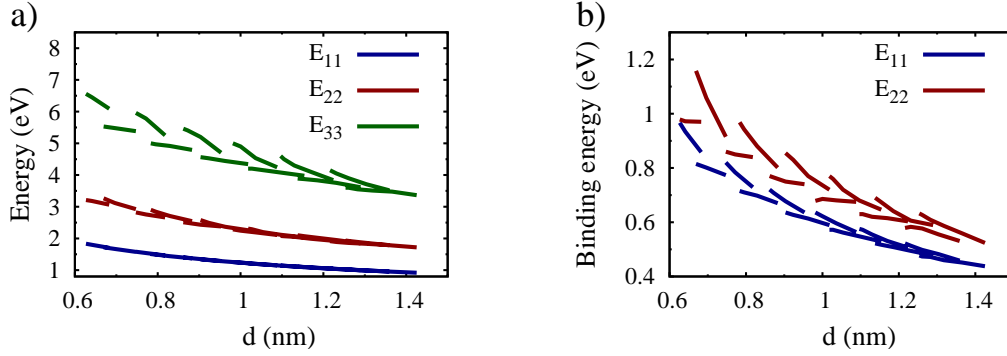


Figure 3.47: Theoretical Kataura plot for a) the three energetically lowest transitions E_{11} , E_{22} , and E_{33} , and b) the corresponding excitonic binding energies (the binding energies are shown only for the first transitions accounting for the increasing absolute error in determination of excitonic binding energy for higher transitions).

pronounced Kataura branches for higher transitions attract attention. This is in agreement with the statement that the branches reflect the chirality dependence which, in turn, is a consequence of trigonal warping. The latter is stronger at higher energies, since the deviation from circles in the energy contour of graphene is enhanced with increasing distance from the K point, see Fig. 3.8. An increased chirality spread for E_{22} can also be observed in the experimental Kataura plot, see Fig. 3.44a.

Finally, the dependence of the excitonic binding energy on the diameter and the chirality is shown in Fig. 3.47b. It exhibits more pronounced Kataura branches than the corresponding Kataura plot for the transition energy. The reason lies in the origin of the excitonic binding energy, which is given by the difference between the renormalized transition energy and the exciton excitation energy. Consequently, the more pronounced Kataura branches of the excitonic binding energy can be traced back to the renormalized free-particle transition, see Fig. 3.46b. The binding energy predicted for E_{22} is larger than for E_{11} . So far, experimentally E_b has only been determined for E_{11} ; the magnitude for binding energies for higher transitions is still controversially discussed in literature.^{104,105}

The comparison of absolute values for the transition energy with the experiment yields a blue-shift of theoretical results of about 0.2 eV for the first transition E_{11} . One aspect that needs to be considered is that the experimental measurements of E_b have been performed on single-walled carbon nanotubes isolated in aqueous surfactant suspensions,^{10,11} i.e. the background dielectric constant describing the surrounding medium is larger than 1. The influence of the environment^{106,107} induces red-shifts of up to 0.1 eV. Another correction, also leading to a red-shift, is due to the curvature effects known from ETB calculations.⁷¹ The calculated excitonic binding energies are in the range of 0.4 – 0.9 eV in agreement with ab-initio results.^{16,17,108} The experimental values^{10,11} are in the range between 0.3 – 0.4 eV. This discrepancy can be traced back to environmental effects. To obtain a better insight into the optical properties of CNTs, the these effects are discussed in detail in the next section.

3.6.6 Background screening

The surrounding environment created by solvents and adsorbed molecules has a considerable influence on the optical properties of carbon nanotubes.^{13,16,17,106,107} Currently, there is no microscopic description of these environmental influences. So far, a dielectric background constant ϵ_{bg}

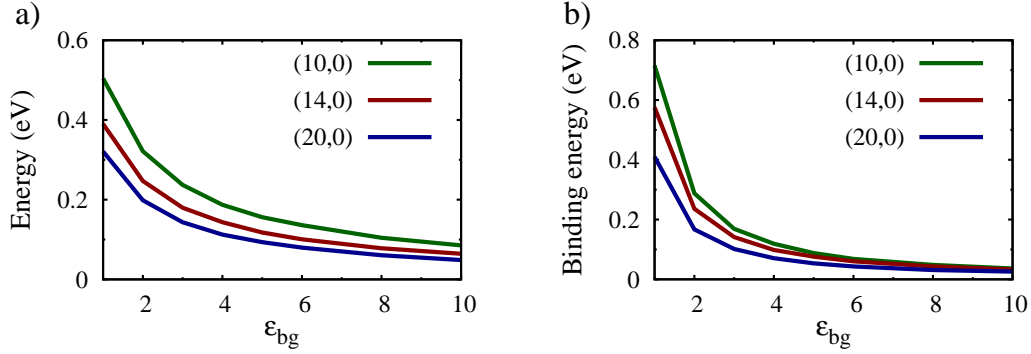


Figure 3.48: The environmental influence on a) the transition energy E_{11} and b) the exciton binding energy $E_{b,11}$ for nanotube with different diameters ($d = 0.8 - 1.6$ nm) and a constant chiral angle ($\phi = 0^\circ$). Note, that in a) the energy difference ΔE_{ii} is plotted as a function of ϵ_{bg} , i.e. $\Delta E_{ii} = E_{ii}^{exc} - E_{ii}^{free}$ with the excitonic and free particle excitation energy, respectively (corresponding to the excitonic net - blue shift).

has been introduced to model the effects of the environment. Introducing such an ϵ_{bg} into Eq. (3.66) leads to an effective screening of the Coulomb potential. This has an influence on both the transition energies E_{ii} as well as the excitonic binding energies $E_{b,ii}$. As a result, the influence of the environment leads to a recalibration of the Kataura plot depending on the used medium. For historical reasons the experimentally available Kataura plots (Fig. 3.44) are based on nanotubes suspended in the standard aqueous dispersion of SWCNTs with the sodium dodecylsulfate (SDS) surfactant. The dependence on the environment offers a possibility to tailor the band gap of a nanotube by changing its surrounding medium. However, the creation of adjustable environments is still a challenge in current research.

The influence of environment on transition energies of nanotubes are controversially discussed in literature.^{106,107,109-112} Up to now, most experimental studies^{107,109-114} have observed red-shifts of the energetically lowest transitions E_{11} and E_{22} by approximately 20 – 90 meV for tubes in a SDS medium ($\epsilon_{bg} > 1$) compared to measurements in air ($\epsilon_{bg} \approx 1$). However, also blue-shifts of E_{22} by approximately 70 – 90 meV have been reported.¹¹²

In this section, the environmental influence on the optical properties of CNTs is modeled by including a dielectric background constant ϵ_{bg} . In contrast to the approach based on the Bethe-Salpeter equation and the GW-method where only the excitonic contribution is screened,¹⁶ the density matrix theory treats all Coulomb contributions equally, i.e. all Coulomb matrix elements are screened by ϵ_{bg} .^{36,42} In the following, the influence of the environment on both the transition energy E_{ii} and the excitonic binding energy $E_{b,ii}$ is investigated. The dielectric background constant is increased up to a value of 10 to obtain a better insight into the functional dependence for both small and large ϵ_{bg} (even though a practical limit for external screening of SWCNTs is assumed¹⁰⁷ to be around $\epsilon_{bg} \approx 5$). The influence of the dielectric background screening on transition energies and the corresponding excitonic binding energies is shown for tubes with: i) varying diameters and constant chiral angles (Fig. 3.48), ii) varying chiral angles and similar diameters (Fig. 3.50), and iii) for the three lowest transitions and corresponding binding energies in the (10, 0) zigzag nanotube. In agreement with experimental results,^{107,110,113,114} a general decrease of both transition and excitonic binding energies with the dielectric background constant is observed. The change between air ($\epsilon_{bg} = 1$) and SDS as the surrounding medium of nanotubes is of great importance. The dielectric background constant of the SDS medium is difficult to determine, since it depends on the largely unknown surface coverage of the surfactant.^{106,113}

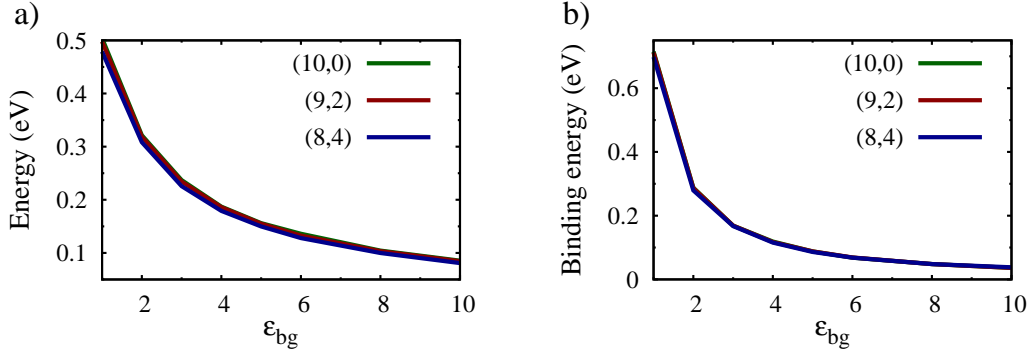


Figure 3.49: The environmental influence on a) the transition energy shift ΔE_{11} and b) the exciton binding energy $E_{b,11}$ for nanotubes with different chiral angles and similar diameters. +1 semiconducting tubes along the Kataura branch $2n_1 + n_2 = 20$ are shown, i.e. the chiral angle decreases from the zigzag (10,0) tube to the chiral (8,4) tube, while the diameter varies only weakly. Similar results are obtained for the corresponding branch belonging to the -1 family.

In Kiowski et al.,¹⁰⁷ it is assumed to be $\epsilon_{bg}^{SDS} \approx 2$. The theory predicts a strong red-shift of the transition energy when the dielectric background constant is increased from $\epsilon_{bg} = 1$ to $\epsilon_{bg} = 2$. This shift is in the range of 0.1 – 0.2 eV and depends on the tube diameter, see Fig. 3.48a. The smaller the diameter, the lower is the observed red-shift. The excitonic binding energies $E_{b,ii}$ show even a stronger dependence on the background screening. An increase of ϵ_{bg} from 1 to 2 leads to a reduction of $E_{b,ii}$ by 0.3 – 0.5 eV. This is a sign for a strongly suppressed electron-hole coupling. The predicted energy shifts due to the environment are higher than measured in most experimental studies. However, since the dielectric background constant for the media, in which nanotubes are suspended, cannot be exactly determined, a direct comparison is difficult.

Figure 3.49 illustrates is the same for nanotubes with different chiral angles. Also tubes with different diameters follow the same functional dependence on ϵ_{bg} . A simple scaling law for the transition energies in dependence on the dielectric background screening is found

$$E_{b,ii} \propto A\epsilon_{bg}^{-\beta_0} \quad (3.69)$$

with $\beta_0 \approx 1.3$ for all considered transitions E_{ii} , diameters d and chiral angles ϕ . The parameter A

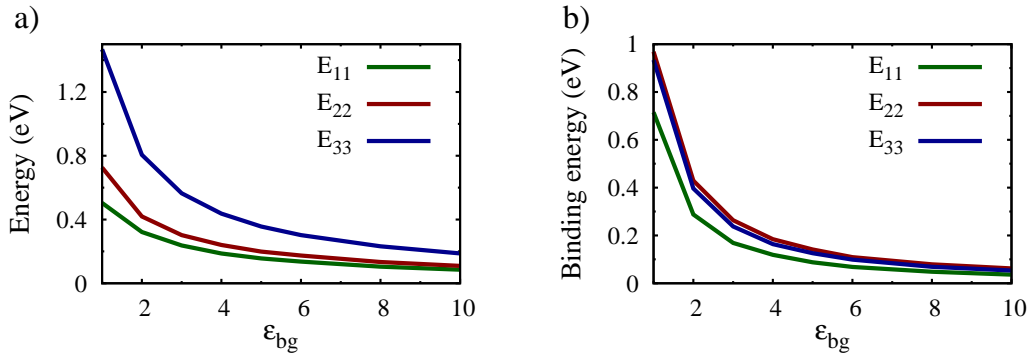


Figure 3.50: The influence of the surrounding environment is investigated for a) the three lowest transitions E_{11} , E_{22} , and E_{33} and b) the corresponding excitonic binding energies.

varies with E_{ii} and d . A similar scaling law has been found within the Bethe-Salpeter approach by Parabeinos et al.¹³ and Capaz et al.¹⁶ with a slightly different parameter $\beta_0 = 1.4$.

The environmental effect on transition energies is more complicated, since a different behavior is observed for $\epsilon_{bg} \rightarrow 0$ and $\epsilon_{bg} \rightarrow \infty$ yielding the scaling law

$$\Delta E_{ii} \propto B \exp(-\beta_1 \epsilon_{bg}) + C \epsilon_{bg}^{-\beta_2} \quad (3.70)$$

with $\beta_1 \approx 0.2$, $\beta_2 \approx 0.8$. The parameters B and C vary with the diameter d and the transition E_{ii} , but the functional dependence on the dielectric background constant remains the same.

A semiempirical scaling relation for the transition energy shift due to the environmental influence has been presented by Choi et al.¹⁰⁶ This relation is derived within the solvatochromic formalism.¹¹⁵ The change of electronic absorption and luminescence spectra due to the molecule-medium interaction is called solvatochromic shift. They arise from the change in the dipole moment due to the presence of a dipolar solvent. The resulting shift in the transition energy can be described by¹⁰⁶

$$\Delta E_{ii}^{\epsilon_{bg}} = c E_{ii}^{-2} d^{-4} \quad (3.71)$$

with the nanotube diameter d and the constant c , which only varies with the solvent. Consequently, this approach predicts a linear scaling, when $\Delta E_{ii}^{\epsilon_{bg}} E_{ii}^2$ is plotted over d^{-4} . This prediction is nicely confirmed by experimental results, as shown in Fig. 3.51a for the case of the SDS medium. The slope for the first transition E_{11} is $0.05(\text{eV})^3 \text{nm}^4$. Also for other dielectric media, such as NMP solvent, DNA, or NaCholate a linear scaling with similar slopes in the range of $0.05 - 0.06(\text{eV})^3 \text{nm}^4$ is observed.¹⁰⁶

Figure 3.51b shows the corresponding theoretical calculation. It confirms the experimentally predicted linear scaling for diameters up to 1.2 nm. Larger tubes with $d > 1.2$ nm corresponding to

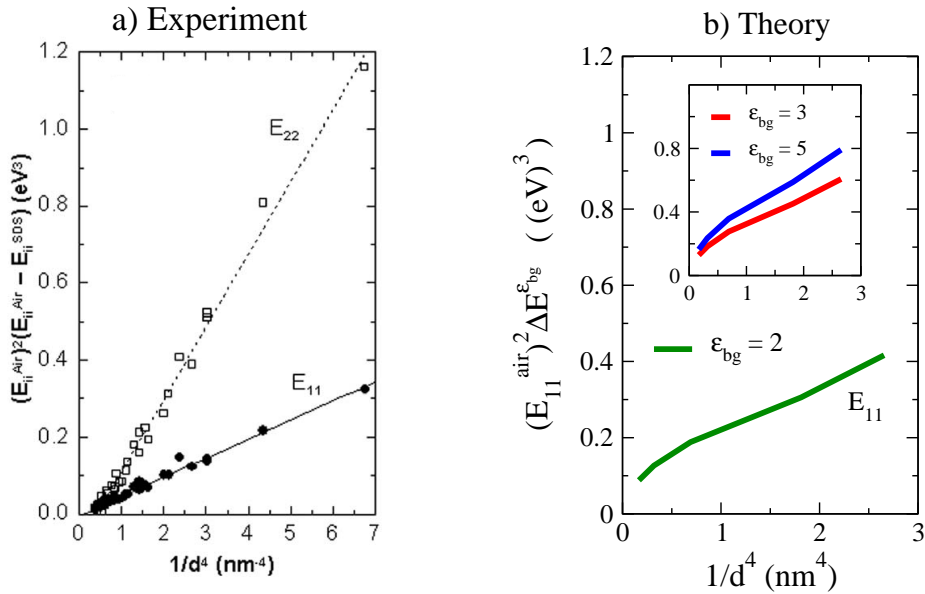


Figure 3.51: a) Experimental solvatochromic shifts $E_{ii}^{\text{air}} - E_{ii}^{\text{SDS}}$ determined from photoluminescence energies of SW-CNTs in air with $\epsilon_{bg} \approx 1$ and SDS encapsulations (taken from Choi et al.).¹⁰⁶ b) The corresponding theoretical calculation. The SDS medium is assumed¹⁰⁷ to have a dielectric background constant $\epsilon_{bg} = 2$. The inset shows the shifts for $\epsilon_{bg} = 3$ and $\epsilon_{bg} = 5$. The experimentally predicted linear scaling is reproduced for the energetically lowest transition E_{11} .

$d^{-4} < 0.5 \text{ nm}^{-4}$ seem rather to scale with d^{-3} . The resulting slope of the linear region is about $0.11(eV)^3 \text{ nm}^4$, i.e. double as large as in the experiment. Increasing the dielectric background constant to 3 (5) further enhances the slope to $0.17 (0.22)(eV)^3 \text{ nm}^4$. The influence of the environment again seems to be overestimated in the theory. Assuming the dielectric constant of the modeled SDS medium to be smaller than 2 would also reduce the predicted slope and improve the agreement with experimental results.

3.6.7 Excitonic oscillator strength

In Sec. 3.5.1, it was assumed that band-to-band transitions can give good insight into the chirality dependence of the optical properties of carbon nanotubes. The underlying assumption was that excitonic absorption follows the oscillator strength found for uncorrelated electron-hole pairs. In this section, this assumption is verified.

The abundance of nanotube chiralities has already been determined experimentally from the intensities in photoluminescence excitation (PLE) experiments.^{5,6} The results predict an increase in the PLE intensity for both semiconducting families with increasing chiral angle. Furthermore, higher intensities are measured for tubes belonging to the -1 family. Under the assumption that the relaxation rate between the second and the first excitonic state is constant,⁶⁷ the PLE intensity is already determined by the absorption intensity α for the second transition E_{22} .

The calculations based on the free-particle Bloch equation [Eq. (3.45)] have already confirmed this experimentally observed trend. The absorption intensity of the second transition E_{22} is shown to increase with the chiral angle by approximately 11% for -1 tubes and by 1% for $+1$ tubes. The corresponding absolute intensities are found higher for -1 tubes than for $+1$ tubes - in accord with experimental results.⁶ However, the theoretically predicted chirality dependence is generally much weaker. After including the Coulomb interaction and evaluating the excitonic Bloch equation [Eq. (3.58)], the investigations from Sec. 3.5.1 are repeated within the excitonic picture. The intensity of the two energetically lowest transitions E_{11} and E_{22} for i) $+1$ nanotubes belonging to the Kataura branch with $2n_1 + n_2 = 26$ (corresponding to diameters of $d \approx 1.02 - 1.15 \text{ nm}$)

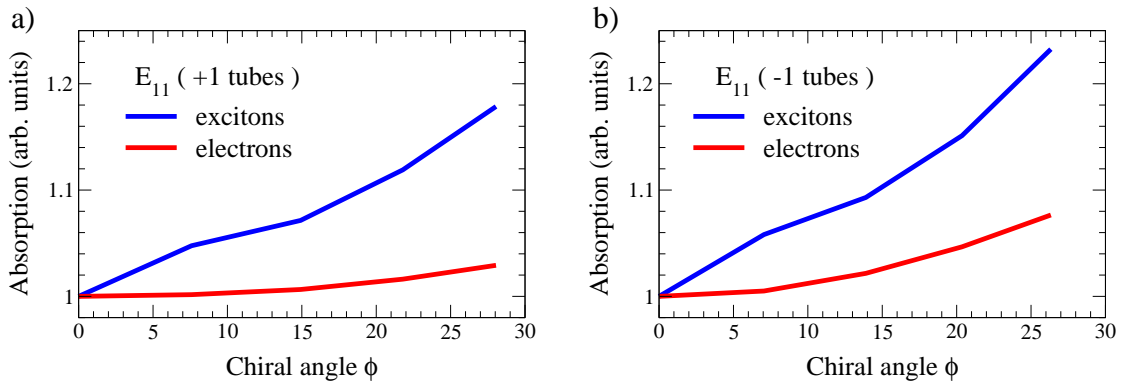


Figure 3.52: Chirality and family dependence of the absorption intensity for the first transition E_{11} are shown for a) $+1$ nanotubes with $2n_1 + n_2 = 26$ ($d \approx 1.02 - 1.15 \text{ nm}$) and b) for -1 nanotubes with $2n_1 + n_2 = 28$ and $d \approx 1.10 - 1.22 \text{ nm}$. The figure also shows a comparison of free-particle (red line) with excitonic (blue line) results. To achieve a better comparison, the absorption intensities are normalized to the value for the zigzag tube with $\phi = 0^\circ$, respectively.

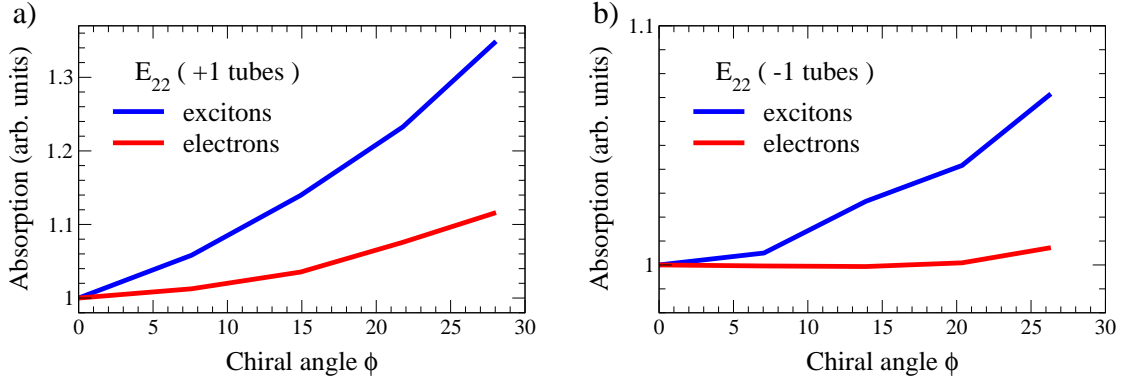


Figure 3.53: Chirality and family dependence of the absorption intensity for the second transition E_{22} are shown for a) +1 tubes and b) -1 tubes. For details, see the caption of Fig. 3.52.

and ii) -1 nanotubes along the Kataura branch with $2n_1 + n_2 = 28$ (corresponding to diameters of $d \approx 1.10 - 1.22$ nm) have been investigated as a function of the chiral angle. The selected tubes have a relatively large diameter justifying the assumption that curvature effects are of minor importance. Consequently, the applied zone-folded tight-binding wave functions are a good approximation.

Figure 3.52 shows the results obtained for the intensity of the first transition E_{11} . Both excitonic and free-particle intensities (corresponding to results from Sec. 3.5.1) are plotted over the chiral angle ϕ . The figure verifies the assumption, that the excitonic absorption basically follows the oscillator strength found for free electrons. The trend obtained from free-particle calculations is confirmed. The excitonic effects merely enhance the chirality dependence. However, this enhancement is considerable. The increase of the excitonic intensity from the zigzag ($\phi = 0^\circ$) towards the armchair constellation ($\phi = 30^\circ$) is enhanced to 23% for -1 tubes and to 18% for +1 tubes. A similar trend is obtained for the second transition E_{22} , as shown in Fig. 3.53. The increase from the zigzag towards the armchair constellation is approximately 35% for -1 tubes and 7% for +1 tubes. This clearly stronger chirality dependence improves the comparison to experimental reports observing a considerably stronger PLE signal for tubes close to the armchair constellation.^{5,6} Note also that the absolute intensity for $\alpha(E_{22})$ is by 40% larger for -1 tubes than for the +1 tubes (for $\phi = 0^\circ$). This agrees well with the higher experimental PLE intensity of -1 tubes.⁶

3.6.8 Metallic nanotubes

In this section, the investigation is extended to metallic single-walled carbon nanotubes. The calculation of excitonic effects in these tubes requires an accurate description of screening effects. In particular, the internal \mathbf{k} -dependent screening plays an essential role in metallic nanotubes with a zero band gap. Due to the presence of other electrons, the Coulomb interaction affecting one single electron is screened. This internal screening is independent of environmental effects. It is calculated within an effective single-particle Hamiltonian approach leading to the renowned Lindhard approximation^{17,36,42}

$$\varepsilon(q) = 1 - 2V(\mathbf{q}) \sum_{\lambda, \lambda'}^{c, v} \sum_{\mathbf{k}} \frac{\rho_{\mathbf{k}-\mathbf{q}}^{\lambda'} - \rho_{\mathbf{k}}^{\lambda}}{\hbar(\omega + i\gamma) + \varepsilon_{\mathbf{k}-\mathbf{q}}^{\lambda'} - \varepsilon_{\mathbf{k}}^{\lambda}} \left| \int \psi_{\mathbf{k}, \lambda}^*(\mathbf{r}) e^{-i\mathbf{q} \cdot \mathbf{r}} \psi_{\mathbf{k}-\mathbf{q}, \lambda'} \right|^2 \quad (3.72)$$

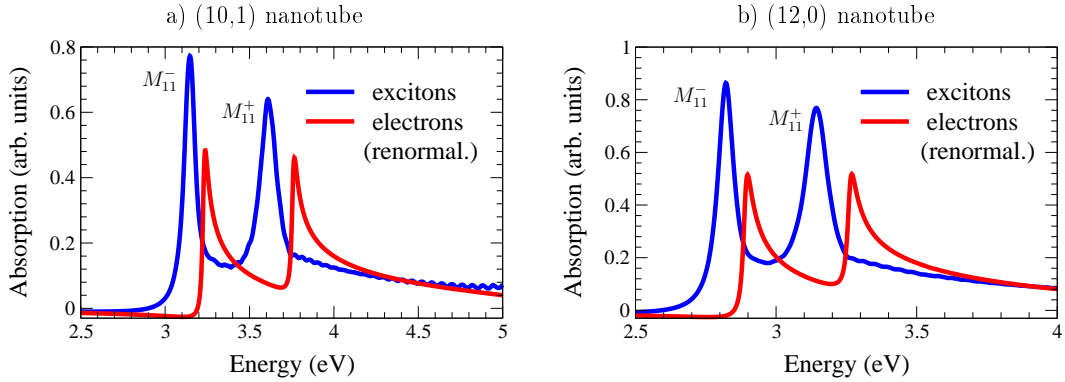


Figure 3.54: Absorption spectra for the first two transitions in metallic nanotubes. The absorption coefficient is calculated with an incorporated internal screening according to Eq. (3.73). The figure shows a comparison of the absorption obtained when the electron-hole interaction is included (excitonic Lorentzians: blue lines) and when only the electron-electron part of the Coulomb interaction is considered (renormalized Van Hove singularities: red lines). The excitonic binding energy corresponding to the energy distance between these two peaks is found to be 90 meV for the (10, 1) tube and 75 meV for the (12, 0) tube.

with the k -dependent dielectric function $\varepsilon(q)$. As shown in Sec. 3.4.2, Eq. (3.72) can be evaluated for CNTs by including the TB wave functions. Within the limit of linear optics with completely populated valence bands and empty conduction bands, the internal screening can be expressed as

$$\varepsilon(q) = 1 - V(q) \sum_{\mathbf{k}} \frac{2}{\gamma_0 |e(\mathbf{k} - \mathbf{q})| + \gamma_0 |e(\mathbf{q})|} \left[1 - \text{Re} \left(\frac{e^*(\mathbf{k}) e(\mathbf{k} - \mathbf{q})}{|e(\mathbf{k}) e(\mathbf{k} - \mathbf{q})|} \right) \right]. \quad (3.73)$$

The equation illustrates that screening effects are crucial for metallic nanotubes, where the denominator can be very small, see Fig. 3.22. The internal screening has also an influence on semiconducting tubes, but compared to metallic tubes, the screening is assumed to be predominantly determined by the environment (see the comparison of semiconducting and metallic tubes in Fig. 3.22).

The strong screening suppresses the formation of excitons. Up to recently, the assumption that excitonic effects should be of minor importance in metallic nanotubes was widely spread. In 2004, Spataru et al.¹⁰⁸ performed first-principle calculations on metallic nanotubes predicting bound exciton states even in metallic nanotubes. They calculated excitonic binding energies for the (3, 3) armchair nanotube to be nearly 100 meV, which is approximately one order of magnitude smaller than in corresponding semiconducting nanotubes. Nevertheless, these are still strongly bound excitons, compared, e.g. to excitonic binding energies in bulk semiconductors, which are in the order of few meV.³⁶ In 2007, Wang et al.¹¹⁶ have developed a sensitive technique to measure directly the optical absorption of individual metallic SWCNTs. They showed that optical transitions in metallic nanotubes are dominated by excitons with binding energies of up to 50 meV. The reason why bound electron-hole states can appear even though the screening of Coulomb interaction is very high, can be traced back to the specific properties of one-dimensional structures. Here, the formation of at least one bound electron-hole state is predicted, if the Coulomb potential is repulsive on average.¹¹⁷ Furthermore, the effectiveness of the screening in one dimension is drastically reduced in comparison to three-dimensional metals.¹¹⁶

The calculation of the optical susceptibility from Eq. (2.57) including the internal dielectric screening of the Coulomb matrix elements according to Eq. (3.73) allows the investigation of arbitrary metallic nanotubes. The calculated absorption spectra for two exemplary metallic nanotubes are

shown in Fig. 3.54. The spectra of both exemplary tubes, (10, 1) and (12, 0), illustrate the formation of excitons characterized by Lorentzians (blue lines), which are red-shifted comparing to the (renormalized) free-particle Van Hove singularities (red lines). The excitonic binding energies are found to be 90 meV for the (10, 1) tube and 75 meV for the (12, 0) tube. This is in good agreement with both first-principle calculations^{108,117} and the experiment¹¹⁶. The smaller binding energies of 50 meV have been experimentally estimated for the larger (21, 21) nanotube. As shown in Sec. 3.6.3, the excitonic binding energies scale approximately with d^{-1} , see Fig. 3.47b. Consequently, a smaller exciton binding energy for the (21, 21) tube is expected.

Due to the strong screening, the electron-hole coupling is weak resulting in small excitonic binding energies for metallic tubes in comparison to semiconducting nanotubes with a similar diameter. As a consequence, the oscillator strength of the continuum contribution is not as low as in semiconducting nanotubes. This can be seen in Fig. 3.54, where the excitonic Lorentzian is followed by a smaller tail at the high-energy wing, which can be ascribed to the Van Hove singularity of the (renormalized) free-particle transition. This feature might be useful for the structural assignment of metallic nanotubes.

3.6.9 Excitonic Rayleigh scattering spectra

In Sec. 3.5.2, the microscopic calculation of the Rayleigh scattering cross section for single-walled carbon nanotubes of arbitrary chiral angle and family index has been presented. This calculation was based on the free-particle Bloch equation, see Eq. (3.45). In agreement with experiments,^{9,80,81} it was shown that the Rayleigh spectra of metallic nanotubes have a double-peaked structure resulting from the trigonal warping effect, see Fig. 3.32. For all nanotubes within a given Kataura branch, the lower-lying transition in the double-peaked structure was shown to be stronger in intensity, i.e. $M_{11}^- (M_{22}^-)$ is greater in intensity than $M_{11}^+ (M_{22}^+)$ - in agreement with experimental results.⁸¹ This feature was explained by the different behavior of the optical matrix element along the two high-symmetry lines $K\Gamma$ and KM , see Fig. 3.33b-d. Furthermore, in accord with experiment,^{9,80,81} the Rayleigh peaks were shown to have an asymmetry towards lower energies, i.e. the scattering cross section is enhanced at lower energies. This behavior was found to be the result of non-resonant contributions.

In this section, the free-particle approach is extended by including the Coulomb interaction according to Eq. (3.58). In analogy to the investigation of the oscillator strength, discussed in Sec. 3.6.7, the trends found for uncorrelated electrons are qualitatively confirmed within the excitonic picture. Both the asymmetry and the characteristic behavior of the intensity ratio in the double-peaked structure in the Rayleigh spectra of metallic nanotubes remain unchanged. Excitonic effects merely enhance these features. A comparison of results obtained within the free-particle and the excitonic approach is shown in Fig. 3.55 for two exemplary metallic tubes. Since here the focus lies on the peak shape and relative peak intensities, the free-particle spectra are corrected according to the excitonic shift, discussed in Sec. 3.6.3. The figure illustrates that: i) the asymmetry towards lower energies remains almost completely unchanged, when excitonic effects are included, ii) the intensity ratio of the double-peaked structure is increased, and iii) the cross section at the higher-energy tail of both peaks is reduced. Both the increased intensity ratio and the reduced cross-section at higher energies can be explained by the formation of excitons characterized by Lorentzians in the absorption spectra. The oscillator strength is almost completely transferred into the excitonic transition. As a result, the Van Hove singularities showing a long tail towards higher energies are strongly suppressed. This explains why the cross section at higher energies is reduced. It is also the reason for the enhanced intensity ratio in the double-peaked structure since

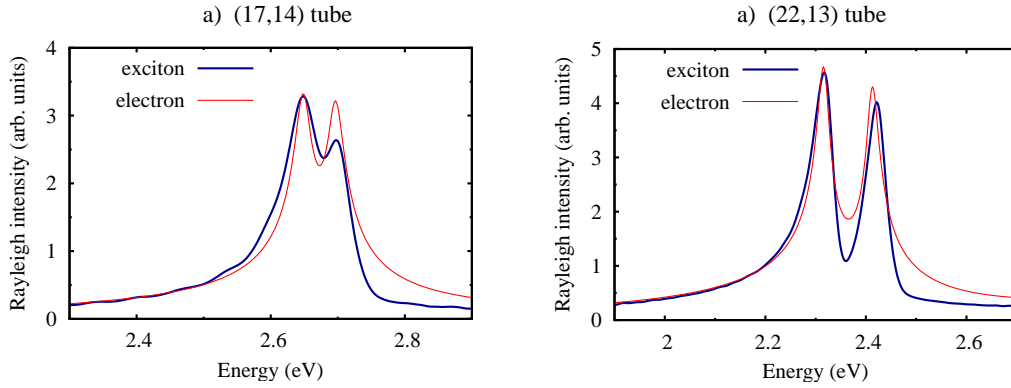


Figure 3.55: Comparison between the free-particle and excitonic Rayleigh scattering spectra from two exemplary metallic nanotubes. The second transitions M_{22}^- and M_{22}^+ are shown. Since the peak shape and the relative intensity is in the focus of investigation, the free-particle spectra are rescaled in intensity and blue-shifted by 0.38 eV and 0.43 eV for the (17, 14) and (22, 13) tube, respectively, according to the excitonic blue-shift. The slight oscillations in the theoretical spectra of the (17, 14) tubes are due to numerical artifacts.

the second peak does not interfere any more with the long tail of the first Van Hove singularity. The observation that the increase of the intensity ratio is much larger for the (17, 14) nanotube, where the distance of the two peaks is much smaller, supports this interpretation.

As assumed in Sec. 3.5.2, including excitonic effects improves the agreement with the experiment.⁸² Figure 3.56 illustrates the fairly good agreement of theoretical and experimental Rayleigh scattering spectra for both considered tubes with respect to the peak asymmetry, peak ratio, and the energetical separation of the two peaks. The transition energies, however, differ considerably. The theoretical energies are blue-shifted by approximately 0.3 – 0.4 eV compared to the experimental data. This can be traced back to a large extent to the nearest-neighbor approximation, which is known to be a good description for transitions close to the K point. For higher energies, however, a considerable discrepancy in comparison to first-principle calculations is predicted.⁵⁵ Nearest-neighbor and ab-initio transition energies are compared in Reich et al.⁵⁵ yielding, e.g. for the metallic (12, 3) tube a blue-shift of the nearest-neighbor energy M_{22}^- by approximately 0.3 eV.

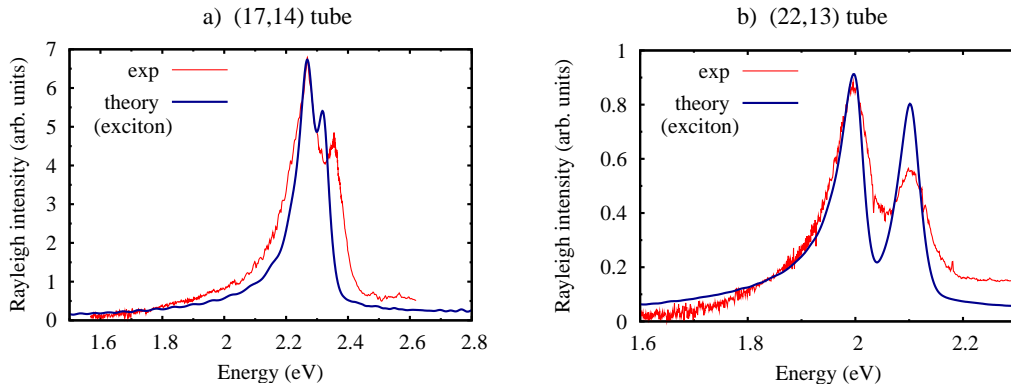


Figure 3.56: Comparison between the experimental and theoretical (including excitons) Rayleigh scattering spectra for the (17, 14) and (22, 13) metallic nanotubes. The experiments were performed by Wu et al.⁸² at Columbia University, New York. For comparison with respect to the peak shape, the theoretical spectra of the (17, 14) and the (22, 13) tube from Fig. 3.55 are rescaled in intensity and red-shifted by 0.38 eV and 0.32 eV, respectively.

3.6.10 Summary

In this section, excitonic effects have been discussed in detail. The Coulomb interaction is shown to be strongly reduced for intersubband processes with a momentum transfer perpendicular to the nanotube axis. The contributions describing the electron-electron repulsion are shown to lead to a considerable renormalization of the energy gap. The attractive part of the Coulomb interaction causes the formation of bound electron-hole pairs in both semiconducting and metallic nanotubes. The excitonic binding energies in metallic tubes turn out to be one order of magnitude smaller than in semiconducting tubes of similar diameter. The chirality and diameter dependence of transition energies and excitonic binding energies is presented in Kataura plots. Furthermore, the influence of the environment on optical properties of SWCNTs is investigated, as well as the dependence of the oscillator strength on the chiral angle and the family index. Finally, theoretically calculated Rayleigh spectra are successfully compared with experimental results with respect to the peak shape and their intensity ratio.

3.7 Exciton-phonon coupling - an outlook

Over the last years, optical phonons were shown to be of crucial importance for understanding the dynamics in carbon nanotubes. The peaks of highest intensity in Raman spectra can be ascribed to optical phonons.⁴⁶ Furthermore, high field transport measurements show that electron-phonon scattering by optical phonons at the K and the Γ point breaks down the ballistic behavior.¹¹⁸ Recently, the presence of a phonon sideband in PLE spectra has been measured lying 200 meV above the zero-phonon line,^{119,120} corresponding to the energy of optical phonons. Perebeinos et al.^{121,122} have investigated theoretically the role of electron-phonon and exciton-phonon coupling in the optical spectra of carbon nanotubes. They ascribed the strong phonon sideband peaked around 200 meV above the zero-phonon line to exciton-phonon coupling. The latter transfers up to 15% of oscillator strength from the zero-phonon line to the phonon sideband. However, up to now, there have been no further studies on exciton-phonon coupling in absorption and Rayleigh spectra in carbon nanotubes. In addition, the effect on metallic nanotubes is unknown. First experimental studies could not find the corresponding sideband in the spectra of metallic tubes.¹²³

This section gives an outlook for a planned investigation of the chirality, diameter, and family dependence of electron-phonon and exciton-phonon coupling in single-walled carbon nanotubes of arbitrary chiral angle. The equations necessary to describe the exciton-phonon dynamics in SWCNTs are sketched briefly.

The starting point is the Hamilton operator for the system including the interaction with the phonons

$$H = H_{0,c} + H_{c-f} + H_{c-c} + H_{0,ph} + H_{c-ph} \quad (3.74)$$

with the free phonon part $H_{0,ph}$ and the the part describing the electron-phonon interaction H_{c-ph}

$$H_{0,ph} = \sum_i \hbar\omega_i \left(b_i^\dagger b_i + \frac{1}{2} \right), \quad H_{c-ph} = \sum_{l,l'} \sum_j (g_{l,l'}^i a_l^\dagger b_i a_{l'} + g_{l,l'}^{i*} a_{l'}^\dagger b_i^\dagger a_l). \quad (3.75)$$

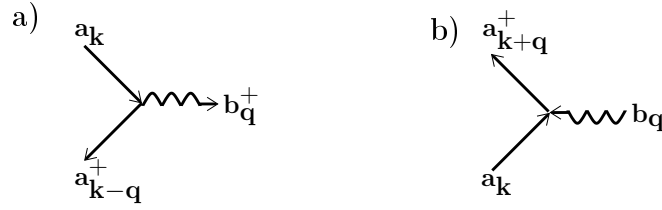


Figure 3.57: Feynman diagrams describing the processes of a) phonon emission and b) phonon absorption. $a_{\mathbf{k}}^+$ and $a_{\mathbf{k}}$ are the creation and the annihilation operators for electrons with the wave vector \mathbf{k} , respectively. In analogy, the creation and the annihilation operators for phonons are denoted by $b_{\mathbf{q}}^+$ and $b_{\mathbf{q}}$.

Using the Heisenberg equation, an equation of motion for the microscopic polarisation $p_{\mathbf{k}}$ can be derived yielding

$$\dot{p}_{\mathbf{k}}(t)|_{c-ph} = \frac{i}{\hbar} \sum_{\mathbf{q}, \gamma, \lambda} \left[g_{\mathbf{k}, \mathbf{q}, \mathbf{k}+\mathbf{q}}^{c\lambda, \gamma*} S_{\mathbf{k}, \mathbf{q}, \mathbf{k}+\mathbf{q}}^{v\lambda, \gamma} - g_{\mathbf{k}+\mathbf{q}, \mathbf{q}, \mathbf{k}}^{\lambda v, \gamma*} S_{\mathbf{k}+\mathbf{q}, \mathbf{q}, \mathbf{k}}^{\lambda c, \gamma} + g_{\mathbf{k}+\mathbf{q}, \mathbf{q}, \mathbf{k}}^{\lambda c, \gamma} S_{\mathbf{k}+\mathbf{q}, \mathbf{q}, \mathbf{k}}^{\lambda v, \gamma*} - g_{\mathbf{k}, \mathbf{q}, \mathbf{k}+\mathbf{q}}^{v\lambda, \gamma} S_{\mathbf{k}, \mathbf{q}, \mathbf{k}+\mathbf{q}}^{c\lambda, \gamma*} \right]. \quad (3.76)$$

The appearing phonon-assisted quantities

$$S_{\mathbf{k}_1, \mathbf{q}, \mathbf{k}_2}^{\lambda_1 \lambda_2, \gamma} = \langle a_{\lambda_1 \mathbf{k}_1}^+ b_{\gamma \mathbf{q}} a_{\lambda_2 \mathbf{k}_2} \rangle, \quad S_{\mathbf{k}_1, \mathbf{q}, \mathbf{k}_2}^{\lambda_1 \lambda_2, \gamma*} = \langle a_{\lambda_2 \mathbf{k}_2}^+ b_{\gamma \mathbf{q}}^+ a_{\lambda_1 \mathbf{k}_1} \rangle \quad (3.77)$$

describe the transition of a carrier accompanied by phonon emission or absorption, see Fig. 3.57. Their dynamics is calculated beyond the Markov approximation since the formation of phonon sidebands is in the focus of interest. The latter can only appear if energy conservation is not strictly valid for all times. Using again the Heisenberg equation and the Hamiltonian from Eq. (3.74) leads to an equation of motion for the phonon-assisted quantities

$$\dot{S}_{\mathbf{k}_1, \mathbf{q}, \mathbf{k}_2}^{vc, \gamma} = -i(\omega_{c\mathbf{k}_2} - \omega_{v\mathbf{k}_1} + \omega_{\gamma\mathbf{q}}) S_{\mathbf{k}_1, \mathbf{q}, \mathbf{k}_2}^{vc, \gamma} + (n_{\gamma\mathbf{q}} + 1) g_{\mathbf{k}_1, \mathbf{q}, \mathbf{k}_2}^{cc, \gamma*} (p_{\mathbf{k}_1} - p_{\mathbf{k}_2}) + \sum_{\mathbf{k}'} \left[\left(V_{v\mathbf{k}_1, c\mathbf{k}'+\mathbf{q}}^{ck_2, vk'} - V_{c\mathbf{k}'+\mathbf{q}, v\mathbf{k}_1}^{ck_2, vk'} \right) S_{\mathbf{k}', \mathbf{q}, \mathbf{k}'+\mathbf{q}}^{vc, \gamma} + \left(V_{c\mathbf{k}_2, v\mathbf{k}'}^{ck_2, vk'} - V_{v\mathbf{k}', v\mathbf{k}_2}^{ck_2, vk'} \right) S_{\mathbf{k}_1, \mathbf{q}, \mathbf{k}_2}^{vc, \gamma} \right]. \quad (3.78)$$

The phonon occupation number $n_{\gamma\mathbf{q}}$ is given by the Bose-Einstein distribution within the bath approximation.¹ The first term coming from the free-carrier and the free-phonon part of the Hamiltonian reveals the expected position of the phonon sidebands corresponding to the phonon energy $\hbar\omega_{\gamma\mathbf{q}}$. The second contribution stems from the carrier-phonon Hamiltonian. It shows that the phonon assisted quantity $S_{\mathbf{k}_1, \mathbf{q}, \mathbf{k}_2}^{vc, \gamma}$ is driven by the electron-phonon matrix element $g_{\mathbf{k}_1, \mathbf{q}, \mathbf{k}_2}^{cc, \gamma*}$ and the difference of the microscopic polarization for the two wave vectors \mathbf{k}_1 and \mathbf{k}_2 . Finally, the third term describes the exciton-phonon coupling containing the Coulomb matrix elements $V_{l_3, l_4}^{l_1, l_2}$ where l_i is a compound index containing the band index $\lambda_i = c, v$ and the wave vector \mathbf{k}_i . In analogy to the excitonic contribution in the Bloch equation for $p_{\mathbf{k}}$, there is one part ($\propto S_{\mathbf{k}', \mathbf{q}, \mathbf{k}'+\mathbf{q}}^{vc, \gamma}$) that leads to a renormalization of the energy and one part ($\propto S_{\mathbf{k}', \mathbf{q}, \mathbf{k}'+\mathbf{q}}^{vc, \gamma}$) that is responsible for a transfer of the oscillator strength to the phonon sidebands.

Now, all ingredients are available to describe the exciton-phonon dynamics in carbon nanotubes. The numerical evaluation of the differential equations for the microscopic polarisation and the phonon-assisted quantities will be carried out in the near future.

Chapter 4

Quantum Dots

In this chapter, a theoretical description of the nonlinear turn-on dynamics of electrically pumped InAs/GaAs QD semiconductor lasers is presented. Furthermore, the gain dynamics in QD semiconductor optical amplifiers is investigated. The chapter starts with an introduction into the structure and symmetry of quasi-zero-dimensional QDs. The theoretical model is based on the semiconductor Bloch equations including microscopically calculated Coulomb scattering rates, which describe Auger transitions between localized QD and continuous WL states. The latter are shown to be crucial for a better understanding of both the ultrafast gain dynamics in quantum dot amplifiers and the turn-on dynamics in quantum dot lasers.

4.1 Introduction

Quantum dots are semiconductor heterostructures with a size of a few nanometers in all three dimensions. They are in the focus of current research activities and attract a tremendous technological interest due to their unique optical and electronic properties.¹²⁴

In the last decades rapid progress in the area of growth techniques enabled scientists to produce semiconductor structures providing carrier confinement in all three spatial directions.¹⁹ In the beginning, the focus was on techniques, such as lithographic patterning and etching of quantum wells. In the 90s, Stranski-Krastanow growth, which is driven by self-organisation phenomena at the surface of strongly strained semiconductor structures, was realised. This process enables easy and fast fabrication of large densities ($> 10^{10} \text{ m}^{-2}$) of small QDs ($< 10 \text{ nm}$).¹⁹ Such dots form the basis of novel opto-electronic devices for future communication systems, such as edge and surface emitting lasers and amplifiers. To achieve good performance, the density of defects in a QD material and its interface to the surrounding matrix has to be as low as possible. QD fabrication using self-organised growth

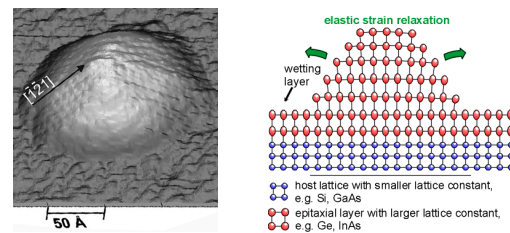


Figure 4.1: A pyramidal quantum dot (taken from Marquez et al.)¹⁸ and elastic strain evolving during the Stranski-Krastanow growth of self-assembled QDs (Max-Planck Institute for Solid State Research) are illustrated.

seems to be predestined to achieve this goal, since all interfaces are formed in-situ during crystal growth.¹⁹ In this chapter, semiconductor structures based on InAs/GaAs are in the focus of investigation. In these structures, QDs are small regions consisting of InAs buried in a GaAs substrate. They form spontaneously on a wetting-layer under certain conditions during molecular beam epitaxy (MBE) as well as in metal organic chemical vapour deposition (MOCVD) growth, when a material is grown on a substrate to which it is not lattice-matched. The resulting strain produces pyramid-shaped (Fig. 4.1) as well as lens-, cone-, or dome-shaped QDs in the interface between the materials.¹⁹

QDs have unique optical and electronic properties arising from their low dimensionality. Their size in all three dimensions is comparable to the carriers' de Broglie wavelength $\lambda_b = \frac{h}{\sqrt{3mk_B T}} \approx 6$ nm at room temperature. The consequence of this quantum confinement is that the charge carriers in a QD can only have discrete energy levels - like in atoms. This is the reason why QDs are often called *artificial atoms*. The energy levels can be controlled by changing the size and the shape of QDs. Since they can only be populated by two charge carriers due to the Pauli exclusion principle, it is easier to reach an efficient inversion and, hence, ultra low threshold current densities for QD lasers are predicted.³⁶ The reason for this advantageous characteristic is due to their characteristic density of states (DOS), see Fig. 1.1.

Currently, there is an increasing interest in developing infrared QD lasers for high-speed data transmission. These lasers show a high potential for fast dynamical response, which is strongly characterized by the frequency and the damping rate of relaxation oscillations (ROs).²⁰ The latter are oscillations of the photon density around its steady state evolving during turn-on processes of a gain switched laser, see Fig. 4.2. Damped ROs are known to be advantageous for open eyes* and low bit-error rates (BER) at large bit rates.¹²⁶⁻¹²⁸ QD lasers have been found to show a strong damping of ROs compared to quantum well lasers.^{21,22} The underlying dynamic mechanisms are still being discussed in literature^{23,24} One goal of this work is to contribute to a better understanding of the turn-on dynamics in QD lasers.

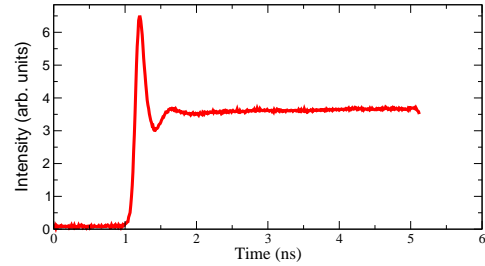


Figure 4.2: Relaxation oscillations evolving during the turn-on dynamics of QD lasers (measured by M. Kuntz).¹²⁵

In addition to the application as semiconductor lasers, InAs/GaAs QDs are also used for the development of semiconductor optical amplifiers (QD-SOAs). Their application in ultrafast ethernet networks requires a high frequency response, which demands an ultrafast gain recovery. Consequently, efficient scattering channels are needed to refill the QD ground state. Having a signal pulse sequence with a delay time τ_0 between the single pulses requires a gain recovery time shorter than τ_0 to enable the amplification of the following pulse. One way to accelerate the refilling of QD states is to increase the injection current, see Fig. 4.3. The latter enhances the probability for capture of charge carriers from the continuous WL states into the bound QD states. As a result, the gain recovery is accelerated.

*An eye pattern diagram consists of a successive bitwise superposition of an optical signal stream. It shows the capability of a laser to send data at a certain transmission rate and a certain output power. Open eyes are an important sign for an optimal performance of a laser.¹²⁵

However, recent experiments show that there is a limiting delay time τ_0 , below which the QDs cannot be refilled completely. The limiting mechanisms for the ultrafast gain recovery in QD-SOAs are still not understood and present a substantial challenge in current research.

In this chapter, both the generation of strongly damped relaxation oscillations in QD lasers as well as the ultrafast gain recovery in QD-SOAs are addressed by a microscopic approach containing the semiconductor Bloch equations for the polarisation and population dynamics. In the case of QD lasers, the rate equation limit is considered, since the turn-on dynamics is on a nanosecond time scale. The incorporated microscopically calculated Coulomb scattering rates describe the Auger transitions between localized QD and continuous WL states. The Coulomb interaction is found to strongly influence both the turn-on dynamics of QD lasers and the gain dynamics of QD amplifiers.

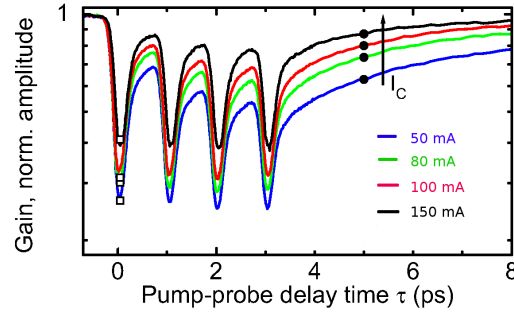


Figure 4.3: Experiment: Ultrafast gain dynamics in electrically pumped QD-SOAs as a function of the injection current (measured by Gomis et al.).²⁵

4.2 Structure and symmetry

The investigated QD-WL structure is illustrated in Fig. 4.4. In self-organized growth quantum dots of pyramidal shape are obtained,¹⁹ see Fig. 4.1. However, a quantum dot laser consists of several QD layers. In these structures, the QDs are likely to lose their tip and rather resemble lenses, as sketched in Fig. 4.4a. Then, the ground state wave function has cylindrical symmetry.¹⁹ Furthermore, the confinement in the z -direction is much stronger than within the plane. The wave function of such a QD-WL structure can be separated in an in-plane and a z -component within the effective mass approximation.¹²⁹ The quantum dots are assumed to have a small aspect ratio, i.e. the height is considered to be small in comparison to the in-plane size. Throughout

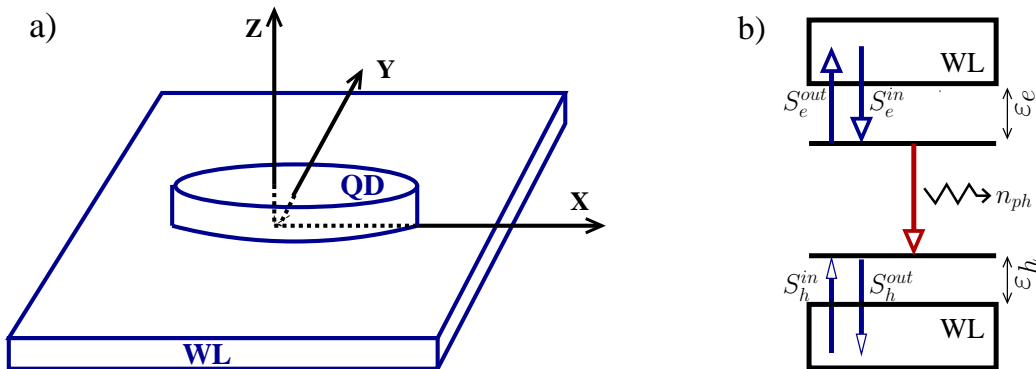


Figure 4.4: a) Lens-shaped quantum dot and the surrounding wetting layer. b) Sketch of electron and hole QD and WL states and their interaction via Coulomb scattering described by the rates S^{in} and S^{out} . The generated photons are described by the photon density n_{ph} .

this work, QDs with an in-plane size of 17 nm and a height of 4 nm are considered. Under this condition, the eigenstates describing the in-plane component of the QD can be approximated by the eigenfunctions of a two-dimensional harmonic oscillator.¹³⁰ The z -component corresponds to the eigenfunctions of a finite barrier well.

The in-plane energy of the charge carriers in WL states is calculated within the effective-mass approximation (see Sec. 2.3.1), yielding

$$E_b(\mathbf{k}) = \frac{\hbar^2 \mathbf{k}^2}{2m_b^*} \quad (4.1)$$

with the effective mass m_b^* . The energy of charge carriers in QDs is determined by simple \mathbf{k} -independent levels $E_{b,n}$ with $b = e, h$ and $n = 0, 1, 2, \dots$. Since the charge carriers are entirely confined in all three spatial directions, they cannot have a defined wave vector according to the uncertainty principle of quantum mechanics. The energies of bound QD states in dependence on the length of the QD can be found in Stier et al.¹³¹ For the investigated QDs, the energy of the electron ground state $\varepsilon_e = 240$ meV and of the hole ground state $\varepsilon_h = 105$ meV are given with respect to the energy of the corresponding WL edge, see Fig. 4.4b. These values are valid at a temperature of 0 K. The Varshni equation¹³² can be used to calculate the corresponding energies at higher temperatures. However, here only the relative energies are of importance. Assuming the same Varshni coefficients for both WL and QD states, the energy difference does not change with the temperature. Note that the WL consists of both InAs and GaAs, while the QDs only contain InAs. Hence, an increase in temperature might slightly change the energy separation between the QD ground state and the WL. This difference is assumed to be small and are neglected in the following.

Figure 4.4b sketches the dynamics of an electrically pumped QD laser. A two-level system for electrons and holes in QDs is considered, assuming the carrier relaxation processes within the QD states to be much faster than capture processes from the WL states.¹²⁹ As a result, only the energetically lowest electron and hole levels in QDs contribute crucially to the laser dynamics. The laser is pumped by a Gaussian-shaped electrical pulse injecting charge carriers into the continuous WL states. Then, driven by the Coulomb interaction, electrons and holes can be captured into bound QD states and relax radiatively via spontaneous or induced emission. The corresponding scattering and radiative processes are described within an approach combining the rate equations (QD laser) or the semiconductor Bloch equations (QD amplifier) with microscopically calculated Coulomb scattering rates. The latter are determined by considering the Coulomb interaction up to the second order in the screened Coulomb potential. Since the focus lies on the investigation of the gain regime, i.e. the WL carrier density is very high, the capture dynamics within the QD-WL structure is assumed to be dominated by Coulomb scattering (nonlocal Auger recombination).^{133,134} Hence, electron-phonon processes are expected to be of less importance, and thus will be neglected.

4.3 Wave functions

For a WL extended in the x - y plane, as shown in Fig. 4.4a, the wave function for the entire QD-WL system can be separated into an in-plane and a z -component within the effective mass approximation yielding¹²⁹

$$\Psi_{i,\sigma}^b(\mathbf{r}) = \varphi_i^b(\boldsymbol{\rho}) \xi_\sigma^b(z) u^b(\mathbf{r}), \quad (4.2)$$

where $u^b(r)$ are Bloch functions with $b = e, h$ denoting the charge carrier type, $\varphi_i^b(\rho)$ is the in-plane part of the wave function, and $\xi_\sigma^b(z)$ is the z -component of the wave function with the quantum number σ . As mentioned above, the in-plane component of the wave function for lens-shaped QD with a small aspect ratio resembles in good approximation the eigenfunctions of the two-dimensional harmonic oscillator^{27,130} (Fig. 4.5a)

$$\varphi_{QD}^b(\rho) = \frac{\beta_b \sqrt{A}}{\sqrt{\pi}} \exp\left(-\frac{1}{2}\beta_b^2 \rho^2\right) \quad (4.3)$$

with $\beta_b = \sqrt{\frac{m_b^* \omega_b}{\hbar}}$, the electron (hole) effective mass m_b^* , the oscillator frequency ω_b , and the normalization area A . The values for the effective mass for electrons $m_e^* = 0.043m_0$ and holes $m_h^* = 0.45m_0$ are taken as the average of the corresponding values for GaAs and InAs.¹³⁵ Assuming that only the ground state is of importance for scattering processes, the oscillator energy $\hbar\omega_b$ corresponds to the QD ground state energy ε_b .

The strong confinement in the direction perpendicular to the WL is described by the eigenfunctions of the finite barrier well. To reduce the numerical complexity, the eigenfunctions of an infinite barrier well is considered within the effective well width approximation. Here, the wave function of a finite barrier well with a physical well width L is approximated by the infinite barrier wave function with an effective width L_{eff} , as shown in Fig. 4.5b. The perpendicular component of the wave function is given by

$$\xi_n^{(+)}(z) = \begin{cases} \sqrt{\frac{2}{L_{\text{eff}}}} \cos\left[\frac{\pi}{L_{\text{eff}}}(2n+1)z\right] & \text{for } |z| \leq L_{\text{eff}}/2, \\ 0 & \text{for } |z| > L_{\text{eff}}/2, \end{cases} \quad (4.4)$$

$$\xi_n^{(-)}(z) = \begin{cases} \sqrt{\frac{2}{L_{\text{eff}}}} \sin\left[\frac{\pi}{2L_{\text{eff}}}nz\right] & \text{for } |z| \leq L_{\text{eff}}/2, \\ 0 & \text{for } |z| > L_{\text{eff}}/2 \end{cases} \quad (4.5)$$

with the effective well width $L_{\text{eff}} = 8$ nm, see Fig. 4.5b. These eigenfunctions are independent of the charge carrier type b . $\xi_n^{(+)}(z)$ is valid for even parity, while $\xi_n^{(-)}(z)$ describes the case of uneven parity. For a small WL thickness and a small QD height, the energy spacing of the levels due to the confinement in the z -direction is large. Hence, it is sufficient to consider only the lowest quantum number $n = 0$. Furthermore, the limit of equal heights of the QDs and the WL is assumed leading to the same z -confinement for both QDs and the WL. In this case, the confinement of the investigated QD-WL system is completely given by the strain in the x-y plane.¹²⁹

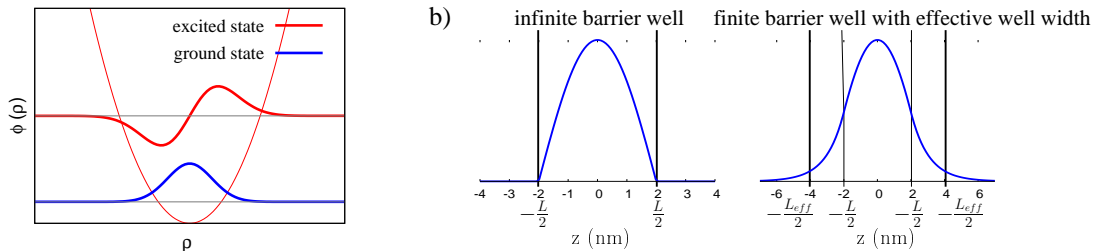


Figure 4.5: a) Ground and first excited state of the two-dimensional harmonic oscillator. b) Illustration of the effective well width approximation. At $\frac{L_{\text{eff}}}{2}$, the wave functions of the finite well have decreased to one tenth of their maximal value. Within the effective well width approximation, the eigenfunction of the infinite barrier well can be considered by including the effective well width L_{eff} .

The in-plane component of the wave function of the WL states is described by orthogonalized plane waves (OPWs)¹³⁶

$$|\varphi_{\mathbf{k}}^b\rangle = \frac{1}{N_b(\mathbf{k})} \left(|\tilde{\varphi}_{\mathbf{k}}\rangle - \langle\varphi_{QD}^b|\tilde{\varphi}_{\mathbf{k}}\rangle |\varphi_{QD}^b\rangle \right) \quad (4.6)$$

with the normalization factor $N_b(\mathbf{k}) = \sqrt{1 - |\langle\varphi_{QD}^b|\tilde{\varphi}_{\mathbf{k}}\rangle|^2}$ and the plane waves (PWs) $\tilde{\varphi}_{\mathbf{k}} = \frac{1}{\sqrt{A}} \exp(i\mathbf{k} \cdot \boldsymbol{\rho})$. The overlap between the QD eigenfunction φ_{QD}^b and the PWs (as eigenfunctions of the WL without QDs) is given by

$$\langle\varphi_{QD}^b|\tilde{\varphi}_{\mathbf{k}}\rangle = \frac{1}{A} \int_A \varphi_{QD}^b(\boldsymbol{\rho}) \tilde{\varphi}_{\mathbf{k}}(\boldsymbol{\rho}) d^2\rho = \frac{2\sqrt{\pi}}{\sqrt{A}\beta_b} \underbrace{\exp\left(-\frac{k^2}{2\beta_b^2}\right)}_{\equiv \alpha_b(k)}.$$

This overlap will turn out to be of great importance especially for hole states, since they are energetically closer to the WL states. The OPWs read in real space

$$\varphi_{\mathbf{k}}^b(\boldsymbol{\rho}) = \frac{1}{N_b(k)} \left[\exp(i\mathbf{k} \cdot \boldsymbol{\rho}) - 2\alpha_b(k) \exp\left(-\frac{1}{2}\beta_b^2\rho^2\right) \right]. \quad (4.7)$$

Exploiting the normalization condition $\langle\varphi_{\mathbf{k}}^b|\varphi_{\mathbf{k}}^b\rangle = 1$ yields

$$N_b(k) = \sqrt{1 - \frac{4\pi}{A\beta_b^2} \alpha_b^2(k)}. \quad (4.8)$$

The OPWs are more realistic than PWs, since they take the influence of the QD confinement potential into account by orthogonalizing the plane waves $\tilde{\varphi}_{\mathbf{k}}$ to the bound QD state $\varphi_{QD}^b(\boldsymbol{\rho})$. The PW approach leads to considerably larger Coulomb matrix elements and scattering rates, as will be shown in the next section.

4.4 Matrix elements

The dynamics of QD lasers and amplifiers is described by taking the light-matter and the Coulomb interaction into account. The strength of the first is given by the optical matrix element and of the second by the Coulomb matrix element.

4.4.1 Optical matrix elements

In this work, the $\mathbf{r} \cdot \mathbf{E}$ approach is used for the investigations on QDs, since the optical matrix element $\mathbf{d}_{l,l'}$ (also called optical dipole matrix element) is available from experimental data. Within this approach, the carrier-field coupling is described by (for more details, see Sec. 2.4)

$$H_{c-f}^{(r \cdot E)} = \sum_{l,l'} \mathbf{d}_{l,l'} \cdot \mathbf{E}(t) a_l^\dagger a_{l'} \quad (4.9)$$

with the dipole matrix element

$$\mathbf{d}_{l,l'} = \frac{e_0}{V} \int d^3r \Phi_l^*(\mathbf{r}) \mathbf{r} \Phi_{l'}(\mathbf{r}). \quad (4.10)$$

According to experimental results,²⁵ the interband dipole moment d_{vc} is in the range of 0.3 – 0.6 e_0 nm.

4.4.2 Coulomb matrix elements

In this subsection, only the key steps of the derivation of Coulomb matrix elements are shown. A more detailed description is given in App. C.2.

The starting point is the carrier-carrier Hamiltonian (see also Sec. 2.4)

$$H_{\text{c-c}} = \frac{1}{2} \sum_{l_1, l_2, l_3, l_4} V_{l_3, l_4}^{l_1, l_2} a_{l_1}^+ a_{l_2}^+ a_{l_4} a_{l_3} \quad (4.11)$$

with the unscreened Coulomb interaction matrix element

$$V_{l_3, l_4}^{l_1, l_2} = \int d^3 r \int d^3 r' \Phi_{l_1}^*(\mathbf{r}) \Phi_{l_2}^*(\mathbf{r}') V(\mathbf{r} - \mathbf{r}') \Phi_{l_3}(\mathbf{r}') \Phi_{l_4}(\mathbf{r}). \quad (4.12)$$

Using the two-dimensional Fourier transform of the Coulomb potential

$$V_q = \frac{e^2}{2\epsilon_0 q} e^{-q|z-z'|}, \quad (4.13)$$

furthermore applying the separation of the wave function [Eq. (4.2)] and the orthogonality of the Bloch functions $\int_V d^3 r u_i^*(r) u_j(r) = V \delta_{b_i, b_j}$ yields

$$\begin{aligned} V_{l_3, l_4}^{l_1, l_2} &= \frac{1}{A} \sum_q \frac{e^2}{2\epsilon_0 q} \int dz \int dz' \xi_0(z) \xi_0^*(z') e^{-q|z-z'|} \xi_0^*(z') \xi_0(z) \delta_{b_1 b_4} \delta_{b_2 b_3} \times \\ &\quad \times \int d^2 \rho \varphi_{i_1}^{b_1*}(\boldsymbol{\rho}) \varphi_{i_4}^{b_4}(\boldsymbol{\rho}) e^{-i\mathbf{q}\cdot\boldsymbol{\rho}} \int d^2 \rho' \varphi_{i_2}^{b_2*}(\boldsymbol{\rho}') \varphi_{i_3}^{b_3}(\boldsymbol{\rho}') e^{i\mathbf{q}\cdot\boldsymbol{\rho}'} . \end{aligned} \quad (4.14)$$

In this work, the focus lies on the capture of charge carriers from arbitrary WL states with the wave vectors \mathbf{k} into the electron or hole QD ground state. Due to the complete localization of charge carriers within QDs, the wave vector \mathbf{k} is not well defined. These processes are described by the Coulomb matrix element $V_{b\mathbf{k}_1, b'\mathbf{k}_3}^{b, b'\mathbf{k}_2}$, see Fig. 4.6. The Coulomb interaction is a two-particle process, i.e. while one charge carrier, denoted by (b, \mathbf{k}_1) , is captured into a QD state b , another carrier (electron or hole) relaxes within the WL guaranteeing the conservation of energy for the entire process.

After inserting the corresponding wave functions (described in the previous subsection) into Eq. (4.14), an expression for the Coulomb matrix element is found (see also App. C.2)

$$\begin{aligned} V_{b\mathbf{k}_1, b'\mathbf{k}_3}^{b, b'\mathbf{k}_2} &= C_1 \frac{1}{q} F(q) \left[\alpha_b(\mathbf{k}_1 - \mathbf{q}) - \alpha_b(\mathbf{k}_1) \alpha_{b'}^{\frac{1}{2}}(\mathbf{q}) \right] \delta_{\mathbf{q}, \mathbf{k}_2 - \mathbf{k}_3} \\ &\quad - \sum_q C_2 \frac{1}{q} F(q) \left[\alpha_b(\mathbf{k}_1 - \mathbf{q}) \alpha_{b'}^{\text{opw}}(\mathbf{q}, \mathbf{k}_2, \mathbf{k}_3) + \alpha_b(\mathbf{k}_1) \alpha_{b'}^{\frac{1}{2}}(\mathbf{q}) \alpha_{b'}^{\text{opw}}(\mathbf{q}, \mathbf{k}_2, \mathbf{k}_3) \right] \end{aligned} \quad (4.15)$$

with

$$\alpha_{b'}^{\text{opw}}(\mathbf{q}, \mathbf{k}_2, \mathbf{k}_3) = \alpha_{b'}(\mathbf{k}_3) \alpha_{b'}(\mathbf{q} - \mathbf{k}_2) + \alpha_{b'}(\mathbf{k}_2) \alpha_{b'}(\mathbf{q} + \mathbf{k}_3) - \alpha_{b'}(\mathbf{k}_2) \alpha_{b'}(\mathbf{k}_3) \alpha_{b'}(\mathbf{q}). \quad (4.16)$$

Here, the abbreviation $\alpha(\mathbf{k}) = \exp(-\frac{|\mathbf{k}|^2}{2\beta^2})$ and the coefficients $C_1 = \frac{e_0^2 \sqrt{\pi}}{\beta_b \epsilon_0 A^{\frac{3}{2}} N_b(\mathbf{k}_1) N_{b'}(\mathbf{k}_2) N_{b'}(\mathbf{k}_3)}$ and $C_2 = \frac{4}{A} \frac{\pi}{\beta_b^2}$ have been introduced. The first blue colored term in Eq. (4.15) stems from the plane wave part of the WL wave function. The normalization area A vanishes in the calculation

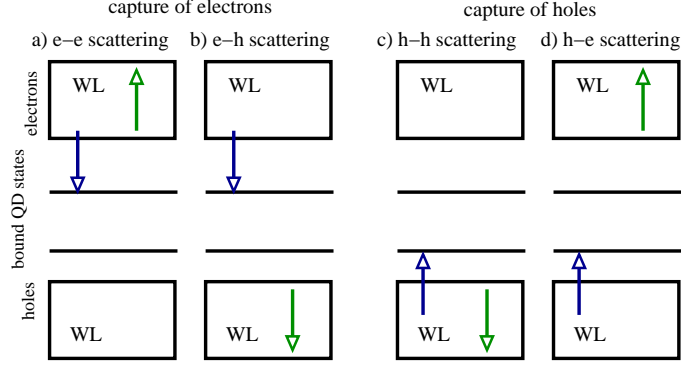


Figure 4.6: Illustration of the considered electron and hole Auger processes between the bound QD and continuous WL states. Both pure scattering (electron-electron and hole-hole) as well as mixed scattering (electron-hole and hole-electron) is shown.

and does not have any influence on the scattering rates. The form factor $F(q)$ arising from the z -integral in Eq. (4.14) is defined as

$$F(q) = \left[\frac{2}{Lq} + \frac{1}{Lq + \frac{4\pi^2}{Lq}} - \frac{2}{L^6} (1 - e^{-Lq}) \left(\frac{4\pi^2}{q(q^2 + \frac{4\pi^2}{L^2})} \right)^2 \right] \quad (4.17)$$

with L corresponding to the effective well width (QD and WL height), as discussed in the previous section. Furthermore, due to a high charge carrier density w_b in the wetting layer, screening effects play an important role and have to be included in the model. They are considered within the Lindhard approximation^{36,42}

$$\varepsilon(q, \omega) = 1 - V_q \sum_{b,k} \frac{\rho_{k-q}^b - \rho_k^b}{\hbar(\omega + i\gamma) + \varepsilon_{k-q}^b - \varepsilon_k^b}. \quad (4.18)$$

Applying the static limit, i.e. $(\omega + i\gamma) \rightarrow 0$, and the long-wavelength limit, i.e. $q \propto \lambda^{-1} \rightarrow 0$, Eq. (4.18) can be Taylor expanded in terms of q leading to the screened Coulomb potential $W(q)$ (for more details, see App. A)

$$W(q) \equiv \frac{V_q}{\varepsilon_{bg}\varepsilon(q)} = \frac{V_q}{1 + \frac{\kappa}{q}} \quad (4.19)$$

with the two-dimensional inverse screening length

$$\kappa = \sum_{b=e,h} \frac{m_b e_0^2}{2\pi\varepsilon_0\varepsilon_{bg}\hbar^2} \left[1 - \exp\left(-\frac{\hbar^2\pi w_b}{k_B T m_b}\right) \right]. \quad (4.20)$$

Furthermore, the screening effects arising from the surrounding medium have been considered by introducing the dielectric background constant $\varepsilon_{bg} = 14.2$. Its value is taken as the average of the corresponding values for GaAs and InAs.¹³⁵

4.5 Coulomb scattering rates

The description of the dynamics in InAs/GaAs QD lasers requires the inclusion of the interaction between discrete QD states and the continuous electron and hole WL states. The corresponding

Coulomb scattering rates are calculated microscopically as a function of the WL electron and hole density w_e and w_h . As shown in Sec. 2.4, the Coulomb contributions are taken into account up to the second order Born approximation, yielding the Boltzmann equation^{2,3}

$$\dot{\rho}_b = S_b^{in}(1 - \rho_b) - S_b^{out}\rho_b, \quad (4.21)$$

where ρ_b is the occupation probability in the electron or hole QD state ($b = e, h$). A detailed microscopic derivation of Eq. (4.21) is presented in App. A. The Boltzmann equation contains Coulomb in- and out-scattering rates S_b^{in} and S_b^{out}

$$S_b^{in/out} = \frac{2\pi}{\hbar} \sum_{\mathbf{k}_1 \mathbf{k}_3 \mathbf{k}_2 b'} W_{b\mathbf{k}_1, b'\mathbf{k}_3}^b (2W_{b\mathbf{k}_1, b'\mathbf{k}_3}^{b, b'\mathbf{k}_2*} - \delta_{b,b'} W_{b'\mathbf{k}_3, b\mathbf{k}_1}^{b, b'\mathbf{k}_2*}) f_{\mathbf{k}_1 \mathbf{k}_2 \mathbf{k}_3 b'}^{in/out, b} \delta(\varepsilon_0^b + \varepsilon_{\mathbf{k}_2}^{b'} - \varepsilon_{\mathbf{k}_1}^b - \varepsilon_{\mathbf{k}_3}^{b'}) \quad (4.22)$$

with the characteristic functions for in- and out-scattering

$$f_{\mathbf{k}_1 \mathbf{k}_2 \mathbf{k}_3 b'}^{in, b} = \rho_{\mathbf{k}_1}^b \rho_{\mathbf{k}_3}^{b'} (1 - \rho_{\mathbf{k}_2}^{b'}) \quad \text{and} \quad f_{\mathbf{k}_1 \mathbf{k}_2 \mathbf{k}_3 b'}^{out, b} = \rho_{\mathbf{k}_2}^{b'} (1 - \rho_{\mathbf{k}_3}^{b'}) (1 - \rho_{\mathbf{k}_1}^b). \quad (4.23)$$

The sum in Eq. (4.22) runs over all WL states (occupation probabilities $\rho_{\mathbf{k}_1}^b, \rho_{\mathbf{k}_3}^{b'}$, and $\rho_{\mathbf{k}_2}^b$). The respective single particle energies in the WL are denoted by $\varepsilon_{\mathbf{k}_1}^b, \varepsilon_{\mathbf{k}_2}^{b'}, \varepsilon_{\mathbf{k}_3}^{b'}$ and in the QD by ε_0^b . The summation over spin leads to a factor 2 in front of the direct term assuming that the wetting layer population is independent of the carrier spin. It also accounts for the Kronecker symbol in front of the exchange term. The latter only contributes to the pure electron-electron and hole-hole scattering processes due to the vanishing interference when electrons and holes with anti-parallel spin collide.¹³⁷

Furthermore, the relaxation rate approximation has been applied assuming that the carrier distributions are close to the quasi-equilibrium Fermi distributions, i.e. $\rho_{\mathbf{k}}^b = f_{\mathbf{k}}^b + \delta f_{\mathbf{k}}^b$ with $\delta f_{\mathbf{k}}^b \ll 1$ and the Fermi-Dirac distribution

$$f_{\mathbf{k}}^b = \frac{1}{1 + \exp\left(\frac{1}{k_B T} (\varepsilon_{\mathbf{k}}^b - \mu_b(T, w_b))\right)} \quad (4.24)$$

and the quasi-Fermi level $\mu_b(T, w_b)$. The latter can be obtained analytically in the two-dimensional case.⁴² First, the WL charge carrier density w_b is calculated

$$\begin{aligned} w_b &= \frac{1}{A} \sum_{\mathbf{k}, s} f_{b, \mathbf{k}} = \frac{2}{A} \sum_{\mathbf{k}} f_{b, \mathbf{k}} = \frac{1}{2\pi^2} \int d^2 k f_{b, \mathbf{k}} = \frac{1}{\pi} \int_0^\infty dk k \left[\exp\left(\frac{1}{k_B T} (\varepsilon_{\mathbf{k}}^b - \mu_b)\right) + 1 \right]^{-1} \\ &= \frac{m_b k_B T}{\pi \hbar^2} \int_1^\infty dx \left[x \left(x \exp\left[-\frac{1}{k_B T} \mu_b\right] + 1 \right) \right]^{-1} = \frac{m_b k_B T}{\pi \hbar^2} \ln \left[1 + \exp\left[\frac{1}{k_B T} \mu_b\right] \right] \end{aligned}$$

with the substitution $x \equiv \exp\left(\frac{1}{k_B T} \varepsilon_{\mathbf{k}}^b\right)$. Then, the quasi-Fermi level* can be obtained yielding

$$\mu_b(T, w_b) = k_B T \ln \left[\exp\left(\frac{\hbar^2 \pi w_b}{m_b k_B T}\right) - 1 \right]. \quad (4.25)$$

According to the relaxation rate approximation,³⁶ it can be assumed that the influence of $\delta f_{\mathbf{k}}$ on the scattering rates S^{in} and S^{out} is negligible, i.e. $S^{in}(\rho_{\mathbf{k}}) \approx S^{in}(f_{\mathbf{k}})$ and $S^{out}(\rho_{\mathbf{k}}) \approx S^{out}(f_{\mathbf{k}})$.

*In thermodynamical equilibrium, the system is characterized by an uniform, common temperature of the charge carriers and the lattice (thermal equilibrium) and an uniform chemical potential of the carriers (chemical equilibrium). In an electrically pumped laser, a global temperature can still be defined, but not a common chemical potential (Fermi level).¹³⁸ However, there is a quasi-equilibrium for electrons and holes with different quasi-Fermi levels. The latter are defined by the corresponding non-equilibrium electron or hole density.

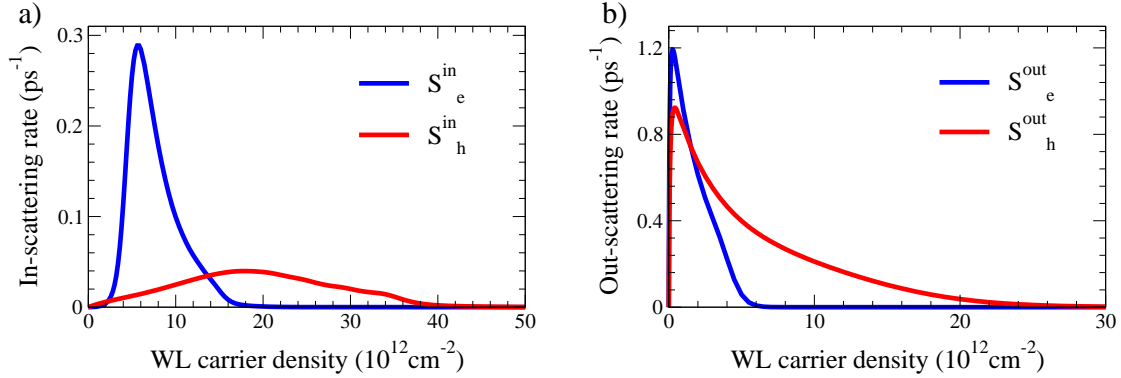


Figure 4.7: a) Coulomb in-scattering rates S_b^{in} for electrons and holes as a function of the electron and hole WL carrier density, respectively. b) Coulomb out-scattering rates S_b^{out} for electrons and holes.

Inserting the Coulomb matrix elements from Eq. (4.15) into Eq. (4.22), an expression for the Coulomb scattering rates is obtained. Unfortunately, the integrals cannot be solved analytically. They are evaluated using the Simpson rule, a numerical method for solving definite integrals by approximating the function by a quadratic polynomial.¹³⁹

The scattering rates S_b^{in} and S_b^{out} are dependent on the WL carrier density w_b . The larger w_b , the more efficient is the scattering due to an increasing number of scattering partners. According to Fig. 4.6, the capture of electrons into the QD ground state is accompanied by another processes taking place either in the electron or hole WL. The electron in-scattering rate S_e^{in} , e.g., contains both the electron-electron (Fig. 4.6a) as well as the electron-hole process (Fig. 4.6b). Consequently, the scattering rate is a function of both the electron and hole WL carrier density $S_e^{in}(w_e, w_h)$. For the capture of holes, the argumentation is analogous, see Fig. 4.6c-d. Since the numerical evaluation of Eq. (4.22) contains six integrals, it would be very time and memory consuming to include the full dependence on both WL carrier densities. As will be shown in Sec. 4.7.2, the dynamics of $w_e(t)$ and $w_h(t)$ are similar. The different stationary values suggest the approximation $w_e(t) = g_c(j)w_h(t)$ with the ratio coefficient $g_c(j)$, which varies with the injection current density j .¹⁴⁰ A self-consistent calculation between the value of g_c and the ratio of the stationary values of w_e and w_h yields $g_c = 2.3$ for an injection current density of $1.9j_{th}$, where j_{th} is the threshold current density. This value is used throughout the work, unless explicitly stated otherwise. Now, the electron and hole scattering rates can be calculated as a function of w_e and w_h , respectively.

In Fig. 4.7, the Coulomb scattering rates for electron and hole capture processes in the investigated InAs/GaAs QD-WL structure are shown as a function of the respective WL electron and hole densities. Generally, the Coulomb scattering rates become larger for increasing WL carrier densities w_b due to the increase of available scattering partners. The Pauli exclusion principle, however, stops the increase at high w_b , resulting in maximal values for the scattering rates. The Pauli blocking terms affect the out-scattering processes much earlier (Fig. 4.7b), since they are proportional to $(1 - \rho_l^b)(1 - \rho_m^{b'})$, see Eq. (4.23). Due to their larger effective mass, the hole bands have a smaller curvature and the population of hole WL states is distributed over a larger k -range, as shown in Fig. 4.8. As a result, the Pauli exclusion principle influences the electrons more strongly explaining the quicker decrease of S_e^{out} . Furthermore, since the hole states are energetically closer to the WL edge, it is surprising to find S_e^{out} to be larger than S_h^{out} . This, however, is only the case, as long as the OPWs are used, see Fig. 4.9. Considering only the PWs, the hole out-scattering is, as expected, stronger. The larger reduction of the hole out-scattering arises from the stronger overlap between the QD and WL wave functions, see Eq. (4.6).

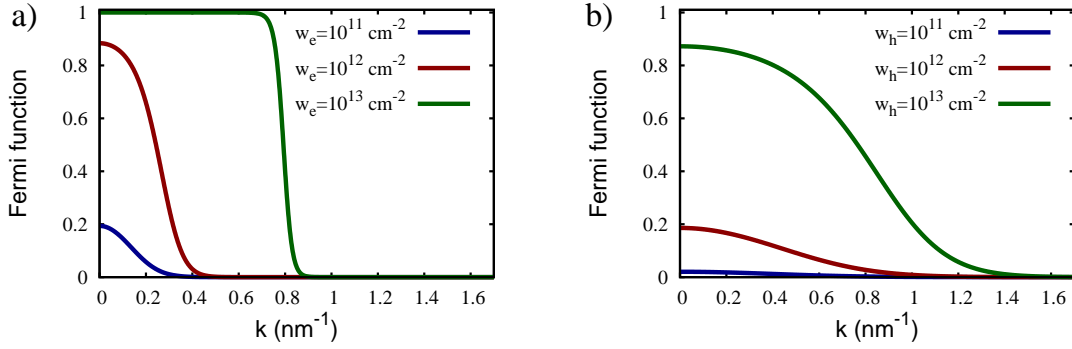


Figure 4.8: Fermi distribution of electrons and holes in the WL states for three different WL carrier densities at room temperature.

The in-scattering rates are proportional to the product of two occupation probabilities in the WL states $\rho_i^b \rho_m^b$, see Eq. (4.23). Consequently, they become dominant at higher WL carrier densities (at which the out-scattering is already diminished by Pauli blocking). At small w_b , the number of available scattering partners is low, as shown in Fig. 4.8. The WL states need to be filled first. Then, the in-scattering becomes more and more efficient and finally dominates over the out-scattering. At very high w_b , even the in-scattering becomes weaker, since the WL states become filled to a high percentage leading to a considerable decrease of the probability for the scattering processes within the WL (processes illustrated by red arrows in Fig. 4.6).

Figure 4.9 compares the Coulomb scattering rates for electrons and holes obtained within the approach of orthogonalized plane waves to the rates resulting from simple plane waves. Taking the influence of the QD confinement potential into account, i.e. applying the OPW method, leads to a general reduction of scattering rates. The hole rates are reduced by a factor of three, and the electron scattering is approximately half as efficient as within the PW approach. The enhanced Coulomb matrix elements and scattering rates within the OPW method are due to the non-vanishing overlap of QD and WL wave functions $\langle \varphi_{QD}^b | \tilde{\varphi} \rangle$. This overlap is higher for hole states, since they are energetically closer to the corresponding WL states. As a result, the enhancement of the scattering rates for holes is stronger, as can be seen in Fig. 4.9.

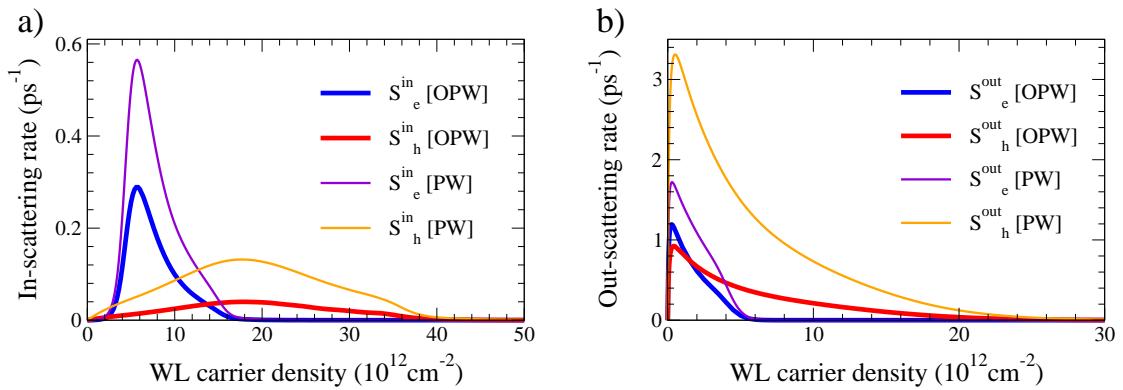


Figure 4.9: Comparison of a) Coulomb in-scattering and b) out-scattering rates for electrons and holes calculated within the orthogonalized plane wave (OPW) and the plane wave (PW) approach. The latter leads to enhanced rates due to the neglected overlap between QD and WL wave functions.

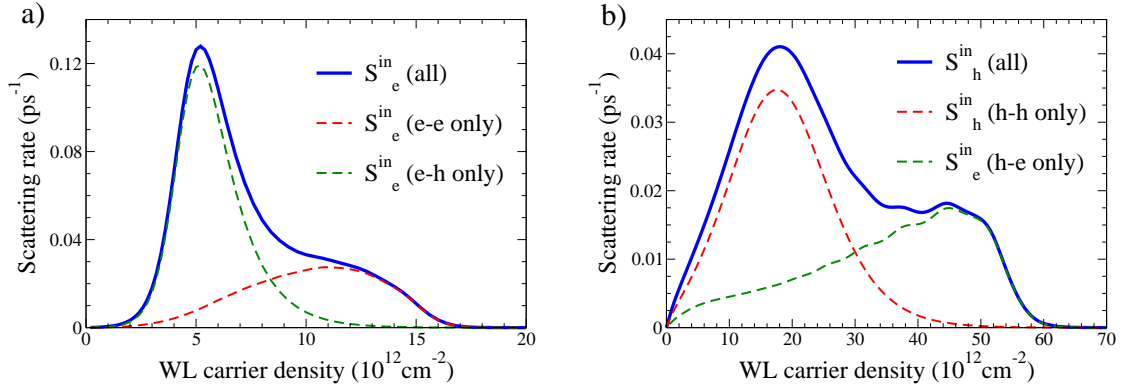


Figure 4.10: The importance of mixed charge carrier scattering processes is illustrated: a) Electron capture via electron-electron and electron-hole scattering, see Fig. 4.6a-b. b) Hole capture via hole-hole and hole-electron scattering, see Fig. 4.6c-d. To show the influence of mixed scattering process, the rates are calculated for a higher ratio between electron and hole WL stationary values: $w_h = 3.5w_e$. This can be achieved for low injection currents, as shown in Lüdge et al.¹⁴⁰ Note that the electron and hole scattering rates are plotted as a function of w_e and w_h , respectively.

The scattering rates for mixed electron-hole capture processes (Fig. 4.6b,d) are dependent on both electron and hole WL carrier densities. As described above, for numerical reasons the relation $w_h = 2.3w_e$ is assumed accounting for similar dynamics of w_e and w_h . Figure 4.10 illustrates the importance of the mixed process for the electron and hole in-scattering rates. The electron in-scattering S_e^{in} shows a maximum followed by a shoulder at higher WL carrier densities. The latter is ascribed to the pure electron-electron scattering, while the mixed scattering leads to the maximal value of S_e^{in} at $w_e = 5.7 \times 10^{12} \text{ cm}^{-2}$, see Fig. 4.10a. Due to the assumption that the hole WL carrier density w_h is 2.3 times larger than the corresponding electron WL carrier density w_e , electron-hole scattering already increases at relatively small w_e leading to the maximal in-scattering. Figure 4.10b shows the hole in-scattering rate calculated with and without the mixed hole-electron process. Here, the maximum at $w_h = 18 \times 10^{12} \text{ cm}^{-2}$ stems from the pure hole-hole scattering, while the shoulder arises from the mixed process. This again accounts for different stationary values of the electron and hole WL carrier densities. Since w_e is smaller than w_h , the pure hole-hole process is enhanced with respect to the mixed hole-electron process. The calculated ratio between the electron and the hole WL carrier density has an important influence on the in-scattering rates, as discussed in detail in Lüdge et al.¹⁴⁰ For out-scattering processes, the mixed contributions turn out to have an influence on the height of the scattering rates, but less on their qualitative shape, since the out-scattering is only important at low WL densities and decreases sharply right after the maximal value is reached.

4.5.1 T_1 and T_2 times

The $T_{1,b}$ time given by $(S_b^{in} + S_b^{out})^{-1}$ determines the decay of the electron and hole population ($b = e, h$), respectively. The T_2 time describes the decay of the coherence. Both times are calculated microscopically using the Boltzmann equation including Auger transitions between WL and QD states, as described in Sec. 4.5. Figure 4.11 shows both times as a function of the WL carrier density w_b . In agreement with the discussion of the scattering rates in the last section, both $T_{1,b}$ times decrease with increasing w_b , accounting for the stronger Coulomb scattering. The times are the shortest (≈ 1 ps) in the range of $(1-5) \times 10^{12} \text{ cm}^{-2}$. Then, the scattering rates are reduced and $T_{1,b}$ increase.

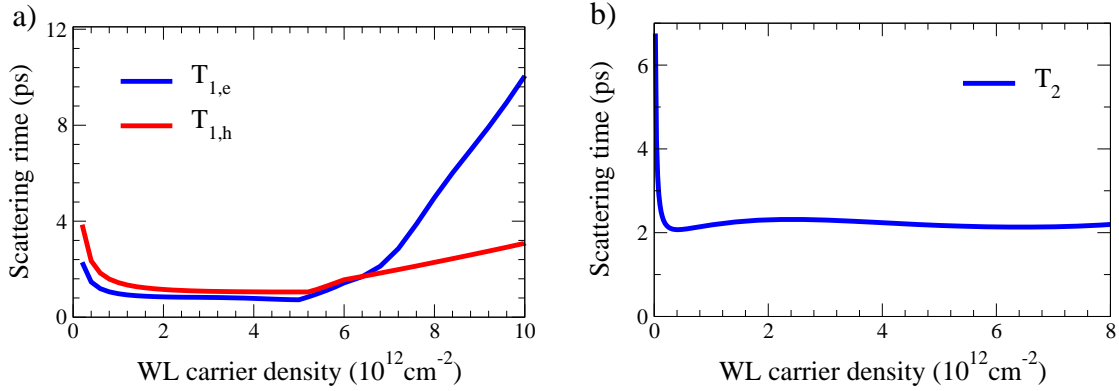


Figure 4.11: a) The Coulomb scattering times $T_{1,e}$ and $T_{1,h}$ for electrons and holes and b) the dephasing time¹⁴¹ T_2 are plotted as a function of the WL carrier density.

The T_2 time describing the coherence decay shows a similar behavior. It has been calculated by Kim et al.¹⁴¹, yielding

$$T_2 = \left[\frac{2\pi}{\hbar} \sum_{k_1 k_2 k_3 b'} \left(|W_{hk_1, b'k_3}^{h0, b'k_2}|^2 \delta(\varepsilon^e + \varepsilon_{k_2}^{b'} - \varepsilon_{k_3}^h - \varepsilon_{k_1}^{b'}) - |W_{ek_1, b'k_3}^{e0, b'k_2}|^2 \delta(\varepsilon^h + \varepsilon_{k_2}^{b'} - \varepsilon_{k_3}^e - \varepsilon_{k_1}^{b'}) \right) \left(f_{k_1}^{b'} f_{k_3}^e (1 - f_{k_2}^{b'}) + (1 - f_{k_1}^{b'}) (1 - f_{k_3}^e) f_{k_2}^{b'} \right) \right]^{-1}. \quad (4.26)$$

After a strong decrease at low WL carrier densities, the T_2 time remains approximately constant (≈ 2 ps). In conventional three-dimensional systems, the dephasing, i.e. the destruction of the phase coherence between the valence and conduction band, arises mainly from transitions between different states, i.e. from thermalization, energy relaxation, or recombination processes. In quantum dots, however, the dephasing of optical coherence stems mainly from virtual transitions.¹⁴² These do not lead to a change in the population dynamics. Hence, this contribution is often called pure dephasing. Since the energy separation between QD states can be few hundreds of meV, the probability for transitions between real states is suppressed, and pure dephasing plays an important role.¹⁴³ Dephasing times in QDs have been experimentally demonstrated to be in the range of picoseconds to femtoseconds, which strongly depends on the temperature.¹⁴⁴ The dephasing time can be separated into two different contributions

$$\frac{1}{T_2} = \frac{1}{T_{2,\text{scat}}} + \frac{1}{T_{2,\text{pure}}}. \quad (4.27)$$

The first term accounts for Coulomb driven scattering processes between the QD and WL states and is calculated microscopically,¹⁴¹ see Fig. 4.11b. The second term describes the contribution stemming from pure dephasing. The latter has been discussed in Lorke et al.¹³⁴ In this work, the value for the overall dephasing time $T_2 = 25$ fs at room temperature is adjusted to experimental data.¹⁴⁴ Its temperature dependence is assumed to be guided by the Coulomb part $T_{2,\text{scat}}$. This way, only the T_2 time for one temperature needs to be obtained from the experiment. Then, the corresponding values at other temperatures can be determined microscopically. Starting from the above value for room temperature, the T_2 times at 350 K, 400 K, 450 K, and 500 K, are calculated using Eq. (4.26), yielding $T_2 = 20$ fs, 17 fs, 15 fs, 13 fs, respectively.

4.6 Quantum dot amplifiers

Quantum dot semiconductor optical amplifiers (QD-SOAs) are gain media in which the signal pulse is amplified by the processes of induced emission. The main difference to QD lasers is the lack of a resonator. QD-SOAs have great potential for applications in high-speed data communication, since they show a much faster gain recovery time than conventional or quantum well SOAs.¹²⁴ This can be ascribed to the presence of the two-dimensional WL, which acts as a charge carrier reservoir enabling an ultrafast refilling of QD states. However, the amplification of ultrafast optical pulse trains with pulse repetition rates of up to 1 THz (corresponding to pulse delay times of 1 ps) is still a great challenge for current research.

4.6.1 Experiment

Figure 4.12 illustrates the experimental setup designed by Gomis et al.²⁵ at the TU University, Dortmund, for pump-probe studies of femtosecond pulse trains. Using two Michelson interferometers, up to four 150 fs long pulses with a delay time of $0.5 \text{ ps} < \tau_0 < 10 \text{ ps}$, corresponding to repetition rates of $100 \text{ GHz} < f_{rep} < 2 \text{ THz}$, are generated. The basic idea of a pump-probe experiment is that first, the sample is excited into a non-equilibrium state by a short strong pulse (pump pulse), then the relaxation of the sample back into the equilibrium is studied using a weak time delayed pulse, which has approximately no influence on the sample (probe pulse). Gomis et al.²⁵ investigated the gain dynamics of QD-SOAs at room temperature by a femtosecond pump-probe technique with heterodyne detection.²⁵ The latter is a standard technique to measure the amplitude and the phase of signals in collinear geometry in spatially extended sample. Here, pump and probe pulses are distinguished by inducing a small frequency shift between them. Before being injected into the amplifier, the probe pulse passes through an acousto-optical modulator, which shifts its frequency into the microwave range. The pump pulse remains unshifted. Furthermore, a frequency shifted reference pulse is injected into the amplifier before the pump-probe pulse. The detection consists of an interferometer, where the probe pulse is mixed with the reference pulse. The amplitude of the probe is measured by detecting the amplitude of the beat evolving due to the difference in the frequency shifts of the reference and the probe pulse. Note that a stream of frequency shifted reference pulses is needed to detect the change of the probe pulse due to the

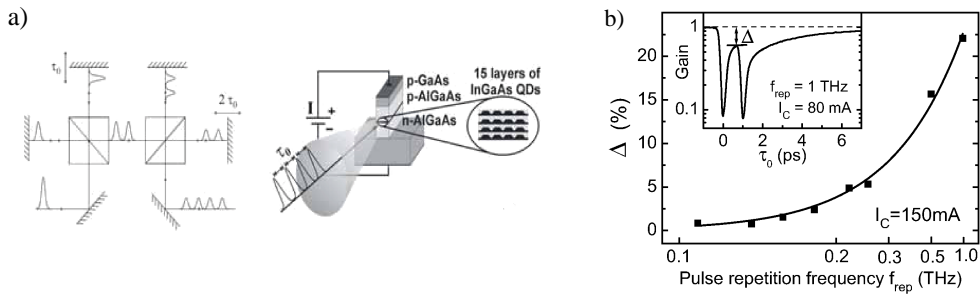


Figure 4.12: a) Sketch of the experimental setup (taken from Gomis et al.)²⁵ showing a two-stage Michelson interferometer where the ultrafast femtosecond pulse trains with a delay time of $\tau_0 = 1 \text{ ps}$ are generated. The wavelength is selected to be in resonance with the QD ground state. b) The pulse sequence is sent through an electrically contacted QD-SOA, and the gain is measured as a function of the electrical injection current and the repetition rate f_{rep} . The gain offset Δ , a measure of the gain recovery, is plotted over the pulse repetition frequency. It shows that the gain recovery becomes more and more incomplete with the increasing repetition frequency.

influence of the pump pulse.¹⁴⁵ When pump and probe pulse overlap, the resulting interference pattern produces a spatial modulation of the polarization. The corresponding absorption gratings scatter a part of the pump beam in the probe direction. This contribution has only an influence on the polarization dynamics. It is known as *coherent coupling* or *coherent artifact*.^{145,146}

The gain medium in the SOA is formed by 15 InAs/GaAs QD layers with a QD density of $2 \times 10^{10} \text{ cm}^{-2}$. The gain is normalized to the value measured at the transparency current $I = 7.5 \text{ mA}$. In pump-probe experiments, the pump pulse depletes the ground state resulting in a reduction of the gain, which is tested by the probe pulse. The gain recovers on a time scale of few hundreds of femtoseconds up to picoseconds. The gain recovery time is determined by the capture of charge carriers into the QD ground state from the two-dimensional WL states. It increases with the injection current. However, a complete gain recovery could not be reached for pulse repetition rates above 200 GHz, i.e. for delay times $\tau_0 \ll 5 \text{ ps}$, as shown in Fig. 4.12b. The higher the repetition frequency f_{rep} , i.e. the shorter the distance between the two pulses τ_0 in the sequence, the larger is the gain offset Δ and the more incomplete is the gain recovery. To achieve a better gain recovery at high f_{rep} , the refilling of QD states needs to be accelerated. The underlying mechanisms of the gain recovery are discussed in the following section.

4.6.2 Gain dynamics

The gain dynamics in QD-SOAs can be theoretically described by the semiconductor QD Bloch equations (derived in Sec. 2.4). Since the focus lies on obtaining a better insight into the elementary processes, which determine the gain dynamics of QD amplifier, a single pump-pulse experiment is modeled theoretically. Within the RWA (see Sec. 2.4.1), and for the resonant case with $\hbar\omega = \hbar\omega_{qd} = 0.95 \text{ eV}$ equations of motion for the microscopic polarisation $p(t)$, and the QD population probability of electrons $\rho^e(t)$ and holes $\rho^h(t)$ (Fig. 4.13) are obtained

$$\dot{p}(t) = -i\Omega(t)[\rho^e(t) + \rho^h(t) - 1] - \frac{1}{T_2}p(t), \quad (4.28)$$

$$\dot{\rho}^e(t) = -2\text{Im}[\Omega(t)p^*(t)] - \frac{1}{T_{1,e}}\rho^e(t) + S_e^{in}, \quad (4.29)$$

$$\dot{\rho}^h(t) = -2\text{Im}[\Omega(t)p^*(t)] - \frac{1}{T_{1,h}}\rho^h(t) + S_h^{in}. \quad (4.30)$$

The described dynamics is k -independent due to the complete localization of charge carriers in QDs. Since the experiments are performed within the gain regime where WL charge carrier densities are in the range of $10^{12} - 10^{13} \text{ cm}^{-2}$, it is assumed that the Coulomb interaction dominates over the electron-phonon coupling, which is neglected in Eqs. (4.28)-(4.30). However, the influence of phonon induced processes for the decay of the coherence is taken into account, when the T_2 time is calculated, see Sec. 4.5.1. Furthermore, in this first study, excitonic effects and memory contribution in the electron-electron scattering are not considered. In contrast to carbon nanotubes, the RWA is applicable here, since only the region around the resonance is of interest. The stationary values before the arrival of the pulse are given by $\rho_0^e(0) = S_e^{in}T_{1,e}$, $\rho_0^h(0) = S_h^{in}T_{1,h}$, and $p_0(0) = 0$.

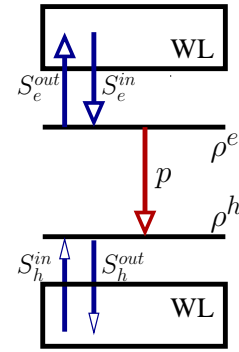


Figure 4.13: Illustration of the QD-WL structure with energy separations $\varepsilon_e = 240 \text{ meV}$ and $\varepsilon_h = 105 \text{ meV}$.

Then, the gain condition $\rho_0^e(0) + \rho_0^h(0) > 1$ can be expressed in terms of the scattering rates

$$\frac{S_e^{in}}{S_e^{in} + S_e^{out}} + \frac{S_h^{in}}{S_h^{in} + S_h^{out}} > 1. \quad (4.31)$$

The gain condition is independent of the T_2 time, since the stationary values are reached long after the polarisation has decayed. For the following calculations the WL carrier density is varied under the condition that the QD-SOA is operating in the gain regime, i.e. that the gain condition from Eq. (4.31) is fulfilled. The strength of the light-matter interaction is given by the Rabi frequency $\Omega(t) = \frac{d_{vc}E(t)}{\hbar}$ with the electrical field $E(t) = E_0 \exp\left(-\frac{t^2}{2\sigma^2}\right)$ and the interband dipole moment d_{vc} , which is set to $0.6 e_0 \text{nm}$ according to experimental data.²⁵ The amplitude E_0 determines the pulse area Θ (expressed in units of π)

$$\Theta \equiv \int \Omega(t) dt = \frac{d_{vc}\sqrt{2}\sigma}{\hbar\sqrt{\pi}} E_0 \implies E_0 = \frac{\hbar\sqrt{\pi}}{d_{vc}\sqrt{2}\sigma} \Theta. \quad (4.32)$$

This definition goes back to the generation of Rabi flops.¹⁴² For a pulse area of $\Theta = 2\pi$, the populations ρ^e and ρ^h are inverted corresponding to one complete Rabi flop. The pump-probe experiment is modeled with two sets of Bloch equations: i) including only the pump pulse and ii) including both the pump and the probe pulse. The length of both pulses is set to 150 fs, and their intensity ratio is $I_{probe}/I_{pump} = 0.01$ in agreement with the experimental setup. To model the gain dynamics, the absorption coefficient $\alpha(\omega, \tau)$ is calculated as a function of the pulse frequency ω and the delay time τ between the pump and probe pulse. The system is in the gain regime, if the absorption coefficient $\alpha(\omega, \tau)$ is negative. In Sec. 2.5, the latter was shown to be determined by the imaginary part of the optical susceptibility $\chi(\omega)$. Within the $r \cdot E$ approach (see Sec. 2.2) the absorption coefficient can be expressed in the frequency space as the ratio between the macroscopic polarisation $P(\omega)$ and the electrical field $E(\omega)$

$$\alpha_{pp}(\omega, \tau) \propto \omega \text{Im} \left[\frac{P_{\text{pump+probe}}(\omega, \tau) - P_{\text{pump}}(\omega)}{E_{\text{probe}}(\omega)} \right]. \quad (4.33)$$

In a pump-probe experiment, only the probe signal is measured probing the changes arising from the passed pump pulse. The macroscopic polarisation $P_{\text{pump}}(\omega)$ describing the contribution arising from the pump pulse alone needs to be subtracted from $P_{\text{pump+probe}}(\omega, \tau)$ obtained when considering both the pump and the probe pulse. This method ensures that only the response coming from the probe pulse (after the influence of the pump pulse) is obtained.¹⁴⁷

Finally, the macroscopic polarisation $P(t) = d_{vc}p(t)$ is determined by the optical dipole moment d_{vc} and the microscopic polarisation $p(t)$. The first is known from experiments, the second is calculated using the semiconductor Bloch equations. In general, Eqs. (4.28)-(4.30) cannot be solved analytically. In this thesis, the Bloch equations are evaluated numerically using the Runge-Kutta method. An analytic solution performed within a perturbation approach up to the χ^3 order will be performed in future work. In agreement with the experiment, the gain dynamics is calculated for the case that the pulse is in resonance to the QD energy $\omega = \omega_{qd}$, i.e. the gain is given as a function only of the delay time τ . Furthermore, it is normalized to the value at times long before the pump pulse arrives. The gain dynamics is shown to depend on the temperature T , the WL charge carrier density w_b , the pulse area Θ , and the dephasing time T_2 . In the following, these dependencies are discussed in detail.

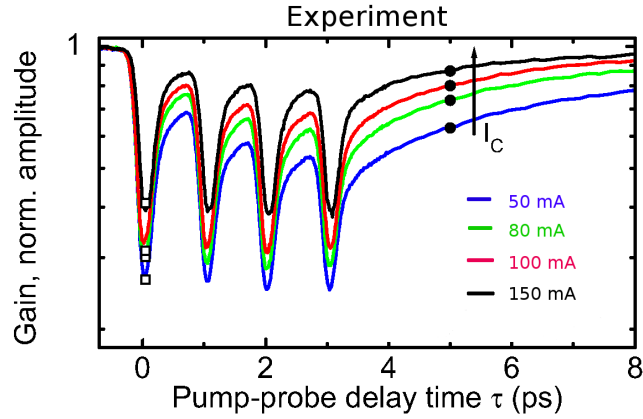


Figure 4.14: The normalized gain is plotted as a function of the pump-probe delay time τ for different injection currents I_C . The experiment was performed by Gomis et al.²⁵ with a pulse sequence consisting of four 150 fs long pulses with a repetition frequency of $f_{rep} = 1$ THz (corresponding to a pulse delay time of $\tau_0 = 1$ ps). The larger the current, the shorter is the gain recovery time and the smaller is the gain depletion.

Gain dynamics - temperature and WL carrier density dependence

Figure 4.14 shows the normalized gain measured for injection currents I_c between 80 mA and 150 mA as a function of the pump-probe delay time τ . A four-pulse sequence with a repetition rate of 1 THz was generated in the experiment.²⁵ The pump-probe measurements show a gain depletion followed by gain recovery. The higher the injection current, the smaller is the gain reduction resulting in a faster gain recovery. However, as shown in Fig. 4.12b, at this very short repetition rate, the gain signal could not be completely switched back, even for $I_C = 150$ mA. The increase of the injection current has two effects: i) the number of charge carriers in the WL increases and ii) the temperature of the device is enhanced. In the experiment, the device temperature is increased by 75 K for a variation of I_C from 0 mA to 150 mA.

The evaluation of the Bloch equations for different temperatures and WL carrier densities allows a comparison with the experimental results. In Fig. 4.15a, the normalized gain is plotted as a function of the pump-probe delay time τ for temperatures between 300 K and 500 K for a fixed pulse area of $\Theta = 1.5\pi$ and for dephasing times as described in Sec. 4.5.1. The figure shows that the gain recovery time is reduced with increasing temperatures. The faster gain recovery is due to the stronger scattering rates at higher temperatures, as shown in Fig. 4.16. Consequently, the QD ground state can be refilled more efficiently with charge carriers from the WL, resulting in a shorter gain recovery time. An increase in temperature affects, in particular, the in-scattering processes, since S_b^{in} is proportional to the product of two fermi functions $f_{\mathbf{k}_2}^b f_{\mathbf{k}_3}^b$, see Eq. (4.22). The Fermi distributions become broader at higher temperatures increasing the probability for the capture of charge carriers into the QD ground state. This has a stronger influence on holes due to their larger effective mass and a flatter band structure. A temperature increase of $\Delta T = 200$ K leads to a more than twice as large hole in-scattering rate S_h^{in} . The application of QD-SOAs as high-speed communication devices requires both a fast gain recovery and a deep gain depletion. The latter is important to obtain pronounced signal pulses. Unfortunately, the enhanced temperatures do not only accelerate the gain recovery time, but at the same time, they reduce the gain depletion. The optimisation of the refilling of QD states leads at the same time to a less pronounced gain peak.

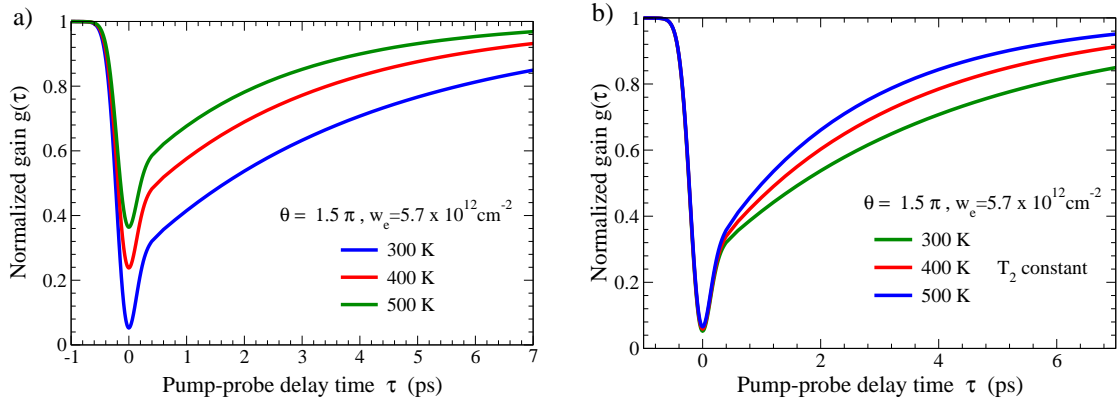


Figure 4.15: Normalized gain $g(\tau) = -\alpha(\tau, \omega_{qd})$ as a function of the pump-probe delay time τ for different temperatures (for a fixed WL carrier density of $w_e = 5.7 \times 10^{12} \text{ cm}^{-2}$, corresponding to the density at which the electron in-scattering S_e^{in} is maximal). In a) the normalized gain is calculated for a realistic situation, where the T_2 time varies with the temperature, see Sec. 4.5.1. To illustrate the pure temperature dependence of the gain, in b) the T_2 is artificially set to 25 fs for all temperatures. For both figures, the pulse area is fixed to $\Theta = 1.5\pi$. Furthermore, note that the gain is normalized to the value long before the pump pulse has arrived. The higher the temperature, the faster is the gain recovery and the smaller is the gain depletion. The increase of the WL carrier density increases the gain recovery time due to the less efficient scattering rates.

The difference in gain depletion is reduced by approximately 30% at a temperature increase of $\Delta T = 200 \text{ K}$. Note that the gain depletion depends only indirectly on the temperature. It is the change of the dephasing time T_2 with the temperature that causes the reduction of the gain depletion. Plotting the gain dynamics in dependence of T with artificially fixed constant dephasing times T_2 leaves the gain depletion largely unchanged, see Fig. 4.15b. The figure also illustrates the decrease of the absolute gain recovery time with the increasing temperature.

The other effect of the experimental increase of the injection current, namely the increase of the WL carrier density, is shown in Fig. 4.17. Here, the dependence of the normalized gain on the WL carrier density w_e is illustrated. At first sight, the result seems to be surprising: the higher w_e , the slower is the gain recovery. One would expect higher WL carrier densities to be advantageous for a fast gain recovery. However, the scattering rates have a complex dependence on w_b , see Sec. 4.5. At the WL electron density $w_e = 5.7 \times 10^{12} \text{ cm}^{-2}$, the electron in-scattering rate S_e^{in} has

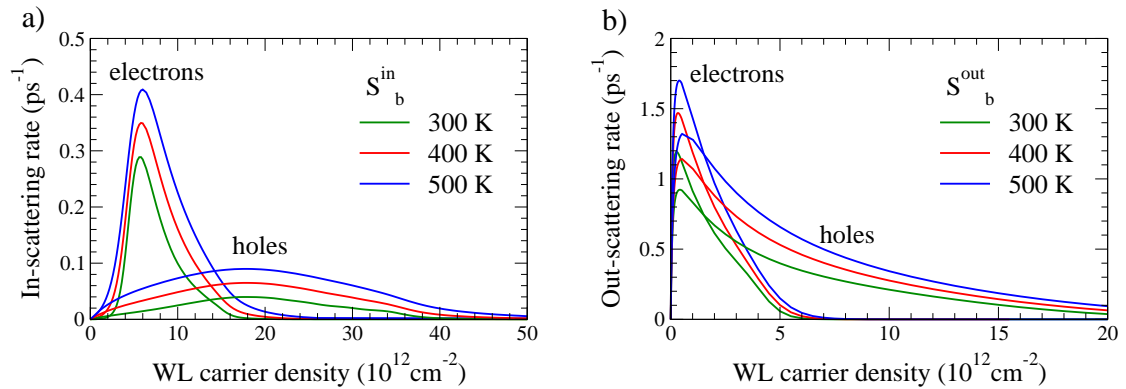


Figure 4.16: Temperature dependence of Coulomb a) in-scattering and b) out-scattering rates for electrons and holes. Generally, the scattering becomes more efficient with increasing temperatures.

its maximum, see Fig. 4.16. For $w_e = 6.7 \times 10^{12} \text{ cm}^{-2}$ and $w_e = 7.7 \times 10^{12} \text{ cm}^{-2}$, the capture of electrons via Auger processes is already reduced. The scattering rates increase with increasing WL carrier densities up to a certain value, then they decrease due to Pauli blocking. As a result, Fig. 4.17 reflects how efficient the refilling of the QD ground state is. The gain recovery is fastest at $w_e = 5.7 \times 10^{12} \text{ cm}^{-2}$, where the electron in-scattering is maximal.

Increasing the injection current in experiment has a similar effect, namely an acceleration of the gain recovery and a reduction of gain depletion, see Fig. 4.14. For a current of 150 mA, the gain recovery is almost complete. With decreasing currents, i.e. with a smaller number of scattering partners, the refilling of QDs with charge carriers is slowed down. The gain offset Δ becomes larger and increases with every pulse in the sequence. At the same time, the gain depletion is enhanced. An injection current increase of $\Delta I_C = 100 \text{ mA}$ enhances the gain reduction by approximately 20%. The variation of the injection current in the experiment can be obviously modeled by a variation of the temperature in theory. The comparison gives a good qualitative agreement.

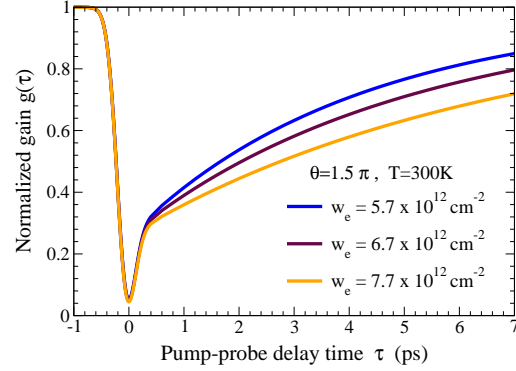


Figure 4.17: Normalized gain as a function of the pump-probe delay time τ for different WL carrier densities (for a fixed temperature of $T = 300 \text{ K}$).

The gain behavior in the first 200 fs is surprising. The gain peak passes a minimum followed by an ultrafast gain recovery on a femtosecond time scale. This effect cannot be explained by Coulomb induced refilling processes, since the latter are on a picosecond time scale. This characteristic feature of the gain peak can be explained by the so-called *coherent artifact*, a coherent effect describing the interference between the pump and the probe pulse. The overlap generates a grating in the absorption which scatters a part of the pump pulse in the probe direction. As a result, the probe signal is enhanced. This effect turns out to be sensitive to the T_2 time, as discussed below.

Gain dynamics - pulse area dependence

Besides the temperature dependence, the gain dynamics is influenced by the pulse area Θ . In Fig. 4.18a, the normalized gain is shown as a function of the pump-probe delay time τ for three different pulse areas $\Theta = 0.75\pi, 1.0\pi$, and 1.5π . The WL carrier density is fixed to $w_e = 5.7 \times 10^{12} \text{ cm}^{-2}$, corresponding to the density at which the electron in-scattering S^{in} is maximal. The temperature is set to 300 K and the corresponding dephasing time T_2 is 25 fs. The figure illustrates that the gain depletion is strongly dependent on the pulse area Θ . Increasing Θ from 0.75π to 1.5π enhances the amplitude of the renormalized gain approximately by a factor of three. However, at the same time, the gain recovery is slowed down. Similar to the temperature dependence, the influence of the pulse area on the gain depletion and gain recovery is opposite. The optimisation of a QD-SOA is a trade-off between the gain amplitude and the recovery time. Note that the absolute refilling time of the QD ground state does not depend on the pulse area. The system needs longer to recover, since the gain reduction at large pulse areas is high.

Figure 4.18b illustrates the importance of taking the dynamics of both electrons and holes into account. The dashed curves show a pure electron dynamics, i.e. the electrons and holes are assumed to be identical. Considering only electrons leads to strongly reduced in-scattering processes, as

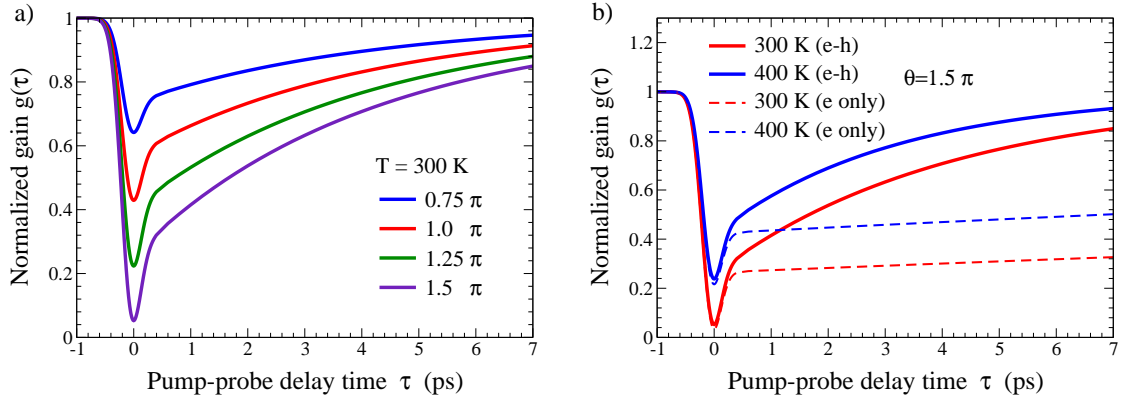


Figure 4.18: a) Normalized gain as a function of the pump-probe delay time τ for different pulse areas Θ (for a fixed temperature of 300 K and the WL carrier density $w_e = 5.7 \times 10^{12} \text{ cm}^{-2}$). The stronger the pulse area, the larger is the gain depletion and the slower is the gain recovery. b) Illustration of the importance of the hole dynamics. The dashed lines show the normalized gain under the condition that only the electron dynamics is taken into account. It is clearly seen how important the holes are for a correct simulation of ultrafast gain dynamics.

can be seen in Fig. 4.10. The capture of electrons described by S_e^{in} is one order of magnitude weaker at the considered WL carrier density of $w_e = 5.7 \times 10^{12} \text{ cm}^{-2}$ due to the missing efficient electron-hole processes. Consequently, the gain recovery is considerably slowed down. This shows a possible way to accelerate the gain dynamics by further increasing the importance of holes, e.g. by p-doping of the device. Furthermore, Fig. 4.18b illustrates that holes have no influence on the gain depletion.

Gain dynamics - dephasing time dependence

The gain dynamics has a particular behavior in the first 200 fs after the arrival of the pump pulse. As can be seen in Fig. 4.19a, the gain dynamics follows the microscopic polarisation as long as the pump pulse is present, then it reflects the population dynamics. The gain depletion right after the arrival of the pump pulse is strongly influenced by the T_2 time, while the gain recovery

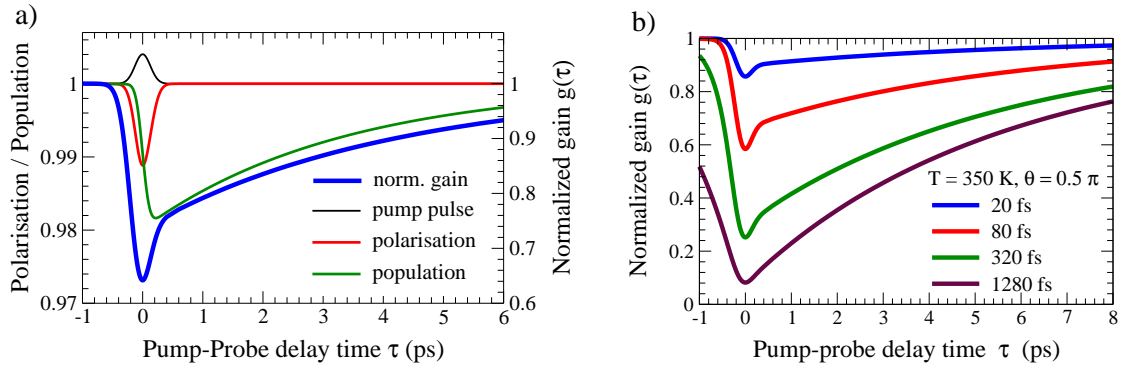


Figure 4.19: a) Illustration of the coupled population and coherence dynamics and their influence on the characteristic gain peak. In the first 200 fs, the gain dynamics is dominated by the coherence, then, the population dynamics is crucial. b) Normalized gain as a function of the pump-probe delay time τ for different dephasing times T_2 showing that the characteristic gain peak disappears for long T_2 times. The behavior for negative delay times is ascribed to the optical Stark effect.

time is determined by the $T_{1,e/h}$ times. At very short pump-probe delay times, interference effects between the pump and the probe pulse play a crucial role. The resulting characteristic gain peak shows a strong dependence on the dephasing time T_2 , as shown in Fig. 4.19b. The pronounced minima only appears if the T_2 time is low enough, i.e. in the order of some femtoseconds - the time scale of the coherence artifact. Then, the gain dynamics is completely reflected by the population dynamics.

The gain curve possesses a turning point after a delay time of approximately 200 fs, when the influence of the pump pulse is diminished and the gain recovery via charge carrier capture from the neighboring WL states begins. This feature has been discussed controversially in literature.¹⁴⁸ One widely spread explanation is obtained by including the two-photon absorption (TPA). This assumption accounts for the quadratic-like dip in the gain curve within a rate equation approach. However, the dependence of the gain depletion on the injection current, as shown in Fig. 4.14, does not support this explanation. Furthermore, preliminary experiments¹⁴⁹ have been done showing that the normalized gain has a linear dependence on the optical pump power over a wide range. In the theory, this statement was confirmed. In Fig. 4.20, the normalized gain for $\tau = 0$ is plotted over the pump power, which is given by the time integral over the intensity

$$\int_{-\infty}^{\infty} |E(t)|^2 dt = E_0^2 \sqrt{\pi} \sigma = \frac{\hbar^2 \pi^{\frac{3}{2}}}{2d_{vc}^2 \sigma} \Theta^2 \left[\frac{\text{eV}}{\text{fs nm}^2} \right].$$

The stronger the pump power, the larger is the gain depletion. Over a wide range of pump powers, the dependence is approximately linear, see Fig. 4.20. This is a strong indication that the two-photon absorption cannot play an important role. At very high pump powers, the system is not in the gain region any more. The processes of induced absorption become crucial. Increasing further the pump power leads to an equilibrium situation, where both QD states are equally filled. There is no gain and no absorption, i.e. the system is transparent. In contrast, in the experiment, the gain is saturated at high pump powers, but a transition to the absorption regime has not been observed so far. This might be due to the inhomogeneous distribution of QDs accounting for a considerable number of non-resonant QDs.

Additionally, the impact of the coherent artifact turns out to depend on the width of the pump σ_{pump} and the probe pulse σ_{probe} . The broader the pulses, the broader is the gain peak. The position of the maximal gain depletion (corresponding to the minimum in the gain curve) is determined by the relative width of the gain and pump pulse. In the case $\sigma_{\text{pump}} \leq \sigma_{\text{probe}}$, the gain minima can be found at a positive delay time τ . For $\sigma_{\text{pump}} \geq \sigma_{\text{probe}}$, the maximal gain depletion is already reached at a negative τ . Moreover, the width of the pump and probe pulse has also an influence on the strength of the gain depletion. These observations reflect the importance of interference effects for a better understanding of the coherent artifact. In future work, a quantitative analysis of these dependencies will be performed in a limiting case, where an analytical solution of the Bloch equations [Eqs. (4.28)-(4.30)] is possible.

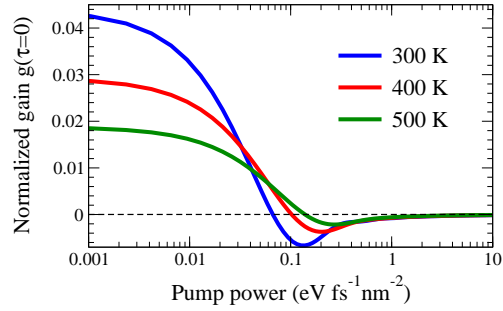


Figure 4.20: Normalized gain as a function of the optical pump power (at the pump-pulse delay time of $\tau = 0$) showing a long region with a linear dependence.

4.6.3 Summary

In this section, the gain dynamics of QD optical amplifiers has been investigated. The theoretical approach is based on the semiconductor QD Bloch equations describing the charge carrier population and coherence dynamics. The interaction between the charge carriers in the QD ground state and the delocalized two-dimensional WL states is included by a microscopic calculation of the Coulomb scattering rates.

The gain recovery time is shown to be determined by the strength of the Coulomb scattering between the QD and WL states as well as by the temperature, while the gain depletion is found to be a function of the dephasing time and the pump power. Up to now, the processes of two-photon absorption have been assumed to play a crucial role for the explanation of the so-called coherent artifact. In this work, the latter has rather been found to be a result of interference effects between the pump and the probe pulse. The obtained results contribute to a better understanding of the limiting mechanisms for the ultrafast gain recovery in QD amplifiers.

4.7 Quantum dot laser

Semiconductor QD lasers are excellent candidates for future data and telecom applications.¹²⁴ They show a high potential for a fast dynamical response, which strongly depends on the frequency and the damping rate of relaxation oscillations (ROs).²⁰ Quantum dot based lasers show many important advantages over conventional quantum well based lasers, such as lasing at data and telecom wavelengths in the range of 1300 nm with very low threshold current densities below 10 Acm^{-2} as well as high internal quantum efficiencies approaching 100%, and high temperature stability. Moreover, ROs in QD lasers have been measured to be strongly damped, which is advantageous for low bit-error rates and high-speed data transmission.^{126–128} This indicates their potential for modulation bandwidths higher than 10 GHz. The underlying mechanisms are still being discussed in literature.^{23,24}

In this section, a detailed microscopic analysis of the turn-on dynamics of single-mode InAs/GaAs quantum dot lasers pumped by a nanosecond current pulse¹⁵⁰ is presented. The approach goes beyond standard phenomenological laser rate equations^{151–158} similar to those used in quantum well lasers^{159–161} by incorporating microscopic kinetic equations which describe Coulomb scattering processes.^{129,162,163} This approach takes the microscopic interaction and charge transfer between QDs and the WL evolving in the process of fabricating self-organized QDs into account.^{133,136}

4.7.1 Experiment

The measurement of relaxation oscillations was performed by Kuntz et al.¹²⁵ at the TU Berlin. The corresponding experimental setup is illustrated in Fig. 4.21a. A double-spectrometer was used to compensate path differences of interfering beams, enabling a temporal resolution of 5 ps and transients up to 10 ns. Furthermore, a pulse generator with a maximum voltage of 5 V and QD laser diodes with dimensions of $1 \text{ mm} \times 4 \mu\text{m}$ were used. The measurements were performed for different current densities at room temperature, see Fig. 4.21b. The threshold current density was 290 Acm^{-2} . The laser diodes were driven by electrical pulses with a length of 5 ns and a rise and a fall time of 100 fs.

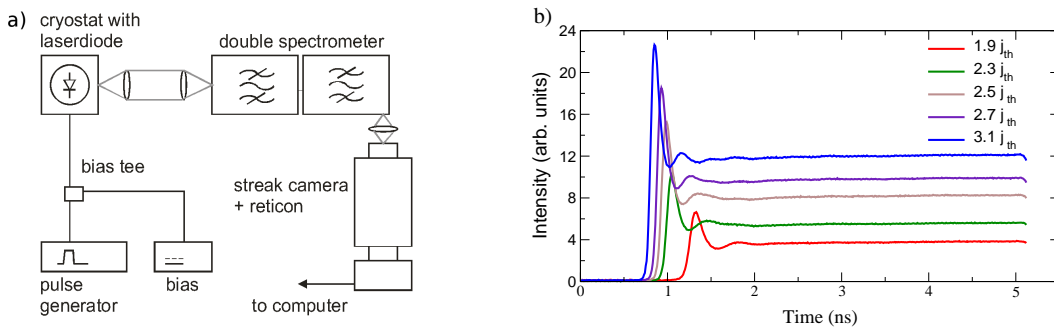


Figure 4.21: Experimental setup for measurements of relaxation oscillations designed by Kuntz et al.¹²⁵ shows a He cryostat with the QD laser diode inside. A pulsed current is applied to the cryostat chamber. The optical output of the diode is focused into a double-spectrometer. The selected wavelength of $1.3 \mu\text{m}$ reaches the streak camera, which is connected to a computer.

The measured relaxation oscillations are strongly damped. As a result, only one or two peaks were detectable, see Fig. 4.21b. The damping was shown to be much stronger than in conventional quantum well lasers.^{21,22} Furthermore, a characteristic turn-on delay time of approximately $\tau = 1$ ns is observed. It is proportional to the inverse of the current density j , while the RO frequency is proportional to the square root of j . The RO frequency allows the determination of the maximal bandwidth frequency f_{max} . In the case of strong damping,¹²⁵ small signal measurements yield an experimental relation between these two frequencies $f_{max} = 1.2f_{ro}$. Consequently, the faster the laser reaches its stationary value, the higher is the maximal bandwidth frequency.

4.7.2 Turn-on-dynamics

The turn-on dynamics of a QD lasers is modeled within the rate equation model, which presents a suitable method to describe the dynamics of laser processes at room temperature.^{20,159} The rate equations follow from the Bloch equations for ultrashort coherence times, i.e. $T_1 \gg T_2$. At low temperatures, the approach of master equations for micro-states is more suitable for QDs, considering the carrier capture and recombination in QDs as random processes.¹⁶⁴ At room temperature, however, it is a good approximation to average the level populations over the QD ensemble.¹⁹ Some simplifying assumptions have to be made to obtain the rate equations from the QD Bloch equations, presented in the previous section. The latter are valid for processes within one QD and need to be averaged over the entire ensemble of QDs present in the laser active region. In this work, it is assumed that all QDs contribute equally to the dynamics of the system, i.e. the inhomogeneous broadening due to the Gaussian size distribution of QDs is not considered directly. Instead, the QD density N^{QD} is assumed to be smaller by a factor 2 than experimentally measured accounting for the fact that not all QDs are in resonance with the considered laser mode due to their size distribution. As shown in the description for QD-SOAs, the coherence decay occurs within some tens of femtoseconds, while the relaxation oscillations are on a nanosecond time scale. As a result, the turn-on dynamics of QD lasers can be well described by considering only the population dynamics.

QD charge carrier densities

The polarisation and the Rabi frequency can be separated in a fast oscillating part and a slow time dependent amplitude: $p(t) = \tilde{p}_0(t)e^{-i\omega t}$ and $\Omega(t) = \Omega_0(t) \cos(\omega t)$. Then, the rate equation approximation $\frac{d\tilde{p}_0(t)}{dt} \ll \frac{\tilde{p}_0}{T_2}$ is applied, i.e. it is assumed that the decay of the coherence is very fast (T_2 time short). As a result, the stationary value of \tilde{p}_0 is reached very quickly, and the derivative of $\tilde{p}_0(t)$ can be set to zero. Then, the equation of motion for the polarisation [Eq. (4.28)] can be solved analytically, yielding

$$\tilde{p}_0(t) = -i\Omega_0 (\rho^e(t) + \rho^h(t) - 1) T_2. \quad (4.34)$$

Inserting this solution into Eq. (4.29) and Eq. (4.30) leads to rate equations for the electron and hole densities n_e and n_h in the QD ground state

$$\dot{n}_e = -\frac{1}{T_{1,e}} n_e + S_e^{in} N^{QD} - R_{ind}(n_e, n_h) - R_{sp}(n_e, n_h), \quad (4.35)$$

$$\dot{n}_h = -\frac{1}{T_{1,h}} n_h + S_h^{in} N^{QD} - R_{ind}(n_e, n_h) - R_{sp}(n_e, n_h). \quad (4.36)$$

Here, the occupation densities n_b are obtained by summing the corresponding occupation probabilities ρ^b over all QDs, i.e. $n_b = \frac{1}{A} \sum_i \rho_i^b = N^{QD} \rho^b$ with the QD density N^{QD} .

The first terms in Eqs. (4.35)-(4.36) express the charge carrier capture from WL states via Coulomb scattering, see Fig. 4.22. The electron and hole scattering rates S_b^{in}, S_b^{out} and the corresponding scattering times $T_{1,b}$ ($b = e, h$) are a measure for the strength of the non-local Auger processes between the bound QD and continuous WL states. They have already been discussed in detail in Sec. 4.5.

The second contribution to the dynamics of the QD charge carrier density describes the radiative relaxation of charge carriers within a QD (see Fig. 4.22)

$$R_{ind} \equiv \hat{W}(n_e + n_h - N^{QD}) n_{ph} \quad (4.37)$$

with $\hat{W} \equiv WA$ where A is the WL normalization area and W the Einstein coefficient, which is a measure for the strength of the light-matter interaction. Its microscopic derivation performed within a full quantum mechanical approach is sketched below. In Eqs. (4.35)-(4.36), it was introduced as $W \equiv 2\hat{\Omega}_0^2 T_2$ with $\hat{\Omega}_0 = \Omega_0 b_0$ containing the dimensionless quantity b_0 . The latter leads to the definition of the photon density $n_{ph} = \frac{1}{A} |b_0|^2$. The induced processes of emission and absorption are proportional to the photon density n_{ph} and to the difference of the electron densities in the two QD levels. Note that the hole density n_h can be easily transformed into the corresponding electron density in the lower QD level with $n_e^v = N^{QD} - n_h$.

Finally, the third contribution to the QD charge carrier dynamics in Eqs. (4.35)-(4.36) is given by the spontaneous emission rate

$$R_{sp}(n_e, n_h) \equiv \tilde{W} n_e n_h, \quad (4.38)$$

with $\tilde{W} = W/N^{QD}$. The spontaneous emission is governed by bimolecular recombination.^{159,160} This has been discussed controversially in literature.¹⁶⁵ The crucial point is whether the Hartree-Fock approximation, necessary to obtain the above bimolecular expression, is applicable in QDs with only one localized, gain active electron. Assuming the QD and the WL states to belong to one QD-WL structure justifies the Hartree-Fock approximation,* since the WL can be treated as a two-dimensional charge carrier gas. However, the spontaneous emission cannot be obtained from the semiconductor Bloch equations presented in Sec. 2.4, since a semiclassical approach was applied treating the electromagnetic field $\mathbf{E}(\mathbf{r}, t)$ classically. In the following section, the spontaneous emission is derived quantum mechanically.

Photon density

A quantum mechanical approach is needed to derive the equation of motion for the photon density n_{ph} , which has been introduced phenomenologically so far. Here, a brief derivation is presented; for more details, see App. B. Starting from the quantized field $E(z, t)$ within a cavity along the z -axis

$$E(z, t) = \sum_i E_{0,i} \sin(q_i z) (c_i^+ + c_i) \quad (4.39)$$

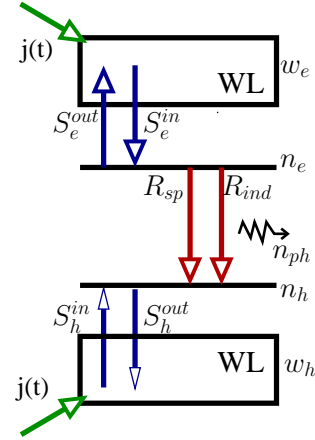


Figure 4.22: Illustration of the investigated QD-WL structure.

*Within the Hartree-Fock approximation, the bimolecular expression is only obtained, if the states are not degenerate.¹³⁸

with the photon creation and annihilation operators c_i^+ and c_i and the field amplitude $E_0 = \sqrt{\frac{\hbar\omega}{2\epsilon_0 V}}$. The sum runs over all modes i of the field. Then, the carrier-field Hamilton operator from Eq. (2.15) can be generalized to

$$H_{c-f} = \sum_i \sum_{l,l'} d_{l,l'} E_0 \sin(q_i z) (c_i^+ + c_i) a_l^+ a_{l'}. \quad (4.40)$$

It contains the photon-assisted quantities $c_i^+ a_l^+ a_{l'}$ and $c_i a_l^+ a_{l'}$. The first quantity describes the emission of a photon and the corresponding annihilation of an electron-hole pair. The second quantity describes the reverse process of a photon absorption. Now, using the Heisenberg equation from Eq. (2.33) and the Hamilton operator including the free carrier and photon part and the electron-light coupling, the dynamics of the photon number $\langle c_i^+ c_i \rangle$ of the mode i can be determined. Within the RWA, the corresponding equation of motion reads

$$\frac{d}{dt} \langle c_i^+ c_i \rangle = -\frac{i}{\hbar} d_{vc} E_0 \sin(q_i z) \left(\langle c_i^+ a_v^+ a_c \rangle - \langle c_i a_c^+ a_v \rangle \right). \quad (4.41)$$

To obtain a closed set of equations, the dynamics of the appearing photon-assisted quantities $\langle c_i^+ a_v^+ a_c \rangle$ and $\langle c_i a_c^+ a_v \rangle$ needs to be determined. Applying the Heisenberg equation with the Hamilton operator from above yields an equation of motion for those quantities, see App. B. Since radiative processes are on a nanosecond time scale, while carrier scattering occurs within some picoseconds, the derivative of the photon-assisted quantities is small.³⁶ Then, the corresponding equation of motion can be solved formally. The solution Inserted in Eq. (4.41) gives

$$\frac{d}{dt} \langle c_i^+ c_i \rangle = |\Omega(\omega_i)|^2 \left(\langle c_i^+ c_i \rangle (\rho^e + \rho^h - 1) + \rho^e \rho^h \right) \frac{2\gamma}{(\omega_{cv} - \omega_k)^2 + \gamma^2} \quad (4.42)$$

with $|\Omega(\omega_i)|^2 = \frac{1}{\hbar^2} |d_{vc}|^2 |E_0 \sin(q_i z)|^2$. Up to now, only a single mode of the radiation field has been considered. To calculate the total radiative rate for the spontaneous emission all possible modes need to be taken into account. They are characterized by the wave vector $q = \frac{\omega}{c}$. Applying this dispersion relation for light, the sum over the photon modes denoted by i can be expressed as an integral over frequency ω_i . The latter is evaluated using the relation $\lim_{\gamma \rightarrow 0} \frac{\gamma}{(\omega_{cv} - \omega_k)^2 + \gamma^2} = \pi \delta(\omega_{cv} - \omega_k)$. Finally, an equation of motion for the photons density $n_{ph} = N^{QD} \sum_i \langle c_i^+ c_i \rangle$ is obtained

$$\frac{d}{dt} n_{ph} = \underbrace{\frac{|d_{vc}|^2}{3\pi \epsilon_0 \hbar} \left(\frac{\omega_k}{c_m} \right)^3}_{\text{Einstein coeff. } W} \left[\underbrace{\Gamma n_{ph} (n_e + n_h - N^{QD})}_{\text{induced processes}} + \underbrace{\beta n_e n_h}_{\text{spont. emission}} \right] - 2\kappa n_{ph}. \quad (4.43)$$

The first contribution is proportional to the photon density n_{ph} . It describes the processes of induced emission and absorption. In contrast, the second contribution is proportional only to the occupation probabilities for electrons and holes. This term describes the spontaneous emission. The strength of both processes is given by the Einstein coefficient W .

$$W = \frac{|d_{vc}|^2}{3\pi \epsilon_0 \hbar} \left(\frac{\omega}{c_m} \right)^3, \quad (4.44)$$

with the dipole momentum d_{vc} , the gap frequency ω_k , the speed of light in medium $c_m = \frac{c}{\sqrt{\epsilon_{bg}}}$, the dielectric background constant ϵ_{bg} , and the vacuum permittivity ϵ_0 .

Furthermore, the coefficient

$$\kappa = \frac{\gamma}{2} = \left(\kappa_{int} - \frac{1}{2L} \ln(r_1 r_2) \right) c_m \quad (4.45)$$

has been introduced. It describes the total cavity loss, which depends on the cavity length L , the facet reflection coefficients¹⁹ $r_1 = r_2$, and the internal losses κ_{int} , which are adapted to the experimental realisation of quantum dot lasers,¹²⁵ see Table 4.1. The optical confinement factor Γ in Eq. (4.43) is introduced to take the difference of the optical and electronic active area in the QD-WL structure into account. It can be split into an in-plane and a vertical confinement factor $\Gamma \equiv N_l \Gamma_{xy} \Gamma_z$ with N_l as the number of QD layers.¹⁹ The in-plane component Γ_{xy} is given by the product of the QD density N^{QD} and the in-plane size of a QD A_{xy} (coverage with QDs). The vertical confinement $\Gamma_z = 2.5 \times 10^{-3}$ expresses the vertical overlap of QDs and optical modes, averaged over the plane of area A

$$\Gamma_z = \frac{1}{A} \frac{\int_{-L/2}^{L/2} |E(z)|^2 dz}{\int_{-\infty}^{\infty} |E(z)|^2 dz}. \quad (4.46)$$

Finally, the spontaneous emission coefficient β has been introduced to describe the efficiency of the spontaneous emission with respect to the considered laser mode in the cavity, since only a fraction of generated photons will contribute to the considered laser mode.

WL charge carrier densities

In contrast to the investigations of the gain dynamics of QD amplifiers in the previous section, now, the turn-on dynamics of QD lasers is in the focus. Starting with initially empty WL and QD states, the injection current density $j(t)$ is applied leading to a rapid change of both WL and QD charge carrier densities. The Coulomb scattering rates in Eqs. (4.35)-(4.36) describing the capture/escape processes into/out of the QD states strongly depend on the WL charge carrier density w_b . As a result, taking the full dynamics of w_e and w_h into account is crucial for a better understanding of the turn-on dynamics. In analogy to the rate equations for the QD charge carrier densities n_e and n_h , corresponding rate equations for w_e and w_h are found

$$\dot{w}_e = \frac{j(t)}{e_o} + \frac{n_e}{T_{1,e}} \frac{N^{WL}}{N^{QD}} - S_e^{in} N^{WL} - \tilde{R}_{sp}(w_e, w_h), \quad (4.47)$$

$$\dot{w}_h = \frac{j(t)}{e_o} + \frac{n_h}{T_{1,h}} \frac{N^{WL}}{N^{QD}} - S_h^{in} N^{WL} - \tilde{R}_{sp}(w_e, w_h). \quad (4.48)$$

Equations (4.47)-(4.48) were derived assuming the conservation of charge carriers within the QD-WL structure. The loss terms in the dynamics of n_e and n_h are gain terms in the corresponding dynamics of w_e and w_h , respectively.* In analogy to the QD density N^{QD} , an effective WL density $N^{WL} = \frac{1}{A_{eff}} \approx 0.2 \text{ nm}^{-2}$ is introduced. Due to the strong screening, Coulomb scattering is only effective within a WL area $A_{eff} = 5 \text{ nm}^2$ corresponding to a screening length of 2.2 nm, see Eq. (4.20).

The WL charge carrier dynamics is crucially determined by the pump process described by the injection current density $j(t)$

$$j(t) = j_0 \exp \left[- \left(\frac{t - t_0}{2.5} \right)^n \right] \quad (4.49)$$

* A better way to introduce the WL carrier densities w_b is to consider that the WL consists of many states characterised by a wave vector \mathbf{k} . To obtain a \mathbf{k} -independent WL carrier density w_b , a \mathbf{k} -integral over the Fermi function and the two-dimensional density of states is to be performed. As a result, an overall WL charge carrier density denoted by w_b is obtained.

with $n = 90$ and $t_0 = 2.49$ ns ensuring a rise and fall time of 100 ps in agreement with the experiment.¹²⁵ For high injection currents, it is important to include the coefficient $\eta_b \propto (N^{WL} - w_b)$ describing the efficiency of the injection of charge carriers into the WL.³⁶ The larger the WL charge carrier density, the less efficient is the injection due to the Pauli exclusion principle.

Finally, the spontaneous recombination rate within the WL is expressed by $\tilde{R}_{sp}(w_e, w_h) = W' w_e w_h$ with $W' = W/N^{WL}$, in analogy to the spontaneous emission in QDs.

Turn-On Dynamics

For a better overview, the entire set of coupled nonlinear differential equations for the QD charge carrier densities n_e, n_h , the WL charge carrier densities w_e, w_h , and the photon density n_{ph} is shown

$$\dot{n}_{ph} = -2\kappa n_{ph} + \Gamma R_{ind}(n_e, n_h) + \beta R_{sp}(n_e, n_h), \quad (4.50)$$

$$\dot{n}_e = -\frac{1}{T_{1,e}} n_e + S_e^{in} N^{QD} - R_{ind}(n_e, n_h) - R_{sp}(n_e, n_h), \quad (4.51)$$

$$\dot{n}_h = -\frac{1}{T_{1,h}} n_h + S_h^{in} N^{QD} - R_{ind}(n_e, n_h) - R_{sp}(n_e, n_h), \quad (4.52)$$

$$\dot{w}_e = \frac{j(t)}{e_o} + \frac{n_e}{T_{1,e}} \frac{N^{WL}}{N^{QD}} - S_e^{in} N^{WL} - \tilde{R}_{sp}(w_e, w_h), \quad (4.53)$$

$$\dot{w}_h = \frac{j(t)}{e_o} + \frac{n_h}{T_{1,h}} \frac{N^{WL}}{N^{QD}} - S_h^{in} N^{WL} - \tilde{R}_{sp}(w_e, w_h). \quad (4.54)$$

These equations describe the dynamics of an InAs/GaAs QD laser. The parameters are either calculated or obtained from experimental realisation of the investigated QD-WL structure,¹²⁵ see Table 4.1. Now, Eqs. (4.50)-(4.54) can be numerically evaluated using the Runge-Kutta algorithm.¹³⁹

parameter	value	from	parameter	value	from
W	1.3 ns^{-1}	Eq. (4.44)	κ	0.12 ps^{-1}	Eq. (4.45)
d_{vc}	$0.3 e_0 \text{ nm}$	experiment ¹²⁵	κ_{int}	220 m^{-1}	experiment ¹²⁵
ε_{gap}	0.96 eV	experiment ¹²⁵	r_1, r_2	0.32	experiment ¹²⁵
ε_{bg}	14.2	experiment ¹³⁵	L	1 mm	experiment ¹²⁵
m_e^*	$0.04 m_0$	experiment ¹³⁵	A	$4 \times 10^{-5} \text{ cm}^2$	experiment ¹²⁵
m_{hh}^*	$0.450 m_0$	experiment ¹³⁵	N^{WL}	$2 \times 10^{13} \text{ cm}^{-2}$	Eq. (4.20)
β	5×10^{-6}	adjusted	N^{QD}	$1 \times 10^{10} \text{ cm}^{-2}$	experiment ¹²⁵
Γ	1×10^{-3}	Eq. (4.46)	N_l	15	experiment ¹²⁵

Table 4.1: Parameters used in the numerical evaluation of Eqs. (4.50)-(4.54) to model the turn-on dynamics of QD semiconductor lasers. The material parameters, such as effective masses and the background dielectric constant, are assumed to be the average of the corresponding values for GaAs and InAs,¹³⁵ since the QD-WL structure contains both InAs and GaAs.

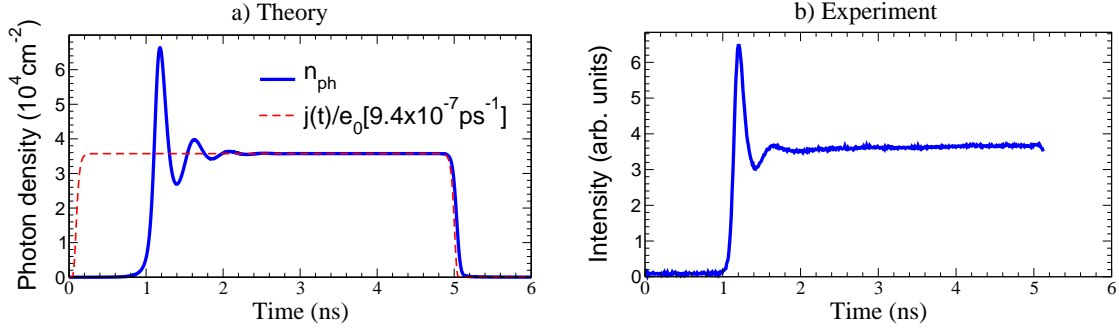


Figure 4.23: a) Response of the photon density $n_{ph}(t)$ to a current pulse (dashed line) of 5 ns length and with a rise and a fall time of 100 ps, see Eq. (4.49). The current density is set to be 1.9 times over the threshold density. Pronounced strongly damped relaxation oscillations are generated during the turn-on processes. b) The corresponding experimental result¹²⁵ showing only the turn-on dynamics.

First, an injection current density pulse $j(t)$ of 5 ns width is applied to obtain inversion. The current density is set to be 1.9 times above the laser threshold.* The dynamics of the photon density n_{ph} is shown in Fig. 4.23a. After a characteristic turn-on delay of approximately 1 ns, the photon density increases exponentially. The initial period after the injection current is applied is dominated by filling processes of the WL states and the processes of spontaneous emission. After the WL carrier density w_b reaches a certain value, the Coulomb scattering becomes efficient, and the induced processes become crucial. Now, the laser is switched on. The photon density performs pronounced strongly damped relaxation oscillations with a frequency of approximately 2 GHz. These results are in good agreement with experimental data, shown in Fig. 4.23b, with respect to the frequency, delay time, and the full width half maximum.

The ROs result from the interplay of electron filling, induced emission, and absorption processes. The oscillations only appear if these contributions are of comparable magnitude. The stronger the filling processes, the less damped are the ROs. In the limiting case of very weak scattering rates or a very strong damping, the photon density reaches the stationary value without performing oscillations. The phase portrait in Fig. 4.24b illustrates this interplay. It shows the evolution of the photon density n_{ph} as a function of the QD electron carrier density n_e . In the beginning, n_{ph} increases exponentially with increasing n_e . Then, the photon density performs clockwise rotations around its steady state. When the current pulse is switched off, n_{ph} decreases exponentially with decreasing n_e (not shown in the phase portrait).

The Coulomb scattering rates S_b are essential for a better understanding of the turn-on dynamics. Unfortunately, they cannot be given in an analytical form. They show a strongly nonlinear dependence on the WL carrier densities. As a result, the frequency and the damping rate of relaxation oscillations cannot be expressed analytically. They both show a strong dependence on the injection current $j(t)$. The higher the current, the more pronounced are the ROs, see Fig. 4.21. Their frequency increases with the square root of the current, while the damping rate has a linear dependence on $j(t)$. In this work, the focus lies on the qualitative description of the turn-on dynamics of QD lasers. A detailed study on the characteristics of ROs and especially their dependence on the injection current is given in Lüdge et al.¹⁴⁰ There, it has been shown that a

*The threshold current density is determined by plotting the photon density n_{ph} over the current. Its value $j_{th} = 2 \times 10^{10} \text{ e}_0 \text{ cm}^{-2} \text{ ps}^{-1}$ corresponding to $j_{th} = 3 \times 10^3 \text{ A cm}^{-2}$. This value is approximately one order of magnitude larger than the measured experimental value. This discrepancy arises from the optically active area, which is necessary to calculate the threshold injection current density. Here, the active area is assumed to correspond to the WL area A . However, in the experiment, the active area is expected to be larger.

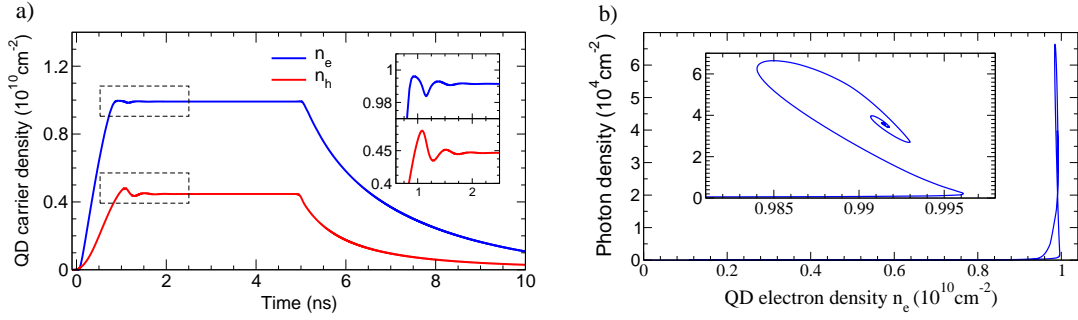


Figure 4.24: a) Response of the QD charge carrier densities $n_e(t)$, $n_h(t)$ to a current pulse (shown in Fig. 4.23). The insets show the generation of weak ROs even for the charge carrier densities. b) The Phase portrait of the photon density n_{ph} vs. the QD electron density n_e illustrates the interplay of electron filling and induced emission and absorption processes leading to an oscillation of the photon density. In the inset, a zoom into the oscillating region during the turn-on processes is shown.

good quantitative agreement with the experiment over a wide range of current densities can be achieved. Furthermore, studies based on the presented model have been performed to describe the modulation response and eye pattern diagrams of QD lasers. A good agreement with experimental findings was found.

Figure 4.24a illustrates the dynamics of the QD carrier densities n_e, n_h . Both quantities show weak relaxation oscillations before reaching the corresponding stationary values. These are less pronounced than in the dynamics of the photon density due to the capacitive inertia of the charge carriers. Other interesting features are the rise and fall times of n_e and n_h . While the rise time is dominated by the in-scattering contributions (on a picosecond time scale), the fall time is much longer due to slower radiative processes (on a nanosecond time scale). Furthermore, the electron density n_e has a higher stationary value than the hole density n_h due to the larger electron in-scattering rate S_e^{in} , see Fig. 4.7a.

Finally, in Fig. 4.25a, the evolution of the WL carrier densities $w_e(t), w_h(t)$ as a response to the application of the injection current pulse $j(t)$ is shown. In analogy to QD carrier densities $n_e(t), n_h(t)$, their rise and fall time are determined by scattering and radiative processes, respectively, resulting in clearly different time scales. In contrast to $n_e(t), n_h(t)$, the stationary value of the WL hole density w_h is higher than the one of w_e . The reason lies again in the higher in-scattering rate S_e^{in} ,

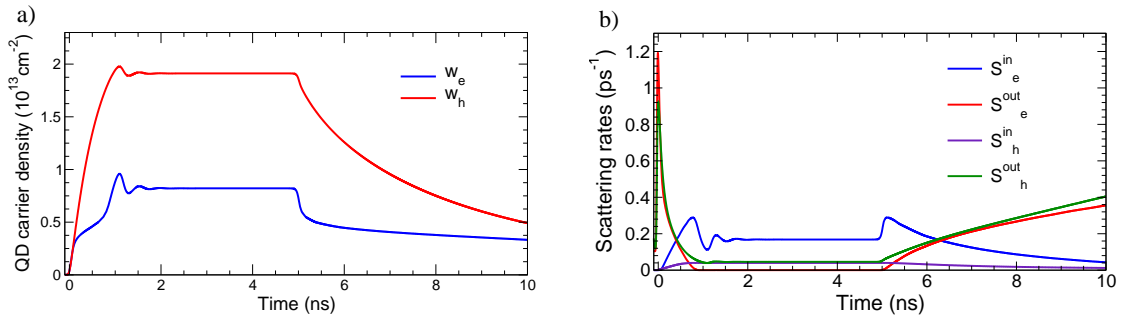


Figure 4.25: a) The dynamics of the WL carrier densities $w_e(t), w_h(t)$ during the turn-on processes of a QD laser. b) The time dependence of the Coulomb scattering rates S_e^{in} , S_e^{out} , S_h^{in} and S_h^{out} as a response to the injection current pulse $j(t)$.

that leads to a loss of charge carriers in the WL. Furthermore, the dynamics of the WL electron density w_e shows a peculiar behavior during both turn-on and switch-off processes. After the injection current is applied, an initial exponential increase of w_e is followed by a considerable slow-down. When the current pulse is switched off, the decrease of w_e in the first picoseconds is accelerated, before the radiative processes start to dominate the decrease of w_e . This can be explained with the dynamics of the scattering rates, shown in Fig. 4.25b. In the first picoseconds, the out-scattering processes dominate the dynamics. After the WL states are filled to a certain percentage, the in-scattering increases. Especially the capture of electrons into the QD ground states is considerably enhanced, accounting for the observed slow-down in the dynamics of the WL electron density w_e . S_e^{in} even performs well pronounced oscillations around its steady state. As long as the the injection pulse has a plateau and the charge carriers remain in their stationary states, the scattering rates are constant. Finally, when the current pulse is switched off, the scattering rates increase again, especially the electron in-scattering S_e^{in} , leading to a very fast decrease of w_e in the first picoseconds of the turn-off dynamics.

4.7.3 Summary

In this section, the turn-on dynamics of electrically pumped InAs/GaAs QD lasers has been investigated. The theoretical approach is based on rate equations describing the photon density and the charge carrier densities in QDs and the WL. The interaction between the charge carriers in the QD ground state and the delocalized two-dimensional WL states is included by a microscopic calculation of the Coulomb scattering rates.

The theoretical simulation of the turn-on dynamics shows the generation of relaxation oscillations in both the photon and the charge carrier density dynamics. They start after a characteristic delay time of approximately 1 ns which is due to the charge carrier filling of initially empty quantum dot states. The complex interplay between the strongly nonlinear Coulomb scattering rates and radiative processes gives rise to the relaxation oscillations and determines their frequency and damping rate. In agreement with experiments, a strong damping of relaxation oscillations in QD lasers is obtained. The results indicate the crucial importance of the Coulomb scattering processes between QD and the WL states. Other processes, such as electron-phonon scattering and WL-bulk interaction are assumed to play a minor role for a qualitative description of the turn-on dynamics. However, their inclusion as well as an extension to a multi-mode theory would improve the model.

I am convinced that not only what I am saying is wrong, but so will be what is said against it. Still one has to start somewhere. The truth does not lie in the middle, but rather somewhere around it - like a sack which changes its form with every opinion one puts into it, but at the same time becomes firmer and firmer.

Robert Musil

Chapter 5

Conclusions

This work presents a detailed theoretical investigation of optical properties of single-walled carbon nanotubes (SWCNTs) and self-assembled InAs/GaAs quantum dots (QDs).

Carbon nanotubes

A microscopic calculation of the absorption coefficient and the Rayleigh scattering cross section for carbon nanotubes is performed by a novel approach combining the density-matrix formalism with zone-folded tight-binding wave functions. The derived excitonic Bloch equations allow the study of SWCNTs of arbitrary chirality. Analytical expressions for the optical matrix elements are derived containing all symmetry-imposed selection rules. The Coulomb matrix elements are calculated within the Ohno-parametrization allowing the description of both intra- and inter-(sub)band processes. As a result, also the dark-bright splitting due to the Coulomb-induced intervalley mixing is covered.

In agreement with experiment, the calculated spectra of metallic nanotubes show a double-peaked structure resulting from the trigonal warping effect. The intensity ratios of the four lowest-lying transitions in both absorption and Rayleigh spectra can be explained by the different behavior of the optical matrix elements along the high-symmetry lines $K\Gamma$ and KM . Also in agreement with experiment, the Rayleigh line shape is predicted to be asymmetric, with an enhanced cross section for lower photon energies arising from non-resonant contributions of the optical susceptibility.

Furthermore, the Coulomb interaction is shown to be strongest when the momentum transfer is low. For intersubband processes with a perpendicular momentum transfer, the coupling strength is reduced to less than 5%. Due to their reduced dimensionality, SWCNTs have a strong Coulomb interaction that considerably changes their optical spectra. While the electron-electron interaction renormalizes the band gap by almost 100%, the electron-hole coupling leads in both semiconducting and metallic SWCNTs to the formation of excitons with binding energies of up to 1 eV. Due to the stronger internal screening, the excitonic binding energies in metallic nanotubes are shown to be one order of magnitude smaller than in semiconducting nanotubes. Higher transitions are also predicted to have considerable excitonic binding energies. The chirality and diameter dependence of the excitonic binding energy and the transition frequency is presented

in excitonic Kataura plots. The influence of the surrounding environment on the optical properties of SWCNTs is investigated, in particular the theoretical description of solvatochromic shifts in SDS medium is shown to be in good agreement with experimental results. The experimental trend for an increasing oscillator strength towards the armchair constellations is also confirmed. The latter is shown to be more pronounced if excitonic effects are taken into account. Finally, a brief outlook on exciton-phonon coupling in SWCNTs is given, accounting for the observation of pronounced phonon-sidebands in the absorption spectra.

Further investigations on i) the behavior of metallic nanotubes, ii) the dark-bright splitting and the role of dark excitons for relaxation mechanisms in SWCNTs, and iii) exciton-phonon coupling in metallic and semiconducting nanotubes need to be performed to obtain a better insight into the optical properties of SWCNTs. The evaluation of the excitonic Bloch equations including the integration over the entire Brillouin zone and the consideration of all subbands and the corresponding interactions is a numerical challenge with respect to CPU time and memory. Moreover, the nearest-neighbor tight-binding method can be improved by including more neighbors and considering curvature effects (in analogy to the ETB calculations). Future investigations will focus on non-linear optics, exciton relaxation, and functionalization of carbon nanotubes.

Quantum dots

Extending the confinement to all three spatial dimensions, semiconductor Bloch equation are derived to describe the dynamics in QD semiconductor lasers and amplifiers.

The Coulomb interaction, which is expected to dominate over the electron-phonon coupling due to the high charge carrier densities in the investigated gain regime, is considered beyond the Hartree-Fock approximation, taking scattering processes between the bound QD and continuous WL states into account. A detailed microscopic analysis of the nonlinear turn-on dynamics of electrically pumped InAs/GaAs QD lasers is performed, showing the generation of relaxation oscillations on a nanosecond time scale in both the photon and charge carrier density. The complex interplay between strongly nonlinear Coulomb scattering rates and radiative processes gives rise to these oscillations, which are generated after a characteristic delay time of approximately 1 ns. In agreement with experiments, the theory predicts a strong damping of relaxation oscillations, indicating the crucial importance of Coulomb scattering for a fast dynamical response of QD lasers.

Moreover, the ultrafast gain dynamics in QD semiconductor optical amplifiers has been investigated. It is found to be sensitively affected by the strength of the Coulomb scattering rates as well as by temperature, dephasing time, and pump power. Furthermore, the so called coherent artifact is shown to be a result of interference effects between the pump and the probe pulse rather than a consequence of two-photon absorption processes as often claimed in literature. The obtained results contribute to a better understanding of the limiting mechanisms for the ultrafast gain recovery in QD amplifiers. They are in good qualitative agreement with experimental results.

The theory can be further improved by taking the inhomogeneous distribution of QDs into account. A corresponding inhomogeneous broadening with respect to the gap energies and the dipole moments will be performed in future work. Also, propagation effects, processes leading to pure dephasing, wetting-layer-bulk interaction, multi-mode effects, and intra-QD relaxation need to be considered microscopically to obtain a complete picture of the dynamics in QD based devices.

Appendix A

Bloch Equations

In this chapter the equations of motion for single-particle density matrix elements are derived in the case of a two-band system.

A.1 Hartree-Fock

The starting point is the Hamilton operator (see Sec. 2.2)

$$\begin{aligned} H &= H_{0,c} + H_{c-f} + H_{c-c} + H_{0,ph} + H_{c-ph} \\ &= \sum_l \varepsilon_l a_l^\dagger a_l + \sum_{l,l'} \hbar \Omega_{l,l'} a_l^\dagger a_{l'} + \frac{1}{2} \sum_{l_1, l_2, l_3, l_4} V_{l_3, l_4}^{l_1, l_2} a_{l_1}^\dagger a_{l_2}^\dagger a_{l_4} a_{l_3} \end{aligned} \quad (\text{A.1})$$

$$+ \sum_i \hbar \omega_i (b_i^\dagger b_i + \frac{1}{2}) + \sum_{l,l'} \sum_i (g_{l,l'}^i a_l^\dagger b_i a_{l'} + g_{l,l'}^{i*} a_{l'}^\dagger b_i^\dagger a_l). \quad (\text{A.2})$$

The time evolution of an observable \hat{O} can be obtained from the Heisenberg equation of motion

$$i\hbar \frac{d}{dt} \hat{O}(t) = [\hat{O}(t), H]_- + \frac{\partial}{\partial t} \hat{O}(t). \quad (\text{A.3})$$

If $\hat{O}(t)$ has no explicit time dependence, the second contribution vanishes. To calculate the equations of motion, the well-known commutation relations

$$[a_l, a_{l'}^\dagger]_{\mp} = a_l a_{l'}^\dagger \mp a_{l'}^\dagger a_l = \delta_{l,l'}, \quad (\text{A.4})$$

$$[a_l, a_{l'}]_{\mp} = [a_l^\dagger, a_{l'}^\dagger]_{\mp} = 0. \quad (\text{A.5})$$

need to be considered. The fermion's (electrons, holes) operators anti-commute ($[\dots]_+$), while the boson's (phonons, photons) operators commute ($[\dots]_-$).

In the following, the dynamics of the microscopic polarization $p_{\mathbf{k}}(t) = \langle a_{v\mathbf{k}}^\dagger a_{c\mathbf{k}} \rangle$ and the population probabilities $\rho_{\mathbf{k}}^i(t) = \langle a_{i\mathbf{k}}^\dagger a_{i\mathbf{k}} \rangle$ (with $i = c, v$ denoting the conduction and the valence band) is determined separately for different part of the Hamiltonian.

Free particles: $H_c = H_{0,c} + H_{c-f}$

$$i\hbar\dot{p}_{\mathbf{k}} |_{H_c} = (\varepsilon_{c\mathbf{k}} - \varepsilon_{v\mathbf{k}})p_{\mathbf{k}} + \hbar\Omega_{vc}(\rho_{\mathbf{k}}^c - \rho_{\mathbf{k}}^v), \quad (\text{A.6})$$

$$i\hbar\dot{p}_{\mathbf{k}}^i |_{H_c} = 2i\hbar \text{Im}(\Omega_{vc}p_{\mathbf{k}}^*). \quad (\text{A.7})$$

Coulomb interaction within Hartree-Fock: H_{c-c}

$$i\hbar\dot{p}_{\mathbf{k}} |_{H_{c-c}} = \sum_{ABC} (V_{BC}^{c\mathbf{k}A} \langle a_{v\mathbf{k}}^+ a_A^+ a_C a_B \rangle - V_{v\mathbf{k}D}^{AB} \langle a_A^+ a_B^+ a_C a_{c\mathbf{k}} \rangle). \quad (\text{A.8})$$

The four-operator term is factorized into products of two-operator terms with:

$$\langle a_1^+ a_2^+ a_3 a_4 \rangle = \langle a_1^+ a_4 \rangle \langle a_2^+ a_3 \rangle - \langle a_1^+ a_3 \rangle \langle a_2^+ a_4 \rangle + \langle a_1^+ a_2^+ a_3 a_4 \rangle^c, \quad (\text{A.9})$$

where $\langle \dots \rangle^c$ denotes the correlation term. This factorisation leads to a closed set of equations of motion for the single-particle elements of the density matrix. If the correlation term is neglected, the truncation of a four-operator is called Hartree-Fock factorisation. Within this approximation and after applying the random phase approximation (see Sec. 2.4.1) the equation of motion for the microscopic polarisation $p_{\mathbf{k}}$ reads

$$i\hbar\dot{p}_{\mathbf{k}} |_{H_{c-c}^{\text{Hartree}}} = \sum_{\mathbf{k}'} \left[\underbrace{\left(V_{v\mathbf{k},v\mathbf{k}'}^{v\mathbf{k},v\mathbf{k}'} - V_{c\mathbf{k},v\mathbf{k}'}^{c\mathbf{k},v\mathbf{k}'} \right)}_{\rightarrow 0} p_{\mathbf{k}} \rho_{\mathbf{k}'}^v + V_{v\mathbf{k},v\mathbf{k}'}^{c\mathbf{k},c\mathbf{k}'} p_{\mathbf{k}'}^* (\rho_{\mathbf{k}}^c - \rho_{\mathbf{k}}^v) \right. \\ \left. + \underbrace{\left(V_{v\mathbf{k},c\mathbf{k}'}^{v\mathbf{k},c\mathbf{k}'} - V_{c\mathbf{k},c\mathbf{k}'}^{c\mathbf{k},c\mathbf{k}'} \right)}_{\rightarrow 0} p_{\mathbf{k}} \rho_{\mathbf{k}'}^c + V_{v\mathbf{k},c\mathbf{k}'}^{c\mathbf{k},v\mathbf{k}'} p_{\mathbf{k}'} (\rho_{\mathbf{k}}^c - \rho_{\mathbf{k}}^v) \right],$$

$$i\hbar\dot{p}_{\mathbf{k}} |_{H_{c-c}^{\text{Fock}}} = \sum_{\mathbf{k}'} \left[\left(V_{v\mathbf{k}',c\mathbf{k}'}^{c\mathbf{k},v\mathbf{k}'} - V_{v\mathbf{k},v\mathbf{k}'}^{v\mathbf{k}',v\mathbf{k}} \right) p_{\mathbf{k}} \rho_{\mathbf{k}'}^v - V_{v\mathbf{k}',v\mathbf{k}}^{c\mathbf{k},c\mathbf{k}'} p_{\mathbf{k}'}^* (\rho_{\mathbf{k}}^c - \rho_{\mathbf{k}}^v) \right. \\ \left. + \left(V_{c\mathbf{k}',c\mathbf{k}'}^{c\mathbf{k},c\mathbf{k}'} - V_{v\mathbf{k},c\mathbf{k}'}^{c\mathbf{k}',v\mathbf{k}} \right) p_{\mathbf{k}} \rho_{\mathbf{k}'}^c - V_{c\mathbf{k}',v\mathbf{k}}^{c\mathbf{k},v\mathbf{k}'} p_{\mathbf{k}'} (\rho_{\mathbf{k}}^c - \rho_{\mathbf{k}}^v) \right].$$

In the limit of linear optics, i.e. $\rho_{\mathbf{k}}^v = 1$ and $\rho_{\mathbf{k}}^c = 0$, the contributions simplify to

$$i\hbar\dot{p}_{\mathbf{k}} |_{H_{c-c}} = \sum_{\mathbf{k}'} \left[\left(V_{v\mathbf{k}',c\mathbf{k}}^{c\mathbf{k},v\mathbf{k}'} - V_{v\mathbf{k},v\mathbf{k}'}^{v\mathbf{k}',v\mathbf{k}} \right) p_{\mathbf{k}} + \left(V_{c\mathbf{k}',v\mathbf{k}}^{c\mathbf{k},v\mathbf{k}'} - V_{v\mathbf{k},c\mathbf{k}'}^{c\mathbf{k},v\mathbf{k}'} \right) p_{\mathbf{k}'} + \left(V_{v\mathbf{k}',v\mathbf{k}}^{c\mathbf{k},c\mathbf{k}'} - V_{v\mathbf{k},v\mathbf{k}'}^{c\mathbf{k},c\mathbf{k}'} \right) p_{\mathbf{k}'}^* \right], \quad (\text{A.10})$$

where the blue contributions stem from the Fock part and the red ones from the Hartree part of the Coulomb interaction.

Electron phonon interaction within Hartree-Fock: $H_{\text{ph}} = H_{0,\text{ph}} + H_{\text{c-ph}}$

$$i\hbar\dot{p}_{\mathbf{k}} |_{H_{\text{ph}}} = \sum_{\mathbf{q},\gamma,\lambda} \left[g_{\mathbf{k},\mathbf{q},\mathbf{k}'}^{c\lambda,\gamma*} S_{\mathbf{k},\mathbf{q},\mathbf{k}'}^{v\lambda,\gamma} - g_{\mathbf{k}',\mathbf{q},\mathbf{k}}^{\lambda v,\gamma*} S_{\mathbf{k}',\mathbf{q},\mathbf{k}}^{\lambda c,\gamma} + g_{\mathbf{k}',\mathbf{q},\mathbf{k}}^{\lambda c,\gamma} S_{\mathbf{k}',\mathbf{q},\mathbf{k}}^{\lambda v,\gamma*} - g_{\mathbf{k},\mathbf{q},\mathbf{k}'}^{v\lambda,\gamma} S_{\mathbf{k},\mathbf{q},\mathbf{k}'}^{c\lambda,\gamma*} \right] \quad (\text{A.11})$$

with the phonon-assisted quantities

$$S_{\mathbf{k},\mathbf{q},\mathbf{k}'}^{\lambda\lambda',\gamma} = \langle a_{\lambda\mathbf{k}}^+ b_{\gamma\mathbf{q}} a_{\lambda'\mathbf{k}'} \rangle \quad \text{and} \quad S_{\mathbf{k}',\mathbf{q},\mathbf{k}}^{\lambda'\lambda,\gamma*} = \langle a_{\lambda'\mathbf{k}'}^+ b_{\gamma\mathbf{q}}^+ a_{\lambda\mathbf{k}} \rangle. \quad (\text{A.12})$$

A.2 Coulomb scattering

The Coulomb interaction is given in second quantization as

$$V = \frac{1}{2} \sum_{ABCD} V_{CD}^{AB} a_A^+ a_B^+ a_D a_C \quad (\text{A.13})$$

with the Coulomb matrix elements

$$V_{CD}^{AB} = \langle \Psi_A \Psi_B | V | \Psi_C \Psi_D \rangle. \quad (\text{A.14})$$

Renaming indices and exploiting the commutation relations from Eqs. (A.4)-(A.5), following relations can be derived

$$V_{CD}^{AB} = -V_{CD}^{BA} = V_{DC}^{BA}, \quad V_{CD}^{AB} = V_{AB}^{CD*}. \quad (\text{A.15})$$

In this section, a detailed derivation of the Boltzmann equation is presented. The starting point is the Hamiltonian $H = H_{0,c} + H_{\text{c-c}}$ describing the Coulomb interaction. In contrary to the last section, the calculation is performed beyond the Hartree-Fock approximation. The correlation expansion applied to Eq. (A.8) leads to the following equation

$$\begin{aligned} i\hbar \frac{d}{dt} \langle a_1^+ a_2 \rangle &= (\varepsilon_2 - \varepsilon_1) \langle a_1^+ a_2 \rangle + \sum_{abc} [V_{bc}^{2a} \langle a_1^+ a_a^+ a_c a_b \rangle^c - V_{1c}^{ab} \langle a_a^+ a_b^+ a_c a_2 \rangle^c] \\ &+ \sum_{abc} \{ V_{bc}^{2a} [\langle a_1^+ a_b \rangle \langle a_a^+ a_c \rangle - \langle a_1^+ a_c \rangle \langle a_a^+ a_b \rangle] - V_{1c}^{ab} [\langle a_a^+ a_2 \rangle \langle a_b^+ a_c \rangle - \langle a_a^+ a_c \rangle \langle a_b^+ a_2 \rangle] \}. \end{aligned} \quad (\text{A.16})$$

Now, the correlations terms are taken into account. To obtain a more compact equation, the following abbreviations are introduced

$$\begin{aligned} \varepsilon_{1a}^{HF} &:= \varepsilon_1 \delta_{1a} + 2 \sum_{bc} V_{1c}^{ab} \langle a_b^+ a_c \rangle, \\ \varepsilon_{a2}^{HF} &:= \varepsilon_2 \delta_{a2} + 2 \sum_{bc} V_{ac}^{2b} \langle a_b^+ a_c \rangle. \end{aligned}$$

After some simple rewriting, one obtains

$$i\hbar \frac{d}{dt} \langle a_1^+ a_2 \rangle = \sum_a [\varepsilon_{a2}^{HF} \langle a_1^+ a_a \rangle - \varepsilon_{1a}^{HF} \langle a_a^+ a_2 \rangle] - \sum_{abc} [V_{1c}^{ab} \langle a_a^+ a_b^+ a_c a_2 \rangle^c - V_{bc}^{2a} \langle a_1^+ a_a^+ a_c a_b \rangle^c]. \quad (\text{A.17})$$

The dynamics of four-operator-products needs to be determined. Applying again the Heisenberg equation yields

$$\begin{aligned}
i\hbar \frac{d}{dt} \langle a_1^\dagger a_2^\dagger a_3 a_4 \rangle &= -(\varepsilon_1 + \varepsilon_2 - \varepsilon_3 - \varepsilon_4) \langle a_1^\dagger a_2^\dagger a_3 a_4 \rangle \\
&+ \sum_{abc} V_{1c}^{ab} [\langle a_a^\dagger a_b^\dagger a_2^\dagger a_c a_3 a_4 \rangle - \delta_{2c} \langle a_a^\dagger a_b^\dagger a_3 a_4 \rangle] \\
&- \sum_{abc} V_{2c}^{ab} \langle a_1^\dagger a_a^\dagger a_b^\dagger a_c a_3 a_4 \rangle \\
&+ \sum_{abc} V_{3c}^{ab} \langle a_1^\dagger a_2^\dagger a_c^\dagger a_b a_a a_4 \rangle \\
&- \sum_{abc} V_{4c}^{ab} [\langle a_1^\dagger a_2^\dagger a_c^\dagger a_3 a_b a_a \rangle - \delta_{3c} \langle a_1^\dagger a_2^\dagger a_b a_a \rangle].
\end{aligned}$$

Carrier-carrier interaction couples the four-operator term to six-operator terms. These have to be further factorised³⁸

$$\begin{aligned}
\langle a_1^\dagger a_2^\dagger a_3^\dagger a_4 a_5 a_6 \rangle &= \langle a_1^\dagger a_4 \rangle (\langle a_2^\dagger a_6 \rangle \langle a_3^\dagger a_5 \rangle - \langle a_2^\dagger a_5 \rangle \langle a_3^\dagger a_6 \rangle) \\
&- \langle a_1^\dagger a_5 \rangle (\langle a_2^\dagger a_6 \rangle \langle a_3^\dagger a_4 \rangle - \langle a_2^\dagger a_4 \rangle \langle a_3^\dagger a_6 \rangle) \\
&+ \langle a_1^\dagger a_6 \rangle (\langle a_2^\dagger a_5 \rangle \langle a_3^\dagger a_4 \rangle - \langle a_2^\dagger a_4 \rangle \langle a_3^\dagger a_5 \rangle) \\
&+ \langle a_1^\dagger a_2^\dagger a_4 a_5 \rangle^c \langle a_3^\dagger a_6 \rangle - \langle a_1^\dagger a_2^\dagger a_4 a_6 \rangle^c \langle a_3^\dagger a_5 \rangle + \langle a_1^\dagger a_2^\dagger a_5 a_6 \rangle^c \langle a_3^\dagger a_4 \rangle \\
&- \langle a_1^\dagger a_3^\dagger a_4 a_5 \rangle^c \langle a_2^\dagger a_6 \rangle + \langle a_1^\dagger a_3^\dagger a_4 a_6 \rangle^c \langle a_2^\dagger a_5 \rangle - \langle a_1^\dagger a_3^\dagger a_5 a_6 \rangle^c \langle a_2^\dagger a_4 \rangle \\
&+ \langle a_2^\dagger a_3^\dagger a_4 a_5 \rangle^c \langle a_1^\dagger a_6 \rangle - \langle a_2^\dagger a_3^\dagger a_4 a_6 \rangle^c \langle a_1^\dagger a_5 \rangle + \langle a_2^\dagger a_3^\dagger a_5 a_6 \rangle^c \langle a_1^\dagger a_4 \rangle.
\end{aligned} \tag{A.18}$$

The correlation expansion is truncated at this level, i.e. the six-operator correlation terms are neglected. Then, the equation of motion for the four-operator correlation terms is determined

$$\langle a_1^\dagger a_2^\dagger a_3 a_4 \rangle^c = \langle a_1^\dagger a_2^\dagger a_3 a_4 \rangle - \underbrace{\langle a_1^\dagger a_4 \rangle \langle a_2^\dagger a_3 \rangle + \langle a_1^\dagger a_3 \rangle \langle a_2^\dagger a_4 \rangle}_{\text{Hartree-Fock part}}.$$

Some of the terms from Eq. (A.18) cancel with the Hartree-Fock part resulting in

$$\begin{aligned}
i\hbar \frac{d}{dt} \sigma_{1234}^c \Big|_{\text{first three rows of Eq. (A.18)}} &= -(\varepsilon_1 + \varepsilon_2 - \varepsilon_3 - \varepsilon_4) \sigma_{1234}^c \\
&+ 2 \sum_{abc} V_{dc}^{ab} \left[\sigma_{a4} \sigma_{b3} ((\sigma_{2c} - \delta_{2c}) \delta_{1d} + \sigma_{1d} (\delta_{2c} - \sigma_{2c})) + \sigma_{1a} \sigma_{2b} ((\delta_{4a} - \sigma_{a4}) \delta_{b3} - \sigma_{b3} (\delta_{4a} - \sigma_{a4})) \right] \\
&+ \sum_{abc} V_{dc}^{ab} \left[\sigma_{ab34}^c [-\delta_{1d} \delta_{2c} + \sigma_{2c} \delta_{1d} + \sigma_{1d} \delta_{2c}] + \sigma_{12dc}^c [\delta_{d4} \delta_{c3} - \sigma_{d4} \delta_{c3} - \sigma_{c3} \delta_{d4}] \right].
\end{aligned}$$

At this step an useful zero-addition (**bold printed**) has been introduced. With the relation

$$(\sigma_{2c} - \delta_{2c}) \delta_{1d} + \sigma_{1d} (\delta_{2c} - \sigma_{2c}) = -\sigma_{2c}^+ \sigma_{1d}^+ \quad \text{with} \quad \sigma_{2c}^+ = \langle a_c a_2^\dagger \rangle,$$

one obtains the following result including all contributions from Eq. (A.18)

$$\begin{aligned}
i\hbar \frac{d}{dt} \sigma_{1234}^c &= -(\varepsilon_1 + \varepsilon_2 - \varepsilon_3 - \varepsilon_4) \sigma_{1234}^c \\
&- \sum_{abdc} V_{dc}^{ab} \left(2 [\sigma_{a4} \sigma_{b3} \sigma_{2c}^+ \sigma_{1d}^+ - \sigma_{a4}^+ \sigma_{b3}^+ \sigma_{2c} \sigma_{1d}] + \sigma_{ab34}^c [\sigma_{2c}^+ \sigma_{1d}^+ - \sigma_{2c} \sigma_{1d}] - \sigma_{12ba}^c [\sigma_{d4}^+ \sigma_{c3}^+ - \sigma_{d4} \sigma_{c3}] \right) \\
&+ \sum_a \left(\varepsilon_{1a}^{cor} \sigma_{a234}^c + \varepsilon_{2a}^{cor} \sigma_{1a34}^c - \varepsilon_{3a}^{cor} \sigma_{123d}^c - \varepsilon_{a4}^{cor} \sigma_{12d4}^c \right) \\
&- \sum_{abdc} V_{dc}^{ab} \left(\sigma_{2ca3}^c [\sigma_{d4}^+ \sigma_{1b} - \sigma_{1b}^+ \sigma_{d4}] + \sigma_{2ca4}^c [\sigma_{d3}^+ \sigma_{1b} - \sigma_{1b}^+ \sigma_{d3}] \right. \\
&\quad \left. - \sigma_{a1d4}^c [\sigma_{b3}^+ \sigma_{2c} - \sigma_{2c}^+ \sigma_{b3}] + \sigma_{a1d3}^c [\sigma_{b4}^+ \sigma_{2c} - \sigma_{2c}^+ \sigma_{b4}] \right).
\end{aligned}$$

Here, the abbreviation $\varepsilon_{1a}^{cor} = 2 \sum_{bc} V_{1c}^{ab} \sigma_{bc}$ has been introduced. To derive the Boltzmann equation for scattering processes only the blue colored terms are taken into account. They correspond to the contributions stemming from the two-operator parts from Eq. (A.18). Higher order terms are ascribed, e.g. , to screening which corrects the bare Coulomb potential. They are partially considered by including a dephasing constant γ . Then, the equations reads

$$\frac{d}{dt} \sigma_{1234}^c(t) = \frac{i}{\hbar} (\varepsilon_1 + \varepsilon_2 - \varepsilon_3 - \varepsilon_4) \sigma_{1234}^c(t) + \frac{i}{\hbar} Q(t) - \gamma \sigma_{1234}^c(t)$$

$$\text{with } Q(t) = 2 \sum_{abdc} V_{dc}^{ab} [\sigma_{a4} \sigma_{b3} \sigma_{2c}^+ \sigma_{1d}^+ - \sigma_{a4}^+ \sigma_{b3}^+ \sigma_{2c} \sigma_{1d}].$$

Finally, the Markov approximation is used neglecting all memory effects

$$\sigma_{1234}^c(t) = \frac{i}{\hbar} \int_{-\infty}^t dt' e^{(\frac{i}{\hbar} \Delta\varepsilon + \gamma)(t-t')} Q(t') = \frac{i}{\hbar} \int_0^{\infty} ds e^{(\frac{i}{\hbar} \Delta\varepsilon + \gamma)s} Q(t-s) \approx \frac{i}{\hbar} Q(t) \int_0^{\infty} ds e^{(\frac{i}{\hbar} \Delta\varepsilon + \gamma)s}$$

with the abbreviation $\Delta\varepsilon = (\varepsilon_1 + \varepsilon_2 - \varepsilon_3 - \varepsilon_4)$ and $s \equiv t - t'$. In the limiting case of $\gamma \rightarrow 0$, the solution can be written in an analytical form

$$\sigma_{1234}^c(t) = iQ(t)\pi\delta(\Delta\varepsilon). \tag{A.19}$$

Since in this section, the focus lies on the derivation of the Boltzmann equation, which expresses an occupation probability, in the following the consideration will be restricted to the special case of identical indices in Eq. (A.16), i.e. $2 = 1$. Then, the equation for the occupation probability $\rho_1 = \langle a_1^\dagger a_1 \rangle$ reads

$$\begin{aligned}
\frac{d}{dt} \rho_1 &= -\frac{2\pi}{\hbar} \sum_{abc} \sum_{ABCD} V_{1c}^{ab} V_{DC}^{AB} \left(\sigma_{A1} \sigma_{Bc} \sigma_{bC}^+ \sigma_{aD}^+ - \sigma_{A1}^+ \sigma_{Bc}^+ \sigma_{bC} \sigma_{aD} \right) \delta(\varepsilon_a + \varepsilon_b - \varepsilon_c - \varepsilon_1) \\
&+ \frac{2\pi}{\hbar} \sum_{abc} \sum_{ABCD} V_{ba}^{1c} V_{DC}^{AB} \left(\sigma_{Ab} \sigma_{Ba} \sigma_{cC}^+ \sigma_{1D}^+ - \sigma_{Ab}^+ \sigma_{Ba}^+ \sigma_{cC} \sigma_{1D} \right) \delta(\varepsilon_1 + \varepsilon_c - \varepsilon_a - \varepsilon_b) \\
&= -\frac{2\pi}{\hbar} \sum_{abc} V_{1c}^{ab} V_{ab}^{1c} \left(\rho_1 \rho_c (1 - \rho_b)(1 - \rho_a) - \rho_a \rho_b (1 - \rho_1)(1 - \rho_c) \right) \delta(\varepsilon_a + \varepsilon_b - \varepsilon_c - \varepsilon_1) \\
&+ \frac{2\pi}{\hbar} \sum_{abc} V_{ba}^{1c} V_{1c}^{ba} \left(\rho_a \rho_b (1 - \rho_1)(1 - \rho_c) - \rho_1 \rho_c (1 - \rho_b)(1 - \rho_a) \right) \delta(\varepsilon_1 + \varepsilon_c - \varepsilon_a - \varepsilon_b).
\end{aligned}$$

The second sum has been evaluated using $\sigma_{A1} = \rho_1 \delta_{A1}$ and $\sigma_{bC}^+ = 1 - \rho_b \delta_{bC}$. Furthermore, relations between the Coulomb matrix elements from Eq. (A.15) have been exploited. Finally, one obtains the **Boltzmann equation**

$$\frac{d}{dt} \rho_1 = \frac{2\pi}{\hbar} \sum_{abc} V_{ab}^{1c} \left(V_{ab}^{1c*} - V_{ba}^{1c*} \right) \left(\rho_a \rho_b (1 - \rho_1)(1 - \rho_c) - \rho_1 \rho_c (1 - \rho_b)(1 - \rho_a) \right) \delta(\varepsilon_1 + \varepsilon_c - \varepsilon_a - \varepsilon_b).$$

The derivation of the corresponding equation of motion for the microscopic polarization $\langle a_1^+ a_2 \rangle$ with different indices is straight-forward.¹⁴¹ It reads

$$p = -\frac{i}{\hbar} (\varepsilon_2 - \varepsilon_1) p + \frac{2\pi}{\hbar} \sum_{abc} \left(|V_{ab}^{1c}|^2 \delta(\varepsilon_2 + \varepsilon_c - \varepsilon_a - \varepsilon_b) - |V_{ab}^{2c}|^2 \delta(\varepsilon_1 + \varepsilon_c - \varepsilon_a - \varepsilon_b) \right) \times \\ \times \left(\rho_c (1 - \rho_b)(1 - \rho_a) + (1 - \rho_c) \rho_b \rho_a \right) p. \quad (\text{A.20})$$

If you are lonely when you're alone, you are in bad company.

Jean-Paul Sartre

Appendix B

Spontaneous Emission

In this section, a quantum mechanical description of the spontaneous emission is presented. The latter is crucial, e.g. during turn-on processes of a laser. Induced emission responsible for the laser process is proportional to the photon density, i.e. at the beginning some photons need to be created by spontaneous emission before the laser process can start. Furthermore, the simplifying assumption of only one light mode in the laser resonator will be dropped in this section to be able to calculate the Einstein coefficient analytically.

For most investigations of this work, the semiclassical approach treating the electromagnetic field classically is sufficient. For a description of the spontaneous emission, however, the electromagnetic field needs to be quantized. The starting point is the classical, single-mode electromagnetic field within a cavity along the z -axis³⁶

$$\mathbf{E}(z, t) = q(t) \sqrt{\frac{\omega^2}{\epsilon_0 V}} \sin(kz) \mathbf{e}_p \quad (\text{B.1})$$

with the single-mode frequency ω , the wave vector k , the cavity volume V , and the polarization vector \mathbf{e}_p . $q(t)$ is a measure of the field amplitude. The corresponding classical Hamilton operator is given by

$$H = \int dV (\epsilon_0 |\mathbf{E}|^2 + |\mathbf{B}|^2 \mu^{-1}). \quad (\text{B.2})$$

Inserting the electric field from Eq. (B.1) and the corresponding magnetic field, that can be derived from the Maxwell equation $\text{rot } \mathbf{E} = -\dot{\mathbf{B}}$, the Hamilton operator can be written as

$$H = \frac{1}{2} (\omega^2 q^2 + p^2). \quad (\text{B.3})$$

It corresponds to the Hamiltonian of a harmonic oscillator. The quantization of the electromagnetic field can be traced back to the quantization of a harmonic oscillator. Introducing photon annihilation and photon creation operators c and c^+

$$c = \frac{1}{\sqrt{2\hbar\omega}(\omega q + ip)}, \quad c^+ = \frac{1}{\sqrt{2\hbar\omega}(\omega q - ip)}, \quad (\text{B.4})$$

the well-known quantized Hamilton operator is obtained

$$H = \hbar\omega \left(c^+ c + \frac{1}{2} \right). \quad (\text{B.5})$$

Inserting q , obtained from Eq. (B.4) into Eq. (B.1) yields the quantized single-mode electric field

$$E(z, t) = E_0 \sin(q_i z) (c^+ + c) \quad (\text{B.6})$$

with $E_0 = \sqrt{\frac{\hbar\omega}{2\epsilon_0 V}}$. The derivation of the spontaneous emission rate requires the inclusion of all modes of the field. The generalization of Eq. (B.6) is straight-forward. The Hamilton operator of a multi-mode field is the sum of the Hamiltonians of a single mode. As a result, the multi-mode electric field is given by

$$E(z, t) = \sum_i E_{0,i} \sin(q_i z) (c_i^+ + c_i). \quad (\text{B.7})$$

The modes are characterized by the frequency, wave vector and the polarization. Now, the carrier-field Hamilton operator from Eq. (2.15) can be generalized to

$$H_{c-f} = \sum_i \sum_{l,l'} d_{l,l'} E_0 \sin(q_i z) (c_i^+ + c_i) a_l^+ a_{l'} \quad (\text{B.8})$$

including a sum over the photon modes i and the electronic quantum numbers l, l' . The latter are compound indices containing the band index λ and the wave vectors i . Performing the sum over λ for a two-level system with $\lambda = c, v$ and applying the rotating wave approximation (see Sec. 2.4.1) yields

$$H_{c-f} = \sum_i \sum_{\mathbf{k}} E_0 \sin(q_i z) (d_{vc} c_i^+ a_{v\mathbf{k}}^+ a_{c\mathbf{k}} + d_{cv} c_i a_{c\mathbf{k}}^+ a_{v\mathbf{k}}). \quad (\text{B.9})$$

The Hamilton operator contains the photon-assisted quantities $c_i^+ a_{v\mathbf{k}}^+ a_{c\mathbf{k}}$ and $c_i a_{c\mathbf{k}}^+ a_{v\mathbf{k}}$. The first quantity describes the emission of a photon and the corresponding annihilation of an electron-hole pair. The second quantity describes the reverse process of a photon absorption. Now, the Heisenberg equation can be applied to obtain an equation of motion for the photon number $N_{ph}^i = \langle c_i^+ c_i \rangle$ of the mode i . Using the Hamilton operator $H = H_{0,c} + H_{0,p} + H_{c-f}$ with the free carrier part given in Eq. (A.1), the free photon part $H_{0,p} = \sum_j (\hbar\omega_j + \frac{1}{2}) c_j^+ c_j$, and the quantized electron-light part from Eq. (B.9) yields

$$\frac{d}{dt} \langle c_i^+ c_i \rangle = -\frac{i}{\hbar} d_{vc} E_0 \sin(q_i z) \sum_{\mathbf{k}} \left(\langle c_i^+ a_{v\mathbf{k}}^+ a_{c\mathbf{k}} \rangle - \langle c_i a_{c\mathbf{k}}^+ a_{v\mathbf{k}} \rangle \right). \quad (\text{B.10})$$

Here, only the electron-light part of the Hamiltonian contributes directly to the dynamics of the photon number N_{ph}^i . To obtain a closed set of equations, also the dynamics of the appearing photon-assisted quantities needs to be calculated. Applying again the Heisenberg equation, one obtains commutators, such as

$$\begin{aligned} [c_i^+ a_{v\mathbf{k}}^+ a_{c\mathbf{k}}, H_{0,c}]_- &= \sum_{\mathbf{k}} (\varepsilon_{c\mathbf{k}} - \varepsilon_{v\mathbf{k}}) c_i^+ a_{v\mathbf{k}}^+ a_{c\mathbf{k}}, \\ [c_i^+ a_{v\mathbf{k}}^+ a_{c\mathbf{k}}, H_{0,p}]_- &= -\hbar\omega_i c_i^+ a_{v\mathbf{k}}^+ a_{c\mathbf{k}}, \\ [c_i^+ a_{v\mathbf{k}}^+ a_{c\mathbf{k}}, H_{c-f}]_- &= d_{cv} E_0 \sin(q_i z) \left(\sum_i (c_\lambda^+ c_i a_{v\mathbf{k}}^+ a_{v\mathbf{k}} - c_\lambda^+ c_i a_{c\mathbf{k}}^+ a_{c\mathbf{k}}) \right. \\ &\quad \left. - a_{c\mathbf{k}}^+ a_{c\mathbf{k}} + \sum_{\mathbf{k}'} a_{c\mathbf{k}'}^+ a_{v\mathbf{k}} a_{v\mathbf{k}'}^+ a_{c\mathbf{k}} \right). \end{aligned}$$

Considering the expectation values and factorizing the four-operator terms within the Hartree-

Fock approximation,* the equation of motion for the photon-assisted quantities can be determined

$$\frac{d}{dt} \langle c_i^+ a_{v\mathbf{k}}^+ a_{c\mathbf{k}} \rangle = -i(\omega_{\mathbf{k}} - \omega_i + i\gamma) \langle c_i^+ a_{v\mathbf{k}}^+ a_{c\mathbf{k}} \rangle - \frac{i}{\hbar} d_{cv} E_0 \sin(k_i z) \left(\langle c_i^+ c_i \rangle (1 - \rho_{\mathbf{k}}^h - \rho_{\mathbf{k}}^e) - \rho_{\mathbf{k}}^e \rho_{\mathbf{k}}^h - p_{\mathbf{k}} p_{\mathbf{k}}^* \right). \quad (\text{B.11})$$

Here, the random phase approximation (see Sec. 2.4.1) has been applied neglecting expectation values with different wave vectors (modes), i.e. $\sum_{\mathbf{k}'} \langle a_{c\mathbf{k}'}^+ a_{c\mathbf{k}} \rangle \approx \langle a_{c\mathbf{k}}^+ a_{c\mathbf{k}} \rangle$. Furthermore, the occupation probabilities for electrons $\rho_{\mathbf{k}}^e = \langle a_{c\mathbf{k}}^+ a_{c\mathbf{k}} \rangle$ and holes $\rho_{\mathbf{k}}^h = 1 - \langle a_{v\mathbf{k}}^+ a_{v\mathbf{k}} \rangle$, the gap frequency $\omega_{\mathbf{k}} = \omega_{c\mathbf{k}} - \omega_{v\mathbf{k}}$, as well as the decay rate γ have been introduced. The phenomenological rate γ describes neglected scattering processes. It is responsible for a broadening of spectral lines. The last term in Eq. (B.11) driven by the quadratic microscopic polarisation $p_{\mathbf{k}} p_{\mathbf{k}}^*$ is assumed to be vanishingly small, since the microscopic polarization decays much faster than the occupation probabilities for electrons and holes, as shown in chapter 4. Furthermore, radiative processes are on a nanosecond time scale while carrier scattering occurs within some ps. As a result, the derivative of the photon-assisted quantities is small.³⁶ Assuming $\frac{d}{dt} \langle c_i^+ a_{v\mathbf{k}}^+ a_{c\mathbf{k}} \rangle \approx 0$, Eq. (B.11) can be solved formally

$$\langle c_i^+ a_{v\mathbf{k}}^+ a_{c\mathbf{k}} \rangle = -\frac{i}{\hbar} d_{cv} E_0 \sin(k_i z) \frac{\langle c_i^+ c_i \rangle (1 - \rho_{\mathbf{k}}^h - \rho_{\mathbf{k}}^e) - \rho_{\mathbf{k}}^e \rho_{\mathbf{k}}^h}{i(\omega_{\mathbf{k}} - \omega_i) + \gamma}. \quad (\text{B.12})$$

Inserting the solution in Eq. (B.10) gives

$$\frac{d}{dt} \langle c_i^+ c_i \rangle = |\Omega(\omega_i, \Theta)|^2 \left(\langle c_i^+ c_i \rangle (1 - \rho_{\mathbf{k}}^h - \rho_{\mathbf{k}}^e) + \rho_{\mathbf{k}}^e \rho_{\mathbf{k}}^h \right) \frac{2\gamma}{(\omega_{\mathbf{k}} - \omega_i)^2 + \gamma^2} \quad (\text{B.13})$$

with $|\Omega(\omega_i, \Theta)|^2 = \frac{1}{\hbar^2} |d_{vc}|^2 |E_0 \sin(k_i z)|^2$. In the limit $\gamma \rightarrow 0$, the described ansatz corresponds to the Markov approximation, see Sec. 2.4.1. In this limit, the solution from Eq. (B.12) simplifies considerably due to the relation⁴²

$$\lim_{\gamma \rightarrow 0} \frac{2\gamma}{(\Delta\omega_{\mathbf{k}} - \omega)^2 + \gamma^2} = 2\pi\delta(\omega_{\mathbf{k}} - \omega). \quad (\text{B.14})$$

Up to now, only a single mode of the radiation field has been considered. To calculate the total radiative rate for the spontaneous emission all possible modes need to be taken into account. They are characterized by the wave vector $q = \frac{\omega}{c}$. Applying this dispersion relation for light, the sum over the photon modes denoted by i can be expressed as an integral over frequency ω_i

$$\sum_i \rightarrow \frac{V}{(2\pi)^3} \int d^3q = \frac{V}{(2\pi c)^3} \int_0^\infty d\omega \omega^2 \int_0^\pi d\theta \sin\theta \int_0^{2\pi} d\phi.$$

This integral is evaluated using the relation from Eq. (B.14). Then, an equation of motion for the photons density $n_{ph} = N^{QD} \sum_i \langle c_i^+ c_i \rangle$ is obtained

$$\frac{d}{dt} n_{ph} = \underbrace{\frac{|d_{vc}|^2}{3\pi \epsilon_0 \hbar} \left(\frac{\omega_{\mathbf{k}}}{c_m} \right)^3}_{\text{Einstein coeff. } W} \left[\underbrace{n_{ph} (n_e + n_h - N^{QD})}_{\text{induced processes}} + \underbrace{n_e n_h}_{\text{spont. emission}} \right] - 2\kappa n_{ph}. \quad (\text{B.15})$$

*Considering a QD without the interaction with the surrounding WL, the Hartree-Fock approximation is not applicable, since a QD has only few bound states, which can only be populated with maximally two carriers. The basic assumption of the Hartree-Fock approximation, however, is the presence of many particles. Here, the four-operator product can be analysed by exploiting the relation $\rho_{\mathbf{k}}^h = 1 - \langle a_{v\mathbf{k}}^+ a_{v\mathbf{k}} \rangle$. This results in $\langle a_{c\mathbf{k}}^+ a_{v\mathbf{k}}^+ a_{v\mathbf{k}} a_{c\mathbf{k}} \rangle = \langle a_{c\mathbf{k}}^+ (1 - a_{h\mathbf{k}}^+ a_{h\mathbf{k}}) a_{c\mathbf{k}} \rangle \approx \rho_{\mathbf{k}}^e$ neglecting the four-operator expectation value. Then, the spontaneous emission rate is proportional to the electron population $\rho_{\mathbf{k}}^e$.

The first contribution is proportional to the photon density n_{ph} . It describes the processes of induced emission and absorption. In contrary, the second contribution is proportional only to the occupation probabilities for electrons and holes. This term describes the spontaneous emission. The strength of both processes is given by the Einstein coefficient

$$W = \frac{|d_{vc}|^2}{3\pi \varepsilon_0 \hbar} \left(\frac{\omega}{c_m} \right)^3, \quad (\text{B.16})$$

which is dependent on the dipole momentum d_{vc} and the gap frequency ω_k . Furthermore, the coefficient

$$\kappa = \frac{\gamma}{2} = \left(\kappa_{int} - \frac{1}{2L} \ln(r_1 r_2) \right) c_m \quad (\text{B.17})$$

has been introduced. It describes the total cavity loss, which depends on the cavity length L , the facet reflection coefficients r_1, r_2 , and the internal losses κ_{int} .

Appendix C

Coulomb Matrix Elements

C.1 CNT Coulomb matrix elements

The Coulomb interaction in one-dimensional structures needs to be treated with care since the ground state is known to have an infinite energy.⁶¹ This problem can be avoided by introducing a regularized Coulomb potential that takes into account that CNTs are not strictly one-dimensional.

The Coulomb matrix elements are given by⁴²

$$V_{l_3, l_4}^{l_1, l_2} = \int d\mathbf{r} \int d\mathbf{r}' \Psi_{l_1}^*(\mathbf{r}) \Psi_{l_2}^*(\mathbf{r}') V_{Coul}(|\mathbf{r} - \mathbf{r}'|) \Psi_{l_3}(\mathbf{r}') \Psi_{l_4}(\mathbf{r}) \quad (\text{C.1})$$

with the compound index l containing the band index $\alpha = c, v$ and the wave vector \mathbf{k} . The required wave functions are calculated within the tight-binding method yielding

$$\Psi^\alpha(\mathbf{k}, \mathbf{r}) = \sum_{j=A, B} C_j^\alpha(\mathbf{l}) \frac{1}{\sqrt{N_0}} \sum_{\mathbf{R}_j}^{N_0} e^{i\mathbf{k} \cdot \mathbf{R}_j} \phi_j(\mathbf{r} - \mathbf{R}_j) \quad (\text{C.2})$$

with the lattice vectors \mathbf{R}_j , the atomic wave functions $\phi_j(\mathbf{r} - \mathbf{R}_j)$, and the coefficient functions $C_j^\alpha(\mathbf{l})$. The latter are calculated in Sec. 2.3.2 yielding for the overlap parameter $s_0 = 0$

$$C_A^\alpha(\mathbf{k}) = c_\alpha C_B^\alpha(\mathbf{k}) \frac{e(\mathbf{k})}{|e(\mathbf{k})|} \quad \text{and} \quad C_B^\alpha(\mathbf{k}) = \frac{1}{\sqrt{2}} \quad (\text{C.3})$$

with $c_\alpha = +(-)$ for the valence (conduction) band. Furthermore, the abbreviation

$$e(\mathbf{k}) = \sum_{i=1}^3 \exp(i\mathbf{k} \cdot \mathbf{b}_i) \quad (\text{C.4})$$

has been introduced including the vectors \mathbf{b}_i , which connect the reference atom with its three nearest neighbors. Inserting the tight-binding wave functions from Eq. (C.2) into the Coulomb matrix elements in Eq. (C.1) yields

$$V_{\alpha_3 \mathbf{k}_3, \alpha_4 \mathbf{k}_4}^{\alpha_1 \mathbf{k}_1, \alpha_2 \mathbf{k}_2} = \sum_{i, i', j, j'}^{A, B} C_i^{\alpha_1*}(\mathbf{k}_1) C_j^{\alpha_2*}(\mathbf{k}_2) C_{i'}^{\alpha_3}(\mathbf{k}_3) C_{j'}^{\alpha_4}(\mathbf{k}_4) \frac{1}{N_0^2} \sum_{l, l', n, n'}^N e^{-i\mathbf{k}_1 \cdot \mathbf{R}_l^i} e^{-i\mathbf{k}_2 \cdot \mathbf{R}_n^j} e^{i\mathbf{k}_3 \cdot \mathbf{R}_{l'}^{i'}} e^{i\mathbf{k}_4 \cdot \mathbf{R}_{n'}^{j'}} \times \\ \times \int \int d^3 r d^3 r' \phi^*(\mathbf{r} - \mathbf{R}_l^i) \phi^*(\mathbf{r}' - \mathbf{R}_n^j) V_{Coul}(|\mathbf{r} - \mathbf{r}'|) \phi(\mathbf{r} - \mathbf{R}_{l'}^{i'}) \phi(\mathbf{r}' - \mathbf{R}_{n'}^{j'}).$$

Taking into account only the strongest contribution where the interacting particles are on the same site, i.e. $(i, l) = (i', l')$ simplifies this expression to

$$V_{\alpha_3 \mathbf{k}_3, \alpha_4 \mathbf{k}_4}^{\alpha_1 \mathbf{k}_1, \alpha_2 \mathbf{k}_2} = \sum_{i,j}^{A,B} \gamma_{ij}(\alpha \mathbf{k}) \frac{1}{N_0^2} \sum_{l,n}^{N_0} e^{-i(\mathbf{k}_1 - \mathbf{k}_3) \cdot \mathbf{R}_l^i} e^{-i(\mathbf{k}_2 - \mathbf{k}_4) \cdot \mathbf{R}_n^j} V_{Coul}(|\mathbf{R}_l^i - \mathbf{R}_n^j|).$$

Here, the abbreviation $\gamma_{ij}(\alpha \mathbf{k}) \equiv C_i^{\alpha_1*}(\mathbf{k}_1) C_j^{\alpha_2*}(\mathbf{k}_2) C_{i'}^{\alpha_3}(\mathbf{k}_3) C_{j'}^{\alpha_4}(\mathbf{k}_4)$ has been introduced. Furthermore, since the atoms are located at the positions \mathbf{R}_l^i , it is $|\phi(\mathbf{r} - \mathbf{R}_l^i)|^2 = \delta(\mathbf{r} - \mathbf{R}_l^i)$. After introducing the center-of-mass coordinate $\hat{\mathbf{R}}^{ij} = \frac{\mathbf{R}_l^i + \mathbf{R}_n^j}{2}$ and the relative coordinate $\hat{\mathbf{r}}^{ij} = \mathbf{R}_l^i - \mathbf{R}_n^j$, the equation reads

$$\begin{aligned} V_{\alpha_3 \mathbf{k}_3, \alpha_4 \mathbf{k}_4}^{\alpha_1 \mathbf{k}_1, \alpha_2 \mathbf{k}_2} &= \sum_{i,j}^{A,B} \gamma_{ij}(\alpha \mathbf{k}) \frac{1}{N_0^2} \sum_{\hat{\mathbf{r}}} e^{\frac{i}{2}(\mathbf{k}_3 - \mathbf{k}_1 + \mathbf{k}_2 - \mathbf{k}_4) \cdot \hat{\mathbf{r}}^{ij}} V_{Coul}(|\hat{\mathbf{r}}^{ij}|) \underbrace{\sum_{\hat{\mathbf{R}}} e^{-i(\mathbf{k}_1 - \mathbf{k}_3 + \mathbf{k}_2 - \mathbf{k}_4) \cdot \hat{\mathbf{R}}^{ij}}}_{N_0 \delta_{\mathbf{k}_1 - \mathbf{k}_3, \mathbf{k}_4 - \mathbf{k}_2}} \\ &= \sum_{i,j}^{A,B} \gamma_{ij}(\alpha \mathbf{k}) \delta_{\mathbf{k}_1 - \mathbf{k}_3, \mathbf{k}_4 - \mathbf{k}_2} \frac{1}{N_0} \sum_{\hat{\mathbf{r}}} e^{\frac{i}{2}(\mathbf{k}_3 - \mathbf{k}_1 + \mathbf{k}_2 - \mathbf{k}_4) \cdot \hat{\mathbf{r}}^{ij}} V_{Coul}(|\hat{\mathbf{r}}^{ij}|) \\ &= \sum_{i,j}^{A,B} \gamma_{ij}(\alpha \mathbf{k}) \delta_{\mathbf{k}_1 - \mathbf{k}_3, \mathbf{k}_4 - \mathbf{k}_2} V^{ij}(\mathbf{q}). \end{aligned}$$

Finally, the Coulomb matrix element can be expressed in a short form as

$$V_{\alpha_3 \mathbf{k}_3, \alpha_4 \mathbf{k}_4}^{\alpha_1 \mathbf{k}_1, \alpha_2 \mathbf{k}_2} = \sum_{i,j}^{A,B} \gamma_{ij}(\alpha \mathbf{k}) \delta_{\mathbf{k}_1 - \mathbf{k}_3, \mathbf{k}_4 - \mathbf{k}_2} V^{ij}(\mathbf{q}). \quad (\text{C.5})$$

Here, the Fourier transform $V^{ij}(\mathbf{q})$ of the Coulomb potential has been introduced by

$$V^{ij}(\mathbf{q}) = \frac{1}{N_0} \sum_{\hat{\mathbf{r}}} e^{i\mathbf{q} \cdot \hat{\mathbf{r}}^{ij}} V^{ij}(|\hat{\mathbf{r}}^{ij}|) \quad (\text{C.6})$$

with the momentum transfer $\mathbf{q} = \mathbf{k}_3 - \mathbf{k}_1 = \mathbf{k}_2 - \mathbf{k}_4 = (q_z, \Delta m)$. The conservation of the momentum follows from the Kronecker delta $\delta_{\mathbf{k}_1 - \mathbf{k}_3, \mathbf{k}_4 - \mathbf{k}_2}$.

The unscreened Coulomb interaction $V^{ij}(|\hat{\mathbf{r}}^{ij}|)$ is parametrized by the Ohno potential⁶²

$$V^{ij}(|\hat{\mathbf{r}}^{ij}|) = \frac{U}{\sqrt{\left(\frac{4\pi\epsilon_0}{e^2} U |\hat{\mathbf{r}}^{ij}| \right)^2 + 1}} \quad (\text{C.7})$$

with $U = 11.3 \text{ eV}$ representing the necessary energy to place two electrons on a single site. The parameter U is given by¹⁷ $U = \int d^3r \int d^3r' |\phi(\mathbf{r})|^2 \frac{e_0^2}{4\pi\epsilon_0 |\mathbf{r} - \mathbf{r}'|} |\phi(\mathbf{r}')|^2$ with π orbital functions $\phi(\mathbf{r})$.

The Fourier transform of the Coulomb potential is performed atom-wise using the line group symmetry operations described in Sec. 3.2, i.e. the sum in Eq. (C.6) is expressed by

$$\sum_{\hat{\mathbf{r}}} \Rightarrow \sum_{c=-N_c}^{N_c} \sum_{t=1-q/2n}^{q/2n} \sum_{s=0}^{n-1} \sum_{u=0}^1 \quad (\text{C.8})$$

with u expressing the the U-operation responsible for mapping atom A to atom B , s denoting the pure rotation about the tube axis C_n^s , t describing the pure translations and screw axis rotations

$(C_q^{rt} | \frac{tna}{q})$, and finally c expressing the number of unit cells considered in the calculation. This atom-wise procedure distinguishes between the atoms of type A and B resulting in four different Fourier transforms, which are related by

$$V^{AA}(\mathbf{q}) = V^{BB}(\mathbf{q}), \quad V^{AB}(\mathbf{q}) = V^{BA*}(\mathbf{q}). \quad (\text{C.9})$$

For the calculation of these quantities, it is important to calculate the scalar product $\mathbf{q} \cdot \hat{\mathbf{r}}^{AA}$ and $\mathbf{q} \cdot \hat{\mathbf{r}}^{BA}$, see Eq. (3.29). Using Eq. (3.4) and considering the cylinder as unrolled (i.e. neglecting curvature effects) leads to the expressions

$$\mathbf{q} \cdot \hat{\mathbf{r}}^{AA} = q_z \hat{\mathbf{r}}_z^{AA} + q_\perp \hat{\mathbf{r}}_\perp^{AA} = q_z \left(t \frac{na}{q} + c_i a \right) + m \left[2\pi \left(t \frac{r}{q} + \frac{s}{n} \right) \right], \quad (\text{C.10})$$

$$\mathbf{q} \cdot \hat{\mathbf{r}}^{AB} = q_z \hat{\mathbf{r}}_z^{BA} + q_\perp \hat{\mathbf{r}}_\perp^{BA} = q_z \left(t \frac{na}{q} + c_i a - 2z_0 \right) + m \left[2\pi \left(t \frac{r}{q} + \frac{s}{n} \right) - 2\phi_0 \right] \quad (\text{C.11})$$

with the reference atom $\mathbf{r}_0 = \mathbf{r}_{000} = (\rho_0, \phi_0, z_0) = \left(\frac{d}{2}, 2\pi \frac{n_1+n_2}{2N}, a_0 \frac{n_1-n_2}{2\sqrt{3}N} \right)$ corresponding to $r_0 = \frac{1}{3}(\mathbf{a}_1 + \mathbf{a}_2)$, see Fig. 3.9.

Now, the specific Coulomb matrix elements needed in Sec. 3.6, are calculated.

Band gap renormalization

Performing the sum over the atoms A, B and inserting the coefficient functions $C_i^\alpha(\mathbf{k})$ from Eq. (C.3) into Eq. (C.5) yields

$$\begin{aligned} V_{vk, vk'}^{vk', vk} &= \sum_{i,j}^{A,B} \gamma_{ij}(\alpha\mathbf{k}) V^{ij}(\mathbf{k}' - \mathbf{k}) \\ &= \frac{1}{4} \frac{e^*(\mathbf{k}')e^*(\mathbf{k})e(\mathbf{k})e(\mathbf{k}')}{|e^*(\mathbf{k}')||e^*(\mathbf{k})||e(\mathbf{k})||e(\mathbf{k}')|} V^{AA}(\mathbf{k}' - \mathbf{k}) + \frac{1}{4} V^{BB}(\mathbf{k}' - \mathbf{k}) \\ &= \frac{1}{4} \frac{e^*(\mathbf{k}')e(\mathbf{k})}{|e^*(\mathbf{k}')||e(\mathbf{k})|} V^{AB}(\mathbf{k}' - \mathbf{k}) + \frac{1}{4} \frac{e^*(\mathbf{k})e(\mathbf{k}')}{|e^*(\mathbf{k})||e(\mathbf{k}')|} V^{BA}(\mathbf{k}' - \mathbf{k}) \\ &= \frac{1}{2} \left[V^{AA}(\mathbf{k}' - \mathbf{k}) + \text{Re} \left(\frac{e^*(\mathbf{k}')e(\mathbf{k})}{|e^*(\mathbf{k}')||e(\mathbf{k})|} V^{AB}(\mathbf{k}' - \mathbf{k}) \right) \right]. \end{aligned} \quad (\text{C.12})$$

In the last step, the relations from Eq. (C.9) have been used. A similar calculation leads to the expression for the second matrix element being responsible for the band gap renormalization

$$V_{vk', ck}^{ck, vk'} = \frac{1}{2} \left[V^{AA}(\mathbf{k}' - \mathbf{k}) - \text{Re} \left(\frac{e^*(\mathbf{k}')e(\mathbf{k})}{|e^*(\mathbf{k}')||e(\mathbf{k})|} V^{AB}(\mathbf{k}' - \mathbf{k}) \right) \right]. \quad (\text{C.13})$$

The only difference is the sign in front of the second term arising from the different sign of the TB coefficient functions for the valence and conduction band, see Eq. (C.3).

Excitonic contribution

In analogy to the calculation presented above, the Coulomb matrix elements accounting for the formation of excitons are determined, yielding

$$V_{ck', vk}^{ck, vk'} = \frac{1}{2} \left[V^{AA}(\mathbf{k}' - \mathbf{k}) + \text{Re} \left(\frac{e^*(\mathbf{k}')e(\mathbf{k})}{|e^*(\mathbf{k}')||e(\mathbf{k})|} V^{AB}(\mathbf{k}' - \mathbf{k}) \right) \right] = V_{vk, vk'}^{vk', vk}, \quad (\text{C.14})$$

$$V_{vk', vk}^{ck, ck'} = \frac{1}{2} \left[V^{AA}(\mathbf{k}' - \mathbf{k}) - \text{Re} \left(\frac{e^*(\mathbf{k}')e(\mathbf{k})}{|e^*(\mathbf{k}')||e(\mathbf{k})|} V^{AB}(\mathbf{k}' - \mathbf{k}) \right) \right] = V_{vk', ck}^{ck, vk'}. \quad (\text{C.15})$$

Depolarization part

Finally, the depolarization part of the Coulomb interaction is given by

$$V_{ck,vk'}^{ck,vk'} = \frac{1}{2} \left[V^{AA}(0) - \text{Re} V^{AB}(0) \right], \quad (\text{C.16})$$

$$V_{vk,vk'}^{ck,ck'} = \frac{1}{2} \left[V^{AA}(0) + \text{Re} V^{AB}(0) \right]. \quad (\text{C.17})$$

C.2 QD Coulomb matrix elements

The starting point is again Eq. (C.1). The wave function for quantum dots can be separated into an in-plane and a z-component

$$\Psi_{i,\sigma}^b(\mathbf{r}) = \varphi_i^b(\boldsymbol{\rho}) \xi_\sigma^b(z) u^b(\mathbf{r}) \quad (\text{C.18})$$

where $u^b(\mathbf{r})$ are Bloch functions with $b = e, h$ denoting the charge carrier type, $\varphi_i^b(\boldsymbol{\rho})$ is the in-plane part of the wave function, and $\xi_\sigma^b(z)$ is the z -component of the wave function with the quantum number σ . After inserting these wave functions in Eq. (C.1), the integrals are separated into a sum of integrals over unit cells with a volume Ω . After some lengthy but straight-forward steps under the assumption that not all contributions vary within an unit cell, and applying the orthogonality of Bloch functions $\int_V d^3r u^{b_i^*}(\mathbf{r}) u^{b_j}(\mathbf{r}) = V \delta_{b_i, b_j}$ one obtains

$$V_{l_3, l_4}^{l_1, l_2} = \delta_{b_1, b_4} \delta_{b_2, b_3} \int d^2\rho \int dz \int d^2\rho' \int dz' \varphi_{i_1}^{b_1}(\boldsymbol{\rho})^* \xi_{\sigma_1}^{b_1}(z) \varphi_{i_2}^{b_2}(\boldsymbol{\rho}')^* \xi_{\sigma_2}^{b_2}(z')^* \frac{e^2}{4\pi\epsilon |\mathbf{r} - \mathbf{r}'|} \times \\ \times \varphi_{i_3}^{b_3}(\boldsymbol{\rho}') \xi_{\sigma_3}^{b_3}(z')^* \varphi_{i_4}^{b_4}(\boldsymbol{\rho}) \xi_{\sigma_4}^{b_4}(z) \quad (\text{C.19})$$

with the compound indices l_1, l_2, l_3 and l_4 containing all relevant quantum numbers of the system. The dielectric background constant ϵ_{bg} has been included by $\epsilon \equiv \epsilon_0 \epsilon_{bg}$. The Coulomb potential is now transformed where the Fourier transform is given by

$$V_q = \int d^2\rho e^{iq \cdot (\boldsymbol{\rho} - \boldsymbol{\rho}')} \frac{e^2}{4\pi\epsilon_0 |\mathbf{r} - \mathbf{r}'|} = \int_0^\infty d\hat{r} \hat{r} \int_0^{2\pi} d\varphi e^{iq\hat{r} \cos\varphi} \frac{e^2}{4\pi\epsilon_0 \sqrt{\hat{r}^2 + |z - z'|^2}} \\ = \frac{e^2}{2\epsilon_0 q} e^{-q|z - z'|} \quad (\text{C.20})$$

with $\hat{r} = |\boldsymbol{\rho} - \boldsymbol{\rho}'|$. The Coulomb matrix element can be expressed in a more convenient form reading

$$V_{l_3, l_4}^{l_1, l_2} = \frac{1}{A} \sum_{\mathbf{q}} \frac{e^2}{2\epsilon q} \int dz \int dz' \xi_{\sigma_1}^{b_1}(z) \xi_{\sigma_2}^{b_2}(z')^* e^{-q|z - z'|} \xi_{\sigma_3}^{b_3}(z')^* \xi_{\sigma_4}^{b_4}(z) \delta_{b_1 b_4} \delta_{b_2 b_3} \times \\ \times \int d^2\rho \varphi_{i_1}^{b_1}(\boldsymbol{\rho})^* \varphi_{i_4}^{b_4}(\boldsymbol{\rho}) e^{-iq \cdot \boldsymbol{\rho}} \int d^2\rho' \varphi_{i_2}^{b_2}(\boldsymbol{\rho}')^* \varphi_{i_3}^{b_3}(\boldsymbol{\rho}') e^{iq \cdot \boldsymbol{\rho}'}. \quad (\text{C.21})$$

These integrals can be solved separately. First, the integral over the z -component is evaluated. Inserting the wave function

$$\xi_0(z) = \sqrt{\frac{2}{L_{\text{eff}}}} \cos \left[\frac{\pi}{L_{\text{eff}}} z \right] \quad (\text{C.22})$$

corresponding to the lowest bound state of an infinite barrier well yields

$$\begin{aligned}
 F(q) &\equiv \frac{4}{L^2} \int_{-L/2}^{L/2} dz \int_{-L/2}^{L/2} dz' \cos^2\left(\frac{\pi}{L}z\right) \cos^2\left(\frac{\pi}{L}z'\right) e^{-q|z-z'|} \\
 &= \frac{4}{L^2} \int_{-L/2}^{L/2} dz \cos^2\left(\frac{\pi}{L}z\right) \int_{-L/2}^{L/2} dz' \cos^2\left(\frac{\pi}{L}z'\right) e^{-q|z-z'|}.
 \end{aligned} \tag{C.23}$$

The second integral in Eq. (C.23) is solved first. The substitution $z' \Rightarrow \frac{L}{\pi}x$ with the abbreviation $\hat{q} = \frac{L}{\pi}q$ is applied resulting in:

$$\begin{aligned}
 \int_{-L/2}^{L/2} dz' \cos^2\left(\frac{\pi}{L}z'\right) e^{-q|z-z'|} &= \frac{L}{\pi} \int_{-\pi/2}^{\pi/2} dx' \cos^2(x') e^{-\hat{q}|x-x'|} \\
 &= \frac{L}{\pi} \left\{ \int_{-\pi/2}^x dx' \cos^2(x') e^{-\hat{q}(x-x')} + \int_x^{\pi/2} dx' \cos^2(x') e^{\hat{q}(x-x')} \right\} \\
 &= \frac{4(1 - e^{-\frac{\pi}{2}\hat{q}} e^{-x\hat{q}}) + \hat{q}^2(1 + \cos(2x)) + 2\hat{q}\sin(2x)}{2\hat{q}(4 + \hat{q}^2)} + \\
 &\quad + \frac{4(1 - e^{-\frac{\pi}{2}\hat{q}} e^{x\hat{q}}) + \hat{q}^2(1 + \cos(2x)) - 2\hat{q}\sin(2x)}{2\hat{q}(4 + \hat{q}^2)} \\
 &= \frac{4(1 - e^{-\frac{\pi}{2}\hat{q}} \cosh(\hat{q}x)) + \hat{q}^2(1 + \cos(2x))}{\hat{q}(4 + \hat{q}^2)}.
 \end{aligned}$$

Then, the entire integral in Eq. (C.23) reads

$$\begin{aligned}
 F(q) &= \frac{4}{\pi^2} \frac{32(e^{-\pi\hat{q}} - 1) + \pi\hat{q}(4 + \hat{q}^2)(8 + 3\hat{q}^2)}{4\hat{q}^2(4 + \hat{q}^2)^2} \\
 &= \frac{4}{\pi^2} \left\{ \frac{\pi}{2\hat{q}} + \frac{1}{4} \frac{\pi\hat{q}}{\hat{q}^2 + 4} - \left[\frac{1}{\hat{q}} - \frac{\hat{q}}{\hat{q}^2 + 4} \right] \frac{2}{(\hat{q}^2 + 4)\hat{q}} (1 - e^{-\pi\hat{q}}) \right\} \\
 &= \frac{2}{Lq} + \frac{1}{Lq + \frac{4\pi^2}{Lq}} - \frac{2}{L^6} \left(\frac{4\pi^2}{\hat{q}(\hat{q}^2 + \frac{4\pi^2}{L^2})} \right)^2 (1 - e^{-qL}).
 \end{aligned}$$

Now, the second integral in Eq. (C.21) is calculated. The in-plane components of the wave function for QD and WL states are given by

$$\varphi_{QD}^b(\rho) = \frac{\beta\sqrt{A}}{\sqrt{\pi}} \exp\left(-\frac{1}{2}\beta^2\rho^2\right), \tag{C.24}$$

$$\varphi_{\mathbf{k}}^b(\rho) = \frac{1}{N_b(\mathbf{k})} \left[\exp(i\mathbf{k} \cdot \boldsymbol{\rho}) - 2\alpha_b(\mathbf{k}) \exp\left(-\frac{1}{2}\beta_b^2\rho^2\right) \right] \tag{C.25}$$

with the normalization factor $N_b(\mathbf{k}) = \sqrt{1 - \frac{4\pi}{A\beta_b^2} \alpha_b^2(\mathbf{k})}$, and the abbreviation $\beta_b = \sqrt{\frac{m_b^* \omega_b}{\hbar}}$. Inserting these wave functions into Eq. (C.21) leads to integrals of the form

$$\begin{aligned} & \sqrt{\frac{m_b \omega_{gs,b}}{\hbar \pi}} \int d^2 \rho \exp\left(-\frac{m_b \omega_{gs,b}}{2\hbar} \rho^2\right) \frac{1}{\sqrt{A}} \exp(i \mathbf{k}_1 \cdot \boldsymbol{\rho}) \exp(-i \mathbf{q} \cdot \boldsymbol{\rho}) \\ &= \sqrt{\frac{m_b \omega_{gs,b}}{\hbar \pi A}} \int_0^\infty d\rho \rho \exp\left(-\frac{m_b \omega_{gs,b}}{2\hbar} \rho^2\right) \underbrace{\int_0^{2\pi} d\varphi \exp(i(\mathbf{k}_1 - \mathbf{q}) \cdot \boldsymbol{\rho})}_{2\pi \text{ Bessel}J(0, |\mathbf{k}_1 - \mathbf{q}| \rho)} \\ & \quad \underbrace{\exp\left(-\frac{\hbar}{2 m_b \omega_{gs,b}} |\mathbf{k}_1 - \mathbf{q}|^2\right)}_{2\pi \frac{\hbar}{m_b \omega_{gs,b}} \exp\left(-\frac{\hbar}{2 m_b \omega_{gs,b}} |\mathbf{k}_1 - \mathbf{q}|^2\right)} \\ &= 2\sqrt{\frac{\hbar \pi}{m_b \omega_{gs,b} A}} \exp\left(-\frac{\hbar}{2 m_b \omega_{gs,b}} |\mathbf{k}_1 - \mathbf{q}|^2\right). \end{aligned}$$

Exploiting this result, the second integral in Eq. (C.21) can be calculated yielding

$$\begin{aligned} & \int d^2 \rho \varphi_{QD}^{b*}(\rho) \varphi_{\mathbf{k}_1}^b(\rho) \exp(-i \mathbf{q} \cdot \boldsymbol{\rho}) \\ &= \frac{2\sqrt{\pi}}{\beta_b \sqrt{A} N_b(\mathbf{k}_1)} \left[\alpha_b(\mathbf{k}_1 - \mathbf{q}) - \alpha_b(\mathbf{k}_1) \exp\left(-\frac{q^2}{4\beta_b^2}\right) \right]. \end{aligned}$$

In a similar calculations, also the third integral in Eq. (C.21) is determined. It reads

$$\begin{aligned} & \int d^2 \rho' \varphi_{\mathbf{k}_2}^{b*}(\rho') \varphi_{\mathbf{k}_3}^b(\rho') \exp(i \mathbf{q} \cdot \boldsymbol{\rho}') \\ &= \frac{1}{A N_b(\mathbf{k}_2) N_b(\mathbf{k}_3)} \left[(2\pi)^2 \delta(\mathbf{q} - (\mathbf{k}_2 - \mathbf{k}_3)) - \frac{2}{\beta_b^2} \alpha_b(\mathbf{k}_3) \alpha_b(\mathbf{q} - \mathbf{k}_2) \right. \\ & \quad \left. - \frac{2}{\beta_b^2} \alpha_b(\mathbf{k}_2) \alpha_b(\mathbf{q} + \mathbf{k}_3) + \frac{2}{\beta_b^2} \alpha_b(\mathbf{k}_2) \alpha_b(\mathbf{k}_3) \exp\left(-\frac{q^2}{4\beta_b^2}\right) \right]. \end{aligned}$$

Bringing together the calculations of all three integrals in Eq. (C.21) yields for capture processes into the ground state of a QD

$$\begin{aligned} V_{b\mathbf{k}_1, b'\mathbf{k}_3}^{b, b'\mathbf{k}_2} &= C_1 \frac{1}{q} F(q) \left[\alpha_b(\mathbf{k}_1 - \mathbf{q}) - \alpha_b(\mathbf{k}_1) \alpha_{b'}^{\frac{1}{2}}(q) \right] \delta_{\mathbf{q}, \mathbf{k}_2 - \mathbf{k}_3} \\ & \quad - \sum_{\mathbf{q}} C_2 \frac{1}{q} F(q) \left[\alpha_b(\mathbf{k}_1 - \mathbf{q}) \alpha_{b'}^{\text{opw}}(\mathbf{q}, \mathbf{k}_2, \mathbf{k}_3) + \alpha_b(\mathbf{k}_1) \alpha_{b'}^{\frac{1}{2}}(q) \alpha_{b'}^{\text{opw}}(\mathbf{q}, \mathbf{k}_2, \mathbf{k}_3) \right] \end{aligned} \quad (\text{C.26})$$

with

$$\alpha_{b'}^{\text{opw}}(\mathbf{q}, \mathbf{k}_2, \mathbf{k}_3) = \alpha_{b'}(\mathbf{k}_3) \alpha_{b'}(\mathbf{q} - \mathbf{k}_2) + \alpha_{b'}(\mathbf{k}_2) \alpha_{b'}(\mathbf{q} + \mathbf{k}_3) - \alpha_{b'}(\mathbf{k}_2) \alpha_{b'}(\mathbf{k}_3) \alpha_{b'}(\mathbf{q}). \quad (\text{C.27})$$

and

$$C_1 = \frac{e_0^2 \sqrt{\pi}}{\beta_b \varepsilon_0 A^{\frac{3}{2}} N_b(\mathbf{k}_1) N_{b'}(\mathbf{k}_2) N_{b'}(\mathbf{k}_3)} \quad \text{and} \quad C_2 = \frac{4 \pi}{A \beta_b^2}. \quad (\text{C.28})$$

In the last step, the relation between the Kronecker symbol δ and the δ -function has been used

$$\delta(\mathbf{k} - \mathbf{k}') = \frac{(2\pi)^2}{A} \delta_{\mathbf{k}, \mathbf{k}'}. \quad (\text{C.29})$$

The normalization area A vanishes in the calculation and does not have any influence on the scattering rates. The first blue colored term in Eq. (C.26) stems from the plane wave part of the WL wave function.

Each person is a graveyard of his thoughts. They are most beautiful for us in the moment of their birth; later we can often sense a deep pain that they leave us indifferent where earlier they enchanted us.

Robert Musil

Appendix D

Rayleigh Scattering Cross Section

The Rayleigh scattering from nanotubes is treated as electromagnetic scattering from an infinite cylinder with a diameter small compared to the wavelength of light. The scattering cross section σ of such a cylinder is also infinite. However, the light scattered per unit length is finite. As a result, the Rayleigh scattering cross section can be calculated per unit length of an infinite cylinder by constructing a closed concentric surface A of length L and radius r . This approximation is good as long as the ratio of cylinder length to diameter is large. The presented approach for solving the problem of scattering by small particles is often called Mie theory.⁴⁵

The scattering cross section is given by the ratio of the rate

$$W_s = rL \int_0^{2\pi} (\mathbf{S}_s)_r d\phi \quad (\text{D.1})$$

at which energy passes through the scattering surface A and the incident irradiance I_i . The rate W_s is determined by the radial component of the Poynting vector of the scattered field $\mathbf{S}_s = \frac{1}{2} \text{Re}[\mathbf{E}_s \times \mathbf{H}_s^*]$. Now, expressions for the electric and the magnetic field need to be found. Both $\mathbf{E}(\mathbf{r}, t)$ and $\mathbf{B}(\mathbf{r}, t)$ satisfy the vector wave equation

$$\square \mathbf{E}(\mathbf{r}, t) = \nabla^2 \mathbf{E}(\mathbf{r}, t) + k^2 \mathbf{E}(\mathbf{r}, t) = 0, \quad \square \mathbf{B}(\mathbf{r}, t) = \nabla^2 \mathbf{B}(\mathbf{r}, t) + k^2 \mathbf{B}(\mathbf{r}, t) = 0 \quad (\text{D.2})$$

with the d'Alembert operator $\square \mathbf{A} = (\frac{\partial^2}{c^2 \partial t^2} - \Delta) \mathbf{A}$ and the Laplace operator $\Delta \mathbf{A} = \nabla^2 \mathbf{A} = \nabla \cdot (\nabla \mathbf{A})$. Their components, however, do not separately fulfil the scalar wave equation $\square \psi = 0$. By introducing the so-called vector harmonics $\mathbf{M} = \nabla \times (\mathbf{c}\psi)$ and $\mathbf{N} = \frac{\nabla \times \mathbf{M}}{k}$ with a scalar function ψ and a constant vector \mathbf{c} , the problem can be considerably simplified, since these functions satisfy both the vector and the scalar wave equation. Once they are calculated, the electric and magnetic field can be expanded in \mathbf{M} and \mathbf{N} with

$$\mathbf{E} = \sum_{n=-\infty}^{\infty} [A_n \mathbf{M}_n + B_n \mathbf{N}_n]. \quad (\text{D.3})$$

From the definition, it follows directly that the divergence of both vector functions vanishes. The curl of \mathbf{M} is proportional to \mathbf{N} . Using the vector identity $\nabla^2 \mathbf{A} = \nabla(\nabla \cdot \mathbf{A}) - \nabla \times (\nabla \times \mathbf{A})$, it can be shown that $\nabla \times \mathbf{N} = k\mathbf{M}$, i.e. also the curl of \mathbf{N} is proportional to \mathbf{M} . Furthermore, playing with the vector identities leads to

$$\nabla^2 \mathbf{M} + k^2 \mathbf{M} = \nabla \times [\mathbf{c}(\nabla^2 \psi + k^2 \psi)]. \quad (\text{D.4})$$

Consequently, if ψ is a solution of the scalar wave equation, it follows immediately that M satisfies the vector wave equation. The same can be shown for N . As a result, the introduced vector harmonics M and N fulfil all required properties of an electromagnetic field (Maxwell equations, wave equation). The scalar function ψ is called a generating function for the vector harmonics F and G . Its choice depends on the investigated system, its symmetries and boundary conditions. The vector c is called the pilot vector. Its choice can be random, however, it is also guided by the investigated problem.

For Rayleigh scattering from a cylinder, the scalar function should satisfy the wave equation in cylindrical polar coordinates (ρ, ϕ, z)

$$\frac{1}{\rho} \frac{\partial}{\partial \rho} \left(\rho \frac{\partial \psi}{\partial \rho} \right) + \frac{1}{\rho^2} \frac{\partial^2 \psi}{\partial \phi^2} + \frac{\partial^2 \psi}{\partial z^2} + k^2 \psi = 0. \quad (\text{D.5})$$

An ansatz for the solution is given by

$$\psi(r, \phi, z) = Z_n(\rho) e^{in\phi} e^{ihz} \quad (\text{D.6})$$

with $Z_n(r)$ as Bessel functions of first and second kind of integral order n and with $r = \sqrt{k^2 - h^2}$. The quantum number $h = -k \cos \zeta$ satisfies the boundary conditions between the cylinder and the surrounding medium. The vector harmonics generated by Eq. (D.6) are⁴⁵

$$\mathbf{M}_n = \sqrt{k^2 - h^2} \left(\frac{in Z_n(\rho)}{\rho} \mathbf{e}_r - Z'_n(\rho) \mathbf{e}_\phi \right) \exp(i(n\phi + hz)), \quad (\text{D.7})$$

$$\mathbf{N}_n = \frac{\sqrt{k^2 - h^2}}{k} \left(in Z'_n(\rho) \mathbf{e}_r - hn \frac{Z'_n(\rho)}{\rho} \mathbf{e}_\phi + \sqrt{k^2 - h^2} Z_n(\rho) \mathbf{e}_z \right) \exp(i(n\phi + hz)). \quad (\text{D.8})$$

For an infinite cylinder of radius r , which is illuminated by a plane homogeneous wave $\mathbf{E}_i = \mathbf{E}_0 e^{ik\mathbf{e}_i \cdot \mathbf{r}}$ with the propagation direction $\mathbf{e}_i = -\sin \zeta \mathbf{e}_x - \cos \zeta \mathbf{e}_z$ with the ζ as the angle between the incident wave and the cylinder axis. Furthermore, the case of a polarization parallel to the axis of the cylinder is of interest. Now, the electromagnetic field can be expanded by the vector harmonics M and N . The coefficients are calculated using the orthogonality of M, N , i.e. $\int_0^{2\pi} \mathbf{M}_i \cdot \mathbf{M}_j^* d\phi = 0$. For the incident fields, one obtains

$$\mathbf{E}_i = \sum_{n=-\infty}^{\infty} E_n \mathbf{N}_n, \quad \mathbf{H}_i = \frac{-ik}{\omega \mu_0} \sum_{n=-\infty}^{\infty} E_n \mathbf{M}_n \quad (\text{D.9})$$

with $E_n = \frac{E_0 (-i)^n}{k \sin \zeta}$. In a similar way, the scattering fields \mathbf{E}_s and \mathbf{H}_s are expanded to

$$\mathbf{E}_s = - \sum_{n=-\infty}^{\infty} E_n \left(b_n \mathbf{N}_n + ia_n \mathbf{M}_n \right), \quad \mathbf{H}_s = \frac{ik}{\omega \mu_0} \sum_{n=-\infty}^{\infty} E_n \left(b_n \mathbf{M}_n + ia_n \mathbf{N}_n \right). \quad (\text{D.10})$$

Applying the boundary condition, that the tangential components of \mathbf{E} and \mathbf{H} are continuous across the boundary separating the cylinder from the surrounding medium, i.e. $\mathbf{E}_2(\mathbf{r}) - \mathbf{E}_1(\mathbf{r}) \times \mathbf{n} = 0$ with \mathbf{n} as the outward directed normal to the surface of the cylinder, the coefficients a_n and b_n can be determined. For $\zeta = 90^\circ$, i.e. the incident light is perpendicular to the cylinder axis⁴⁵

$$a_n = 0, \quad b_n = \frac{J_n(\hat{n}kr) J'_n(kr) - \hat{n} J'_n(\hat{n}kr) J_n(kr)}{J_n(\hat{n}kr) H'_n(kr) - \hat{n} J'_n(\hat{n}kr) H_n(kr)} \quad (\text{D.11})$$

with \hat{n} as the refractive index, J_n as the Bessel function of the first kind and H_n as the Hankel function. The latter can be written as a sum of Bessel functions of the first and second kind:

$H_n = J_n + iY_n$. Furthermore, exploiting $J_{-n} = (-1)^n J_n$ and $Y_{-n} = (-1)^n Y_n$, it follows $a_{-n} = a_n$, $b_{-n} = b_n$ and $a_0 = 0$. The prime indicated functions are differentiations with respect to their argument.

Now, the Poynting vectors can be calculated using the expansions of the electromagnetic fields from Eqs. (D.9)-(D.10). The integration over the angle ϕ yields

$$\sigma = \frac{W_s}{I_s} = \frac{4rL}{\mathbf{k} \cdot \mathbf{r}} \left[|b_0|^2 + 2 \sum_{n=1}^{\infty} (|a_n|^2 + |b_n|^2) \right]. \quad (\text{D.12})$$

In the limit of small particles, i.e. for cylinders with a diameter much smaller than the wavelength of light ($\mathbf{k} \cdot \mathbf{r} \ll 1$), it is sufficient to take the first order of the Bessel functions in Eq. (D.11) yielding

$$J_0(x) = 1 - \frac{x^2}{4}, \quad J_0'(x) = -\frac{x}{2} + \frac{x^3}{16}, \quad Y_0(x) = \frac{2}{\pi} \log\left(\frac{x}{2}\right), \quad Y_0'(x) = \frac{2}{\pi z} \quad (\text{D.13})$$

valid for $|x| \ll 1$. Using these relations, leads to

$$b_0 = \frac{-\pi(kr)^2(\hat{n}^2) - 1}{4}. \quad (\text{D.14})$$

Inserting this coefficient into Eq. (D.11), an expression for the Rayleigh scattering cross section $\sigma(\omega)$ per unit length of the cylinder is obtained exploiting the relation⁴² $\hat{n}(\omega)^2 - 1 = \chi(\omega)$ between the refractive index $\hat{n}(\omega)$ and the optical susceptibility $\chi(\omega)$

$$\sigma(\omega) = \frac{\pi^2}{4c^3} r^4 \omega^3 |\chi(\omega)|^2. \quad (\text{D.15})$$

The most beautiful thing we can experience is the mysterious. It is the source of all true art and all science.

Albert Einstein

Appendix E

Material Parameters

Universal constants

physical constant	symbol	SI units	eV-K-nm-fs- e_0 units
Planck constant	h	$6.626076 \cdot 10^{-34}$ Js	4.135668 eVfs
	\hbar	$1.054573 \cdot 10^{-34}$ Js	0.658212 eVfs
speed of light in vacuum	c	$2.997925 \cdot 10^8$ m/s	$2.997925 \cdot 10^2$ nm/fs
elementary charge	e_0	$1.602177 \cdot 10^{-19}$ C	1.0 e_0
dielectric constant	ϵ_0	$8.854188 \cdot 10^{-12}$ C ² /Jm	$5.526347 \cdot 10^{-2}$ e_0^2 /eVnm
Boltzmann constant	k_B	$1.380658 \cdot 10^{-23}$ J/K	$8.617386 \cdot 10^{-5}$ eV/K
electron mass	m_0	$9.109390 \cdot 10^{-34}$ kg	5.685631 fs ² eV/nm ²

Table E.1: For reasons of numerical simplicity, the calculations have been performed within the eV-K-nm-fs- e_0 unit system.

Quantum dot parameters

parameter	symbol	value
Einstein coefficient	W	1.3 ns^{-1}
Dipole moment	d_{cv}	$0.3 e_0 \text{ nm}$
Gap energy	ε_{gap}	0.96 eV
Dielectric background constant	ε_{bg}	14.2
Electron effective mass	m_e^*	$0.043 m_0$
Hole effective mass	m_{hh}^*	$0.450 m_0$
Spontaneous emission coefficient	β	5×10^{-6}
Optical confinement factor	Γ	1×10^{-3}
Total cavity loss	κ	0.12 ps^{-1}
Internal cavity loss	κ_{int}	220 m^{-1}
Facet reflection coefficients	r_1, r_2	0.32
Cavity length	L	1 mm
WL area	A	$4 \times 10^{-5} \text{ cm}^2$
effective WL density	N^{WL}	$2 \times 10^{13} \text{ cm}^{-2}$
QD carrier density	N^{QD}	$1 \times 10^{10} \text{ cm}^{-2}$
Number of QD layers	N_l	15

Table E.2: Parameters used in the theoretical simulation of the turn-on dynamics of QD semiconductor lasers (Sec. 4.7).

Carbon nanotube parameters

quantity	armchair tubes	zigzag tubes	chiral tubes
Chiral indices	(n, n)	$(n, 0)$	(n_1, n_2)
N	$\sqrt{3}n$	n	$\sqrt{n_1^2 + n_2^2 + n_1 n_2}$
R	3	1	3 if $(n_1 - n_2) \bmod 3n = 0$
Chiral angle Θ	30°	0°	$\arccos\left(\frac{n_1 + \frac{n_2}{2}}{\sqrt{N}}\right)$
Diameter d	$\frac{a_0}{\pi}\sqrt{3}n$	$\frac{a_0}{\pi}n$	$\frac{a_0}{\pi}\sqrt{N}$
Atoms per unit cell $2q$	$4n$	$4n$	$\frac{4N}{nR}$
Unit cell length a	a_0	$\sqrt{3}a_0$	$\frac{\sqrt{3N}a_0}{nR}$
Perp. wave vector \mathbf{k}_\perp	$\frac{1}{2n}(\mathbf{k}_1 + \mathbf{k}_2)$	$\frac{1}{2n}(2\mathbf{k}_1 + \mathbf{k}_2)$	$\frac{2n_1 + n_2}{2N}\mathbf{k}_1 + \frac{2n_2 + n_1}{2N}\mathbf{k}_2$
Axial wave vector \mathbf{k}_z	$\frac{1}{2}(\mathbf{k}_2 - \mathbf{k}_1)$	$\frac{1}{2}\mathbf{k}_2$	$-\frac{n_2}{q}\mathbf{k}_1 + \frac{n_1}{q}\mathbf{k}_2$
Lattice vector \mathbf{a}	$\mathbf{a}_2 - \mathbf{a}_1$	$2\mathbf{a}_2 - \mathbf{a}_1$	$-\frac{2n_2 + n_1}{nR}\mathbf{a}_1 + \frac{2n_1 + n_2}{nR}\mathbf{a}_2$
Chiral vector \mathbf{c}	$n(\mathbf{a}_1 + \mathbf{a}_2)$	$n\mathbf{a}_1$	$n_1\mathbf{a}_1 + n_2\mathbf{a}_2$

Table E.3: Structural parameters of armchair, zigzag and chiral nanotubes with n as the greatest common divisor of n_1 and n_2 and $a_0 = 0.2461$ nm as the lattice constant.⁴⁶ Another useful quantities are the carbon-carbon distance $a_C = a_0/\sqrt{3}$, the reciprocal wave vectors $\mathbf{k}_1 = \frac{2\pi}{a_0}\mathbf{e}_x - \frac{2\pi}{\sqrt{3}a_0}\mathbf{e}_y$ and $\mathbf{k}_2 = \frac{4\pi}{\sqrt{3}a_0}\mathbf{e}_y$ in Cartesian coordinates.

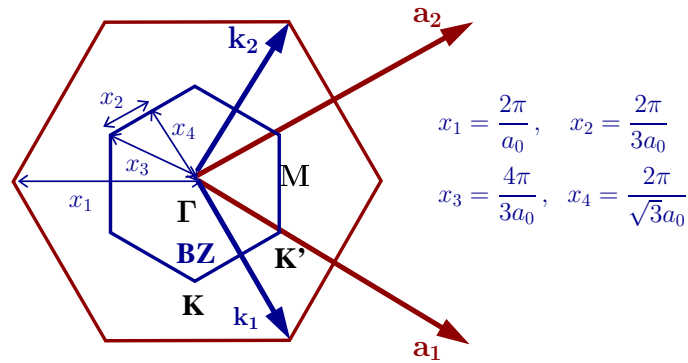


Figure E.1: The Brillouin zone of graphene with the high-symmetry points Γ , K and M including some useful distances in reciprocal space.



Figure E.2: The quantities from E.3 are illustrated in a nanotube periodic system. The source is shown in the bottom right corner of the picture.

Bibliography

1. T. Kuhn. *Density Matrix Theory of Coherent Ultrafast Dynamics in Theory of Transport Properties of Semiconductor Nanostructures*, ed. by E. Schöll (Chapman & Hall, 1998).
2. M. Lindberg and S. W. Koch. Effective Bloch equations for semiconductors. *Phys. Rev. B* **38**, 3342 (1988).
3. F. Rossi and T. Kuhn. Theory of ultrafast phenomena in photoexcited semiconductors. *Rev. Mod. Phys.* **74**, 895 (2002).
4. C. Thomsen and S. Reich. *Raman Scattering in Carbon Nanotubes in Light Scattering in Solids IX*, ed. by M. Cardona and R. Merlin (Springer, Berlin, 2007).
5. S. M. Bachilo, M. S. Strano, C. Kittrell, R. H. Hauge, R. E. Smalley and R. B. Weisman. Structure-assigned optical spectra of single-walled carbon nanotubes. *Science* **298**, 2361 (2002).
6. Y. Miyauchi, S. Chiashi, Y. Murakami, Y. Hayashida and S. Maruyama. Fluorescence spectroscopy of single-walled carbon nanotubes synthesized from alcohol. *Chem. Phys. Lett.* **387**, 198 (2004).
7. H. Telg, J. Maultzsch, S. Reich, F. Hennrich and C. Thomsen. Chirality distribution and transition energies of carbon nanotube. *Phys. Rev. Lett.* **93**, 177401 (2004).
8. C. Fantini, A. Jorio, M. Souza, M. S. Strano, M. S. Dresselhaus and M. A. Pimenta. Optical transition energies for carbon nanotubes from resonant Raman spectroscopy: Environment and temperature effects. *Phys. Rev. Lett.* **93**, 147406 (2004).
9. M. Y. Sfeir, F. Wang, L. Huang, C. Chuang, J. Hone, S. P. O'Brien, T. F. Heinz and L. E. Brus. Probing electronic transitions in individual carbon nanotubes by Rayleigh scattering. *Science* **306**, 1540 (2004).
10. F. Wang, G. Dukovic, L. E. Brus and T. F. Heinz. The optical resonances in carbon nanotubes arise from excitons. *Science* **308**, 838 (2005).
11. J. Maultzsch, R. Pomraenke, S. Reich, E. Chang, D. Prezzi, A. Ruini, E. Molinari, M. S. Strano, C. Thomsen and C. Lienau. Exciton binding energies from two-photon photoluminescence in single-walled carbon nanotubes. *Phys. Rev. B* **72**, 241402(R) (2005).
12. C. D. Spataru, S. Ismail-Beigi, L. X. Benedict and S. G. Louie. Excitonic effects and optical spectra of single-walled carbon nanotubes. *Phys. Rev. Lett.* **92**, 077402 (2004).
13. V. Perebeinos, J. Tersoff and P. Avouris. Scaling of excitons in carbon nanotubes. *Phys. Rev. Lett.* **92**, 257402 (2004).

14. H. Zhao and S. Mazumdar. Electron-electron interaction effects on the optical excitations of semiconducting single-walled carbon nanotubes. *Phys. Rev. Lett.* **93**, 157402 (2005).
15. E. Chang, G. Bussi, A. Ruini and E. Molinari. First-principles approach for the calculation of optical properties of one-dimensional systems with helical symmetry: The case of carbon nanotubes. *Phys. Rev. B* **72**, 195423 (2005).
16. R. B. Capaz, C. D. Spataru, S. Ismail-Beigi and S. G. Louie. Diameter and chirality dependence of exciton properties in carbon nanotubes. *Phys. Rev. B* **74**, 121401 (2006).
17. J. Jiang, R. Saito, G. G. Samsonidze, A. Jorio, S. G. Chou, G. Dresselhaus and M. S. Dresselhaus. Chirality dependence of exciton effects in single-wall carbon nanotubes: Tight-binding model. *Phys. Rev. B* **75**, 035407 (2007).
18. J. Marquez, L. Geelhaar and K. Jacobi. Atomically resolved structure of InAs quantum dots. *Appl. Phys. Lett.* **78**, 2309–2311 (2001).
19. D. Bimberg, M. Grundmann and N. N. Ledentsov. *Quantum Dot Heterostructures* (Wiley, 1999).
20. R. Olshansky, V. Lanzisera, C. B. Su, W. Powazinik and R. B. Lauer. Frequency response of an InGaAsP vapor phase regrown buried heterostructure laser with 18 GHz bandwidth. *Appl. Phys. Lett.* **49**, 128–130 (1986).
21. H. J. Klein, D. Bimberg, H. Beneking, J. Kuhl and E. O. Gobel. High peak power picosecond light-pulses from a directly modulated semiconductor laser. *Appl. Phys. Lett.* **41**, 394–396 (1982).
22. D. Bimberg, K. Ketterer, E. H. Böttcher and E. Schöll. Gain modulation of unbiased semiconductor lasers - ultrashort light-pulse generation in the $0.8 \mu - 1.3 \mu$ wavelength range. *Int. J. Electron.* **60**, 23–45 (1986).
23. D. Deppe, H. Huang and O. Shchekin. Modulation characteristics of quantum-dot lasers: The influence of p-type doping and the electronic density of states on obtaining high speed. *IEEE J. Quantum Electron.* **38**, 1587–1593 (2002).
24. W. W. Chow and S. W. Koch. Theory of semiconductor quantum-dot laser dynamics. *IEEE J. Quantum Electron.* **41**, 495 – 505 (2005).
25. J. Gomis-Bresco, S. Dommers, V. Temnov, U. Woggon, M. Lämmling, D. Bimberg, E. Malić, M. Richter, E. Schöll and A. Knorr. Amplification of ultrafast pulse trains in InGaAs QDs: mechanisms and limitations. *submitted* (2008).
26. P. Meystre and M. Sargent. *Elements of Quantum Optics* (Springer, 1990).
27. C. Cohen-Tannoudji, B. Diu and R. Laloe. *Quantum Mechanics*, vol. 1 (Wiley, 1977).
28. W. Nolting. *Quantenmechanik*, vol. 5.2 (Zimmermann-Neufang, 1993).
29. W. Vogel, D. Welsch and S. Wallentowitz. *Quantum Optics An Introduction* (WILEY-VCH, Berlin, 2001).
30. S. Butscher, F. Milde, M. Hirtschulz, E. Malić and A. Knorr. Hot electron relaxation and phonon dynamics in graphene. *Appl. Phys. Lett.* **91**, 203103 (2007).

31. D. H. Kobe. Gauge-invariant resolution of the controversy over length versus velocity forms of the interaction with electric-dipole radiation. *Phys. Rev. A* **19**, 205–214 (1979).
32. Y. Aharonov and C. K. Au. The question of gauge dependence of transition-probabilities in quantum-mechanics- facts, myths and misunderstandings. *Phys. Lett. A* **86**, 269–272 (1981).
33. K. Rzazewski and R. W. Boyd. Equivalence of interaction hamiltonians in the electric dipole approximation. *J. Mod. Opt.* **51**, 1137 – 1147 (2004).
34. D. Bauer, D. B. Milosevic and W. Becker. Strong-field approximation for intense-laser-atom processes: The choice of gauge. *Phys. Rev. A* **72**, 023415 (2005).
35. M. O. Scully and M. S. Zubairy. *Quantum Optics* (Cambridge University Press, 1997).
36. W. W. Chow, S. W. Koch and M. Sargent. *Semiconductor-Laser Physics* (Springer, 1994).
37. H. Haken. *Light and Matter*, vol. 2 (BI Wissenschaftsverlag, 1995).
38. J. Fricke. Transparent equations including many-particle correlations for an arbitrary quantum system: A general formalism. *Annals of Physics* **252**, 478–498 (1996).
39. I. Waldmüller, J. Förstner and A. Knorr. *Self-Consistent Projection Operator Theory of Intersubband Absorbance in Semiconductor Quantum Wells*, ed. by E. Schöll (Springer, 2004).
40. M. Richter. *Quantentheorie der Terahertz-Emission laserinduzierter Plasmen*. Ph.D. thesis (2005).
41. G. Czycholl. *Theoretische Physik* (Springer, 2004).
42. H. Haug and S. W. Koch. *Quantum Theory of the Optical and Electronic Properties of Semiconductors* (World Scientific, 2004).
43. Y. A. Il'inskii and L. V. Keldysh. *Electromagnetic Response of Material Media* (Springer, 2007).
44. M. Kira, W. Hoyer and S. W. Koch. Microscopic theory of the semiconductor terahertz response. *Phys. Status Solidi B* **238**, 443–450 (2003).
45. C. F. Bohren and D. R. Huffman. *Absorption and Scattering of Light by Small Particles* (Wiley-VCH, Weinheim, 2004).
46. S. Reich, C. Thomsen and J. Maultzsch. *Carbon Nanotubes: Basic Concepts and Physical Properties* (Wiley-VCH, Berlin, 2004).
47. S. Iijima. Helical microtubules of graphitic carbon. *Nature* **354**, 56 (1991).
48. S. Iijima and T. Ichihashi. Single-shell carbon nanotubes of 1-nm diameter. *Nature* **363**, 603 (1993).
49. R. Krupke, F. Hennrich, H. von Lohneysen and M. M. Kappes. Separation of metallic from semiconducting single-walled carbon nanotubes. *Science* **301**, 344–347 (2003).
50. W. Hönlein and F. Kreupl. Kohlenstoff-nanoröhrchen für die mikroelektronik. *Physik Journal* **3**, 39 (2004).
51. M. Damnjanović, I. Milosević, T. Vuković and R. Sredanović. Full symmetry, optical activity, and potentials of single-wall and multiwall nanotubes. *Phys. Rev. B* **60**, 2728 (1999).
52. M. Dresselhaus, G. Dresselhaus and P. Avouris. *Carbon Nanotubes: Synthesis, Structure, Properties, and Applications* (Springer, Berlin, 2001).

53. R. Saito, G. Dresselhaus and M. S. Dresselhaus. Trigonal warping effect of carbon nanotubes. *Phys. Rev. B* **61**, 2981 (2000).
54. S. Reich and C. Thomsen. Chirality dependence of the density-of-states singularities in carbon nanotubes. *Phys. Rev. B* **62**, 4273 (2000).
55. S. Reich, J. Maultzsch, C. Thomsen and P. Ordejón. Tight-binding description of graphene. *Phys. Rev. B* **66**, 035412 (2002).
56. M. Damnjanović, I. Milosević, T. Vuković and J. Maultzsch. Quantum numbers and band topology of nanotubes. *J. Phys. A* **36**, 5707 (2003).
57. H. Ajiki and T. Ando. *J. Phys. Soc. Jpn.* **62**, 4267 (1993).
58. A. Grüneis, R. Saito, G. G. Samsonidze, T. Kimura, M. A. Pimenta, A. Jorio, A. G. SouzaFilho, G. Dresselhaus and M. S. Dresselhaus. Inhomogeneous optical absorption around the K point in graphite and carbon nanotubes. *Phys. Rev. B* **67**, 165402 (2003).
59. T. Vuković, I. Milošević and M. Damnjanović. Carbon nanotubes band assignment, topology, Bloch states, and selectionrules. *Phys. Rev. B* **65**, 045418 (2002).
60. I. Božović, N. Božović and M. Damnjanović. Optical dichroism in nanotubes. *Phys. Rev. B* **62**, 6971 (2000).
61. R. Loudon. *Am. J. Phys.* **27**, 649 (1959).
62. K. Ohno. *Theor. Chim. Acta* **2**, 219 (1964).
63. S. Piscanec, M. Lazzeri, F. Mauri, A. Ferrari and J. Robertson. Kohn anomalies and electron-phonon interaction in graphite. *Phys. Rev. Lett.* **93**, 185503 (2004).
64. M. Lazzeri, S. Piscanec, F. Mauri, A. Ferrari and J. Robertson. Electron transport and hot phonons in carbon nanotubes. *Phys. Rev. Lett.* **95**, 236802 (2005).
65. M. Lazzeri, S. Piscanec, F. Mauri, A. Ferrari and J. Robertson. Phonon linewidths and electron-phonon coupling in graphite and nanotubes. *Phys. Rev. B* **73**, 155426 (2006).
66. S. Piscanec, M. Lazzeri, J. Robertson, A. Ferrari and F. Mauri. Optical phonons in carbon nanotubes: Kohn anomalies, peierls distortions, and dynamic effects. *Phys. Rev. B* **75**, 035427 (2007).
67. P. Y. Yu and M. Cardona. *Fundamentals of Semiconductors* (Springer, 2001).
68. M. Mohr, J. Maultzsch, E. Dobardzic, S. Reich, I. Milosevic, M. Damnjanovic, A. Bosak, M. Krisch and C. Thomsen. Phonon dispersion of graphite by inelastic x-ray scattering. *Phys. Rev. B* **76**, 035439 (2007).
69. J. Maultzsche, S. Reich, C. Thomson, H. Requardt and J. Ordejón. Phonon dispersions in graphite. *Phys. Rev. Lett.* **92**, 75501 (2004).
70. I. Milošević, T. Vuković, S. Dmitrović and M. Damnjanović. Polarized optical absorption in carbon nanotubes: A symmetry-based approach. *Phys. Rev. B* **67**, 165418 (2003).
71. V. N. Popov and L. Henrard. Comparative study of the optical properties of single-walled carbon nanotubes within orthogonal and nonorthogonal tight-binding models. *Phys. Rev. B* **70**, 115407 (2004).

72. E. Malić, M. Hirtschulz, F. Milde, A. Knorr and S. Reich. Analytical approach to optical absorption in carbon nanotubes. *Phys. Rev. B* **74**, 195431 (2006).
73. E. Malić, M. Hirtschulz, F. Milde, Y. Wu, J. Maultzsch, T. F. Heinz, A. Knorr and S. Reich. Theoretical approach to rayleigh and absorption spectra of semiconducting carbon nanotubes. *Phys. Status Solidi (b)* **244**, 4240 (2007).
74. E. Malić, M. Hirtschulz, F. Milde, Y. Wu, J. Maultzsch, T. F. Heinz, A. Knorr and S. Reich. Theory of rayleigh scattering from metallic carbon nanotubes. *Phys. Rev. B* **77**, 045432 (2008).
75. E. Malić, M. Hirtschulz, F. Milde, J. Maultzsch, S. Reich and A. Knorr. Coulomb effects in single-walled carbon nanotubes. *Phys. Status Solidi (b)* (2008).
76. S. Reich, C. Thomsen and J. Robertson. Exciton resonances quench the photoluminescence of zigzag carbon nanotubes. *Phys. Rev. Lett.* **95**, 077402 (2005).
77. G. N. Ostojić, S. Zarić, J. Kono, M. S. Strano, V. C. Moore, R. H. Hauge and R. E. Smalley. Interband recombination dynamics in resonantly excited single-walled carbon nanotubes. *Phys. Rev. Lett.* **92**, 117402 (2004).
78. C. Manzoni, A. Gambetta, E. Menna, M. Meneghetti, G. Lanzani and G. Cerullo. Intersubband exciton relaxation dynamics in single-walled carbon nanotubes. *Phys. Rev. Lett.* **94**, 207401 (2005).
79. X. Blase, L. X. Benedict, E. L. Shirley and S. G. Louie. Hybridization effects and metallicity in small radius carbon nanotubes. *Phys. Rev. Lett.* **72**, 1878 (1994).
80. M. Y. Sfeir, T. Beetz, F. Wang, L. Huang, C. M. H. Huang, M. Huang, J. Hone, S. O'Brien, J. A. Misewich, T. F. Heinz, L. Wu, Y. Zhu and L. E. Brus. Optical spectroscopy of individual single-walled carbon nanotubes of defined chiral structure. *Science* **312**, 554 (2006).
81. F. Wang, M. Y. Sfeir, L. Huang, X. M. H. Huang, Y. Wu, J. Kim, J. Hone, S. O. and Louis E. Brus and T. F. Heinz. Interactions between individual carbon nanotubes studied by rayleigh scattering spectroscopy. *Phys. Rev. Lett.* **96**, 167401 (2006).
82. Y. Wu, J. Maultzsch, E. Knoesel, B. Chandra, M. Y. Huang, M. Y. Sfeir, L. E. Brus, J. Hone and T. F. Heinz. Variable electron-phonon coupling in isolated metallic carbon nanotubes observed by raman scattering. *Phys. Rev. Lett.* **99**, 027402 (2007).
83. T. Ando. Excitons in carbon nanotubes. *J. Phys. Soc. Jap.* **66**, 1066–1073 (1997).
84. R. Egger and A. O. Gogolin. Effective low-energy theory for correlated carbon nanotubes. *Phys. Rev. Lett.* **79**, 5082–5085 (1997).
85. T. G. Pedersen. Variational approach to excitons in carbon nanotubes. *Phys. Rev. B* **67**, 73401 (2003).
86. C. L. Kane and E. J. Mele. Ratio problem in single carbon nanotube fluorescence spectroscopy. *Phys. Rev. Lett.* **90**, 207401 (2003).
87. M. Hirtschulz, F. Milde, E. Malić, C. Thomsen, S. Reich and A. Knorr. Theory of ultrafast intraband relaxation in carbon nanotubes. *Phys. Status Solidi (b)* (2008).
88. M. Hirtschulz, F. Milde, E. Malić, S. Butscher, C. Thomsen, S. Reich and A. Knorr. Carbon nanotube bloch equations: A many-body approach to nonlinear and ultrafast optical properties. *Phys. Rev. B* **77**, 035403 (2008).

89. C. Spataru, S. Ismail-Beigi, R. B. Capaz and S. G. Louie. Theory and ab initio calculation of radiative lifetime of excitons in semiconducting carbon nanotubes. *Phys. Rev. Lett.* **95**, 247402 (2005).
90. V. Perebeinos, J. Tersoff and P. Avouris. Radiative lifetime of excitons in carbon nanotubes. *Nano Lett.* **5**, 2495–2499 (2005).
91. E. Barros, A. Jorio, G. G. Samsonidze, R. B. Capaz, A. G. Souza, G. Antonio, J. Mendes, G. Dresselhaus and M. S. Dresselhaus. Review on the symmetry-related properties of carbon nanotubes. *Phys. Rep.* **431**, 261–302 (2006).
92. T. Ando. Effects of valley mixing and exchange on excitons in carbon nanotubes with aharonov-bohm flux. *J. Phys. Soc. Jap.* **75**, 024707 (2006).
93. H. Seferyan, M. B. Nasr, V. Senekerimyan, R. Zadoyan, P. Collins and V. A. Apkarian. Transient grating measurements of excitonic dynamics in single-walled carbon nanotubes: The dark excitonic bottleneck. *Nano Lett.* **6**, 1757–1760 (2006).
94. E. Chang, D. Prezzi, A. Ruini and E. Molinari. Dark excitons in carbon nanotubes. *cond-mat/0603085 (unpublished)* (2006).
95. F. Wang, G. Dukovic, L. E. Brus and T. F. Heinz. Time-resolved fluorescence of carbon nanotubes and its implication for radiative lifetimes. *Phys. Rev. Lett.* **92**, 177401 (2004).
96. Y. Ma, J. Stenger, J. Zimmermann, S. M. Bachilo, R. E. Smalley, R. B. Weisman and G. R. Fleming. Ultrafast carrier dynamics in single-walled carbon nanotubes probed by femtosecond spectroscopy. *The Journal of chemical physics* **120**, 3368–3373 (2004).
97. A. Hagen, M. Steiner, M. B. Raschke, C. Lienau, T. Hertel, H. Qian, A. J. Meixner and A. Hartschuh. Exponential decay lifetimes of excitons in individual single-walled carbon nanotubes. *Phys. Rev. Lett.* **95**, 197401 (2005).
98. P. Avouris, M. Freitag and V. Perebeinos. Carbon-nanotube photonics and optoelectronics. *Nature Photonics* **2**, 341–350 (2008).
99. S. Berger, C. Voisin, G. Cassaboiss, C. Delalande, P. Roussignol and X. Marie. Temperature dependence of exciton recombination in semiconducting single-wall carbon nanotubes. *Nano Lett.* **7**, 398–402 (2007).
100. S. Zaric, G. N. Ostojic, J. Kono, J. Shaver, V. C. Moore, M. S. Strano, R. H. Hauge, R. E. Smalley and X. Wei. Optical signatures of the aharonov-bohm phase in single-walled carbon nanotubes. *Science* **304**, 1129–1131 (2004).
101. I. Mortimer and R. J. Nicholas. Role of bright and dark excitons in the temperature-dependent photoluminescence of carbon nanotubes. *Phys. Rev. Lett.* **98**, 027404 (2007).
102. H. Kataura, Y. Kumazawa, Y. Maniwa, I. Umezub, S. Suzukic, Y. Ohtsukac and Y. Achibac. Optical properties of single-wall carbon nanotubes. *Synthetic metals* **103**, 2555–2558 (1999).
103. R. B. Weisman and S. S. M. Bachilo. Dependence of optical transition energies on structure for single-walled carbon nanotubes in aqueous suspension: An empirical kataura plot. *Nano Letters* **3**, 1235–1238 (2003).
104. P. Araujo, S. K. Doorn, S. Kilina, S. Tretiak, E. Einarsson, S. Maruyama, H. Chacham, M. A. Pimenta and A. Jorio. Third and fourth optical transitions in semiconducting carbon nanotubes. *Phys. Rev. Lett.* **98**, 067401 (2007).

105. T. Michel, M. Paillet, J. C. Meyer, V. N. Popov, L. Henrard and J. L. Sauvajol. E-33 and e-44 optical transitions in semiconducting single-walled carbon nanotubes: Electron diffraction and raman experiments. *Phys. Rev. B* **75**, 155432 (2007).
106. J. Choi and M. S. Strano. Solvatochromism in single-walled carbon nanotubes. *Appl. Phys. Lett.* **90**, 223114 (2007).
107. O. Kiowski, S. Lebedkin, F. Hennrich, S. Malik, H. Rosner, K. Arnold, C. Surgers and M. M. Kappes. Photoluminescence microscopy of carbon nanotubes grown by chemical vapor deposition: Influence of external dielectric screening on optical transition energies. *Phys. Rev. B* **75**, 075421 (2007).
108. C. Spataru, S. Ismail-Beigi, L. X. Benedict and S. G. Louie. Quasiparticle energies, excitonic effects and optical absorption spectra of small-diameter single-walled carbon nanotubes. *Phys. Rev. B* **78**, 1129 (2004).
109. J. Lefebvre, J. M. Fraser, Y. Homma and P. Finnie. Photoluminescence from single-walled carbon nanotubes: a comparison between suspended and micelle-encapsulated nanotubes. *Appl. Phys. A* **78**, 1107–1110 (2004).
110. T. Okazaki, T. Saito, K. Matsuura, S. Ohshima, M. Yumura and S. Iijima. Photoluminescence mapping of "as-grown" single-walled carbon nanotubes: A comparison with micelle-encapsulated nanotube solutions. *Nano Lett.* **5**, 2618–2623 (2005).
111. Y. Ohno, S. Iwasaki, Y. Murakami, S. Kishimoto, S. Maruyama and T. Mizutani. Chirality-dependent environmental effects in photoluminescence of single-walled carbon nanotubes. *Phys. Rev. B* **73**, 235427 (2006).
112. Y. Yin, S. Cronin, A. G. Walsh, A. Stolyarov, M. Tinkham, A. Vamivakas, W. Basca, M. S. Unlu, B. B. Goldberg and A. K. Swan. *cond-mat/0505004 (unpublished)* (2008).
113. M. Strano, V. C. Moore, M. K. Miller, M. J. Allen, E. H. Haroz, C. Kittrell, R. H. Hauge and R. E. Smalley. The role of surfactant adsorption during ultrasonication in the dispersion of single-walled carbon nanotubes. *J. Nanosci. Nanotechnol.* **3**, 81–86 (2003).
114. V. Moore, M. S. Strano, E. H. Haroz, R. H. Hauge, R. E. Smalley, J. Schmidt and Y. Talmon. Individually suspended single-walled carbon nanotubes in various surfactants. *Nano Lett.* **3**, 1379–1382 (2003).
115. P. Suppan. The influence of the medium on the energy of electronic states. *J. Photochem. Photobiol. A* **50**, 293 (1990).
116. F. Wang, D. J. Cho, B. Kessler, J. Deslippe, P. J. Schuck, S. G. Louie, A. Zettl, T. F. Heinz and Y. R. Shen. Observation of excitons in one-dimensional metallic single-walled carbon nanotubes. *Phys. Rev. Lett.* **99**, 227401 (2007).
117. J. Deslippe, C. D. Spataru, D. Prendergast and S. G. Louie. Bound excitons in metallic single-walled carbon nanotubes. *Nano Lett.* **7**, 1626–1630 (2007).
118. Z. Yao. High-field electrical transport in single-wall carbon nanotubes. *Phys. Rev. Lett.* **84**, 2941–2944 (2000).
119. F. Plentz, H. B. Ribeiro, A. Jorio, M. S. Strano and M. A. Pimenta. Direct experimental evidence of exciton-phonon bound states in carbon nanotubes. *Phys. Rev. Lett.* **95**, 247401 (2005).

120. Y. M. aand S. Maruyama. Identification of an excitonic phonon sideband by photoluminescence spectroscopy of single-walled carbon-13 nanotubes. *Phys. Rev. B* **74**, 035415 (2006).
121. V. Perebeinos, J. Tersoff and P. Avouris. Effect of exciton-phonon coupling in the calculated optical absorption of carbon nanotubes. *Phys. Rev. Lett.* **94**, 027402 (2005).
122. V. Perebeinos, J. Tersoff and P. Avouris. Electron-phonon interaction and transport in semi-conducting carbon nanotubes. *Phys. Rev. Lett.* **94**, 086802 (2005).
123. S. Berciaud, L. Cognet, P. Poulin, R. B. Weisman and B. Lounis. Absorption spectroscopy of individual single-walled carbon nanotubes. *Nano Lett.* **7**, 1203–1207 (2007).
124. D. Bimberg. Quantum dots for lasers, amplifiers and computing. *J. Phys. D* **38**, 2055–2058 (2005).
125. M. Kuntz. *Modulated InGaAs/GaAs quantum dot lasers*. Ph.D. thesis (2005).
126. K. T. Tan, C. Marinelli, M. Thompson, A. Wonfor, M. Silver, R. Sellin, R. Penty, I. White, M. Kuntz, M. Lammlin, N. Ledentsov, D. Bimberg, A. Zhukov, V. Ustinov and A. Kovsh. High bit rate and elevated temperature data transmission using ingaas quantum-dot lasers. *IEEE Photonics Technology Letters* **16**, 1415–1417 (2004).
127. K. Otsubo, N. Hatori, M. Ishida, S. Okumura, T. Akiyama, Y. Nakata, H. Ebe, M. Sugawara and Y. Arakawa. Temperature-insensitive eye-opening under 10-gb/s modulation of 1.3- μm p-doped quantum-dot lasers without current adjustments. *Jap. J. Appl. Phys.* **43**, L1124–L1126 (2004).
128. M. Kuntz, G. Fiol, M. Lämmlin, C. Schubert, A. R. Kovsh, A. Jacob, A. Umbach and D. Bimberg. 10gbit/s data modulation using 1.3 μm ingaas quantum dot lasers. *Electron. Lett.* **41**, 244–245 (2005).
129. T. R. Nielsen, P. Gartner and F. Jahnke. Many-body theory of carrier capture and relaxation in semiconductor quantum dot lasers. *Phys. Rev. B* **69**, 235314 (2004).
130. A. Wojs, P. Hawrylak, S. Fafard and L. Jacak. Electronic structure and magneto-optics of self-assembled quantum dots. *Phys. Rev. B* **54**, 5604–5608 (1996).
131. O. Stier, M. Grundmann and D. Bimberg. Electronic and optical properties of strained quantum dots modeled by 8-band k.p theory. *Phys. Rev. B* **59**, 5688–5701 (1999).
132. Y. P. Varshni. Temperature dependence of the energy gap in semiconductors. *Physica* **34**, 149 (1967).
133. R. Wetzler, A. Wacker and E. Schöll. Coulomb scattering with remote continuum states in quantum dot devices. *J. Appl. Phys.* **95**, 7966–7970 (2004).
134. M. Lorke, T. R. Nielsen, J. Seebeck, P. Gartner and F. Jahnke. Influence of carrier-carrier and carrier-phonon correlations on optical absorption and gain in quantum-dot systems. *Phys. Rev. B* **73**, 085324 (2006).
135. O. Madelung. *Landolt-Börnstein*, vol. III/22a (Springer, 1987).
136. H. C. Schneider, W. W. Chow and S. W. Koch. Influence of coupling between localized and continuum states in ingan quantum-dot systems. *Phys. Status Solidi (b)* **238**, 589–592 (2003).

137. M. Mosko and A. Moskova. Exchange carrier-carrier scattering of spin-polarized 2-dimensional electron-hole plasma - monte carlo study. *Semicond. Sci. Technol.* **9**, 478–481 (1994).
138. E. Schöll. *Nonequilibrium Phase Transitions in Semiconductors* (Springer, 1987).
139. W. H. Press, S. A. Teukolsky, W. T. Vetterling and B. P. Flannery. *Numerical Recipes in C: The Art of Scientific Computing* (Cambridge University Press, 1992).
140. K. Lüdge, M. Bormann, E. Malić, P. Hövel, M. Kuntz, D. Bimberg, A. Knorr and E. Schöll. Turn-on dynamics and modulation response in semiconductor quantum dot lasers. *Phys. Rev. B* **78**, 35316 (2008).
141. J. Kim, E. Malić, M. Richter and A. Knorr (in preparation, 2008).
142. J. Förstner, C. Weber, J. Danckwerts and A. Knorr. Phonon-assisted damping of rabi oscillations in semiconductor quantum dots. *Phys. Rev. Lett.* **91**, 127401 (2003).
143. B. Krummheuer, V. M. Axt, T. Kuhn, I. D’Amico and F. Rossi. Pure dephasing and phonon dynamics in GaAs- and GaN-based quantum dot structures: Interplay between material parameters and geometry. *Phys. Rev. B* **71**, 235329 (2005).
144. P. Borri, W. Langbein, S. Schneider, U. Woggon, R. L. Sellin, D. Ouyang and D. Bimberg. Exciton relaxation and dephasing in quantum-dot amplifiers from room to cryogenic temperature. *IEEE Sel. Topics J. Quantum Electron.* **8**, 984–991 (2002).
145. J. M. A. Mecozzi. Theory of heterodyne pump-probe experiments with femtosecond pulses. *J. Opt. Soc. Am. B* **13**, 2437–2452 (1996).
146. H. A. Ferwerda, J. Terpstra, A. Douwe and A. Wiersma. Discussion of a coherent artifact in four-wave mixing experiment. *J. Chem. Phys.* **91**, 3296 (1989).
147. M. Richter, T. Renger and A. Knorr. A bloch equation approach to intensity dependent optical spectra of light harvesting complex ii. *Photosynth. Res.* **95**, 119–127 (2008).
148. J. Mork and A. Mecozzi. Theory of the ultrafast optical response of active semiconductor waveguides. *J. Opt. Soc. B* **13**, 1803–1816 (1996).
149. J. Gomis and U. Woggon (TU Berlin, private communication (2008)).
150. M. Kuntz, N. N. Ledentsov, D. Bimberg, A. R. Kovsh, V. M. Ustinov, A. E. Zhukov and Y. M. Shernyakov. Spectrotemporal response of 1.3 μm quantum-dot lasers. *Appl. Phys. Lett.* **81**, 3846–3848 (2002).
151. H. Huang and D. G. Deppe. Rate equation model for nonequilibrium operating conditions in a self-organized quantum-dot laser. *IEEE J. Quantum Electron.* **37**, 691–698 (2001).
152. G. Huyet, D. O’Brien, J. G. McInerney, A. V. Uskov, D. Bimberg, C. Ribbat, V. M. Ustinov, A. E. Zhukov, S. S. Mikhlin, A. R. Kovsh, J. K. White, K. Hinzer and A. J. SpringThorpe. Quantum dot semiconductor lasers with optical feedback. *Phys. Status Solidi (a)* **201**, 345–352 (2004).
153. D. O’Brien, S. P. Hegarty, G. Huyet and A. V. Uskov. Sensitivity of quantum-dot semiconductor lasers to optical feedback. *Optics Lett.* **29**, 1072–1074 (2004).

154. H. Dery and G. Eisenstein. The impact of energy band diagram and inhomogeneous broadening on the optical differential gain in nanostructure lasers. *IEEE J. Quantum Electron.* **41**, 26–35 (2005).
155. E. Viktorov, P. Mandel, A. G. Vladimirov and U. Bandelow. Model for mode locking in quantum dot lasers. *Appl. Phys. Lett.* **88**, 201102 (2006).
156. E. Avrutin, J. M. Arnold and J. H. Marsh. Dynamic modal analysis of monolithic mode-locked semiconductor lasers. *IEEE Sel. Topics J. Quantum Electron.* **9**, 844–856 (2003).
157. T. Erneux, E. A. Viktorov and P. Mandel. Time scales and relaxation dynamics in quantum-dot lasers. *Phys. Rev. A* **76**, 023819–1–023819–7 (2007).
158. A. Fiore and A. Markus. Differential gain and gain compression in quantum-dot lasers. *IEEE J. Quantum Electron.* **43**, 287–294 (2007).
159. E. Schöll, D. Bimberg, H. Schumacher and P. T. Landberg. Kinetics of picosecond pulse generation in semiconductor lasers with bimolecular recombination at high current injection. *IEEE J. Quantum Electron.* **20**, 394–398 (1984).
160. E. Schöll. Dynamic theory of picosecond optical pulse shaping by gain-switched semiconductor laser amplifiers. *IEEE J. Quantum Electron.* **24**, 435–442 (1988).
161. W. W. Chow, A. Knorr, S. Hughes, A. Girndt, and S. W. Koch. Carrier correlation effects in a quantum-well semiconductor laser medium. *IEEE Sel. Topics J. Quantum Electron.* **3**, 136–141 (1997).
162. E. Malić, K. J. Ahn, M. J. P. Bormann, P. Hovel, E. Scholl, A. Knorr, M. Kuntz and D. Bimberg. Theory of relaxation oscillations in semiconductor quantum dot lasers. *Appl. Phys. Lett.* **89**, 101107 (2006).
163. E. Malić, J. P. Bormann, P. Hovel, M. Kuntz, D. Bimberg, A. Knorr and E. Scholl. Coulomb damped relaxation oscillations in semiconductor quantum dot lasers. *IEEE Sel. Topics J. Quantum Electron.* **13**, 1242–1248 (2007).
164. M. Grundmann and D. Bimberg. Theory of random population for quantum dots. *Phys. Rev. B* **55**, 9740–9745 (1997).
165. N. Baer, C. Gies, J. Wiersig and F. Jahnke. Luminescence of a semiconductor quantum dot system. *Eur. Phys. J. B* **50**, 411–418 (2006).

Index

- absorption coefficient, 32, 62
- angular momentum, 57
- annihilation operator, 21
- armchair tubes, 39

- band gap renormalization, 75
- band-to-band transition, 37, 62
- Beer-Lambert law, 33
- Bethe-Salpeter, 75
- Bloch equations, 27, 111
- Bloch functions, 100
- Bloch theorem, 41
- Boltzmann equation, 104, 136

- carbon nanotubes (CNTs), 37
- chiral angle, 39
- cluster expansion, 27
- coherence, 20
- coherent artifact, 117
- commutation relation, 21, 131
- confinement factor, 123
- correlation expansion, 28
- Coulomb matrix element
 - CNTs, 55, 75, 141
 - QDs, 102, 144
- Coulomb scattering rates, 29, 104
- creation operator, 21

- dark exciton, 81
- de Broglie wavelength, 19, 98
- density matrix theory, 19
- density operator, 19
- depolarization, 77
- dielectric function, 33, 69
- dipole approximation, 21, 34, 49
- dipole matrix element, 22

- effective mass, 24
- effective well width approximation, 101
- Ehrenfest theorem, 28
- Einstein coefficient, 121, 140
- electron-phonon matrix element
 - CNTs, 59
- exciton, 75
- expectation value, 20
- extended tight-binding model (ETB), 85
- eye pattern, 98

- family patterns, 83
- Fermi-Dirac distribution, 105
- finite barrier well, 101

- gain, 111
- gain condition, 111
- gain depletion, 111
- gain recovery, 98, 111
- graphene, 41

- Hamilton operator, 21, 27
- harmonic oscillator, 2-dim, 100
- Hartree-Fock approximation, 28, 75, 132
- Heisenberg equation, 27, 131
- Heisenberg picture, 28
- helical indices, 48
- heterodyne detection, 111
- hierarchy problem, 28
- high-symmetry lines ($\Gamma K M$), 51
- homogeneous space, 32

- induced emission, 121
- intersubband processes, 57
- intervalley mixing, 81

- K point, 42, 47
- Kataura plot, 42, 83

- length gauge, 23
- light-matter interaction, 21
- Lindhard approximation, 57, 91, 104
- line group, 39
- linear indices, 48

- macroscopic current, 33
- macroscopic polarization, 33
- Markov approximation, 28, 31, 135

- material equations, 32
Maxwell equations, 32
mean-field approximation, 28
metallic nanotubes, 42, 91
microscopic polarisation, 20, 27
Mie theory, 35, 149
mirror planes, 51
mixed state, 20
- nanotube families, 42, 83
nearest-neighbor approximation, 26, 44, 50
Noether theorem, 48
- Ohno potential, 56, 142
optical gap, 64
optical matrix element
 CNTs, 49
 QDs, 102
orthogonalized plane waves (OPWs), 100
- p·A approach, 22
Pauli exclusion principle, 106
phonon sidebands, 30
phonon-assisted quantities, 30
photon density, 121
photons, 137
population probability, 20, 27
Poynting vector, 35
pulse area, 111, 115
pump power, 117
pump-probe experiment, 111
pure dephasing, 109
pure rotation, 39
pure state, 20
- QD charge carrier density, 121
QD laser, 98, 120
QD optical amplifiers, 110
quasi-Fermi level, 2D, 105
- r·E approach, 22
Rabi flopping, 111
Rabi frequency, 77
radiation gauge, 21
random phase approximation, 31, 75
ratio problem, 75
Rayleigh scattering, 69
Rayleigh scattering cross section, 35, 149
refractive index, 33
relaxation oscillations, 98, 120
relaxation rate approximation, 105
repetition rate, 110
rotating wave approximation (RWA), 30, 83
Runge-Kutta method, 112
- scalar potential, 21
Schrödinger equation, 20
Schrödinger picture, 20
screening
 CNTs, 57, 91
 QDs, 104
screw axis, 39
second quantization, 21
selection rules, 51
semiconducting nanotubes, 42
solvatochromic shift, 89
spin, 105
spontaneous emission, 121, 137
Stranski-Krastanow growth, 97
susceptibility, 32, 69
- T_1 time, 109
 T_2 time, 109, 116
telegraph equation, 33
threshold current density, 124
tight-binding approach, 25
trigonal warping effect, 42, 70, 83
two-photon absorption (TPA), 117
- U operation, 39
Umklapp processes, 48
uncertainty principle, 99
- Van Hove singularity, 37
Varshni equation, 99
vector harmonics, 35
vector potential, 21
velocity gauge, 23
Von Neumann equation, 20
- wave equation, 32
wetting layer, 99
Wigner function, 31
WL carrier density, 123
- zigzag tubes, 39
zone-folding approximation, 41

Acknowledgements

I take this opportunity to thank all the people who helped me to write this thesis. Especially, I would like to thank

- Prof. Andreas Knorr for his continuous support, his friendly and encouraging way, for many inspiring ideas, for being an example that even as a successful professor a balanced life besides physics is possible, and for giving me the chance to experience one of the most impressive moments - lava flowing into the Pacific ocean.
- Prof. Stephanie Reich for reviewing this work, for convincing me to do research on carbon nanotubes, for many fruitful discussions on the symmetry of nanotubes, for a wonderful year at MIT including lots of Ben&Jerry's ice cream, and for giving me the opportunity to experience the land of the rising sun.
- Prof. Eckehard Schöll and Kathy Lüdge for a successful cooperation on the theory of the turn-on dynamics in QD lasers, and Prof. Schöll for being my *Vertrauensdozent* in the *Studienstiftung des deutschen Volkes* including many nice theater and exhibition visits.
- Prof. Ulrike Woggon, Jordi Gomis, and Sabine Dommers for a successful cooperation on QD amplifiers, and Prof. Woggon for being the chair of my thesis committee.
- Prof. Dieter Bimberg and Matthias Kuntz for providing experimental data on relaxation oscillations in QD lasers.
- Prof. Janina Maultzsch for many fruitful and encouraging discussions on Rayleigh scattering and excitons, for a wonderful weekend in New York (with my first big talk), and for proof-reading of this manuscript.
- Prof. Tony F. Heinz for support in understanding the Rayleigh scattering from carbon nanotubes.
- Prof. Elisa Molinari, Alice Ruini, and Deborah Prezzi for a great time in Modena, for many helpful discussions on exciton-phonon coupling in nanotubes, for teaching me Italian (good and bad words), for delicious food, and for recommending Cinque Terre, which have become one of my favorite places in Europe.
- Prof. Francesco Mauri and Michele Lazzari for the cooperation on the calculation of electron-phonon matrix elements and many helpful phone calls.
- Carsten Weber for encouraging discussions on physics and topics beyond it, for being easy to convince to go early to Mensa, for a nice weekend in Lund, for reading large parts of the manuscript with much care, and for writing the successful reference letter for the DAAD award.

- AG Knorr for an extraordinarily good working atmosphere, in particular Marten Richter (a walking physics library and the absolute computer expert), Frank Milde (my office mate, table tennis opponent, and music adviser), Matthias Hirtshulz (co-worker in the field of nanotubes and my skiing instructor), Jeong-Eun (co-worker for the scattering rates in QD lasers), Jens Förstner (my former office mate and chocolate provider), Anna Grodecka (*Anna Banana ;)*), and Stefan Butscher (my Berlin marathon fellow sufferer).
- Mareike Godolt (who read the entire manuscript!), Witlef Wieczorek, and Matthias-Rene Dachner for careful reading of the manuscript.
- Studienstiftung des deutschen Volkes for the scholarship giving me the opportunity to focus on my thesis, for financing my research stays in the U.S. and in Italy, for the advanced language course in England, and the great time at summer academies in France in Southern Germany.
- my friends, my sister, and my parents.

Zusammenfassung der Dissertation

Many-particle theory of optical properties in low-dimensional nanotstructures

vorgelegt von Ermin Malić

Die vorgelegte Dissertationsarbeit beschäftigt sich mit optischen Eigenschaften von niederdimensionalen Nanostrukturen am Beispiel von Kohlenstoff-Nanoröhren und Quantenpunkten. Die Kohlenstoff-Nanoröhren sind quasi-eindimensionale Nanostrukturen, deren einzigartige Eigenschaften sie sowohl für die Grundlagenforschung als auch für die Industrie attraktiv machen. In dieser Arbeit wurden mikroskopische Berechnungen des Absorptionskoeffizienten und des Rayleigh-Streuwirkungsquerschnitts im Rahmen eines neuen Ansatzes, der die Dichtematrixtheorie mit Tight-Binding Wellenfunktionen kombiniert, präsentiert. Im Gegensatz zu Ab-Initio-Berechnungen ermöglichen die so hergeleiteten Blochgleichungen die Untersuchung von Nanoröhren beliebiger Chiralität. In Übereinstimmung mit experimentellen Ergebnissen zeigen die berechneten Absorptions- und Rayleigh-Spektren eine Doppelpeak-Struktur bei metallischen Nanoröhren, die sich auf den Trigonal-Warping-Effekt zurückführen läßt. Die Intensitätsverhältnisse der energetisch niedrigsten Anregungen können durch das unterschiedliche Verhalten des optischen Matricelements entlang der hochsymmetrischen Richtungen KT und KM erklärt werden. Die Asymmetrie der Linienform in Rayleighspektren hin zu niedrigeren Energien wurde bestätigt und mit dem Einfluß der nicht-resonanten Beiträge des Brechungsindex begründet.

Außerdem konnte gezeigt werden, dass die Coulomb Wechselwirkung dann maximal ist, wenn der Impulsübertrag gering ist, wobei die Kopplungsstärke für Intersubbandübergänge mit einem senkrechten Impulstransfer auf weniger als 5% abnimmt. Wegen ihrer Eindimensionalität ist die Coulomb Wechselwirkung in Kohlenstoff-Nanoröhren besonders ausgeprägt. Die Elektron - Elektron - Abstoßung führt zu einer Renormierung der Bandlückenenergie, während die anziehende Elektron - Loch - Wechselwirkung zur Ausbildung von Exzitonen mit Bindungsenergien von bis zu 1 eV führt. Die exzitonischen Übergangs- und Bindungsenergien wurden auf ihre Abhängigkeit von der Chiralität, dem Durchmesser und ihrer Familienzugehörigkeit untersucht. Außerdem wurde der Einfluß des die Nanoröhren umgebenden Mediums im Detail studiert.

Das aufgestellte theoretische Modell wurde weiterhin am Beispiel der quasi-nulldimensionalen Quantenpunkte und ihrer Anwendungen als Laser und Verstärker ausgewertet. Eine detaillierte mikroskopische Analyse der nichtlinearen Einschaltdynamik in elektrisch gepumpten InAs/GaAs Quantenpunkt-Lasern zeigt die Ausbildung von Relaxationsoszillationen, die als Folge eines komplexen Zusammenspiels zwischen nichtlinearen Coulomb-Streuprozessen (zwischen gebundenen Quantenpunkt-Zuständen und den sie umgebenden kontinuierlichen Wetting - Layer - Zuständen) und der radiativen Prozesse entstehen. In Übereinstimmung mit experimentellen Ergebnissen sagt die Theorie eine starke Dämpfung dieser Oszillationen für Quantenpunkt-Laser vorher und stellt dabei die entscheidende Bedeutung der Coulomb-induzierten Augerprozesse heraus.

Schließlich wurde die ultraschnelle Gain-Dynamik von quantenpunkt-basierten optischen Verstärkern mikroskopisch untersucht. Dabei wurde diese insbesondere auf ihre Abhängigkeit von der Stärke der Coulomb-Streuung, der Temperatur, der Dephasierungszeit und der Pulsintensität untersucht. Die erhaltenen Ergebnisse tragen zu einem besseren Verständnis sowohl des sogenannten *kohärenten Artefakts* als auch der limitierenden Mechanismen für eine ultraschnelle Gainerholung in quantenpunkt-basierten Verstärkern bei.